広島大学学位請求論文

Measurement of light vector mesons via di-electron decays in Au+Au collisions at $\sqrt{s_{NN}}$ = 200 GeV and measurability in central Pb+Pb collisions at $\sqrt{s_{NN}}$ = 5.5 TeV
(核子対当たり重心系エネルギー200 GeV 金+金衝突における電子対崩壊を用いた低質量ベクトル中間子測定と核子対当たり重心系エネルギー5.5 TeV 鉛+鉛中心衝突における測定可能性)

2014 年

広島大学大学院理学研究科
物理科学専攻

中宮　義英

（広島大学理学研究科 契約技術職員）

目次

主論文

Measurement of light vector mesons via di-electron decays in Au+Au collisions at $\sqrt{s_{NN}} = 200$ GeV and measurability in central Pb+Pb collisions at $\sqrt{s_{NN}} = 5.5$ TeV

Yoshihide Nakamiya[a]

[a] Department of Physics Science, Graduate School of Science
Hiroshima University
Kagamiyama 1-3-1, Higashi-Hiroshima, 739-8526, Japan

2014

Abstract

High-energy heavy-ion collisions provide a unique opportunity to liberate quarks and gluons from nucleons and cause the phase transition from nuclear matter to quark-gluon matter. Heavy-ion collisions have the advantages of studying the QCD phase diagram especially in high-temperature and low-baryon-density domains.

The mass modification of light vector mesons such as ϕ, ω and ρ is one of the important signatures of the QCD phase transition, because their masses are strongly related to chiral condensate. Chiral condensate is one of the prominent order parameters characterizing the QCD phase structure.

The light vector mesons can be "standard candles" to study the properties of quark-gluon matter produced in heavy-ion collisions. The mass modification inside quark-gluon matter is potentially visible because their lifetimes are supposed to be comparable with the duration of the thermal equilibrium state. In addition, electron-positron pairs, which are referred as "di-electrons", decaying from light vector mesons are clear probes because charged leptons carry the original information in quark-gluon matter without strong interaction with hadronic matter in the relatively later stage of the system evolution.

Experimentally the signals of the mass modification are extracted by analyzing the mass spectrum shape of light vector mesons. In addition, the branching ratios between different decay channels can change by the effect of the mass modification, especially the comparison between $\phi \to e^+e^-$ and $\phi \to K^+K^-$ is important because di-kaon decays are expected to be suppressed even in the small mass modification due to the small Q value.

The production of ϕ and ω mesons in Au+Au collisions at $\sqrt{s_{NN}}$= 200 GeV has been studied in the PHENIX experiment at Relativistic Heavy Ion Collider. The invariant yield as a function of transverse momentum with the range of $0 < p_T < 4$ GeV/c has been measured, and the measurement covers the transverse momentum range of $0 < p_T < 8$ GeV/c for ϕ mesons and $0 < p_T < 20$ GeV/c for ω mesons by combining with different decay channels. The transverse momentum spectra of light vector mesons are systematically studied in different collision geometries, that is, from peripheral to central Au+Au collisions. The characteristics of the spectrum shape are investigated in comparison with semi-empirical functions. In addition, the scaling properties of the spectra are studied via the number of binary collisions and the number participant nucleons provided by the Glauber model.

The mass modification is discussed from the viewpoints of the mass spectrum shape and the branching ratio. The signature of the mass modification cannot be extracted from the mass spectrum shape of the light vector mesons due to the poverty of the signal-to-background ratio and the statistical significance so far. The result of the yield fraction between $\phi \to e^+e^-$ and $\phi \to K^+K^-$ is turned out to be as same as that in vacuum within errors. In conclusion, any symptom of the mass modification is not observed in Au+Au collisions at $\sqrt{s_{NN}} = 200$ GeV.

The second main part of the thesis is the feasibility study of di-electron measurement in central Pb+Pb collisions at $\sqrt{s_{NN}} = 5.5$ TeV. The simulation takes the key aspects of heavy-ion collisions and experimental issues relevant to di-electron measurement into account and has capabilities of providing a guideline to be applicable to a concrete detector design with the wide range of experimental parameters. The feasibility is evaluated by the signal-to-background ratio and the statistical significance as a function of the amount of detector materials, the rejection power of background hadrons, the coverage of the detection system. The results of the simulation study suggest that there are realizable parameter ranges to measure light vector mesons via di-electrons with the reasonable significance level for a realistic luminosity in central Pb+Pb collisions at $\sqrt{s_{NN}} = 5.5$ TeV.

Contents

List of Figures

List of Tables

Chapter 1

Introduction

1.1 Quantum chromodynamics

Quantum Chromodynamics is based on the non-Abelian gauge field theory describing the strong interaction of colored quarks and gluons. The QCD Lagrangian is expressed by

$$\mathcal{L}_{\mathcal{QCD}} = \bar{q}^{\alpha}\left(i\not{D}_{\alpha\beta} - m\delta_{\alpha\beta}\right)q^{\beta} - \frac{1}{4}F^{a}_{\mu\nu}F^{\mu\nu}_{a}, \tag{1.1}$$

where q^{α} is the quark filed and $\not{D} \equiv \gamma^{\mu}D_{\mu}$. γ^{μ} are the Dirac γ-matrices. D_{μ} is covariant derivative defined as

$$D_{\mu} \equiv \partial_{\mu} + ig_{s}t^{a}A^{a}_{\mu}, \tag{1.2}$$

where g_s is the QCD coupling constant. t^c corresponds to eight 3×3 matrices and is the generator of the SU(3) group. A^a_μ corresponds to the gluon field with a running from 1 to 8 ($= N_c^2 - 1$, $N_c = 3$), where N_c is the degree of freedom of three "colors". m represents the constituent quark mass shown in Table 1.1. $F^a_{\mu\nu}$ is the field tensor given by

$$F^{a}_{\mu\nu} = \partial_{\mu}A^{a}_{\nu} - \partial_{\nu}A^{a}_{\mu} - g_{s}f_{abc}A^{b}_{\mu}A^{c}_{\nu}, \tag{1.3}$$

$$\left[t^{a}, t^{b}\right] = if_{abc}t^{c}, \tag{1.4}$$

where a is color index from 1 to 3 ($= N_c$) and f_{abc} is the structure constant of the SU(3) group.

The QCD successfully describes the strong interaction, especially reveals two prominent aspects of quark-gluon dynamics. One is the asymptotic freedom [1, 2] and the other is deconfinement. In the framework of the perturbative QCD (pQCD), these features are expressed by the running coupling

constant $\alpha_s(\mu_R) \equiv g_s^2(\mu_R)/4\pi$ as a function of the renormalization scale μ_R via the following renormalization group equation (RGE):

$$\beta(\alpha_s) = \mu_R^2 \frac{d\alpha_s}{d\mu_R^2} = -b_0\alpha_s^2 - b_1\alpha_s^3 - \cdots, \tag{1.5}$$

$$b_0 = (11C_A - 4N_f T_R)/12\pi = (33 - 2N_f)/12\pi, \tag{1.6}$$

$$b_1 = \left(17C_A^2 - N_f T_R (20C_A + 6C_F)\right)/24\pi^2, \tag{1.7}$$

where C_A ($\equiv N_c = 3$) and C_F ($\equiv (N_c^2 - 1)/2N_c = 4/3$) are the color-factor (so-called Casimir factor) associated with gluon emission from a gluon and quark, respectively. N_f is the number of quark flavor. A convenient approximate analytic solution to the RGE is expressed by

$$\alpha_s(\mu_R) \sim \frac{1}{b_0 \ln\left(\mu_R^2/\Lambda_{QCD}^2\right)} \left(1 - \frac{b_1}{b_0^2} \frac{\ln\left[\ln\left(\mu_R^2/\Lambda_{QCD}^2\right)\right]}{\ln\left(\mu_R^2/\Lambda_{QCD}^2\right)}\right), \tag{1.8}$$

where Λ_{QCD} is a constant of integration, that is, non-perturbative scale of QCD. Figure 1.1 shows the energy scale dependence of the running coupling constant α_s. α_s logarithmically decreases as Q increases. In the limit of $Q \to \infty$, α_s is quite small. In other words, quarks and gluons are little interacted at the extremely short distance, which is called "Asymptotic Freedom". While α_s is diverged in the other limit of $Q \to 0$, this fact results in the property of "Confinement".

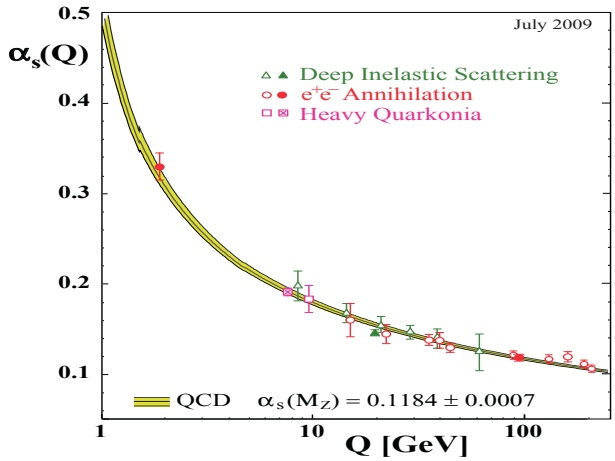

Figure 1.1: The running coupling constant α_s as a function of the respective energy scale Q [3].

1.2 Quark model

The quark model is introduced by M. Gell-Mann [4] and G. Zweig [5, 6] in 1964 to explain the discovery of the many kinds of hadrons. The idea of *color* quantum number is propounded by M. Y. Han, Y. Nambu and O. W. Greenburg [7, 8]. T.Nakano, K.Nishijima and M. Gell-Mann originally relates the baryon number, isospin and strangeness to the charge [9, 10, 11]. The relations, so-called Gell-Mann-Nishijima formula, are extended to relate baryon number and the all *flavor* quantum numbers to the charge in association with the discovery of charm, bottom and top quark as follows.

$$Q = I_z + \frac{\mathcal{B} + S + C + B + T}{2} \tag{1.9}$$

where $\mathcal{B}$ is the baryon number. I_z, S, C, B and T are flavor quantum numbers, that is, isospin z-component, strangeness, charm, bottomness and topness, respectively.

Quarks are strongly interacting fermions with spin $\frac{1}{2}$ and, by convention, positive parity. Antiquarks have negative parity. Quarks and antiquarks have the additive baryon number of $\frac{1}{3}$ and -$\frac{1}{3}$, respectively. Table 1.1 summarizes the other additive quantum number ("*flavor*") for the three generation of the quarks.

The quark model provides the systematic understanding of many hadrons. In the quark model, mesons are $q\bar{q}$ bound states with the baryon number $\mathcal{B}$ = 0. Baryons are fermions consisting of more than three quarks with baryon number $\mathcal{B}$ = 1. In the most general case, baryons are composed of three quarks plus quark-antiquark pairs. So far all observed baryons consist of three quarks. Figure 1.2 and Figure 1.3 show the SU(4) multiplets of the mesons and baryons made of u, d, s and c quarks, respectively.

	Quarks		
Properties	u	d	s
Q - electric charge	$-\frac{1}{3}$	$+\frac{2}{3}$	$-\frac{1}{3}$
I - isospin	$\frac{1}{2}$	$\frac{1}{2}$	0
I_z - isospin z-component	$-\frac{1}{2}$	$+\frac{1}{2}$	0
S - strangeness	0	0	-1
C - charm	0	0	0
B - bottomness	0	0	0
T -topness	0	0	0
Masses (MeV/c^2)	1.7-3.3	4.1-5.8	101^{+29}_{21}
	c	b	t
Q - electric charge	$+\frac{2}{3}$	$-\frac{1}{3}$	$+\frac{2}{3}$
I - isospin	0	0	0
I_z - isospin z-component	0	0	0
S - strangeness	0	0	0
C - charm	+1	0	0
B - bottomness	0	-1	0
T -topness	0	0	+1
Masses (GeV/c^2)	$1.27^{+0.07}_{-0.09}$	$4.19^{+0.18}_{-0.06}$ ($\overline{\text{MS}}$) $4.67^{+0.18}_{-0.06}$ (1S)	172.0± 0.9 ± 1.3 (direct observation)

Table 1.1: The quantum numbers and masses of the three generation of the quarks [12].

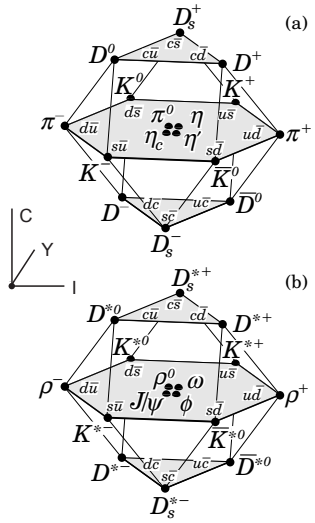

Figure 1.2: SU(4) multiplets (a 15-plet + singlet) for the pseudoscaler mesons (a) and the vector mesons (b) made of u, d, s and c quarks as a function of isospin I, charm C and the hyper charge $Y = S + \mathcal{B} - C/3$. The nonets of light mesons occupy the central places to which the $c\bar{c}$ states have been added.

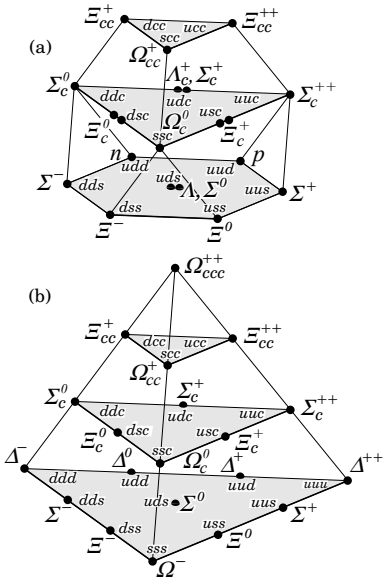

Figure 1.3: SU(4) multiplets of baryons made of u, d, s and c quarks. (a) The 20-plet with with a SU(3) octet. (b) The 20-plet with an SU(3) decuplet.

1.3 Hadron production in high-energy nucleon-nucleon collisions

The hadron production in nucleon-nucleon collisions at high energy is described by hard scattering process of the constituent partons (quarks and gluons) in incident nucleons. The hadron production in a p+p collision, $pp \to hX$, can be factorized into three components, which are the parton distribution function (PDF) f_i^p, parton-parton scattering cross section $\hat{\sigma}^{f_1 f_2 \to f X'}$ and fragmentation function (FF) D_f^h as shown in Fig.1.4. The production cross section is formulated by

$$\sigma^{pp\to hX} = \sum_{f_1,f_2,f} \int dx_1 dx_2 dz f_1^p\left(x_1,\mu^2\right) f_2^p\left(x_2,\mu^2\right) \times \hat{\sigma}^{f_1 f_2 \to f X'}\left(x_1 p_1, x_2 p_2, p_h, \mu\right) \times D_f^h\left(z,\mu^2\right), \quad (1.10)$$

where f_i^p (i=1,2), $\hat{\sigma}^{f_1 f_2 \to f X'}$ and $D_f^h\left(z,\mu^2\right)$ show the PDF, parton-parton scattering cross section and the FF, respectively. f_1, f_2 and f represent partons. X' is unobserved partons. f_1^p and f_2^p are the parton distribution function of partons in incident protons. $D_f^h\left(z,\mu^2\right)$ is the fragmentation function from parton f to final-state hadron h. p_1 and p_2 are the momenta of initial protons. x_1 and x_2 (so-called Bjorken x) are the momentum fractions of partons relative to initial protons. z is the momentum fraction of final-state hadrons relative to initial protons and p_h is the momentum of final-state hadrons. μ is the factorization scale. The factorization scale is arbitrary but frequently assumed to be equal to the renormalization scale μ_R.

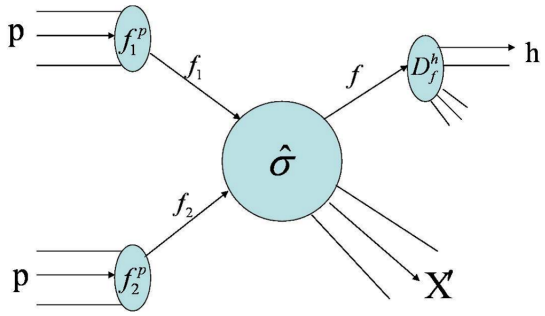

Figure 1.4: The schematic diagram of the hadron production in a hard scattering process in a p+p collision.

1.3.1 Parton distribution function

Parton distribution function is the probability density of partons in a nucleon. The structure function, $F_2(x, Q^2)$, in a proton is well measured at the wide range of x-Q^2 space by lepton deep inelastic scattering (DIS) in many experiments. The results of H1 [13, 14], ZEUS [15, 16] and SLAC [17] are obtained by e-p scattering, and BCDMS [18], E665 [19], NMC [20] and EMC [21] by μ-p scattering. Figure 1.5 shows an example of the measured $F_2(x, Q^2)$. The unpolarized (spin-independent) PDFs are determined by the next-to-leading order or next-to-next-to-leading order (NNLO) perturbative QCD calculations [22, 23, 24, 25]. One example of global analyses is shown in Fig.1.6.

1.3.2 Parton-parton scattering cross section

Parton-parton scattering cross section, $\hat{\sigma}^{f_1 f_2 \to f X'}$, is calculated by the pQCD framework. Hard scattering subprocesses and the associated differential cross-sections in lowest order are listed in Table 1.2.

Process	$\lvert M\rvert^2/16\pi^2\alpha_s^2$
$qq' \to qq'$	$\frac{4}{9}\frac{s^2+u^2}{t^2}$
$q\bar{q}' \to q\bar{q}'$	$\frac{4}{9}\frac{s^2+u^2}{t^2}$
$q\bar{q} \to q'\bar{q}'$	$\frac{4}{9}\frac{t^2+u^2}{s^2}$
$qq \to qq$	$\frac{4}{9}\left(\frac{s^2+u^2}{t^2}+\frac{s^2+t^2}{u^2}\right)-\frac{8}{27}\frac{s^2}{ut}$
$q\bar{q} \to q\bar{q}$	$\frac{4}{9}\left(\frac{s^2+u^2}{t^2}+\frac{t^2+u^2}{s^2}\right)-\frac{8}{27}\frac{u^2}{st}$
$q\bar{q} \to gg$	$\frac{32}{27}\frac{s^2+t^2}{ut}-\frac{8}{3}\frac{u^2+t^2}{s^2}$
$gg \to q\bar{q}$	$\frac{1}{6}\frac{s^2+t^2}{ut}-\frac{3}{8}\frac{u^2+t^2}{s^2}$
$qg \to qg$	$-\frac{4}{9}\frac{u^2+s^2}{us}+\frac{u^2+s^2}{t^2}$
$gg \to gg$	$\frac{9}{2}\left(3-\frac{ut}{s^2}-\frac{us}{t^2}-\frac{st}{u^2}\right)$

Table 1.2: The square amplitude of parton-parton scattering. s,t and u are Mandelstam variables.

1.3.3 Fragmentation function

Fragmentation function, $D_f^h(z, \mu^2)$, is the probability that a parton f fragments into a hadron h carrying a certain fraction z of the parent's momentum. The fragmentation function constraints the conservation of momentum and

probability as follows.

$$\sum_h \int_0^1 z D_f^h \left(z, \mu^2\right) dz = 1 \tag{1.11}$$

Figure 1.7 shows the measured fragmentation function in e^+e^- annihilation in many experiments: ALEPH [27, 28], L3 [29], AMY [30], HRS [31], MARK II [32, 33], OPAL [34, 35, 36, 37, 38, 39], SLD [40], DELPHI [41], TASSO [42, 43] and TPC [44].

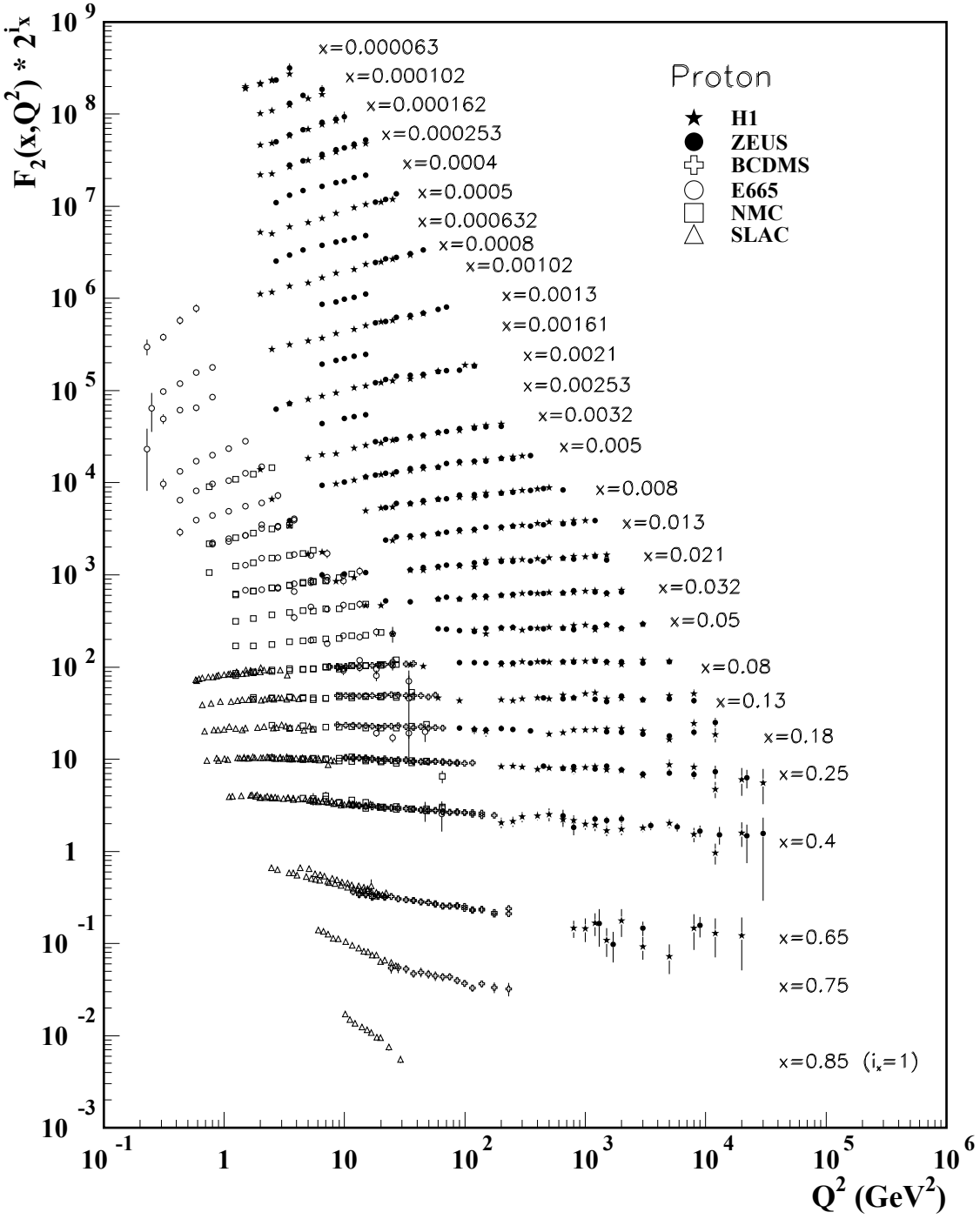

Figure 1.5: The proton structure function $F_2(x, Q^2)$ as a function of Q^2 in bins fixed x.

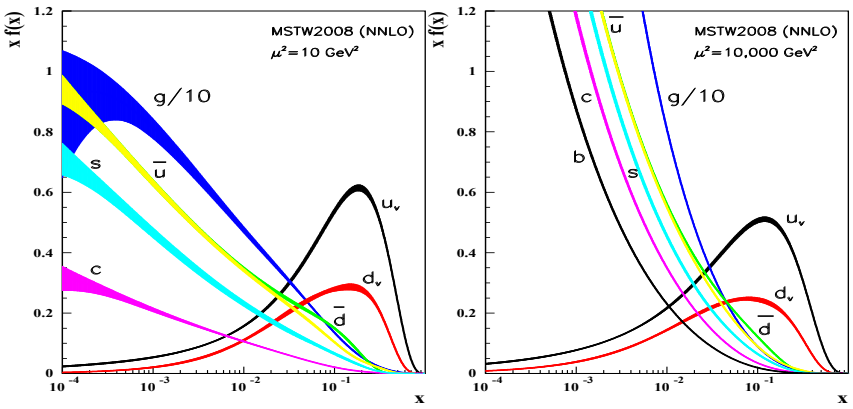

Figure 1.6: The unpolarized parton distribution times x for $u_\nu, d_\nu, \bar{u}, \bar{d}, s, c, b$ and g at a factorization scale of $\mu^2 = 10$ GeV^2 (left) and 10000 GeV^2 (right).

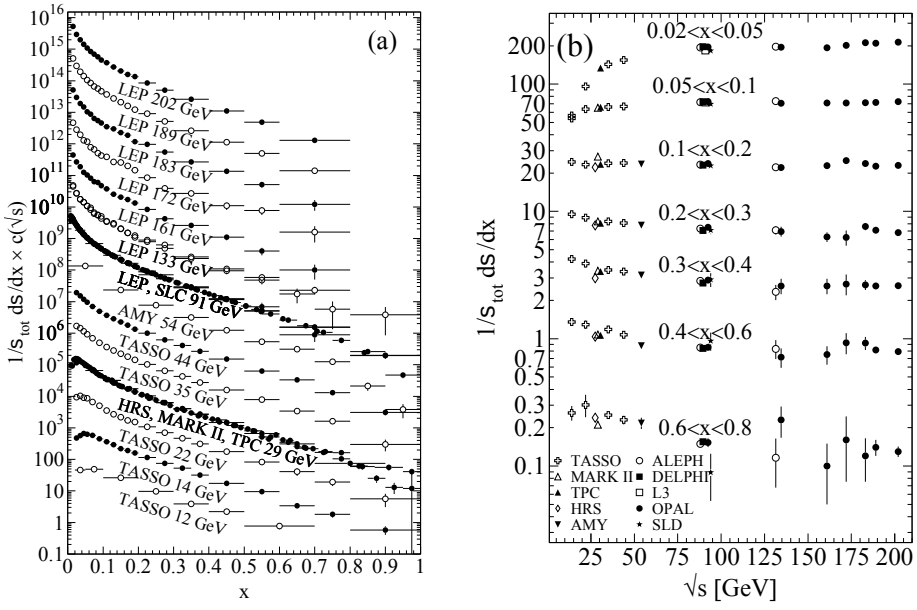

Figure 1.7: The fragmentation function in e^+e^- annihilation for all charged particles. (a) for different center-of-mass energy $\sqrt{s}$ vs x scaled by $c(\sqrt{s}) = 10^i$ with i ranging from $i = 0$ ($\sqrt{s} = 12$ GeV) to $i = 13$ ($\sqrt{s} = 202$ GeV)and (b) for various range of x vs $\sqrt{s}$.

1.4 Heavy-ion collisions

1.4.1 Collision geometry

Collision geometry is an important aspect in heavy-ion collisions. In high-energy heavy-ion collisions, collision geometry is determined by parameters such as the number of binary collisions,N_{coll}, the number of participant nucleons, N_{part} and impact parameter, $\boldsymbol{b}$. All of them are provided by the Glauber model [49]. The Glauber model is semi-classical model which describes nucleus-nucleus reaction and geometry. It treats a nucleus-nucleus collision as multiple nucleon-nucleon interactions. Incident nucleons are assumed to be go straight in parallel with the beam axis and have no scattering angle after collisions. This assumption approximately works out in very high energy collisions such as RHIC energy. The cross section of a nucleus-nucleus collision is estimated by overlapping function $T_{AB}(\boldsymbol{b}, \boldsymbol{s})$. $\boldsymbol{b}$ is impact parameter and $\boldsymbol{s}$ is position vector of nucleons from the center of incident nucleus. They are defined in Fig.1.8. $T_{AB}(\boldsymbol{b}, \boldsymbol{s})$ is formulated as follows.

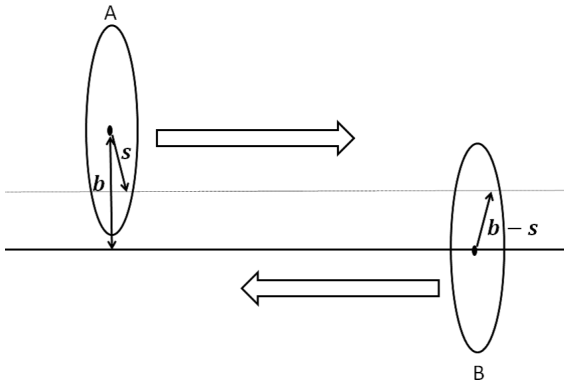

Figure 1.8: Geometry of a nucleus-nucleus collision with the vector of impact parameter $\boldsymbol{b}$ and position vector of nucleons $\boldsymbol{s}$ from the center of the nucleus.

$$T_{AB} = \int d^2\boldsymbol{s} T_A(\boldsymbol{s}) T_B(\boldsymbol{s} - \boldsymbol{b}) \tag{1.12}$$

where A is incident nuclear specie, B is target nuclear specie. Thickness function $T_A(\boldsymbol{s})$ is defined as

$$\begin{aligned} T_A(\boldsymbol{s}) &= \int dz \rho_A(z, \boldsymbol{s}) \\ \rho_A(r) &= \frac{\rho_{nm}}{1 + \exp\left(\frac{r - R_A}{a}\right)} \end{aligned} \tag{1.13}$$

where r is the distance from the center of nucleus, ρ_{nm} is the normal nuclear density and R_A is the radius of nucleus. In order to reproduce realistic condition, the Wood-Saxon parametrization is included in nucleon density ρ_A. Under these parameterizations, the number of binary collisions, N_{coll}, and the number of participant nucleons, N_{part}, are calculated for a given impact parameter, $\boldsymbol{b}$.

$$\begin{aligned} N_{part}(\boldsymbol{b}) &= \int d^2\boldsymbol{s} \mathrm{T_A}(\boldsymbol{s}) \left[1 - \exp\left(-\sigma_{inel}^{NN} T_B(\boldsymbol{s})\right)\right] \\ &\quad + \int d^2\boldsymbol{s} \mathrm{T_B}(\boldsymbol{s}-\boldsymbol{b}) \left[1 - \exp\left(-\sigma_{inel}^{NN} T_A(\boldsymbol{s})\right)\right] \qquad (1.14) \\ N_{coll}(\boldsymbol{b}) &= \int d^2\boldsymbol{s} \sigma_{inel}^{NN} T_A(\boldsymbol{s}) T_B(\boldsymbol{s}-\boldsymbol{b}) \qquad (1.15) \end{aligned}$$

where $\sigma_{\mathrm{inel}}^{NN}$ is the inelastic nucleon-nucleon cross section. The parameters N_{coll} and N_{part} are frequently used for the comparison among the results of different experiments with different collision species and energies. The average number of binary collisions, $\langle N_{coll} \rangle$, and the average number of participant nucleons, $\langle N_{part} \rangle$, are calculated by the Monte Carlo simulations [50] as shown in Fig.1.9.

1.4.2 Particle multiplicity and nuclear stopping power

The particle multiplicity in nucleus-nucleus collisions is an important aspect of heavy-ion collisions. The particle multiplicity is experimentally obtained in the form of the number of charged particles dN_{ch}/dy or $dN_{ch}/d\eta$. Figure 1.10 is detected charged hadron tracks in an event from central Au+Au collisions at $\sqrt{s_{NN}} = 200$ GeV. Figure 1.11 shows the measured $dN_{ch}/d\eta$ in PHOBOS experiment [46]. The multiplicities are empirically known to increase proportional to $s_{NN}^{0.11}$ and $s_{NN}^{0.15}$ as shown in Fig.1.12, where s_{NN} shows total energy per nucleon pair in the center-of-mass frame in nucleon-nucleon collisions and nucleus-nucleus collisions [47].

In high-energy heavy-ion collisions, Lorentz-contracted nuclei collide with each other and multiple nucleon-nucleon collisions with secondary particle production take place. Incoming nucleons lose their kinematic energy and the energy is used for subsequent particle production. The amount of energy loss during the collisions depends on the thickness of the nuclei and the incident collisions energy. The degree of the energy loss is called the nuclear stopping power. The stopping power in nucleus-nucleus collisions can provide the key information of the baryon density. It can be extracted from the measurement of the net-proton ($N_p - N_{\bar{p}}$) rapidity distributions in Fig.1.13. The net-proton distribution has a peak and a dip at AGS and at SPS. At RHIC, the

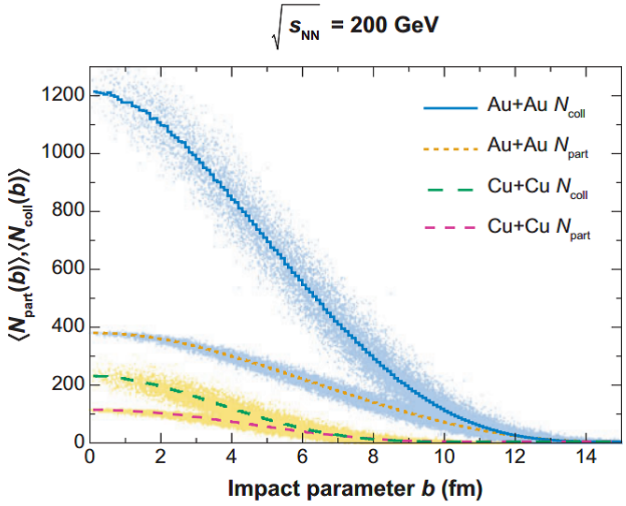

Figure 1.9: The average number of binary collisions, $\langle N_{coll} \rangle$, and that of participant nucleons, $\langle N_{part} \rangle$, as a function of the impact parameter $\boldsymbol{b}$. The event-by-event fluctuations are added as the scatter plot. The Woods-Saxon distribution with $R_A = 6.38$ fm and $a = 0.535$ for ^{197}Au and $R_A = 4.20641$ fm and $a = 0.5977$ fm for ^{63}Cu are assumed, respectively. The measured σ_{inel}^{NN} = 42 mb is used in this calculation [50].

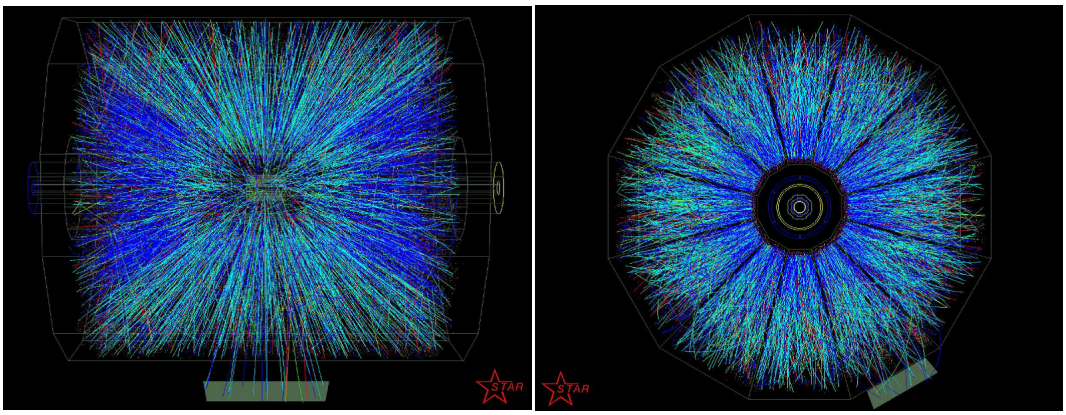

Figure 1.10: The side view (left) and front view (right) of the STAR event display in Au+Au collisions at $\sqrt{s_{NN}} = 200$ GeV [45].

distribution is almost flat at midrapidity but has small peaks near the beam rapidity. The absolute yield of the net-protons decreases as collision energy becomes higher. The fact says that the nuclear stopping power is saturated

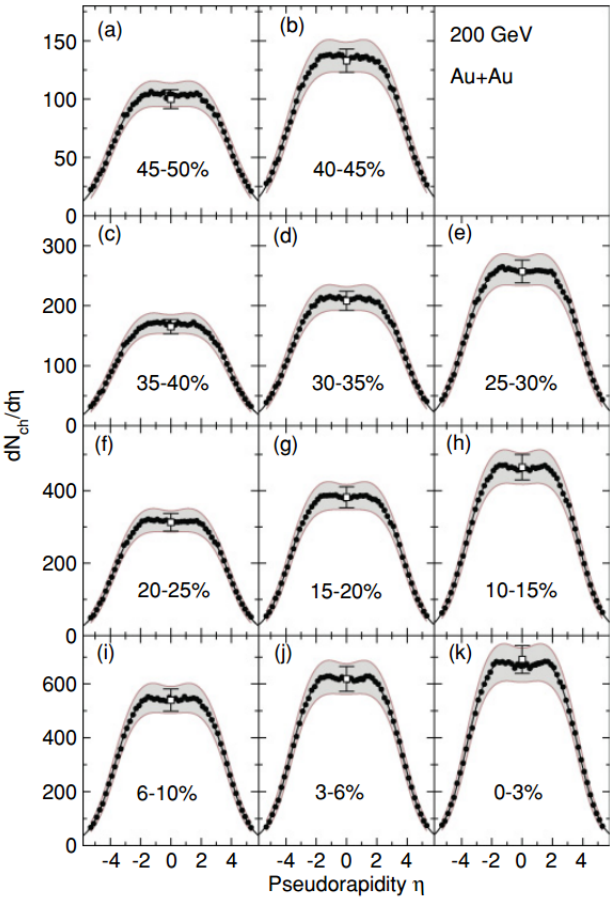

Figure 1.11: The number of charged particle vs pseudo-rapidity η in Au+Au collisions at $\sqrt{s_{NN}} = 200$ GeV. (a) to (h) shows peripheral to central Au+Au collisions [46].

in high-energy heavy-ion collisions, that is, the incident nucleons are unlikely to lose all their kinematic energy but punch through the opponent nucleus. If the stopping power is explained by the extrapolation from p+p collisions, the mean free path of a nucleon l_n in Au+Au 200 GeV is expressed by

$$l_n = \frac{1}{\sigma_{NN}\rho_{nm}} = \left(4.2\,\mathrm{fm}^2 \times 0.18\,\mathrm{fm}^{-3}\right)^{-1} = 0.72\,\mathrm{fm}, \tag{1.16}$$

where σ_{NN} is the nucleon-nucleon cross section and ρ_{nm} is the normal nuclear density. This value is smaller than the size of the nucleus.

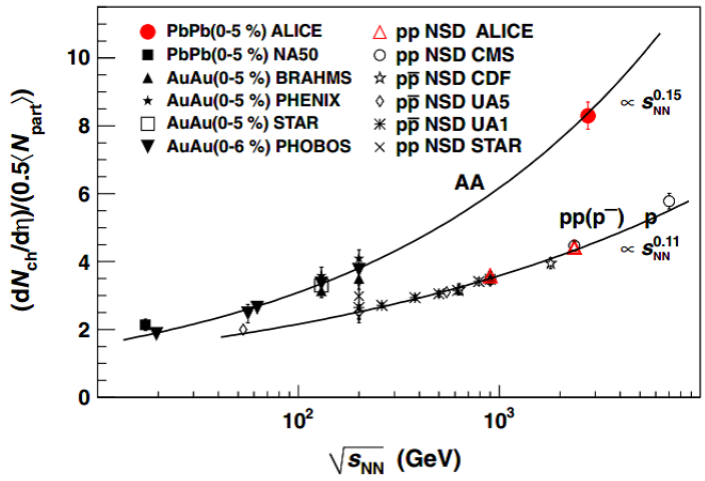

Figure 1.12: Charged-particle pseudo-rapidity density per participant pair as a function of $\sqrt{s_{NN}}$ [47]. The data points in central nucleus-nucleus collisions and non-single diffractive pp ($p\bar{p}$) collisions are shown on the plot.

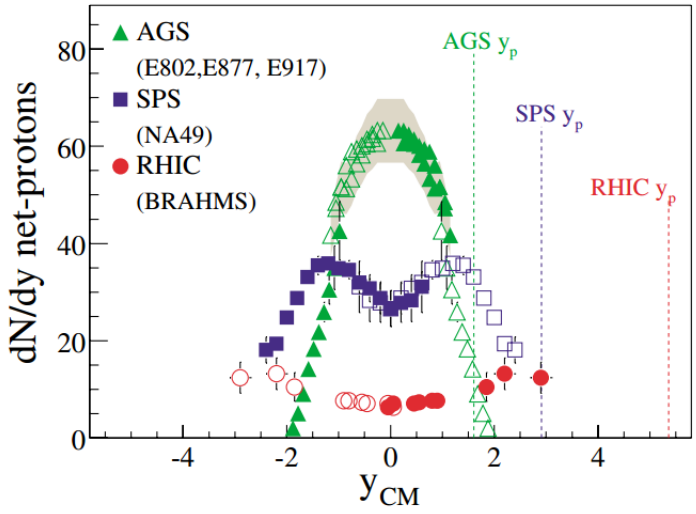

Figure 1.13: The net-proton rapidity distribution at AGS (Au+Au at $\sqrt{s_{NN}}$ = 5 GeV), SPS (Pb+Pb at $\sqrt{s_{NN}}$ = 17 GeV) and RHIC (Au+Au at $\sqrt{s_{NN}}$ = 200 GeV) [48].

1.4.3 Space-time evolution in a heavy-ion collision

The picture of the space-time evolution in heavy-ion collisions is explained in this section, referring to Fig.1.14.

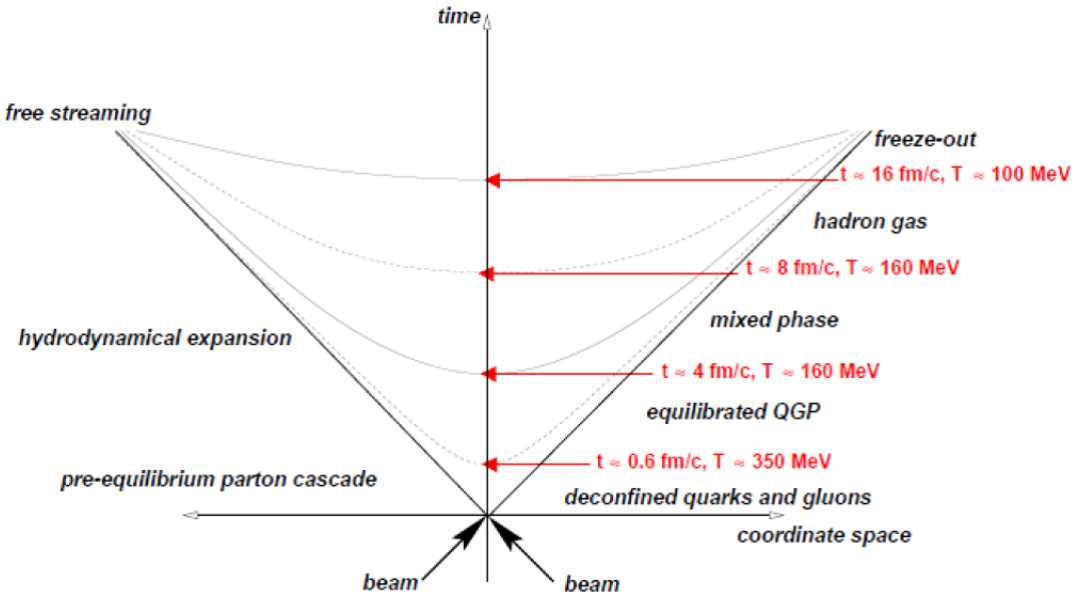

Figure 1.14: A light-cone diagram of space-time evolution in high-energy heavy-ion collisions [52]. The values of time and temperature for various phases are taken from [53]. The mixed phase exists if the phase transition is first order.

Before collision

The Lorentz-contracted nuclei with the thickness of $2R/\gamma_{cm}$ collide with each other, where R is radius of a nucleus and γ_{cm} is the Lorentz factor ($\gamma_{cm} = \sqrt{s_{NN}}/2M_N$, M_N is the nucleon mass) along the longitudinal direction.

Bjorken proposed the picture of nucleus-nucleus reactions based on the parton model of hadrons. The Bjorken picture has two aspects, that is, the existence of wee partons (gluons and sea quarks in nucleon) and the time dilation of particle production. The wee parton is considered as vacuum fluctuations coupling to the valence quarks passing through the QCD vacuum. Alternatively, the wee partons are regarded as part of a coherent classical field created by fast paton, so-called the color glass condensate (CGC). The typical momenta of wee partons correspond to the strong interaction scale of the QCD, that is, $\Lambda_{QCD} \approx 200$ MeV, due to its non-perturbative nature. Accordingly longitudinal size of nuclei Δz can be never smaller than $1/p \approx 1$ fm because of the uncertainty principle at high energy. While the longitudinal size of the wave function of a valence quark in nuclei is $\sim 2\mathrm{R}/\gamma_{cm}$. Therefore

wee partons play a vital role at very high energy which fulfills $\gamma_{cm} > \frac{2R}{1\,\mathrm{fm}}$.

Pre-equilibrium stage and thermalization ($0 < \tau < \tau_0 \sim 0.6$ fm/c)

The central collision of two coming nuclei makes huge entropy production. Theoretically the description of the dynamics in the pre-equilibrium stage is challenging because the difficulty originates from the non-equilibrium process of the Non-Abelian gauge theory. So far two types of approaches are proposed. One is the incoherent models and the other is the coherent models.

In the incoherent models, the incoherent sum of parton-parton collisions produces minijet (semi-hard partons) and the produced minijets subsequently interact with each other to form an equilibrated parton plasma. The minijet production is calculated in pQCD with an infrared cutoff of order 1-2 GeV. The total number of jets for $|y| \leq \Delta y/2$ in a central nucleus-nucleus collision is calculated as follows.

$$\begin{aligned}
\frac{d^3\sigma_{jet}}{dy_3 dy_4 dp_T^2} &= \sum_{i,j} x_1 f_i\left(x_1, p_T^2\right) x_2 f_j\left(x_2, p_T^2\right) \frac{d\hat{\sigma}^{ij\to kl}}{d|\hat{t}|}, \\
\sigma_{jet}\left(\sqrt{s}; p_0, \Delta y\right) &= \sum_{k,l} \frac{1}{1+\delta_{kl}} \int_{p_0 \leq p_T} dp_T^2 \int_{\Delta y} dy_3 \int_{\Delta y} dy_4 \frac{d^3\sigma_{jet}}{dy_3 dy_4 dp_T^2}, \\
N_{jet}^{NN}\left(\sqrt{s}; p_0, \Delta y\right) &\simeq T_{AA}(0)\, \sigma_{jet}\left(\sqrt{s}; p_0, \Delta y\right) \qquad (1.17)
\end{aligned}$$

where $d\hat{\sigma}^{ij\to kl}$ shows the parton-parton scattering cross section of $1{+}2 \to 3{+}4$ for various parton species, $(i, j, k, l) = q, \bar{q}, g$. x_1 and x_2 are Bjorken's x (i.e. p/P, p is momenta of parton in nucleon and P is momentum of parent nucleon). $f_{i\,or\,j}\left(x_1, p_T^2\right)$ and $f_{i\,or\,j}\left(x_2, p_T^2\right)$ are the parton distribution functions in incident nucleons. $\frac{d\hat{\sigma}^{ij\to kl}}{d|\hat{t}|}$ is the differential cross section of parton-parton scattering such as $gg \to gg$. $\hat{t}$ is the Mandelstam variable. p_0 is infrared cutoff p_T and the Kronecker delta δ_{kl} takes care of the symmetry factor of the final state with identical particles. $T_{AA}(0)$ is the nuclear overlap function from the Glauber model in case the impact parameter is zero, that is, head-on nucleus-nucleus collisions. While the equilibration process is calculated by the relativistic Boltzmann equation with pQCD parton-parton scattering cross sections. The relativistic and quantum transport theory for a non-Abelian quark-gluon system is one of the possible approaches to describe the equilibration process.

An example of the coherent models is the color-string breaking model. This theory essentially consists of three steps: (i) After a nucleus-nucleus collision, wounded nucleons in nuclei have color excitation and make color strings between the two outgoing nuclei. The color strings are regarded as a

coherent and classical color electric field. (ii) $q\bar{q}$ and gluon pairs are produced by the dacay of strings due to the Schwinger mechanism. The total emission rate for quarks and gluons depends on the strength of color electric fields, E_c, between two nuclei as

$$\begin{aligned} w_q\left(\sigma \sim gE_c\right) &\sim N_f \frac{\left(gE_c\right)^2}{24\pi}, \\ w_g\left(\sigma \sim gE_c\right) &\sim N_c \frac{\left(gE_c\right)^2}{48\pi}. \end{aligned} \tag{1.18}$$

(iii)The quarks-gluon matter with local equilibrium is produced though the mutual interactions of produced quarks and gluons.

Hydrodynamical evolution of the quark-gluon matter and phase transition ($\tau_0 < \tau < \tau_F \sim 16$ fm/c)

Once the local thermal equilibrium state is formed at τ_0, the system expansion is described in the framework of the hydrodynamics. The basic equations of the system expansion are expressed in forms of the conservation of the energy-momentum tensor and the baryon number as follows.

$$\begin{aligned} \partial_\mu \langle T^{\mu\nu} \rangle &= 0, \\ \partial_\mu \langle j_B^\mu \rangle &= 0, \end{aligned} \tag{1.19}$$

where $T^{\mu\nu}$ is the energy-momentum tensor and j_B^μ is the flux of the baryon number. The expectation value in Equation is taken with respect to the time-dependent state in local thermal equilibrium.

At $\tau = \tau_C\,(\sim 4.0\,\mathrm{fm/c})$, the system reaches the critical temperature T_C between the quark-gluon phase and the hadronic phase. If the phase transition is the first order, the system experiences the mixed phase that partons and hadrons coexist. At $\tau = \tau_H\,(\sim 8.0\,\mathrm{fm/c})$, the system finishes hadronization. The produced hadrons keep interacting each other up to the freeze-out temperature at the proper time, τ_F.

Freeze-out and post-equilibrium ($\tau_F < \tau$)

The freeze-out of the hadronic matter occurs at the proper time τ_F. The freeze-out is defined by a space-time hyper-surface, where the mean free time of the particles becomes larger than the time scale of the system evolution. At this stage, thermal equilibrium is no longer maintained. Two types of the freeze-outs take place in the system evolution. The chemical freeze-out is that the particle species are settled down, that is, the particle production no

longer occurs. The thermal freeze-out is that the momentum distribution of each particle specie is fixed, that is, any particle does not interact with each other. The temperature of the chemical freeze-out is, in general, higher than that of the thermal freeze-out.

1.4.4 Initial energy density

The achieved energy density in heavy-ion collisions can be estimated by the particle multiplicity and the transverse energy from the Bjorken's scenario [54]. In Bjorken's picture, the formed system in center-of-mass heavy-ion collision expands cylindrically and symmetrically in azimuth and straightly in z-direction. Therefore the volume of the system is expressed as $\Delta V = \pi R^2 dz$ where R is radius of a nucleus. The total energy E is described as follows.

$$E = \langle m_T \rangle \frac{dN}{dy} \delta y = \frac{dE_T}{dy} \delta y \tag{1.20}$$

where $m_T = \sqrt{p_T^2 + m^2}$, E_T is the transverse total energy and $\frac{dN}{dy}$ is the number of produced particles per rapidity. The Bjorken energy density ϵ_{Bj} is

$$\begin{aligned} \epsilon_{Bj} &= \frac{E}{\Delta V} \\ &= \frac{\langle m_T \rangle}{\pi R^2} \frac{dN}{\tau_0 dy} \qquad (1.21) \\ &= \frac{1}{\pi R^2 \tau_0} \frac{dE_T}{dy}, \qquad (1.22) \end{aligned}$$

where $dz = \tau dy$ at midrapidity. The initial energy density for several collision species and energies is estimated under the assumption of $\tau_0 = 1.0$ fm/c as shown in Table 1.3. The critical energy density for the QCD phase transition is $\epsilon_C \sim 1.0$ GeV/fm^3.

Accelerator	Collision species	$\sqrt{s_{NN}}$ (GeV)	ϵ_{Bj} (GeV/fm^3)	Ref.
AGS	Au+Au	5	1.5	[55]
SPS	Pb+Pb	17	2.9	[56, 57]
RHIC	Au+Au	19.6	2.2	[59]
	Au+Au	130	4.7	[58, 59]
	Au+Au	200	5.4	[59]

Table 1.3: The Bjorken energy density for various collision species and energies.

1.5 QCD phase transition

One of the most important subjects is to clarify the origin and evolution of the universe. After the Big bang, our universe experiences various phase transitions of the vacuum at the critical energy scales such as the inflation, electro-weak transition at the GUT scale ($T_C \sim 200$ GeV) and the QCD phase transition at the critical temperature $T_C \sim 200$ MeV. The study of the QCD phase transition is important to understand not only the state in the early universe but the quark-gluon dynamics in non-perturbatibe region . The heavy-ion collision is almost unique experimental tool to study the transition between the quark-gluon phase and the hadronic phase. The QCD phase transition has two aspects: Confinement-deconfinement transition and Chiral phase transition. The physics backgrounds mentioned in this section are well detailed in the reference [60].

1.5.1 QCD vacuum structure

Quarks and gluons interact non-perturbatively at low energy because the QCD coupling becomes strong in low-energy limit. Thus the QCD vacuum acquires non-trivial structure, such as quark and gluon condensates. According to analyses of the mass spectrum of charmonium using QCD spectral sum rules [61, 62], gluon has non-perturbative condensation of

$$\left\langle \frac{\alpha_s}{\pi} F^a_{\mu\nu} F^{\mu\nu}_a \right\rangle_{vac} \sim (300\,\mathrm{MeV})^4 . \tag{1.23}$$

The vacuum expectation value of the energy-momentum tensor can be written as

$$\langle T^{\mu\nu} \rangle_{vac} = -\epsilon_{vac} g^{\mu\nu}, \tag{1.24}$$

The energy density of the QCD vacuum at the chiral limit ($m \to 0$) is written as

$$\begin{aligned} \epsilon_{vac} &\sim -\frac{11 - \frac{2N_f}{3}}{32} \left\langle \frac{\alpha_s}{\pi} F^a_{\mu\nu} F^{\mu\nu}_a \right\rangle_{vac} \\ &\sim -0.3\ \mathrm{GeV\ fm^{-3}}. \end{aligned} \tag{1.25}$$

The quark structure of the QCD vacuum, which is obtained by the Gell-Mann-Oakes-Renner (GOR) relation by only requiring chiral symmetry, is expressed as

$$\begin{aligned} f_\pi^2 m_{\pi^\pm}^2 &= -\hat{m} \langle \bar{u}u + \bar{d}d \rangle_{vac} + O\left(\hat{m}^2\right), \\ f_\pi^2 m_{\pi^0}^2 &= -\langle m_u \bar{u}u + m_d \bar{d}d \rangle_{vac} + O\left(\hat{m}^2\right), \end{aligned} \tag{1.26}$$

where f_π (= 93 MeV) is the pion decay constant, $m_{\pi^\pm}$ ($\simeq$ 140 MeV) is the charged pion mass and m_{π^0} ($\simeq$ 135 MeV) is the neutral pion mass. $\hat{m} = (m_u + m_d)/2$ is the average mass of up and down quarks. $\hat{m} \sim 5.6$ MeV at k = 1.0 GeV are obtained by using the quark mass. Therefore the condensate of quark-anti-quark pairs in vacuum is

$$\langle \left(\bar{u}u + \bar{d}d\right)/2 \rangle_{vac} \sim -\left(250\,\mathrm{MeV}\right)^3 \text{ at } k = 1.0\,\mathrm{GeV}. \tag{1.27}$$

1.5.2 The bag model and confinement-deconfinement transition

In the MIT bag model [63, 64], hadrons are considered as bags embedded in a non-perturbative vacuum. In this framework, quarks are treated as massless and non-interacting particles, which are Stefan-Boltzmann limit inside a finite bag. The boundary condition to show the feature of the confinement is controlled via the pressure of the bag. In addition, quarks and gluons are treated perturbatively inside a bag, alternatively, non-perturbative effects are taken care by the bag pressure. The total energy of the system is expressed as a function of the bag pressure, B_{bag}, by

$$E = \frac{nx}{R} + \frac{4\pi R^3}{3} B_{bag}, \tag{1.28}$$

where n is the number of partons and x/R is the kinetic energy of each quark[1]. R is the radius of a spherical bag. The second term shows the energy of the vacuum. The bag model is naturally extended to the many body systems like the quark-gluon matter under several constraints. Equilibrium is obtained if E is a minimum (i.e. $\partial E/\partial R = 0$). In this case, the bag pressure B_{bag} is

$$B_{bag}^{1/4} = \left(\frac{2.04 n^{-4}}{4\pi} \frac{1}{R}\right). \tag{1.29}$$

If the normal QCD vacuum (i.e. $B = -\epsilon_{vac}$) is assumed,

$$B_{bag}^{1/4} = 220\,\mathrm{MeV}. \tag{1.30}$$

If the system produced in a heavy-ion collision is zero net baryon density, the dominant excitation in the hadronic phase is the massless pions, while that in the quark-gluon phase is the massless quarks and gluons. At extremely low temperature (i.e. $T \ll \Lambda_{QCD}$), the typical momenta of pions are small and the interactions among pions are suppressed by the power of

[1] $x \sim 2.04$, which is equivalent to the lowest-energy mode of a massless quark

$T/4\pi {f_\pi}^2$. At extremely high temperature, the typical momenta of quarks and gluons are high and the running coupling constant α_s becomes week due to asymptotic freedom. Therefore pressure, energy density and entropy density in the hadronic phase and the quark-gluon phase are expressed as follows. If free pion gas in hadronic phase is assumed, then

$$P_H = d_\pi \frac{\pi^2}{90} T^4, \tag{1.31}$$

$$\epsilon_H = 3 d_\pi \frac{\pi^2}{90} T^4, \tag{1.32}$$

$$s_H = 4 d_\pi \frac{\pi^2}{90} T^3, \tag{1.33}$$

$$d_\pi = N_f^2 - 1, \tag{1.34}$$

where d_π is the number of massless pions in N_f flavor. In quark-gluon matter,

$$P_Q = d_Q \frac{\pi^2}{90} T^4 - B, \tag{1.35}$$

$$\epsilon_Q = 3 d_Q \frac{\pi^2}{90} T^4 + B, \tag{1.36}$$

$$s_Q = 4 d_Q \frac{\pi^2}{90} T^3, \tag{1.37}$$

$$d_{qg} = d_g + \frac{7}{8} d_q, \tag{1.38}$$

$$d_g = 2_{\text{spin}} \times \left(N_c^2 - 1 \right), \tag{1.39}$$

$$d_q = 2_{\text{spin}} \times 2_{q\bar{q}} \times N_c \times N_f \tag{1.40}$$

In Table 1.4, d_π and d_{qg} are summarized in case of $N_c = 3$ for different N_f.

N_f	0	1	2	3	4
d_π	0	0	3	8	15
d_q	0	12	24	36	48
d_g	16	16	16	16	16
d_{qg}	16	26.5	37	47.5	58

Table 1.4: Degrees of freedom for pions (d_π), quarks (d_q), gluons (d_g) and deduced degrees of freedom in the quark-gluon phase (d_{qg}) for $N_c = 3$ with massless N_f flavors.

[2] $f_\pi = 93$ MeV, f_π is the pion decay constant.

The critical temperature T_c and energy density ϵ_c of the QCD phase transitions can be calculated in this framework. If $B^{1/4} \sim 220$ MeV is assumed with $N_c = 3$, T_c and ϵ_c are

$$\begin{aligned} T_c &= \left(\frac{90}{\pi^2}\frac{B_{bag}}{d_{qg}-d_\pi}\right)^{\frac{1}{4}} \\ &\sim 160\,\mathrm{MeV}, \qquad (1.41) \\ \epsilon_c &\sim 4B_{bag} \\ &\sim 1.2\,\mathrm{GeV/fm^3}. \qquad (1.42) \end{aligned}$$

The critical energy density is larger than the energy density of the normal nuclear matter, $\epsilon_{nm} \sim 0.15$ GeV/fm^3.

1.5.3 The NJL model and chiral phase transition

The Nambu-Jona-Lasinio (NJL) model [65, 66] is originally introduced by Y. Nambu and G. Jona-Lasinio inspired by the phase transition of the superconductivity and extended to describe the nature of the phase transition of the QCD vacuum [67]. The effective Lagrangian from the simplest version of the NJL model for two flavor quarks ($N_f = 2$) is described as

$$\mathcal{L}_{NJL} = \bar{q}\left(-i\gamma_\mu\partial_\mu + m\right)q - \frac{G^2}{2\Lambda^2}\left[\left(\bar{q}q\right)^2 + \left(\bar{q}i\gamma_5\boldsymbol{\tau}q\right)^2\right], \qquad (1.43)$$

where ${}^t q\left(x\right) = \left(u\left(x\right), d\left(x\right)\right)$ and $m = \mathrm{diag}\left(m_u, m_d\right) = m\cdot\mathbf{1}$, where the isospin symmetry, that is, $m_u = m_d$ is assumed for simplicity. G is a dimensionless coupling constant for $q\bar{q}$ attraction in the scaler $((I, J^P) = (0, 0^+)$ and psudoscaler $((I, J^P) = (1, 0^-)$ channels. Λ^{-1} is the characteristic length scale which the $q\bar{q}$ interaction can be regarded as point-like in space-time. Equation 1.43 has a global $\mathrm{SU_L}(2)\times\mathrm{SU_R}(2)\times\mathrm{U_B}(1)$ symmetry but breaks $\mathrm{U_A}(1)$ symmetry.

The partition function of the model at finite T and zero chemical potential may be given by

$$\begin{aligned} Z_{NJL} &= \int \left[d\bar{q}dq\right] e^{-\int_0^{1/T} d\tau \int d^3x \mathcal{L}_{NJL}} \\ &= \int \left[d\bar{q}dq\right]\left[d\Sigma\right] e^{-\int_0^{1/T} d\tau \int d^3x \left[\bar{q}\left(-i\gamma\cdot\partial + m + G\Sigma\right)q + \frac{\Lambda^2}{2}\Sigma\Sigma^\dagger\right]} \\ &\equiv \int \left[d\Sigma\right] e^{-S_{eff}(\Sigma;T)} \\ \Sigma\left(x\right) &= \sigma\left(x\right) + i\gamma_5\boldsymbol{\tau}\cdot\boldsymbol{\pi}\left(x\right), \\ \left[d\Sigma\right] &= \left[d\sigma d\boldsymbol{\pi}\right] \qquad (1.44) \end{aligned}$$

where $\Sigma(x)$ is a bosonic field with a 2×2 matrix structure in the isospin space. After carrying out the Gaussian and Grassmann integration integration, $[d\bar{q}dq]$, (See the reference [60]), The effective action S_{eff} is described as

$$\begin{aligned} S_{eff}(\Sigma;T) &= -\mathrm{Tr}\ln\left(-i\gamma\cdot\partial + m + G\Sigma\right) \\ &\quad + \int_0^{1/T} d\tau \int d^3x \left(\frac{\Lambda^2}{2}\Sigma(x)\,\Sigma(x)^\dagger\right). \end{aligned} \tag{1.45}$$

The main contribution to the integral of Eq.(1.43) is assumed to come from the stationary solution satisfying $\delta S_{eff}/\delta\Sigma(x) = 0$ (Currently this assumption is justified if N_c is large). When the stationary solution is space-time independent and real, that is, $\Sigma(x) = \Sigma(x)^\dagger = \sigma$, the stationary condition is equivalent to

$$\frac{\partial f_{eff}}{\partial\sigma} = 0 \text{ with } S_{eff}(\sigma;T) = f_{eff}(\sigma;T)\,V/T \tag{1.46}$$

In this case, the term of "Tr ln" in Eq.(1.45) is a fermion contribution with a constant mass $M = m + G\sigma$. Then,

$$f_{eff}(\sigma;T) = \frac{\Lambda^2}{2}\sigma^2 + \int \frac{d^3k}{(2\pi)^3}\left[\frac{-d_q E(k)}{2} - d_q T\ln\left(1 + e^{-E(k)/T}\right)\right], \tag{1.47}$$

where $E(k) = \sqrt{k^2 + (m+G\sigma)^2}$ and d_q (=24) is the degrees of freedom in Eq.(1.40). The first term in Eq.(1.47) shows the interaction energy from the four-fermion term in Eq.(1.43). The first term in the integrand is the zero-point energy, $-E/2$, multiplied by the degrees of freedom, d_q, for quark and anti-quark, which can be interpreted as the total energy of quarks in Dirac sea. The last term in the integrand is related to the entropy term $-Ts$ of the thermally excited quarks. Therefore the free energy has the expected structure $f_{eff} = \epsilon - Ts$.

$\partial f_{eff}/\partial\sigma = 0$ in Eq.(1.46) is called the gap equation in analogy with a similar equation in BCS superconductivity. When a true minimum of f_{eff} is defined as $\sigma = \sigma_{min}$, The dynamical quark mass M_q and the chiral condensate $\langle\bar{q}q\rangle$ are expressed in the chiral limit $m \to 0$ as follows.

$$M_q = G\sigma_{min}, \tag{1.48}$$

$$\langle\bar{q}q\rangle \equiv \langle\bar{u}u + \bar{d}d\rangle = -\frac{\Lambda^2}{G}\sigma_{min}. \tag{1.49}$$

High-temperature expansion [60] of the effective free energy in Eq.(1.47)

is described as follows.

$$\begin{aligned} f_{eff}(\sigma;T) &= -\left(\frac{d_q}{16\pi^2}+d_q\frac{7}{8}\frac{\pi^2}{90}T^4\right)+\frac{d_q}{48}\left(T^2-T_c^2\right)(G\sigma)^2 \\ &+ \frac{d_q}{64\pi^2}(G\sigma)^4\left[\ln\left(\frac{1}{\pi^2\mathrm{T}^2}\right)+\mathrm{C}\right]+O\left(\sigma^6\right), \\ T_c &= \sqrt{\frac{24}{d_q}\left(\frac{1}{G_c^2}-\frac{1}{G^2}\right)}, \\ G_c &= \pi\sqrt{\frac{8}{d_q}}, \end{aligned} \tag{1.50}$$

where $C = 2\gamma - 3/2 \simeq -0.346$, γ (=0.577) is the Euler constant. The term proportional to T^4 shows the Stephan-Boltzmann values for massless quarks. The term proportional to σ^2 has a feature to change a sign of the coefficient at $T = T_c$ (a first-order phase transition), while that of the σ^4 term is positive even at $T \ll 1$, this is the behavior expected for a second order phase transition. A direct connection between T_c and the mass-gap, $M_0 = G\sigma_{min}(T=0)$, is derived from the gap equation of Eq.(1.46). For $\Lambda \gg \sigma$, T, the critical temperature is described as

$$\begin{aligned} T_c &\simeq \frac{\sqrt{3}}{\pi}M_0 \\ &\sim 165\,\mathrm{MeV} \end{aligned} \tag{1.51}$$

where the standard dynamical mass, $M_0 = 300$ MeV, is assumed.

1.5.4 Lattice QCD and QCD phase transition

The lattice QCD approach, which is originally proposed by K. Wilson [68], is a powerful method to reveal the properties of non-perturbative nature and the properties of the QCD phase transition. The gauge field on the lattice is defined as the link variable in order to reserve gauge invariance. The path-ordered product of the gauge field is defined by

$$\begin{aligned} U_P(x,y;A) &= P\exp\left(ig\int_P dz_\mu A_\mu\right) \\ &= P\exp\left(ig\int_0^1 ds\lambda_\mu A_\mu\right) \\ &= \sum_{n=0}^{\infty}\frac{(ig)^n}{n!}\int_0^1 ds_1 ds_2\cdots ds_n P\left[\lambda A(s_1)\cdots\lambda A(s_n)\right], \end{aligned} \tag{1.52}$$

where the path-ordered symbol, P, is a generalization of the time-ordered symbol, T. $U_P(x,y;A)$ is called Wilson line. Wilson line is useful to define non-local gauge-invariant object. Suppose a four dimensional hyper-cubic lattice with the discretized size, a. The shortest Wilson line on the lattice is the one connecting the neighbor sites n and $n+\hat{\mu}$,

$$U_\mu(n) = \exp(igaA_\mu(n)) \tag{1.53}$$

This is called the link variable. Then a smallest closed loop is defined by

$$U_{\mu\nu}(n) \equiv U_\nu^\dagger(n)\, U_\mu^\dagger(n+\hat{\nu})\, U_\nu(n+\hat{\mu})\, U_\mu(n), \tag{1.54}$$

$U_{\mu\nu}(n)$ transforms covariantly under a local gauge transformation as $U_{\mu\nu} \to U_{\mu\nu}^V = V(n)\, U_{\mu\nu} V^\dagger(n)$. In the continuum limit $a \to 0$, it is close to the field strength tensor via Baker-Campbel Hausdorff formula[3] as follows,

$$U_{\mu\nu}(n) - 1 \to ia^2 g F_{\mu\nu}(n) \tag{1.55}$$

The trace tr $U_{\mu\nu}(n)$ is a minimal gauge-invariant object, which is called the plaquette.

The smallest gauge-invariant object can be associated with gluons and fermions. A gauge-invariant action of gluons is obtained from the plaquette as follows.

$$S_g = \frac{2N_c}{g^2} \sum_P \left(1 - \frac{1}{N_c} \operatorname{Re} \operatorname{tr} U_{\mu\nu}(n)\right) \tag{1.56}$$

where $\sum_P$ indicates the summation of all plaquette with a definite orientation,

$$\begin{aligned} \sum_P &= \sum_n \sum_{1\le\mu<\nu\le 4} = \frac{1}{2} \sum_n \sum_{1\le\mu\neq\nu\le 4} \\ a^4 \sum_n &\simeq \int d^4x \text{ at } a \to 0 \end{aligned} \tag{1.57}$$

In the continuum limit (i.e. $a \to 0$),

$$S_g \to \frac{1}{4} \int d^4x F_{\mu\nu}^b(x)^2. \tag{1.58}$$

As an analogy of the gluon case, the small gauge-invariant objects can be considered. Up to the nearest neighbor coupling, the three objects are considered as follows.

$$\bar{q}(n)\, q(n),\ \bar{q}(n+\hat{\mu})\, U_\mu(n)\, q(n),\ \bar{q}(n-\hat{\mu})\, U_{-\mu} q(n) \tag{1.59}$$

[3] $\exp A \exp B = \exp(A + B + [A,B]/2 + \cdots)$

A special combination of the above terms is called Wilson's fermion action expressed by

$$\begin{aligned} S_W &= a^4 \sum_n \Big[m\bar{q}(n) q(n) - \frac{1}{2a} \sum_\mu \bar{q}(n+\hat{\mu}) \Gamma_\mu U_\mu(n) q(n) \\ &\quad - \frac{r}{2a} \sum_\mu \left(\bar{q}(n+\hat{\mu}) U_\mu(n) q(n) - \bar{q}(n) q(n) \right) \Big] \\ &\equiv a^4 \sum_{n,n'} \bar{q}(n') \left(m\delta_{n',n} + D_W(n',n;r) \right) q(n), \\ D_W(n',n;r) &= -\frac{1}{2a} \sum_\mu \Big[\delta_{n',n+\hat{\mu}} (r+\Gamma_\mu) U_\mu(n) - r\delta'_{n',n} \Big], \end{aligned} \tag{1.60}$$

where $\Sigma_\mu \equiv \Sigma_{\mu=\pm1,\pm2,\pm3,\pm4}$. Γ_μs are the hermitian γ matrices satisfying $\Gamma_\mu^\dagger = \Gamma_\mu$, $\Gamma_{-\mu} = -\Gamma_\mu$ and $\{\Gamma_\mu, \Gamma_\nu\} = 2\delta_{\mu\nu}$. In the continuum limit $a \to 0$ with $(f(x+a) - f(x-a))/2a = f'(x) + O(a^2)$ and $(f(x+a) + f(x-a) - 2f(x))/a^2 = f''(x) + O(a^2)$,

$$S_W \to \int d^4x \bar{q}(x) \left(m - i\gamma \cdot D - \frac{ar}{2} D^2 \right) q(x). \tag{1.61}$$

The parameter r is introduced in order to avoid the fermion-doubling problem. At $r = 0$, the degree of freedom for fermions becomes $2^4 = 16$. If $r \neq 0$ is taken, one light fermion with $m \approx 0$ and the other 15 fermions with $O(1/a)$ are splitting. Another method to avoid the fermion-doubling problem is the staggered fermion formulation, 16 fermions are reinterpreted as four-component Dirac spinor $\times$ four-flavors. These two approaches should be consistent with each other, though the costs of the numerical calculation are different.

Figure 1.15 shows the dimensionless energy density calculated by the framework of staggered fermion and Wilson fermion. The energy densities are discretely jumped at the critical temperature, T_c.

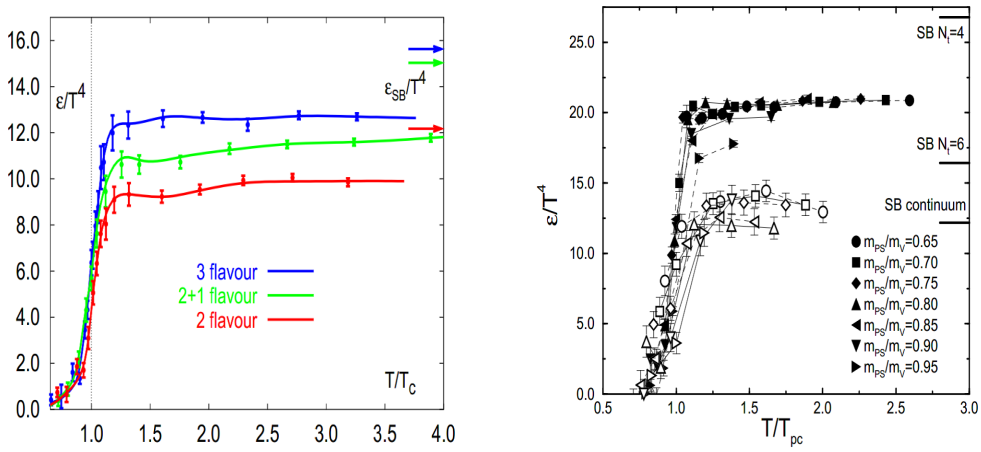

Figure 1.15: The energy density in QCD. The left (right) figure shows results from a calculation with staggered fermion [69, 70] (Wilson fermion [71]) on lattices with temporal extent $N_\tau = 4$ ($N_\tau = 4$, 6). The staggered fermion calculations have been performed for a pseudo-scalar to vector meson mass ratio of $m_{PS}/m_V = 0.7$.

1.6 QCD phase diagram

1.6.1 Theoretical approaches: critical end point

The critical end points in the QCD phase are predicted in various kinds of theoretical calculations. The lattice QCD mainly covers in high-temperature and low-baryon-density regions. In high-baryon-density regions, the effective theories based on the NJL model cover. Figure 1.16 shows the critical end points in the theoretical calculations.

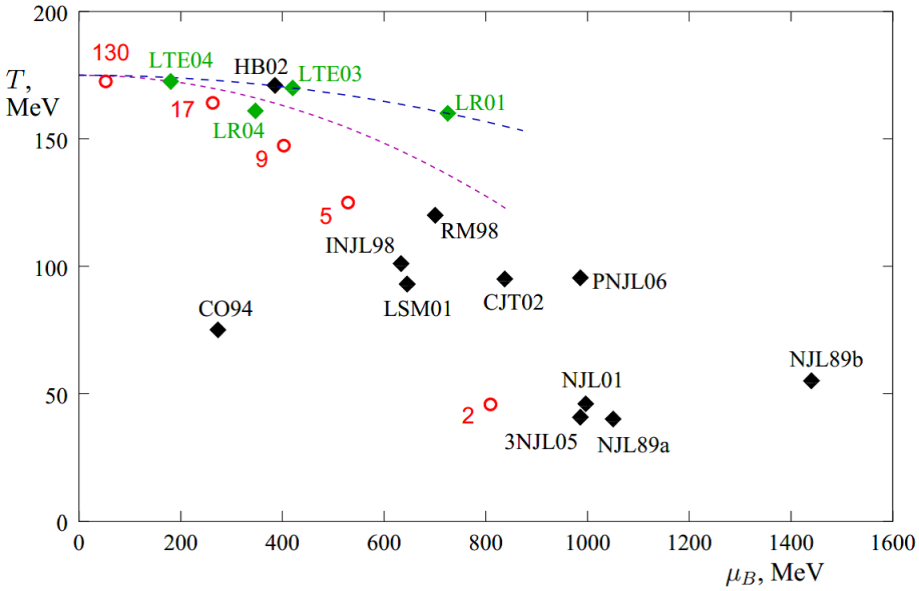

Figure 1.16: Comparison of predictions for the local ot the QCD critical end point on the phase diagram. Black points are model predictions: NJLa89 [72], NJLb89 [72], CO94 [73, 74, 75], INJL98 [76], RM98 [77], LSM01 [78], NJL01 [78], HB02 [79], CJT02 [80], 3NJL05 [81], PNJL06 [82]. Green points are predictions from lattice QDCs: LR01, LR04 [83, 84], LTE3 [85], LTE04 [87, 88]. The two dashed lines are parabolas with slopes corresponding to lattice predictions of the slow $dT/d\mu_B^2$ of the transition line at $\mu_B = 0$ [85, 87, 88]. The red circles are locations of the freeze-out points for heavy-ion collisions at several energies $\sqrt{s_{NN}}$ (indicated by labels in GeV).

1.6.2 Experimental approach: chemical freeze-out properties and initial temperature

Chemical freeze-out temperature and baryon chemical potential

The chemical freeze-out properties are studied by the measured particle abundance ratios such as π^-/π^+ and the chemical freeze-out model [89]. In the chemical freeze-out model, particle abundance in a thermal system with volume V is expressed by

$$\frac{N_i}{V} = \frac{g_i}{(2\pi)^3}\gamma_S \int \frac{1}{\exp\left(\frac{E_i-\mu_B B_i-\mu_S S_i}{T_{ch}}\right)\pm 1} d^3p, \tag{1.62}$$

where N_i is the abundance of particle species i, g_i is the spin degeneracy, B_i and S_i are the baryon number and strangeness number. E_i is the particle energy. The parameters in this model are the chemical freeze-out temperature T_{ch}, the baryon chemical potential μ_B, strangeness chemical potential μ_S and the *ad hoc* strangeness suppression factor γ_S. Figure 1.17 shows the chemical freeze-out temperature as a function of the baryon chemical potential. In 0-5 % most central Au+Au collisions at $\sqrt{s_{NN}} = 200$ GeV, the chemical freeze-out temperature and the baryon chemical potential are

$$\begin{aligned} T_{ch} &= 159.3 \pm 5.8\text{MeV}, \\ \mu_B &= 21.9 \pm 4.5\text{MeV}. \end{aligned} \tag{1.63}$$

Initial temperature

Any source of high-energy real photons can also emit virtual photons which subsequently decay into di-electrons as shown in Fig.1.18. A real photon is emitted by a source labeled as M($Q^2 = 0$) on the left side in Fig.1.18. A analogous diagram on the right side shows the emission of a virtual photon with mass m_{γ^*}. The yield of virtual photons dN_{γ^*} is related to that of di-electrons dN_{ee} as follows.

$$\frac{d^2N_{ee}}{dM^2} = \frac{\alpha}{3\pi}\frac{L(M)}{M^2} dN_{\gamma^*}, \tag{1.64}$$

$$L(M) = \sqrt{1-\frac{4m_e^2}{M^2}}\left(1+\frac{2m_e^2}{M^2}\right) \tag{1.65}$$

where M is the mass of the virtual photon pair or the di-electron pair (i.e. $M = m_{\gamma^*} = m_{ee}$). α is the fine structure constant ($\sim 1/137$). The factor

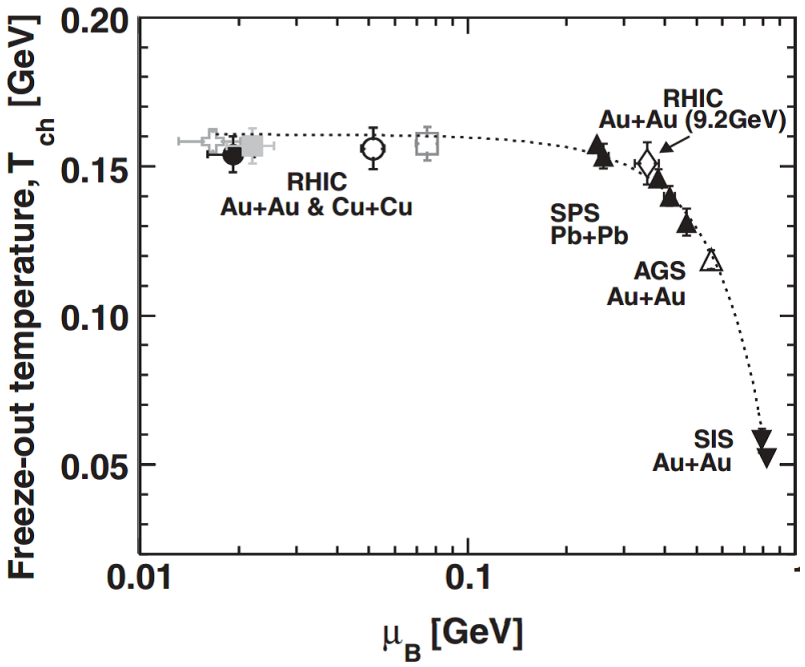

Figure 1.17: Chemical freeze-out temperature T_{ch} as function of the baryon chemical potential μ_B derived for central Au+Au (0-5% for 200 and 62.4 GeV [91] and 0-10 % for 9.2 GeV [92]) and Cu+Cu (0-10%) collisions. For comparison, results for minimum-bias pp collisions at 200 GeV are also shown along with additional heavy-ion data points compiled for lower collision energies [93, 94]. The dashed line represents a common fit to all available heavy-ion data..

$\frac{\alpha}{3\pi}\frac{L(M)}{M^2}$ is a universal factor describing the decay of $\gamma^* \rightarrow e^+e^-$. Equation (1.64) can be described by

$$\frac{d^2N_{ee}}{dM^2} = \frac{\alpha}{3\pi}\frac{L(M)}{M^2}S(M,q)\,dN_\gamma, \tag{1.66}$$

$$S(M,q) = \frac{dN_{\gamma^*}}{dN_\gamma} \tag{1.67}$$

where q is the three momentum of the virtual photon and $S(M,q)$ is the ratio between the real photon emission and the virtual photon emission. The factor $S(M,q)$ is process dependent and accounts for effects such as form factors, phase space and spectral function. Referring to Eq.(1.66), the relation between real photon production and the associated di-electron pair production can be written as follows.

$$\frac{d^2N_{ee}}{dm_{ee}dp_T} = \frac{2\alpha}{3\pi}\frac{1}{m_{ee}}L(m_{ee})\,S(m_{ee},p_T)\,\frac{dN_\gamma}{dp_T}, \tag{1.68}$$

For high p_T ($p_T \gg m_{ee}$), the process dependence is negligible and the $S(m_{ee}, p_T)$ becomes 1 as $m_{ee} \to 0$ or $m_{ee}/p_T \to 0$. For $m_{ee} \gg m_e$, the $L(m_{ee})$ approaches 1. Therefore the relation in Eq.(1.68) simplifies to

$$\frac{d^2N_{ee}}{dm_{ee}dp_T} = \frac{2\alpha}{3\pi}\frac{1}{m_{ee}}\frac{dN_\gamma}{dp_T}, \tag{1.69}$$

Figure 1.19 shows invariant mass spectrum of di-electrons. The yield of virtual photons is extracted by fitting to the mass spectrum with a two-component function,

$$f(m_{ee}; r) = (1-r)\, f_c(m_{ee}) + r f_{dir}(m_{ee}), \tag{1.70}$$

where $f_{dir}(m_{ee})$ is the expected spectra of the virtual photons. Equation (1.69) is good approximation as a functional form of f_{dir}. $f_c(m_{ee})$ is the estimated spectra other than thermal photons and estimated by Monte Carlo simulation of background particles with final-state di-electrons. r is the fitting parameter and indicates the fraction between direct photons and inclusive photons. The inclusive photon yield can be converted to the direct photon yield via the parameter r as follows.

$$dN_\gamma^{dir}(p_T) = r \times dN_\gamma^{incl}(p_T). \tag{1.71}$$

Figure 1.20 shows the invariant yield of direct photons as a function of p_T. The enhancement of the yield with respect to the extrapolation from p+p curve is seen in Au+Au collisions. The information about the temperature of the system produced by heavy-ion collision is extracted by the exponential behavior of the enhancement.

In 0-20 % central collisions, the initial temperature $T_{\rm init}$ of the system, at least, reaches

$$T_{\rm init} = 221 \pm 19 \pm 19\,{\rm MeV}. \tag{1.72}$$

The expected temperature is larger than the critical temperature of the QCD phase transition in theoretical predictions.

1.6.3 Order parameters of the QCD phase transition

High energy Heavy-ion collisions have the advantage of exploring the QCD phase transition in high-temperature and low-baryon-density domain. The behavior of the order parameters in this domain is well studied by the lattice QCD calculations [98, 99, 100, 101, 102, 103, 104]. The order parameters of the QCD phase transition are classified into three types: chiral condensate, strange quark number and Polyakov loop.

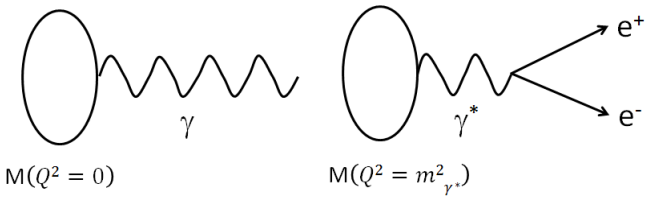

Figure 1.18: Diagram for real photon production (left) and its associated process producing an e^+e^- pair (right). M stands for the matrix element of the photon-producing process, and Q is the four-momentum of the virtual (or real) photon.

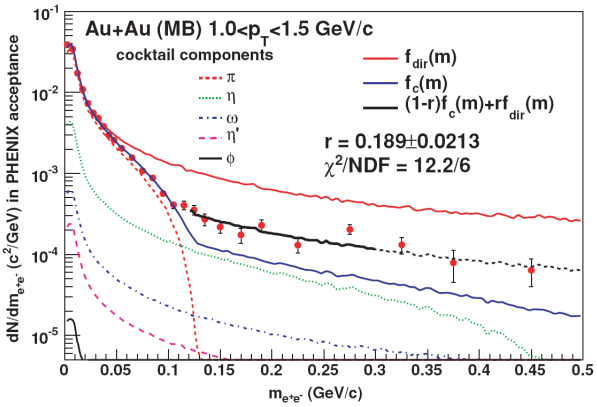

Figure 1.19: Invariant mass spectra of di-electrons for Au+Au (Min.Bias) events for $1.0 < p_T < 1.5$ GeV/c. The solid line is the fitting result via Eq.(1.70). The fit range is $0.12 < m_{e^+e^-} < 0.3$ GeV/c^2. The dashed (black) curve at greater $m_{e^+e^-}$ shows $f\,(m_{e^+e^-})$ outside of the fit range.

Chiral condensate susceptibility is a good order parameter for the chiral phase transition since it diverges in the chiral limit ($m_l \to 0$, where m_l is masses of light quarks), and its local maximum at finite quark mass defines a pseudocritical temperature that approaches the chiral phase transition temperature as the quark mass approaches the chiral limit. Strange quark number susceptibility and Polyakov loop, though these observables are sensitive near the critical temperature so far, provide important insights for the confinement/deconfinement aspect in the QCD vacuum.

Figure 1.21 shows the behavior of the renormalized susceptibilities near

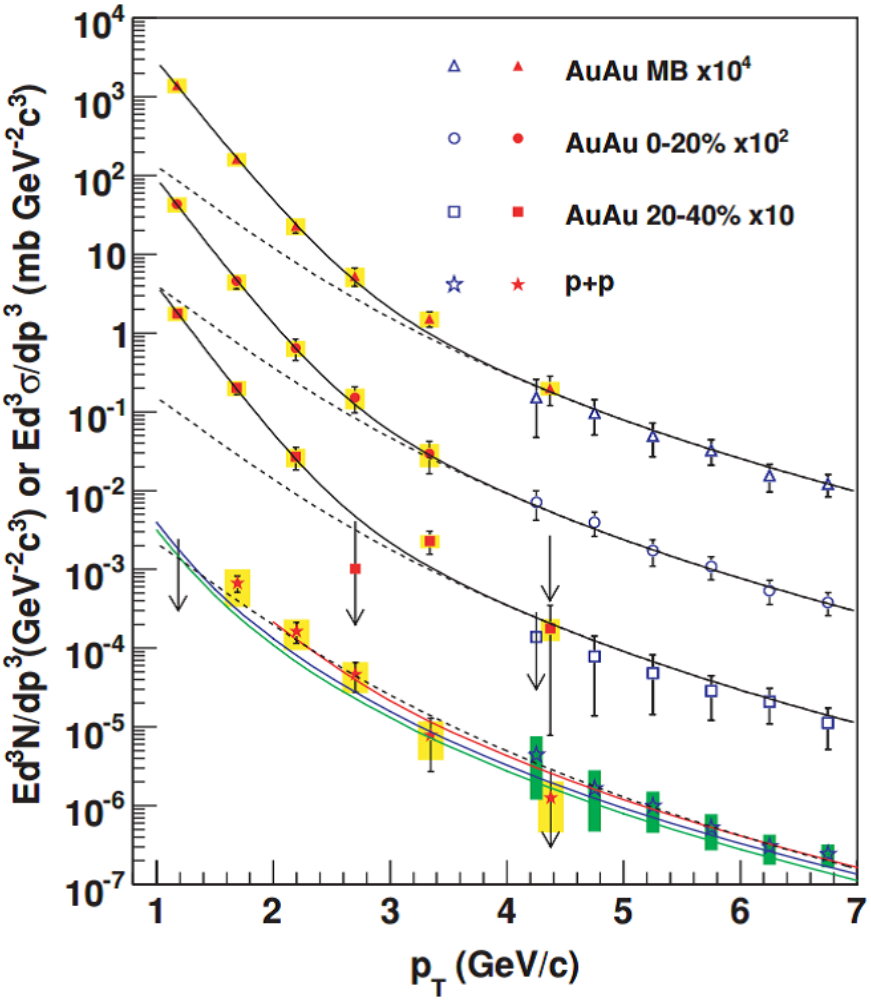

Figure 1.20: Invariant cross section (p+p) and invariant yield (Au+Au) of direct photons as a function of p_T. The filled points are obtained by the virtual photon analysis and open points are from [96, 97]. The three curves on the p+p data represent NLO pQCD calculations, and the dashed curves show a modified power-law fit to the p+p data, scaled by T_{AA}. The dashed (black) curves are exponential plus the T_{AA} scaled p+p fit.

the critical temperature [100].

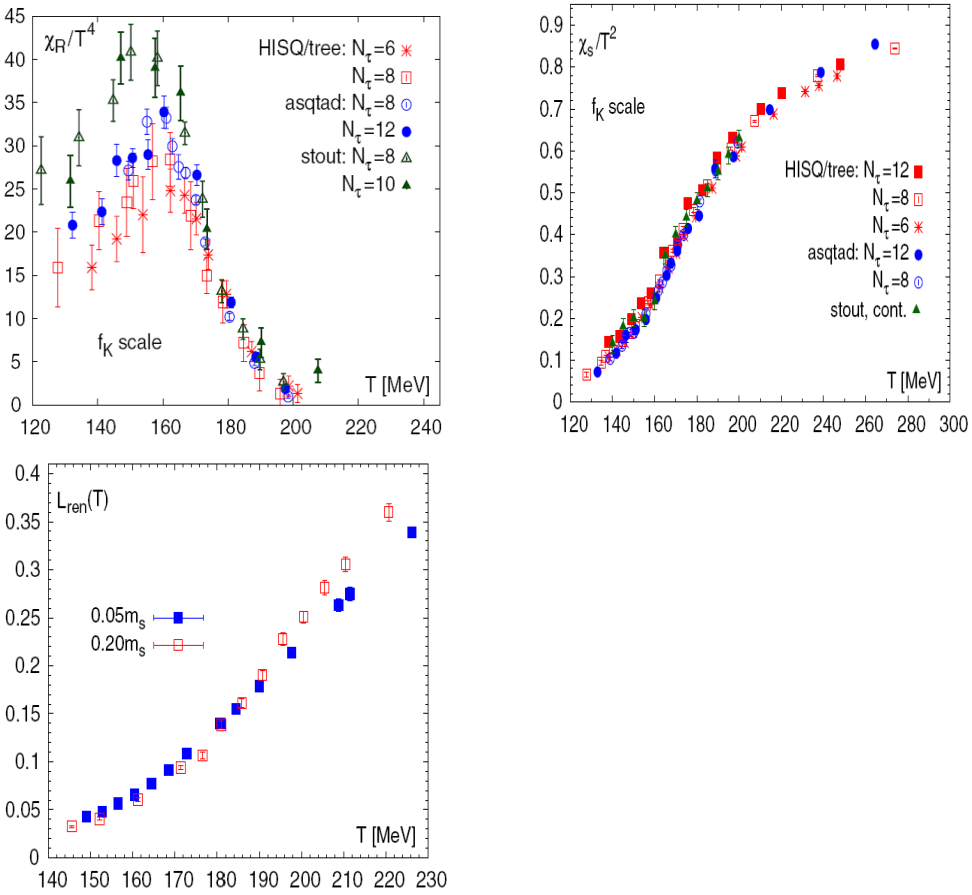

Figure 1.21: The renormalized susceptibilities as a function of temperature with the asqtad and HISQ/tree action compared to the stoud results. The renormalized two-flavor chiral susceptibility χ_R for $m_l = 0.05m_s$ where m_l and m_s are the masses of light quarks and the strange quark, respectively (top-left). The renormalized strange quark number susceptibility (top-right) and the renormalized Polyakov loop (bottom-left) [100].

1.7 Mass modification of light vector mesons

1.7.1 Chiral symmetry restoration in finite temperature

The left-handed and right-handed quarks as two eigenstate of the chirality operator γ_5 with the eigenvalue $\pm$ 1 are written by

$$\begin{aligned} q_L &= \frac{1}{2}\left(1-\gamma_5\right)q, \\ q_R &= \frac{1}{2}\left(1+\gamma_5\right)q. \end{aligned} \tag{1.73}$$

The chirality is equivalent to the helicity $\sigma \cdot \hat{p}$ for the massless quark. The QCD Lagrangian in Eq.(1.1) may be decomposed as follows.

$$\mathcal{L}_{\mathcal{QCD}} = \mathcal{L}_{\mathcal{QCD}}\left(q_L, A\right) + \mathcal{L}_{\mathcal{QCD}}\left(q_R, A\right) - \left(\bar{q_L} m q_R + \bar{q_R} m q_L\right) \tag{1.74}$$

Equation (1.74) is invariant under the $\mathrm{U_L}\left(N_f\right) \times \mathrm{U_R}\left(N_f\right)$ global transformation as,

$$\begin{aligned} q &\rightarrow \mathrm{e}^{-i\lambda^j\theta_L^j} \\ q &\rightarrow \mathrm{e}^{-i\lambda^j\theta_R^j} \end{aligned} \tag{1.75}$$

where the $\theta_{R,L}^j \left(j = 0, 1, \cdots N_f - 1\right)$ are space-time-independent parameters and $\lambda^0 = \sqrt{s/N_f}$, $\lambda^j = 2t^j \left(j = 1, \cdots N_f^2 - 1\right)$. This is called chiral symmetry. Equation (1.75) is rewritten by introducing vector and axial-vector transformations as

$$\begin{aligned} q &\rightarrow \mathrm{e}^{-i\lambda^j\theta_V^j} \\ q &\rightarrow \mathrm{e}^{-i\lambda^j\theta_A^j} \end{aligned} \tag{1.76}$$

where $\theta_V = \theta_L = \theta_R$ and $\theta_A = -\theta_L = \theta_R$, respectively.

In order to simplify the structure of chiral symmetric phase and breaking phase, let us introduce the linear sigma model based on the NJL model. The formula is

$$\mathcal{L}_{\mathcal{QCD}} = \frac{1}{2}\left[\left(\partial_\mu\sigma\right)^2 + \left(\partial_\mu\pi\right)^2\right] + \mathrm{V}\left(\sigma^2 + \pi^2\right), \tag{1.77}$$

where σ and π meson field are define as

$$\sigma = \bar{q}q, \tag{1.78}$$

$$\pi = \bar{q}i\gamma^5 q. \tag{1.79}$$

If the vacuum is changed into the chiral symmetry breaking phase (Nambu-Goldstone phase (b) in Fig.1.22), π mesons are created with zero mass. It is supported by the relatively small mass of π meson compared to other hadrons. In chiral symmetric phase (Winger phase (a) in Fig.1.22), all states of hadrons have a chiral partner with opposite parity and same mass as doublet of parity. For example, the mass of ρ meson ($J^{PC} = 1^{--}$, vector) is 770 MeV/c^2, while the mass of the chiral partner A_1 meson ($J^{PC} = 1^{++}$, axial-vector) is 1250 MeV/c^2. The mass difference between the chiral partners is direct evidence of spontaneous breaking of chiral symmetry in QCD vacuum.

The chiral symmetry is expected to be restored in quark-gluon matter. The effect of chiral symmetry restoration can appear as the modification of hadron mass through the change of chiral condensate in QCD vacuum. Therefore the measurement of the mass spectrum of hadrons is important to investigate the chiral symmetry restoration.

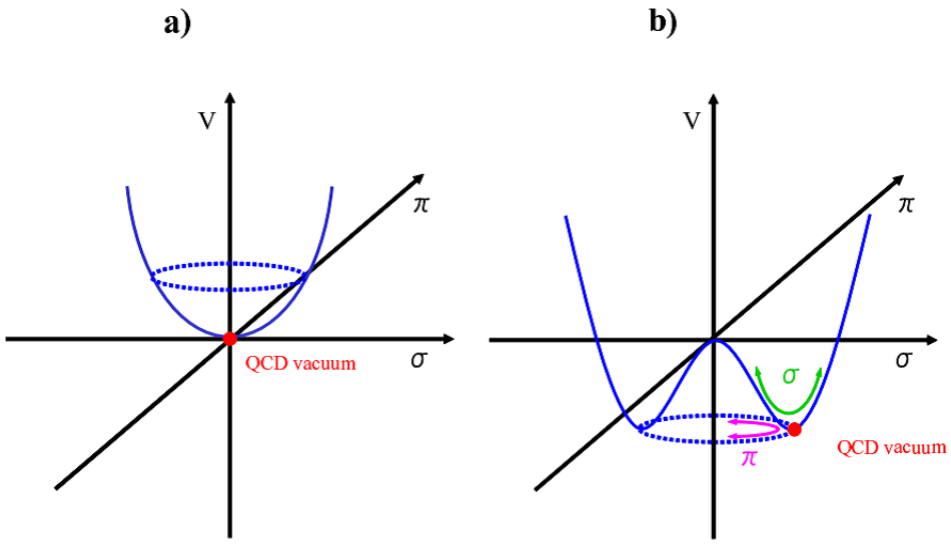

Figure 1.22: (a) Winger phase (b) Nambu-Goldstone phase.

1.7.2 Light vector mesons as a probe

The light vector mesons such as ϕ, ω and ρ mesons are attractive to studying the properties of quark-gluon matter produced in heavy-ion collisions. The mass modification inside quark-gluon matter is potentially visible because

their lifetimes are supposed to be comparable with the duration of the thermal equilibrium state. In addition, di-electrons decaying from the mesons are clear probe to study in-medium modification in quark-gluon matters because because charged lepton carry the original information in quark-gluon matter without strong interaction with hadronic matter in the relatively later stage of the system evolution. Therefore the measurement of light vector mesons via di-electron decay is especially important from experimental viewpoints.

1.7.3 Past studies of the mass modification

The in-medium mass modification has been studied in various experiments. The dropping mass of the light vector mesons at finite density is originally pointed out by Brown and Rho [105]. The density dependence on the masses of the light vector mesons is calculated on the basis of Hatsuda and Lee [106]. Many experiments make effort to observe the mass modification in the normal nuclear density. Figure 1.23-1.25 show the observed mass spectra reported by KEK-PS E325 [107, 108], CLAS [109] and CBELSA/TAPS [110].

The mass modification of the light vector mesons in high-temperature state can be predicted in theoretical models [113, 114, 115, 116]. Figure 1.26 shows an example of the theoretical predictions. The spectral function of $\rho/\omega/\phi$ can significantly change near the critical temperature. Figure 1.27 and 1.28 are the results in high-temperature state reported by the CERES/NA45 experiment [117] and the NA60 experiment [118], respectively.

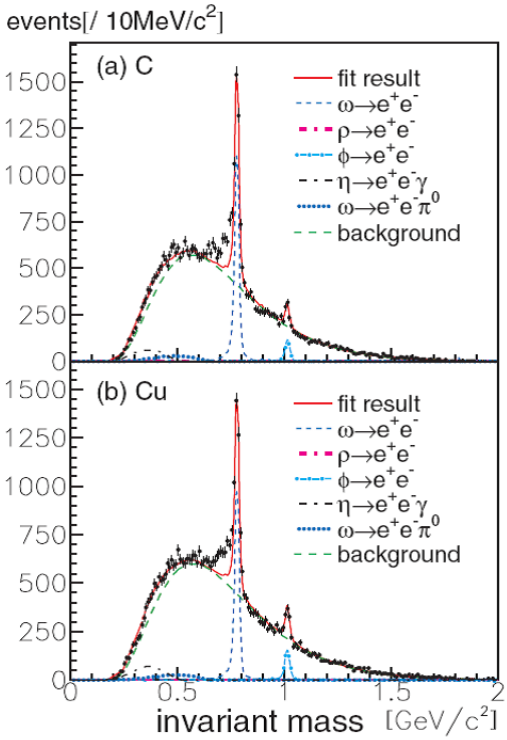

Figure 1.23: The invariant mass spectra of e^+e^- for the C target ((a)) and the Cu target ((b)) [107]. The solid lines are the best-fit result, which is sum of the known hadronic decays, $\omega \to e^+e^-$ (dashed line), $\phi \to e^+e^-$ (thick dashed line), $\eta \to e^+e^-$ (dash-dotted line) and $\omega \to e^+e^-\pi^0$ (dotted line) together with the combinatorial background (long-dashed line) $\rho \to e^+e^-$ is not visible.

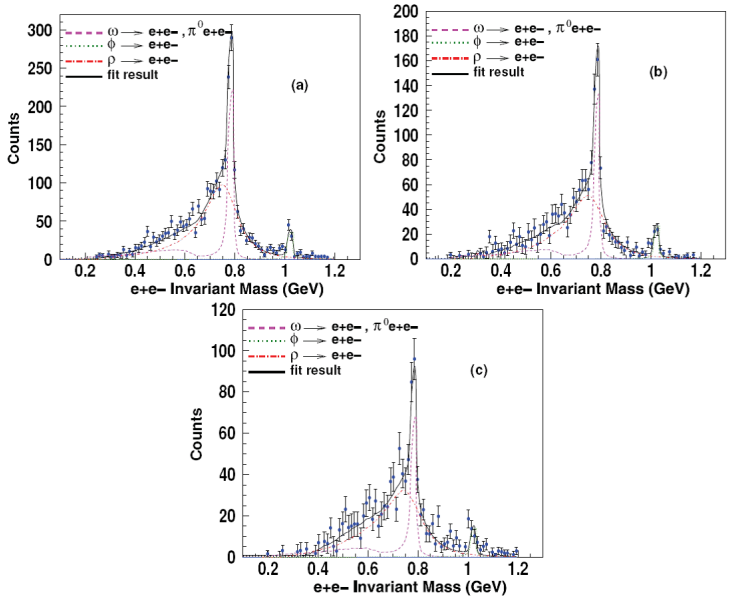

Figure 1.24: The invariant spectra of e^+e^- for the ^{2}H ((a)) target, for the C ((b)) target and Fe-Ti data [109]. The curves are Monte Carlo calculations by the BUU model [111, 112].

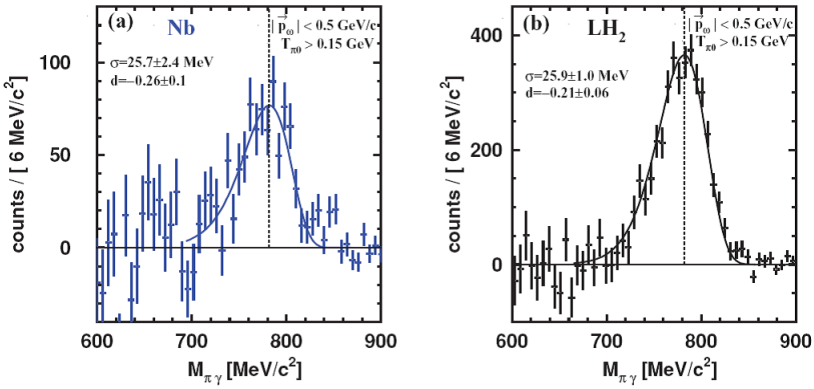

Figure 1.25: The invariant mass spectra of $\pi^0\gamma$ momenta below 500 MeV/c and kinetic energy $T_{\pi^0} > 150$ MeV for the Nb target ((a)), the LH_2 target ((b)) and Monte Carlo simulation [110].The fitting curve takes into account the tail in the region of lower masses resulting from the energy response of the calorimeters .

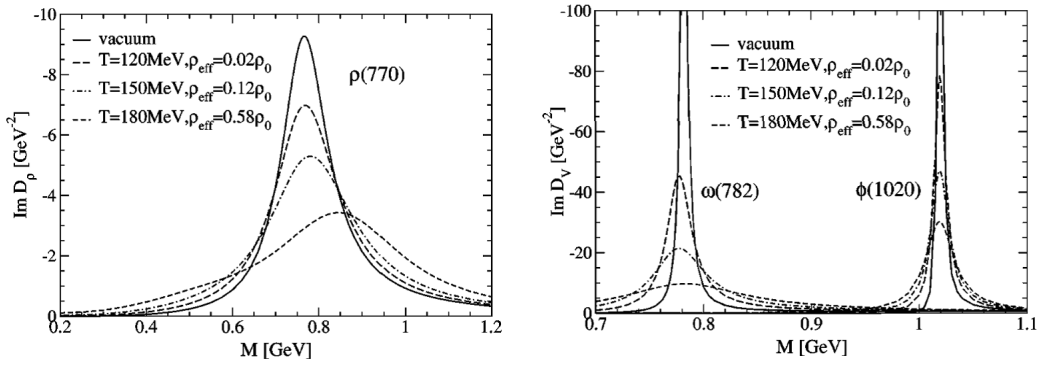

Figure 1.26: Spectral function of the light vector mesons in vacuum (solid line) and in high-temperature and low-baryon-density medium expected under RHIC condition: (T, μ_N) = (120, 91) MeV (long-dashed lines), (T, μ_N) = (150, 40) MeV (dashed-dotted lines) and (T, μ_N) = (120, 91) MeV (long-dashed lines), where μ_N is the net baryon density [115].

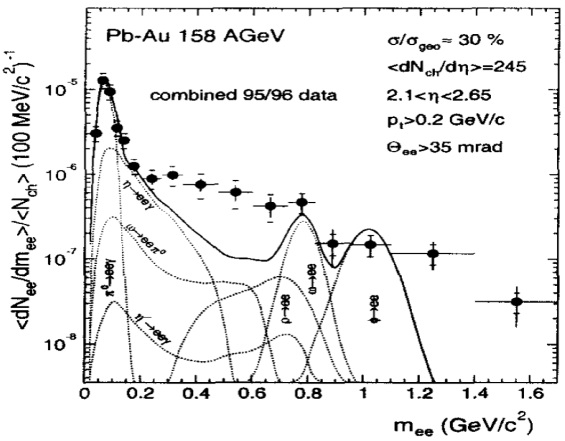

Figure 1.27: Invariant mass spectrum of e^+e^- emitted in 158 AGeV/c Pb+Au collisions from the combined analysis of 1995 and 1996 data [117]. The solid line shows the expected yield from hadron decays, dashed lines indicate the individual contributions to the total yield.

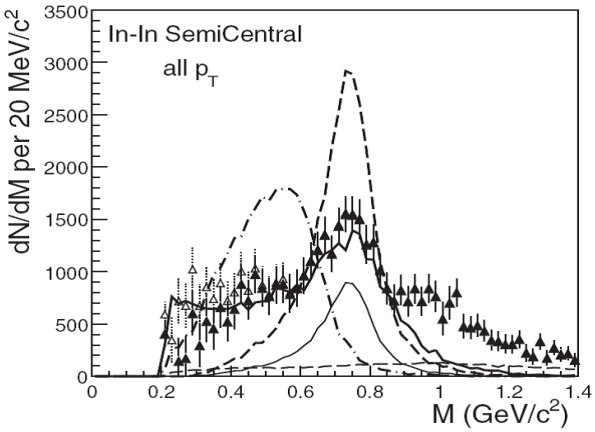

Figure 1.28: Comparison of the excess mass spectrum for the semi-central bin to model predictions, made for In-In at $dN_{ch}/d\eta = 140$ [118]. Cocktail ρ (thin solid line), unmodified ρ (dashed line), in-medium broadening ρ (thick solid line), in-medium moving ρ (dashed-dotted line). The open data points show the difference spectrum resulting from a decrease of the ρ yield by 10 %.

1.8 Motivations and scopes

The mass modification of light vector mesons such as ϕ, ω and ρ is one of the most important signatures of the QCD phase transition produced in heavy-ion collisions, since their masses are strongly related to chiral condensate, which is the most prominent order parameter for the QCD phase transition. Experimentally the signals of the mass modification are extracted by analyzing the mass spectrum shape of light vector mesons. In addition, the branching ratios between different decay channels can change by the effect of the mass modification, especially the comparison between $\phi \to e^+e^-$ and $\phi \to K^+K^-$ is important because di-kaon decays are expected to be suppressed even in the small mass modification due to the small Q value, $Q = (M_\phi - 2 \times M_K) \sim 30$ MeV.

The thesis consists of two parts. The first part describes the production of ϕ and ω mesons in Au+Au collisions at $\sqrt{s_{NN}} = 200$ GeV with the PHENIX detector at RHIC. The invariant transverse momentum spectra of light vector mesons are systematically studied dependent on the individual collision geometry in Au+Au collisions, combining with the different decay channels. The mass modification is discussed from the viewpoints of the mass spectrum shape and the branching ratio.

The second part describes measurability of di-electrons decaying from light vector mesons with the numerical simulation. The feasibility of di-electron measurement in central Pb+Pb collisions at $\sqrt{s_{NN}} = 5.5$ TeV is evaluated by the signal-to-background ratio and the statistical significance as a function of the amount of detector materials, the rejection power of background hadrons, the coverage of the detection system.

Chapter 2

Key issues for di-electron measurement

Di-electrons have the advantages of studying the properties of quark-gluon matter. The detection of di-electrons is, however, challenging from the experimental viewpoint. In this chapter, relevant issues to di-electron measurement are discussed.

2.1 Particle production

The several experiments at RHIC and LHC report that O(100-1000) particles are produced at midrapidity in a heavy-ion collision [46, 47]. The most of them are $\pi^{\pm}$ and π^{0} mesons. The production cross sections of pions are approximately a hundred times larger than that of ϕ meson and ten times larger than that of ω/ρ mesons, respectively.

The production cross sections overall p_T at midrapidity are estimated by fitting with the Tsallis function[1] to the measured data. Figure 2.1 shows the measured production cross sections in p+p collision (panel (a)) and in central Au+Au collisions (panel (b)) at $\sqrt{s_{NN}} = 200$ GeV for signal particles and the backgrounds ones. The published data points of $\pi^{\pm}$ and $K^{\pm}$ at the centrality class of 0-5 % and those of ω at the centrality class of 0-20 % are used. The mismatch of the centrality class is corrected by the weights with the N_{part} and the corrected data points are equivalent to the data at the centrality class of 0-10 %. The solid curves in Fig.2.1 are obtained by directly fitting with Tsallis function to the data. The dotted curves in the panel (b) are scaled by the N_{part} and assumed to be the same spectrum shape as that of p+p 200 GeV. The absolute yield of ρ mesons in Au+Au 200 GeV is determined

[1]The properties of the Tsallis function is explained in Chapter 5.

based on be the ρ/π ratio in p+p 200 GeV since there is no data for ρ meson. The production cross sections and the inclusive yields over all p_T ranges at midrapidity for different collision systems are summarized in Table 2.1.

	p+p 200 GeV		Au+Au 200 GeV (0-10%)	
Particle	$d\sigma/dy(mb)$	Ref.	dN/dy	Ref.
ϕ	0.41	[122]	5.8	[132]
ω	4.3	[122]	33.3	[133]
ρ	7.4	[126]	57.3	
π^0	43.5	[119]	336.8	[128, 129]
π^+/π^-	43.5	[120, 121]	336.8	[130]
η	5.1	[124, 125]	39.5	[131]
K^+/K^-	4.0	[120, 121]	44.7	[130]
K^0_s	4.0	[122, 123]		
$c\bar{c}$	0.18	[127]	4.4	[134]

Table 2.1: The production cross sections and the inclusive yields over all p_T ranges at midrapidity for different collision systems. The used data points to calculate the production cross sections and the inclusive yields are cited from the publications listed in the second column for each collision system. The production cross section of single electrons is obtained by the Tsallis fit to the measured data points and converted into the $c\bar{c}$ cross section with the branching ratio of 9.5 % [127]. The production cross sections of the other particles are obtained by fitting to the measured data points with the Tsallis function, or assuming the proper scaling for missing data points. The errors of the production cross sections and the inclusive yields are expected to be from 10 to 30 % depending on particles.

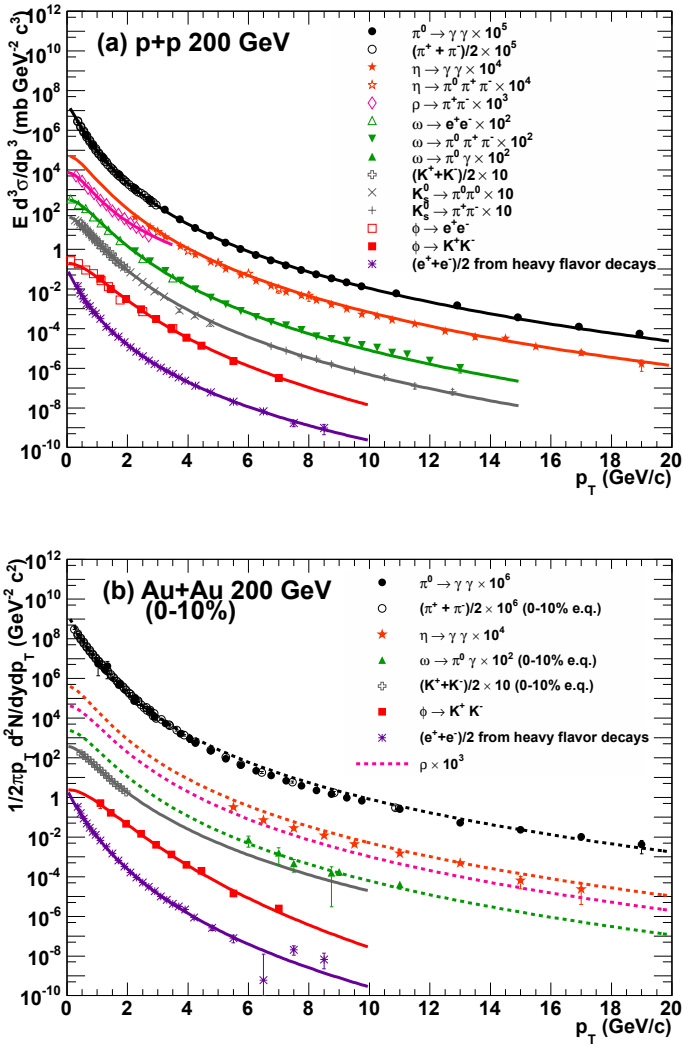

Figure 2.1: (a) The differential cross sections of different particles in p+p 200 GeV. Tsallis fitting curves are depicted as the solid curves on the data points. The solid curve on $\pi^0 \to \gamma\gamma$ [119] and $(\pi^+ + \pi^-)/2$ [120, 121] are obtained by the simultaneous fitting. The curves on the data points of $(K^+ + K^-)/2$ [120, 121], $K^0_s \to \pi^0\pi^0$ [122] and $K^0_s \to \pi^+\pi^-$ [123] are also obtained by the simultaneous fitting. The star symbols show $\eta \to \gamma\gamma$ [124] and $\eta \to \pi^0\pi^+\pi^-$ [125]. The open diamonds show $\rho \to \pi^+\pi^-$ [126]. The triangles show $\omega \to e^+e^-, \pi^0\pi^+\pi^-$ and $\pi^0\gamma$ [122]. The squares show $\phi \to e^+e^-$ and K^+K^- [122]. The asterisks show single electrons from heavy flavor decays [127]. (b) The invariant p_T spectra in Au +Au 200 GeV at the centrality class of 0-10%. The dotted curves are scaled by the N_{part} and assumed to be the same spectrum shape as that of p+p 200 GeV. The scaling curves are consistent with the data points of pions [128, 129, 130] , η [131] and ω [133], respectively. The solid curves are the fitting results to the data points of $K^{\pm}$ [130], ϕ [132] and single electrons from heavy flavor decays [134]. For $K^{\pm}$, the Tsallis parameter q is fixed since there is no data point in the high p_T region.

2.2 Backgrounds for di-electron measurement

In addition to the relatively small production of light vector mesons, the branching ratio (BR) to a di-electron pair is on the order of 10^{-4} for ϕ meson and 10^{-5} for ω/ρ meson. Furthermore many background electrons are produced from several kinds of background sources. The main background sources are listed as follows.

- Dalitz decays $\pi^0 \to \gamma e^+ e^-$ and $\eta \to \gamma e^+ e^-$,
- pair creations by decay photons from π^0 and η meson,
- semi-leptonic decays from charge kaons,
- semi-leptonic decays from heavy quarks (charm and bottom),
- charged hadron contaminations by electron misidentification.

2.2.1 Main background sources of electrons

Dalitz decay

Pseudo-scalar mesons such as π^0 and η mesons mainly decay into two photons. The Dalitz decay corresponds to the case where photons become off-shell and subsequently decay into di-electrons. The relation between 2γ decay process ($P \to \gamma\gamma$) and the Dalitz decay process ($P \to \gamma e^+ e^-$) is described by Kroll-Wada formula [136, 137] as follows.

$$\begin{aligned}
\frac{d\Gamma(P \to e^+e^-\gamma)}{dM_{e^+e^-}} &\propto \sqrt{1-\frac{4m_e^2}{M_{e^+e^-}^2}}\left(1+\frac{2m_e^2}{M_{e^+e^-}^2}\right)\frac{1}{M_{e^+e^-}} S\left(M_{e^+e^-}\right)\Gamma(P\to\gamma\gamma), \\
S\left(M_{e^+e^-}\right) &= |F_P(Q^2)|^2\left(1-\frac{M_{e^+e^-}^2}{m_P^2}\right)^3, \\
F_P\left(Q^2\right) &= \left(1-\frac{Q^2}{\Lambda_P^2}\right)^{-1}, \qquad (2.1)
\end{aligned}$$

where $M_{e^+e^-}$ is the invariant mass of di-electrons, m_e is the rest mass of an electron and m_P is the rest mass of a parent meson. $F_P\left(Q^2\right)$ is the electromagnetic transition form factor. Q^2 is equivalent to the square of the virtual photon mass (i.e. $Q = M_{e^+e^-}$). The measurements of the form factor by the experiments [138, 139] show $\Lambda_P \simeq M_\rho$, where M_ρ is the rest mass of ρ meson. The Kroll-Wada formula determines the branching ratio and the phase space of Dalitz decaying di-electron.

Photon conversion

Final-state real photons can stochastically convert into a di-electron pair by interacting with the detector materials. Photon-conversion probability is defined by

$$P_{cnv} = 1 - \exp\left(-\frac{\rho_m N_A}{Z} dx \sigma_{cnv}\right), \tag{2.2}$$

where ρ_m is material density (g/cm^2), N_A is Avogadro's number ($= 6.002 \times 10^{23}$), Z is molar mass (g/mol), dx is material thickness and σ_{cnv} is the total cross section of photon conversion. σ_{cnv} is parameterized as

$$\sigma_{cnv} = Z\left(Z+1\right)\left[F_1\left(X\right) + F_2\left(X\right)Z + F_3\left(X\right)/Z\right], \tag{2.3}$$

where $X = \ln\left(E_\gamma / m_e c^2\right)$, E_γ is energy of parent photons, m_e is electron mass and c is the velocity of the light. The function $F_i\,(i = 1 \sim 3)$ is an empirical polynomial equation obtained by a least-square fit to the data [140].

The differential cross section is expressed based on Bethe-Heilter formula [142] with some corrections,

$$\begin{aligned}
\frac{d\sigma_{cnv}}{d\epsilon} &= \alpha r_e^2 Z[Z + \xi\left(Z\right)]\left\{[\epsilon^2 + (1-\epsilon)^2]\left[\Psi_1\left(\delta\left(\epsilon\right)\right) - \frac{F\left(Z\right)}{2}\right]\right. \\
&\quad \left. + \frac{2}{3}\epsilon\left(1-\epsilon\right)\left[\Psi_2\left(\delta\left(\epsilon\right)\right) - \frac{F\left(Z\right)}{2}\right]\right\}, \qquad (2.4) \\
\xi\left(Z\right) &= \frac{\ln\left(1440/Z^{2/3}\right)}{\ln\left(183/Z^{1/3}\right) - f_c\left(Z\right)}, \qquad (2.5) \\
\delta\left(\epsilon\right) &= \frac{136}{Z^{1/3}} \frac{\epsilon_0}{\epsilon\left(1-\epsilon\right)}, \qquad (2.6) \\
f_c\left(Z\right) &= \left(\alpha Z\right)^2 \left[\frac{1}{1+\left(\alpha Z\right)^2} + 0.20206 - 0.0369\left(\alpha Z\right)^2\right. \\
&\quad \left. + 0.0083\left(\alpha Z\right)^4 - 0.0020\left(\alpha Z\right)^6 + \cdots\right], \qquad (2.7)
\end{aligned}$$

where $\epsilon = E/E_\gamma$, E is the total energy carried by one particle of the electron-positron pair and E_γ is the energy of parent photon. $\xi\left(Z\right)$ shows the interaction with the electron cloud. $\Psi_1\left(\delta\left(\epsilon\right)\right)$ and $\Psi_2\left(\delta\left(\epsilon\right)\right)$ are corrections of the screening effect. $f_c\left(Z\right)$ is Coulomb correction function to one-photon exchange approximation [145]. The kinematic limit of ϵ in Eq.(2.4) is,

$$\epsilon_0 \left(= \frac{m_e c^2}{E_\gamma}\right) \leq \epsilon \leq 1 - \epsilon_0. \tag{2.8}$$

The polar angle of a electron with respect to the direction of the parent photon is determined by the energy-angle distribution [143, 144]. The formula is

$$\frac{d\sigma_{cnv}}{d\Omega dE_\gamma} = \frac{2\alpha^3}{\pi E_\gamma}\left(\frac{E^2}{m_e^4}\right)\left\{\left[\frac{2x\left(1-x\right)}{\left(1+\mu^2\right)} - \frac{12\mu^2 x\left(1-x\right)}{\left(1+\mu^2\right)^4}\right] Z\left(Z+1\right) + \left[\frac{2x^2-2x+1}{\left(1+\mu^2\right)^2} + \frac{4lx\left(1-x\right)}{\left(1+\mu^2\right)^4}\right]\left(X - 2Z^2 f_c\left(Z\right)\right)\right\}, \quad (2.9)$$

where $\mu = E\theta/m$, θ is polar angle of electron with respect to parent photon.

The photon-conversion probability in Eq.(2.2) depends on the detector materials in a detector system. Photon-conversion probability is expected to be, at least, a few percent because photon conversion from the beam pipe and the first layer of the innermost detectors is not avoidable. In addition, these photon conversions are not removable in any detector system, even if the detector system is designed to be minimum amount of material and photon-conversion electrons are perfectly reconstructed in the detector.

Semi-leptonic decay from kaons

The dominant branches going to electrons are $K^{\pm}_{e3}$ ($K^+ \to \pi^0 e^+ \nu_e$ and $K^- \to \pi^0 e^- \bar{\nu_e}$) and K^0_{e3} ($K^0_L \to \pi^+ e^- \bar{\nu_e}$ and $K^0_L \to \pi^- e^+ \nu_e$). The branching ratio of $K^{\pm}_{e3}$ and $K^{\pm}_{e3}$ decay are 5.1 % and 40.55 %. The contribution from K^0_{e3} decay can be neglected due to the long lifetime of K^0_L[2].

Semi-leptonic decay from heavy quarks

Electrons originating from heavy quarks such as charm and bottom are produced though the complicated processes. The overall history from the heavy quark production to the final-state electron production is expressed by

$$\mathrm{p+p\ or\ A+A} \xrightarrow[\sigma_{pp}]{\mathrm{pQCD}} c\left(b\right) \xrightarrow[D_Q^H(z)]{\mathrm{fragmentation}} D\left(B\right) \xrightarrow{\mathrm{weak\ decay}} \mathrm{electron}. \quad (2.10)$$

The partonic production cross section is expressed in terms of dimensionless scaling function $f_{ij}^{(k,l)}\left(\eta\right)$ [146],

$$\hat{\sigma}_{ij}\left(\hat{s}, m_Q^2, \mu_R^2\right) = \frac{\alpha_s^2\left(\mu_R\right)}{m_Q^2}\sum_{k=0}^{\infty}\left(4\pi\alpha_s\left(\mu_R\right)\right)^k \sum_{l=0}^{k} f_{i,j}^{(k,l)}\left(\eta\right)\ln^l\left(\frac{\mu_R^2}{m_Q^2}\right), \quad (2.11)$$

[2] $c\tau$ of $K^{\pm}$ is 3.712 m and $c\tau$ of K^0_L is 15.34 m. The detector size is typically 2-5 m in radial direction at RHIC and LHC for electron measurement. $c\tau$ of $K^{\pm}$ is comparable to the size of detector but $c\tau$ of K^0_L is not.

where $\hat{s}$ is the partonic center of mass energy squared, m_Q is quark mass, μ_R is the renormalization scale and $\eta = \hat{s}/4m_Q^2 - 1$. The index i and j are combination of partons , that is, quark (q), anti-quark ($\bar{q}$) and gluons (g). $k = 0$ and $k = 1$ correspond to Leading order and Next-to-Leading order processes, respectively. At Leading order calculation, heavy quarks are produced by gg fusion and $q\bar{q}$ annihilation, while at the next-to-leading order qg and $\bar{q}g$ scattering is also included. Based on th factorization theorem, the total partonic cross section in p+p collisions are calculated by convoluting with the parton distribution functions in protons,

$$\begin{aligned}\sigma_{pp}\left(\hat{s}, m_Q^2\right) &= \sum_{i,j=q,\bar{q},g} \int_{\frac{4m_Q^2}{s}}^{1} \frac{d\tau}{\tau} \delta\left(x_1 x_2 - \tau\right) F_i^p\left(x_1, \mu_F^2\right) F_j^p\left(x_2, \mu_F^2\right) \\ &\quad \times \hat{\sigma}_{ij}\left(\tau, m_Q^2, \mu_R^2\right), \end{aligned} \tag{2.12}$$

where the sums i and j are over all massless partons and x_1 and x_2 are fractional momenta of partons. μ_F is the factorization scale. The renormalization scale, μ_R, and the factorization scale, μ_F, are frequently assumed to be same (i.e. $\mu = \mu_R = \mu_F$). The differential cross section of the heavy flavor hadrons such as D (B) mesons is expressed by,

$$\frac{d\sigma_H}{dp_T} = \int d\hat{p}_T dz \frac{d\sigma_Q}{d\hat{p}_T} D_Q^H(z)\, \delta\left(p_T - z\hat{p}_T\right), \tag{2.13}$$

where $z \equiv E_h/E_Q$, E_Q is energy of initial partons and E_H is energy of produced hadrons. p_T and $\hat{p}_T$ are the transverse momenta of heavy flavor hadrons and heavy quarks, respectively. $\frac{d\sigma_Q}{d\hat{p}_T}$ is the differential cross section of heavy quarks. $D_Q^H(z)$ is the fragmentation function of heavy quarks. The popular parameterizations of $D_Q^H(z)$ are listed below.

$$D_Q^H(z) \propto \frac{1}{z}\left(1 - \frac{1}{z} - \frac{\epsilon}{1-z}\right)^{-2} \text{[147]}, \tag{2.14}$$

$$D_Q^H(z) \propto z^{\alpha}(1-z) \text{[148]}, \tag{2.15}$$

$$\begin{aligned} D_Q^H(z) &\propto \left(\frac{1-z}{z} + \frac{(2-z)\,\epsilon_C}{1-z}\right) \times \\ &\quad \left(1+z^2\right)\left(1 - \frac{1}{z} - \frac{\epsilon_C}{1-z}\right)^{-2} \text{[149]}, \end{aligned} \tag{2.16}$$

$$D_Q^H(z) \propto (1-z)^{\alpha} z^{\beta} \text{[150]}, \tag{2.17}$$

$$D_Q^H(z) \propto \frac{(1-z)^{\alpha}}{z^{-\left(1+bm_T^2\right)}} \exp\left(-\frac{bm_T^2}{z}\right) \text{[151]}, \tag{2.18}$$

where ϵ, ϵ_C, a, bm_T^2, α and β are non-perturbative parameters depending on the heavy flavor hadrons. The parameters are determined by the experimental results in $e^+ + e^-$ collisions.

Figure 2.2 illustrates examples of hadronic decay and semi-leptonic decay from heavy quarks. Charm and bottom quark decays into electron bound for D^0 and B^0 mesons.

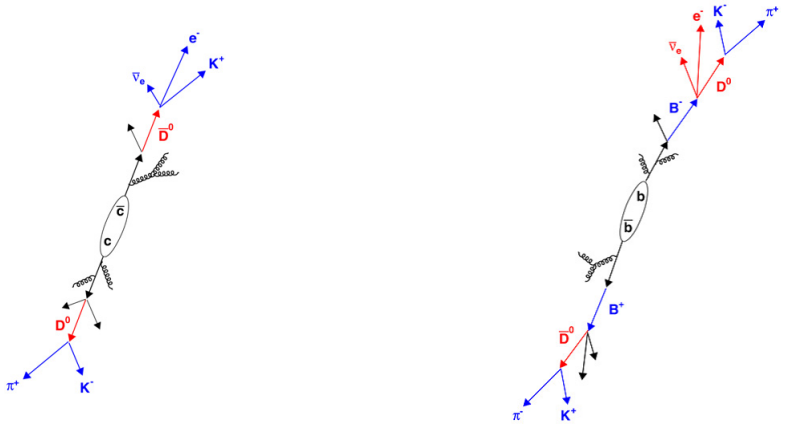

Figure 2.2: Semi-leptonic decay from charm and bottom [152].

Hadron contamination

In a real experiment, charged hadrons are wrongly identified as electrons due to the limitation of the detector performance. Therefore, hadron rejection capability is important and crucial for di-electron measurement. The rejection factor of charged hadrons, which is equivalent to the inverse of the misidentification probability, is often used for indicating hadron rejection capability of a detector system. The rejection factor for the typical electron identification device is from a few hundred to a thousand in stand-alone operation [153, 154, 155, 156].

2.2.2 Masses and branching ratios

Masses and branching ratios to a di-electron pairs for the light vector mesons and the other background particles are summarized in Table 2.2. The branching ratio of $c \to e$ is assumed to be 9.5 % [127]. For the other particles, the branching ratios are cited from the particle data group [12].

Particle	Mass (GeV/c^2)	Decay products	Branching ratio
ϕ	1.01946	e^+e^-	2.954×10^{-4}
ω	0.78265	e^+e^-	7.28×10^{-5}
ρ	0.77549	e^+e^-	4.72×10^{-5}
π^0	0.13498	$\gamma\gamma$	0.98823
		γe^+e^-	0.01174
η	0.54785	$\gamma\gamma$	0.03931
		γe^+e^-	7.0×10^{-3}
π^+	0.13957	-	-
π^-	0.13957	-	-
K^+	0.49368	$e^+\pi^0\nu_e$	0.0507
K^-	0.49368	$e^-\pi^0\bar{\nu_e}$	0.0507
$c\bar{c}$	-	e^+e^-	0.095

Table 2.2: Masses, decay products and branching ratios of the light vector mesons and the other background particles. Masses and branching ratios are cited from the particle data group [12]. The branching ratio of $c \to e$ is assumed to be 9.5 % [127].

2.3 Expected signals and backgrounds in ideal case

Once key physics processes and experimental conditions are taken into account, the expected signals and backgrounds can be estimated via the numerical simulation[3]. The estimations are performed under the minimum requirements of the experimental conditions, that is, the performance of the detector is almost ideal:

- photon conversion probability P_{cnv}: 1 %,
- rejection factor of charged pions $R_{\pi^\pm}$: 1000,
- geometrical acceptance ϵ_{acc}: 100 %,
- electron tagging efficiency ϵ_{tag}: 100 %,
- transverse momentum threshold p_T^{th}: 0.1 GeV/c,

Figure 2.3 shows the experted invariant mass spectra for individual di-electrons sources. The curves of the combinatorial pairs are reconstructed by

[3]The framework of the numerical simulation is explained in Chapter 6. In this section, the expected signals and backgrounds in ideal case are demonstrated in order to clear key issues for di-electron measurement.

all combinations of electrons and positrons but only true combinations are excluded. Figure 2.4 shows the comparison between the invariant mass of the signal pairs, the background pairs and the combinatorial background pairs. The peak structure can be seen in p+p collisions at $\sqrt{s} = 200$ GeV. On the other hand, the peaks are buries on the backgrounds in Au+Au collisions at $\sqrt{s_{NN}} = 200$ GeV, however the statistical significance is enough under the ideal experimental conditions.

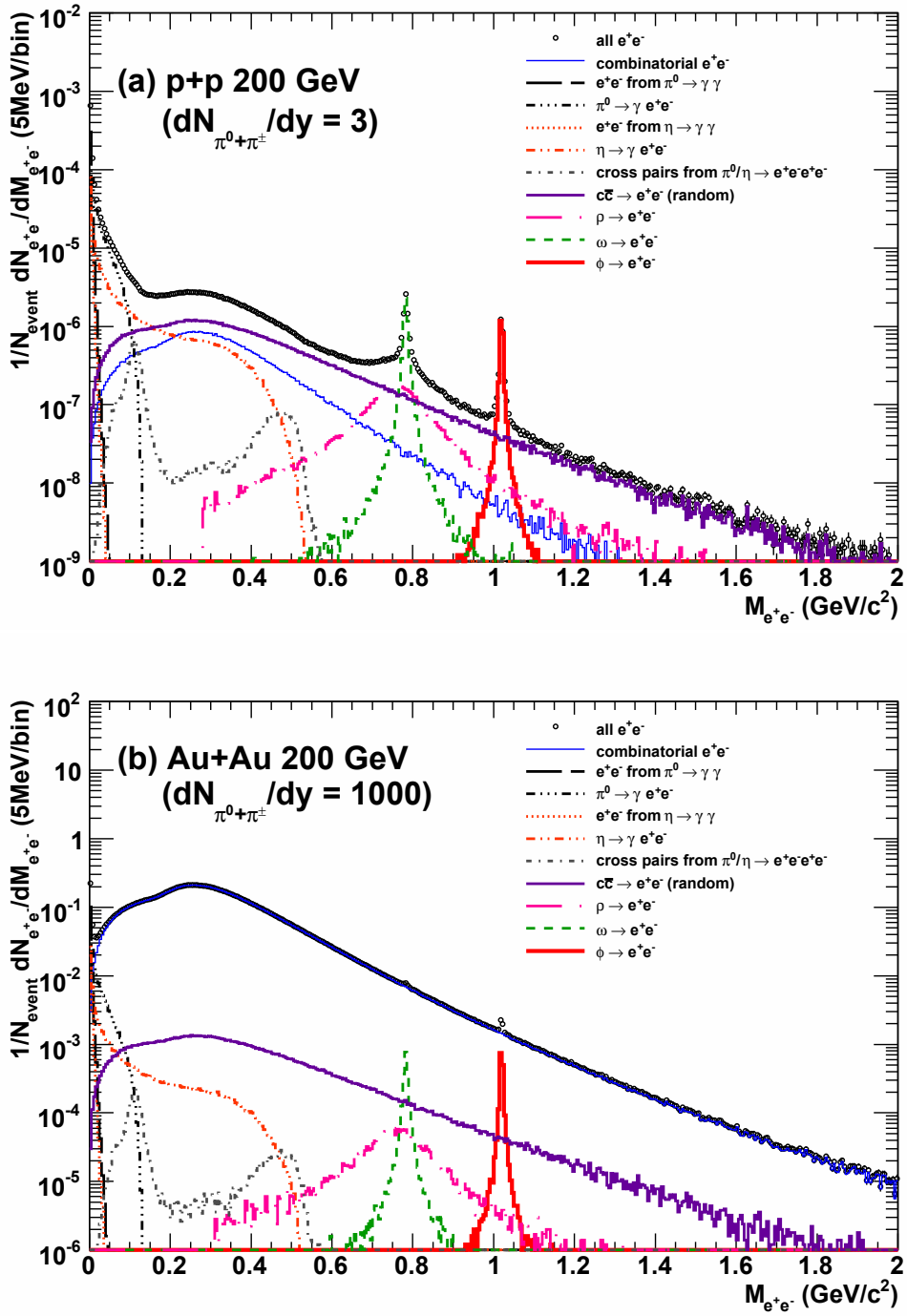

Figure 2.3: The invariant mass spectra of di-electrons from individual sources for the given $dN_{\pi^0+\pi^\pm}/dy$ with $P_{cnv} = 1$ %, $R_{\pi^\pm} = 1000$, $\epsilon_{acc} = 100$ %, $\epsilon_{tag} = 100$ %, $p_T^{th} = 0.1$ GeV/c. The mass spectra from individual origins are shown with different curves specified inside the plot. The curves of the combinatorial pairs are reconstructed by all combinations between electrons and positrons but only true combinations are excluded.

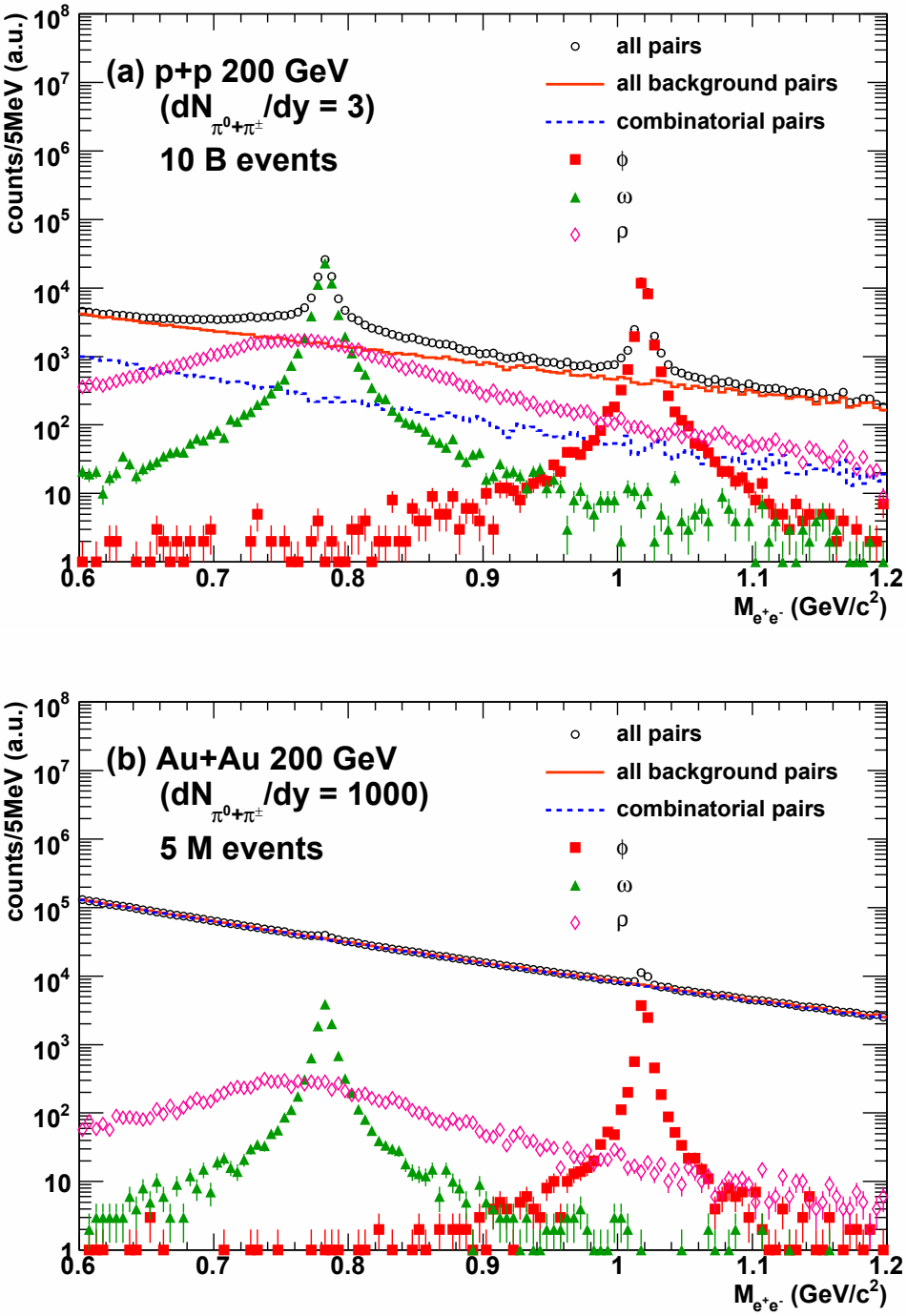

Figure 2.4: The inclusive mass spectra compared to the components of signal pairs, all background pairs and combinatorial background pairs for the given $dN_{\pi^0+\pi^\pm}/dy$ with $P_{cnv} = 1$ %, $R_{\pi^\pm} = 1000$, $\epsilon_{acc} = 100$ %, $\epsilon_{tag} = 100$ % and $p_T^{th} = 0.1$ GeV/c. The simulated number of events for each collision system is shown inside the plot.

Chapter 3

Experimental setup

3.1 RHIC

The Relativistic Heavy Ion Collider (RHIC) is sited at Brookhaven National Laboratory (BNL) in the United states. The RHIC is a colliding-type accelerator and has versatile capabilities of accelerating various nuclear species from protons (p^+) to gold ions ($^{197}Au^{79+}$) at the wide dynamic range of energy. Colliding energy reaches 500 GeV in $p+p$ collisions and 200 GeV per nucleon pair in Au+Au collisions at maximum.

The acceleration cycle starts from producing negative gold ions by a cesium sputter ion source operated in the pulse beam mode. The ions are injected to the Tandem Van de Graaf accelerator (TANDEM) and stripped to a the positive ion state during passing through a thin carbon foil (2 μ g/cm^2). The ions are accelerated to 1 MeV per nucleon by the TANDEM. The ion beam from the TANDEM is again stripped to higher charge state by another carbon stripper foil (15 μ g/cm^2) and goes into the Booster Synchrotron (BOOSTER) through 850-m-long transfer line. In the BOOSTER, the ions are accelerated to 72 MeV per nucleon. Before being injected to the Alternating Gradient Synchrotron (AGS), the gold ions is stripped to the +77 charge state. The last two electrons are removed and the $^{197}Au^{79}$ beam is injected into the two counter-rotating rings of the RHIC. One of them, which is called as "blue" ring, brings the beam in the clockwise direction. The other is "yellow" ring providing the beam in the counterclockwise direction. The beam energy reaches 10-100 GeV per nucleon during rotating the RHIC ring. Two oppositely-incident beams collide at the crossing point of the two rings.

Figure 3.1 shows the overview of the RHIC complex. The RHIC ring has a circumference of 2.8 km with maximum bunch of 120. The designed luminosity is 2.0×10^{26} cm^{-2}s^{-1}. Acceleration and storage of beam bunches are performed by two RF systems. One is operating at 20 MHz to capture

the AGS bunches and accelerates to the maximum energy of ions. The other is operating at 197 MHz. It is used to squeeze the beam profile against the Coulomb scattering of ions in a bunch. Finally 1.1×10^9 ions are stored in a bunch and the ion beams are crossing at 106-ns interval.

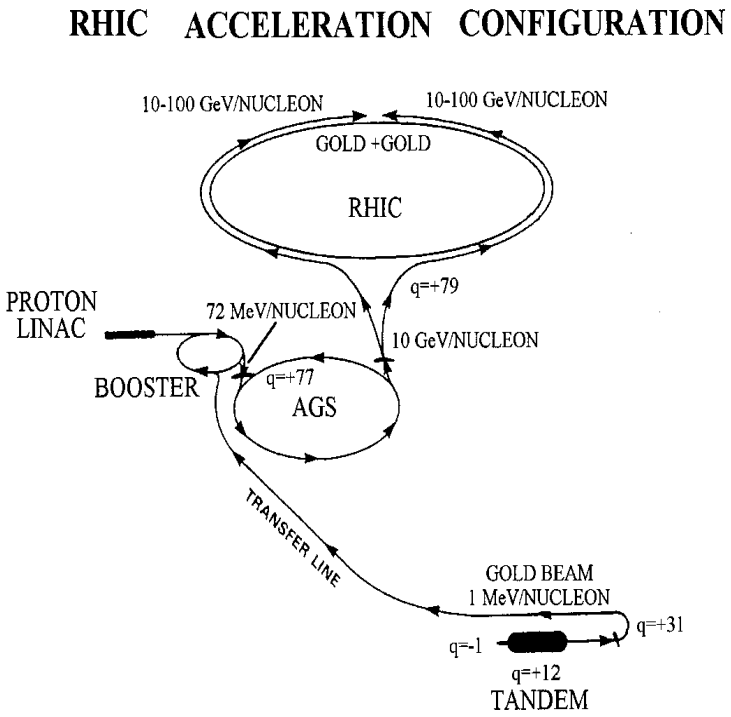

Figure 3.1: The overview of the RHIC complex and acceleration scheme for heavy ions.

3.2 PHENIX overview

Heavy-ion physics are studied by 4 experiments (PHENIX [160], STAR [161], PHOBOS [162] and BRAHMS [163]) at the RHIC. They are approaching by different viewpoints to elucidate the property of the quark-gluon matters and naturally they are designed by different concepts. The PHENIX has prominent capabilities of simultaneously measuring electromagnetic probes such as electrons, photons and muons.

The PHENIX detector comprises the global detectors, the central arms and the forwards arms as shown in Fig.3.2. The central arms are centered at

zero rapidity with azimuthal coverage of about 2π. The forward arms have full azimuthal coverage at forward and backward rapidity. Each arm consists of a number of subsystems. Fig. 3.3 summarized the rapidity and azimuthal angle ϕ coverage and their basic features for each subsystem.

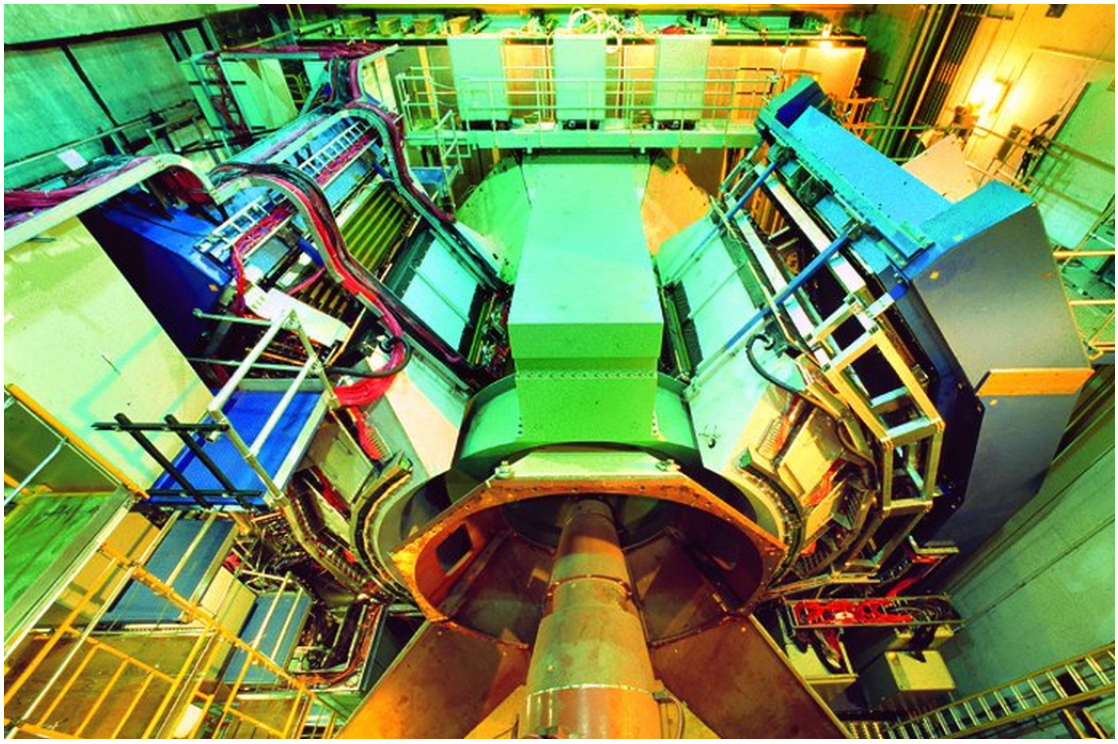

Figure 3.2: Photograph of the PHENIX detector viewed from north to south. The central arms are visible on the right (west) and east (left) sides. In the back the south muon magnet and the muon identifier detectors are visible.

Element	$\Delta\eta$	$\Delta\phi$	Purpose and Special Features
Magnet: central (CM)	±0.35	360°	Up to 1.15 T·m.
muon (MMS)	-1.1 to -2.2	360°	0.72 T·m for $\eta = 2$
muon (MMN)	1.1 to 2.4	360°	0.72 T·m for $\eta = 2$
Silicon (MVD)	±2.6	360°	$d^2N/d\eta d\phi$, precise vertex, reaction plane determination
Beam-beam (BBC)	±(3.1 to 3.9)	360°	Start timing, fast vertex.
NTC	±(1 to 2)	320°	Extend coverage of BBC for p-p and p-A.
ZDC	±2 mrad	360°	Minimum bias trigger.
Drift chambers (DC)	±0.35	90°×2	Good momentum and mass resolution, $\Delta m/m = 0.4\%$ at $m = 1$GeV.
Pad chambers (PC)	±0.35	90°×2	Pattern recognition, tracking for nonbend direction.
TEC	±0.35	90°	Pattern recognition, dE/dx.
RICH	±0.35	90°×2	Electron identification.
ToF	±0.35	45°	Good hadron identification, σ <100 ps.
T0	±0.35	45°	Improve ToF timing for p-p and p-A.
PbSc EMCal	±0.35	90°+45°	For both calorimeters, photon and electron detection.
PbGl EMCal	±0.35	45°	Good $e^{\pm}/\pi^{\pm}$ separation at $p > 1$ GeV/c by EM shower and $p < 0.35$ GeV/c by ToF. $K^{\pm}/\pi^{\pm}$ separation up to 1 GeV/c by ToF.
μ tracker: (μTS)	-1.15 to -2.25	360°	Tracking for muons.
(μTN)	1.15 to 2.44	360°	Muon tracker north installed for year-3
μ identifier: (μIDS)	-1.15 to -2.25	360°	Steel absorbers and Iarocci tubes for
(μIDN)	1.15 to 2.44	360°	muon/hadron separation.

Figure 3.3: Coverages and features for subsystems [160].

3.3 PHENIX coordinate system

Fig.3.4 is the definition of coordinate variables and conventions in PHENIX detectors. Nuclei are delivered by the blue ring and the yellow ring along with the z axis and collide at the original point. Central arm of PHENIX detectors is located at mid-rapidity region (i.e. at the range of $\theta \sim \frac{\pi}{2}$). The detector configurations of the central arm from the view of the beam is shown in the top figure of Fig.3.5. Muon arm of PHENIX detectors is located at forward or backward rapidity region. The bottom figure of Fig.3.5 is the detector configuration of the muon arm on y-z plane.

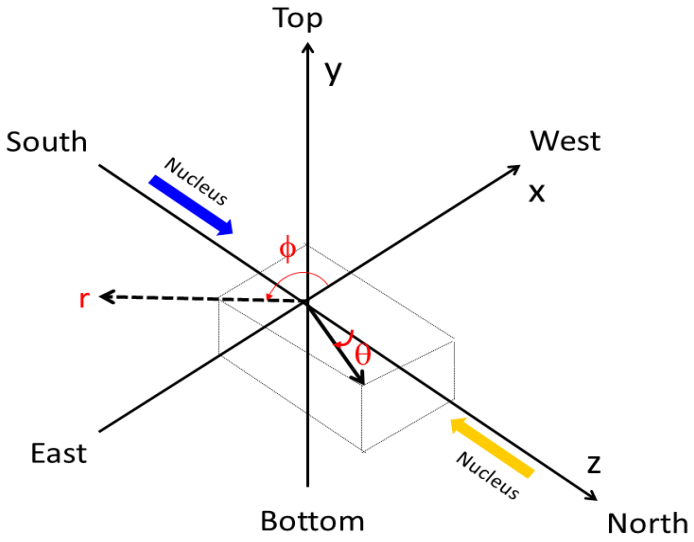

Figure 3.4: The definition of coordinate variables and conventions in PHENIX experiment.

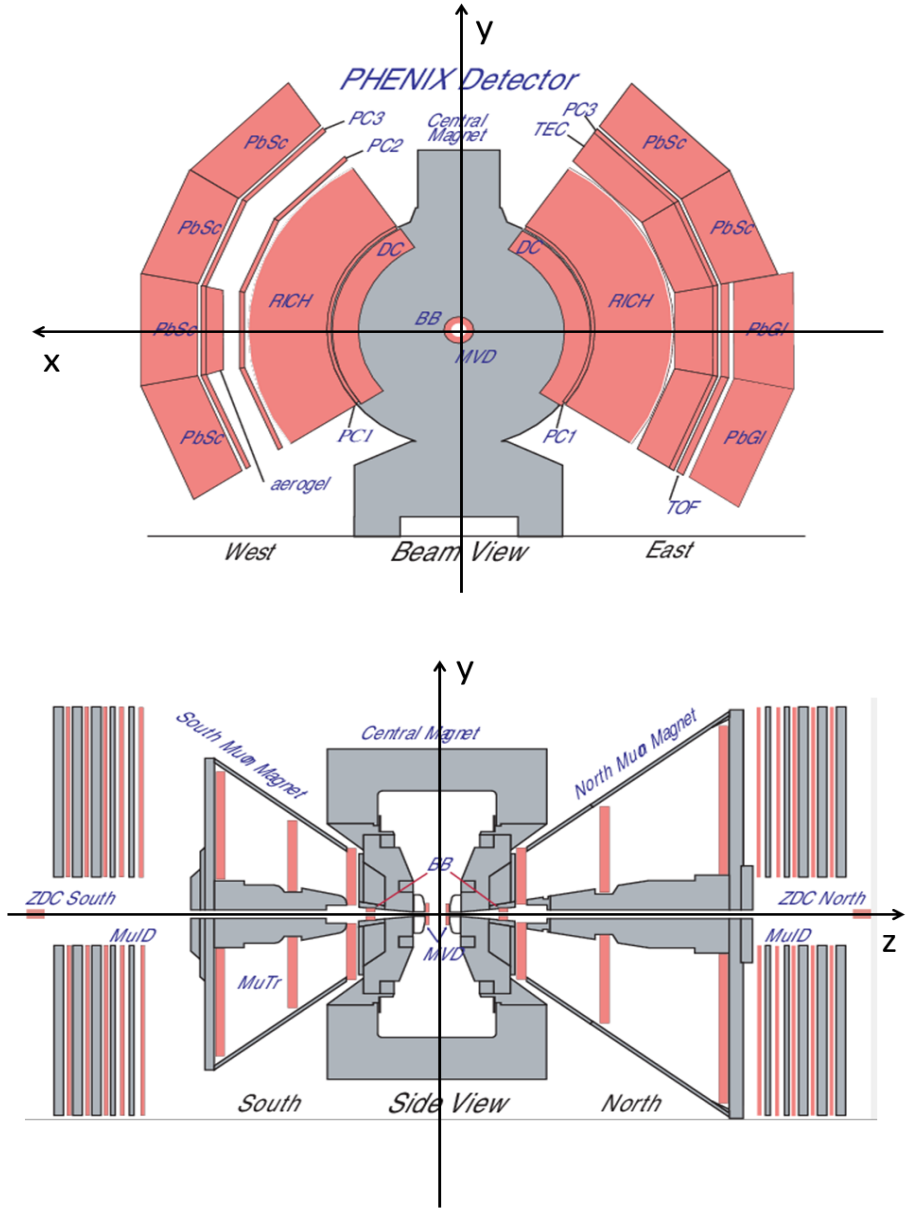

Figure 3.5: The detector configuration of the central arm on x-y plane (top) and the detector configuration of the muon arm on y-z plane (bottom).

3.4 The global detector

The global detectors are used to determine the collision event (trigger) and the event topology (Zvertex, centrality and the reaction plane). Beam Beam Counter (BBC) [164] and the Zero Degree Calorimeter (ZDC) [167, 168] are explained in this section.

3.4.1 Beam Beam Counter

BBC is placed at ± 144 cm far from the center of the central arm along with beam axis and surrounds the beam pipe concentrically as shown in Fig.3.6 and Fig.3.7. BBC consists of two identical sets on both side, one on the north side (BBCN) and the other on the south side (BBCS). BBC covers the rapidity range of $3.1 < |\eta| < 3.9$ and full azimuthal angle of 2π. Each set consists of 64 Cherenkov detector elements with Chrenkov threshold, $\beta_{th} \sim 0.7$. An element is constructed by one-inch mesh dynode phototube (Hamamatsu R6178) on 3-cm-long quartz radiator. The intrinsic timing resolution of each element is about 90 ps in p+p collision and 40 ps in Au+Au collision after correcting the slewing effect[1]. Slewing correction is performed based on the correlation measurement between output charge and intrinsic timing of BBC. Intrinsic timing is calculated by the difference between raw hit timing of each element and reference hit timing, which is given by the truncated timing average of fired elements. The timing resolution depends on multiplicities in a collision. One of the reason is that multiple particles in a Au+Au collision enter into an element and the falling edge of pulse becomes shaper. The second reason is that the number of fired elements in a Au+Au collision is higher than in a p+p collision and the truncated average of timing is measured with higher accuracy in Au+Au collisions. The measured charge is deduced to the number of incident charged particles. The gain of each element is well calibrated and 40 particles can be measured at maximum per element.

BBC provides important information about a collision event. The coincident hit information of BBCN and BBCS is transmitted to the level-1 board and is processed as the trigger of inelastic collisions during taking data. In addition, BBC is used to determine the collision geometry such as the centrality and the reaction plane. The centrality has an information on the overlap region in a nucleus-nucleus collision. The centrality is determined by the multiplicity measurement via BBC and energy measurement of neutrons via ZDC. The reaction plane is determined by the inclination of a nucleus-nucleus collision to the lab frame. This variable is measured by the azimuthal

[1]The detected timing depends on the falling edge of the output pulse. Therefore the output of timing and charge are usually correlated. This effect is called "slewing".

deviation of charged particles on the plane of BBC. In addition, BBC provides the start timing for the time-of-flight measurement. The time-of-flight information is used for particle identification.

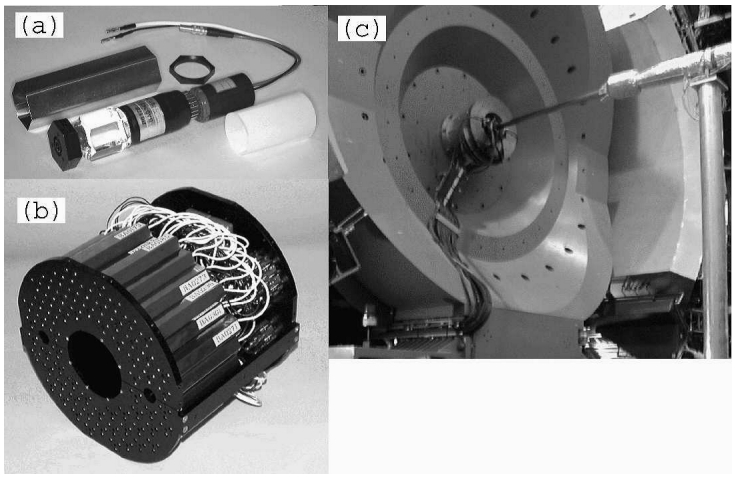

Figure 3.6: (a) A single detector element. (b) An assembled module (64 elements). (c) Installed modules.

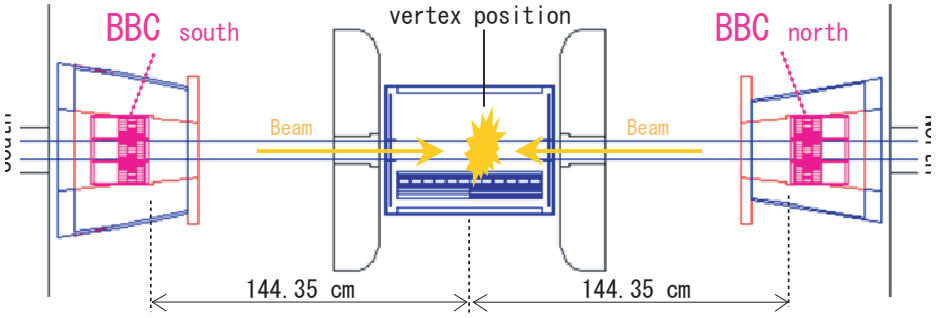

Figure 3.7: The position of BBCs along with the beam axis.

3.4.2 Zero Degree Calorimeter

ZDC is a sandwich-type calorimeter to measure the total energy of evaporating neutrons from the beam ion. ZDC is placed at ± 18 m from the center of the interaction point and behind the DX dipole magnet as shown in Fig.3.8. Due to the upstream DX dipole magnet, charged particles such as protons are bent and go away from the acceptable region of ZDC. On the other hand, neutrons can enter ZDC. At the beam energy of 100 GeV per nucleon, nucleons diverge by less than 2 mrad from the beam axis. The angular acceptance of ZDC is $|\theta| < 2$ mrad. It is comparable to the neutron divergence.

ZDC consists of three identical modules. A single module is a sampling calorimeter with 2 interaction length (Λ_I) and 50 radiation length (X_0). Fig.3.9 shows the mechanical design of a single module. Each module is constructed by 27 layers of tungsten absorber plates and Poly Methyl Meth Acrylate (PMMA) optical fibers. A optical fiber ($\phi = 0.5$ mm) is sandwiched between 5-mm-thick tungsten plates. Fibers are bundled and pulled out to a read-out phototube (Hamamatsu R329-2). The orientation of a module has an inclination of 45° with respect to the beam axis in order to collect effectively Cherenkov lights from secondary charged particles in a shower. The energy resolution of ZDC is about 21 % for 100 GeV neutrons [169]. The measured total energy of neutrons are used for the centrality measurement.

3.5 Magnet system

The PHENIX magnet system consists of three magnets such as Central Magnet (CM), North Muon Magnet (NMN) and South Muon Magnet (MMS) [166]. The configuration of these magnets are illustrated in Fig. 3.10.

3.5.1 The Central Magnet

Two sets of circular coil are implemented in the CM pole face. The several sets of magnetic fields are provided by combining the polarity of the inner coil and the outer one. CM+ configuration is set by operating only outer coil. CM++ configuration is provided under operating both the outer coil and the inner coil with the positive polarity. CM+− configuration is provided by operating the outer coil with the positive polarity and the inner coil with the negative polarity. During Au+Au collision period, the data are taken under CM++ or CM−−. The left figure of Fig. 3.11 shows the magnetic field lines under CM++. The right figure of Fig. 3.11 shows the strength of magnetic field as a function of distance x for individual configurations.

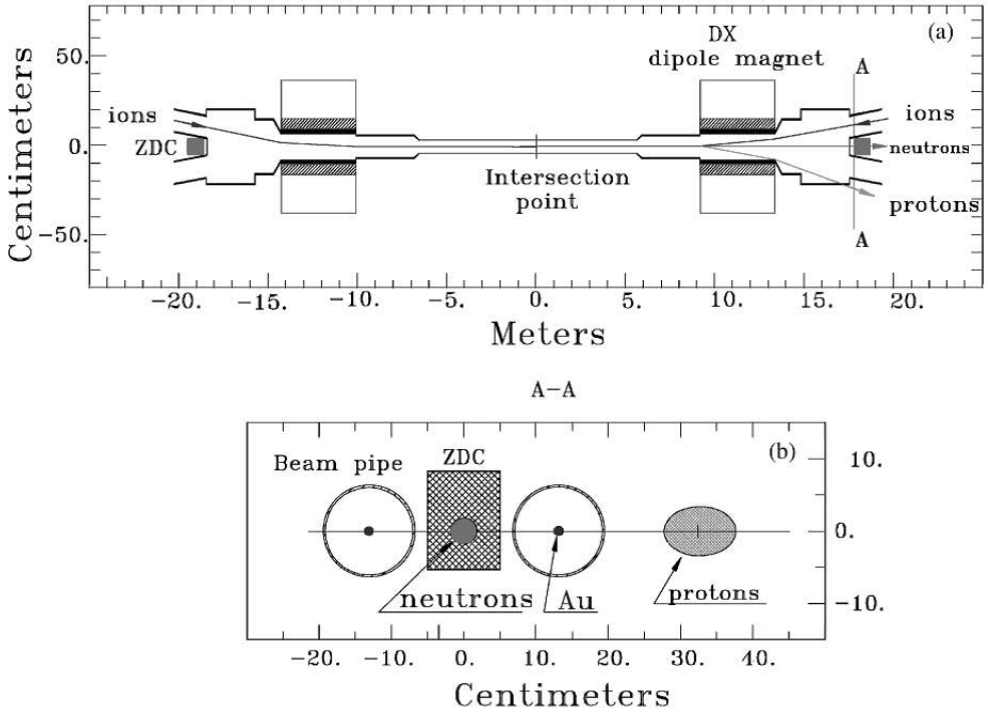

Figure 3.8: The location of ZDC from the beam view and the profile of neutorons and protons (top). The location of ZDC apart from the interaction point (bottom) [167, 168].

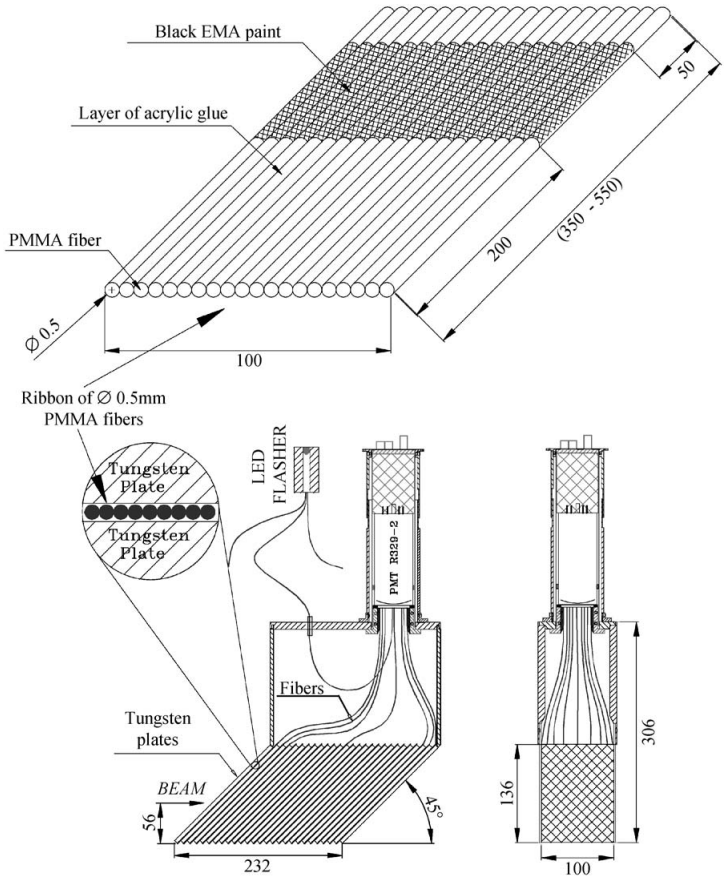

Figure 3.9: Mechanical design of the ZDC tungsten modules [167, 168]. Dimensions are shown by mm.

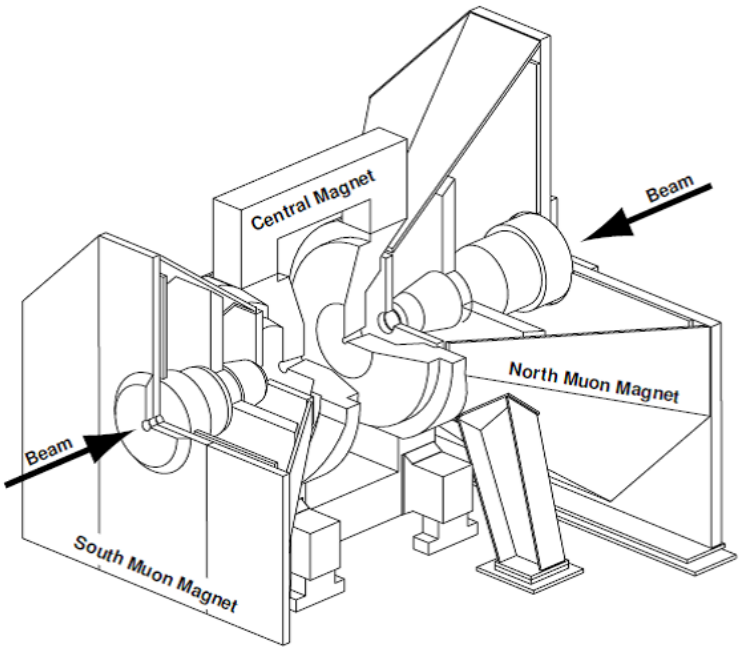

Figure 3.10: Line drawing of the PHENIX magnet system.

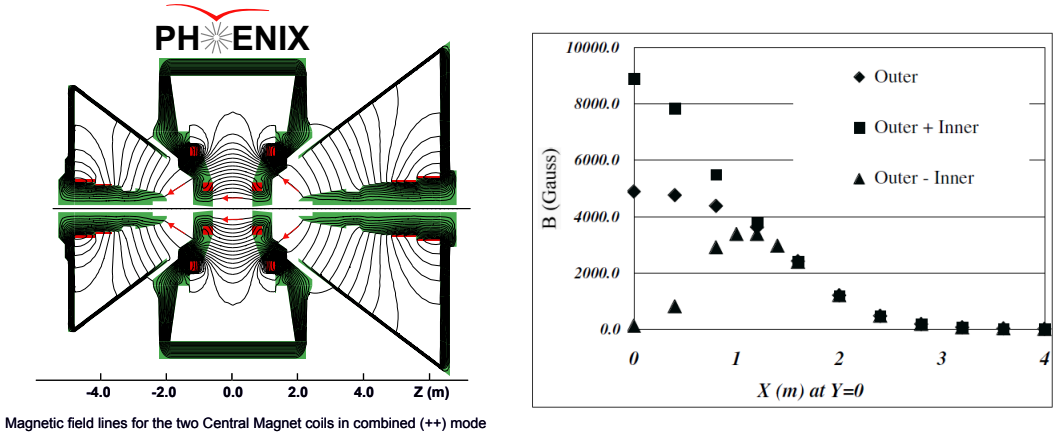

Figure 3.11: Magnetic-field lines for CM++ configuration (left). Red box is the coils. The strength of the magnetic field for each configuration (right) [166].

3.6 The central-arm spectrometers

3.6.1 Drift Chamber

Drift Chamber (DC) is a multi-wire gaseous chamber to measure the trajectories of charged particles in the r-ϕ plane and determines transverse momentum of individual particles. DC is located at a radial distance of $2.02 < R < 2.48$ m from the interaction point.

DC consists of two separated gas volumes located in the west and east sides in the residual magnetic field of 0.06 Tesla. The detector volume is filled with a gas mixture of 50 % argon and 50 % ethane and covered by the Titanium frame. Each frame is cylindrically shaped to cover 90° in azimuth and 1.8 m along the beam axis. A single frame is divided into 20 identical sectors. The mechanical design of a DC is shown in the left of Fig.3.12. Each sector covers 4.5° in azimuth and consists of six types of wire modules, which are called X1, U1, V1, X2, U2 and V2. Each module contains 4 anode plane and 4 cathode plane with a 2.0 to 2.5 cm drift space in the ϕ direction. The X1 and X2 wire cells are aligned in parallel to the beam pipe for precise track reconstruction in the r-ϕ plane. The U and V wire cells run with stereo angle of about 6° with respect to the X wires in order to measure the z coordinate of the track. The stereo angle is selected to match the z resolution of the downstream pad chambers for the good pattern recognition of tracks even at high multiplicity. The X-stereo cells have 12 Sense wires. The U and V-stereo cells have 4 S wires. In total, 40 drift cells are aligned at the unit radius. S wires in an anode plane are separated by Potential (P) wires and surrounded by Gate (G) and Back (B) wires. P wires provide a strong electric field and separate sensitive regions of individual anode wires. G wires limit the the track sample length to roughly 3 mm and terminated undesirable drift lines. B wires have a rather low potential and terminate most of the drift lines from these side. These configurations are helpful to eliminate left-right ambiguity and result in decreasing the signal rate per electronics channel by a factor of two. In order to keep efficient track recognition for up to 500 tracks, each sense wire is separated in the center into two halves. Each half of a S wire is electrically isolated by a 100 μ-m-thick Kapton strip and read out independently. Therefore DC contains, in total, 6500 wires and 13000 read out channels. The electric field in the chamber is adjusted to keep the mean pulse width to near 35 nsec. The double track resolution reaches better than 2 mm and the track-finding efficiency is beyond 99 %. The single wire resolution is found to be 165 μm.

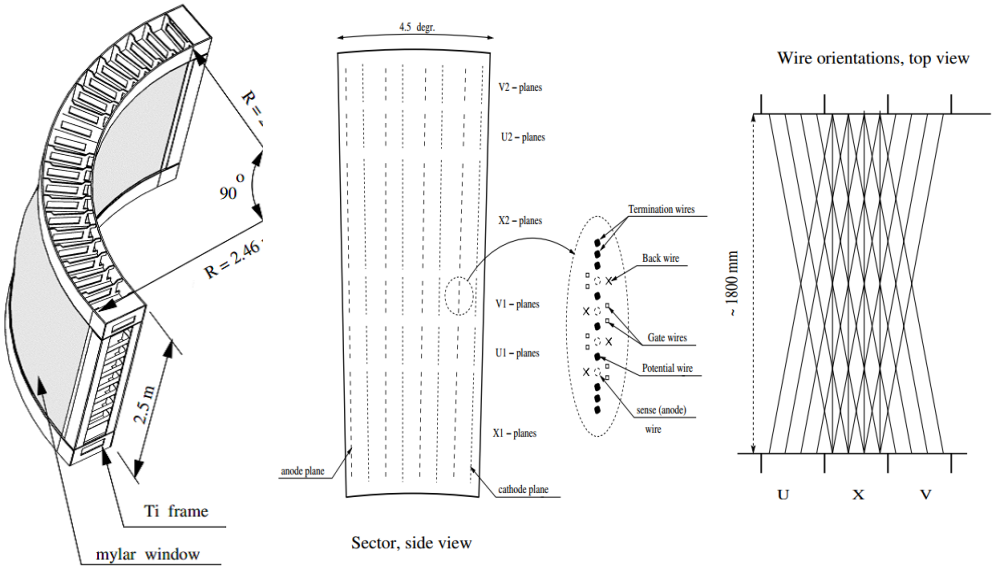

Figure 3.12: A frame of a drift chamber (left). The layout of wire position within one sector and the wire alignment inside the anode plane (middle). A schematic diagram of the stereo wire orientation (right) [170].

3.6.2 Pad Chamber

Pad Chamber (PC) is a multiwire proportional chamber with cathode pad read out to determine the polar angle θ which allows the momentum in the z direction and assists in track hit association to the downstream detectors such as RICH and EMCal. PC consists of three separate layers which are PC1, PC2 and PC3 (Fig. 3.13). PC1 is the innermost detectors installed at the exit of the DC at $2.47 < R < 2.52$ m. The combined information between PC1 and DC provides three dimensional momentum of charged particles and the straight line of particle trajectory outside the magnetic field. PC2 is installed only in the west arm and located behind RICH at $4.15 < R < 4.21$ m. PC3 is located in front of the EMCal at $4.91 < R < 4.98$ m. PC2 and PC3 are used for the track projection to the outer detectors. PC is also used to reject secondary charged particles and to veto charged particles in identifying photons with EMCal. Each detector contains a single plane of wires inside a gas volume bounded by two cathode planes. The gas is chosen to be the mixture of 50 % Argon and 50 % Ethane. One cathode planes are segmented in small cells. Each cell consists of nine pixels but three different read outs. As shown in Fig.3.14, the interleaved pixels are gathering together nine-by-nine and connected to a common readout channel such that three

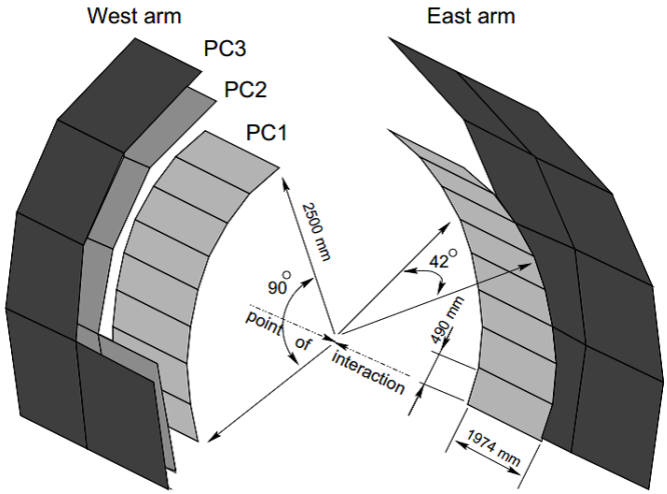

Figure 3.13: The orientation of the PC1, PC2 and PC3 (top).

pixels in a cell are always connected to different but neighboring channels. Therefore hit information in a cell are established as long as three read out coincide. This special pad design saves a factor of nine in readout channels and decreases accidental electrical noise. The PC system has, in total, 172,800 electronic readout channels. The efficiency achieves to be better than 99.9 %

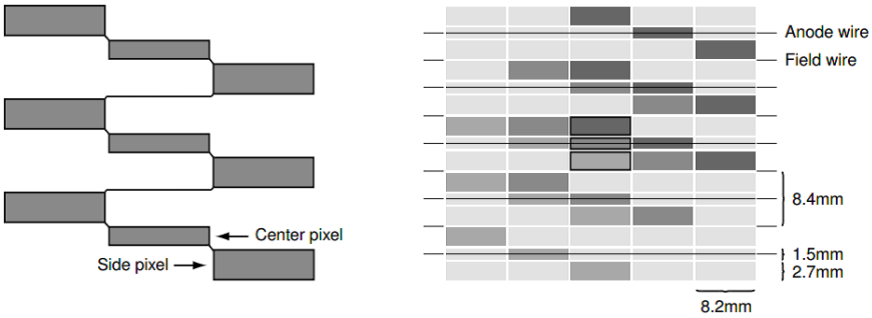

Figure 3.14: The pixel arrays in a pad (left). Single cell is defined by three pixels (right) [170].

for individual PCs as a result of the study with cosmic rays in Run2 (2001-2002). The position resolutions in z direction are 1.7 mm, 3.1 mm and 3.6 mm for the PC1, PC2 and PC3, respectively.

3.6.3 Ring Imaging Cherenkov detector

Ring Imaging Cherenkov detector (RICH) separates electrons from charged hadrons below the Cherenkov threshold of pions. RICH is located in the west and east sides. The radial distance of RICH from the interaction points is 2.5 $< R <$ 4.1 m.

Figure 3.15 contains a cutaway drawing of one of RICH detectors revealing the internal components. Each RICH has a volume of 40 m^3 with an entrance window area of 8.9 m^2 and an exit window area of 21.6 m^2. Each volume is filled with the radiator gas of CO^2, which has a refractive index of $(n-1) = 410 \times 10^{-6}$ at 20°C and 1 atm. The refractive index of CO^2 corresponds to a threshold velocity of $\beta_{th} = 1/n = 0.99590168$ and a γ factor of $\gamma_{th} = 1/\sqrt{1-\beta_{th}^2} = 34.932$. Therefore Cherenkov thresholds are $p_T = m_e\beta_{th}\gamma_{th} = 0.018$ GeV/c for electrons (m_e=0.511 MeV/c^2) and $p_T = m_\pi\beta_{th}\gamma_{th} = 4.87$ GeV/c for pions (m_π = 139.570 MeV/c^2), respectively. Each detector contains 48 composite mirror panel, forming two intersecting spherical surfaces, with a total reflecting area of 20 m^2. The mirrors focus on the emitting Cherenkov light onto two arrays of 1280 PMTs (Hamamatsu H3171S). The PMT arrays are symmetrically aligned at the either side of the entrance window as shown in Fig.3.16. The rejection factor of charged pions

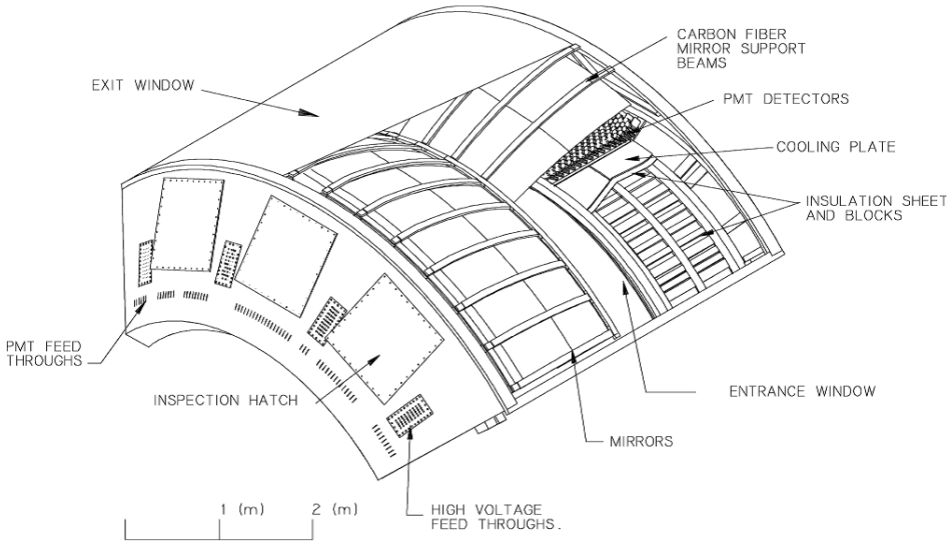

Figure 3.15: A cutaway view of one arm of the RICH detector [165].

is estimated as a function of the electron efficiency in Fig.3.17. The rejection factor of pions is, for example, 500 at the electron efficiency > 80 % with a radiator of CO^2.

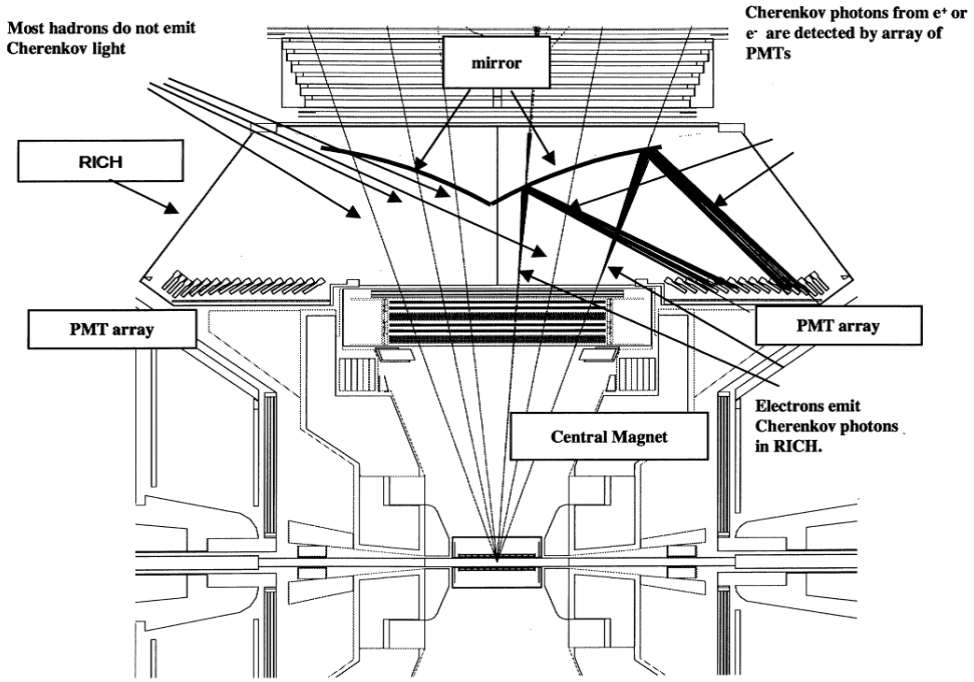

Figure 3.16: The orientation of the components in RICH.

3.6.4 Electromagnetic calorimeter

The main role of Electromagnetic Calorimeter (EMCal) is to measure the energies and spatial positions of photons and electrons. EMCal consists of lead-scintillator calorimeter (PbSc) and lead-glass calorimeter (PbGl). Four sectors of PbSc are installed in the west arm. Two sectors of PbSc and two sectors of PbGl are installed in the east arm.

Lead-scintillator calorimeter

Lead-scintillator calorimeter (PbSc) is a shashlik type sampling calorimeter [173, 172] with radiation length $X_0 = 2.0$ cm, Moliere radius $R_M \sim 3.0$ cm and nuclear interaction length $\lambda_I = 44$ cm. PbSc has the sandwich structure by the lead absorber with 1.5 mm thickness and the scintillator with 4 mm thickness. The scintillating plastic is made of Polystyrene with 1.5 % of p-Terephenyl as the primary fluorescent material and 0.01 % POPOP[2] as wavelength shift material. PbSc consists of 15552 individual towers covering an area of about 48 m^2. Each tower contains 66 sampling cells consisting of

[2]PT stands for p-Terephenyl. POPOP stands for p-bis[2-(5-Phenylloxazolyl)]-benzene

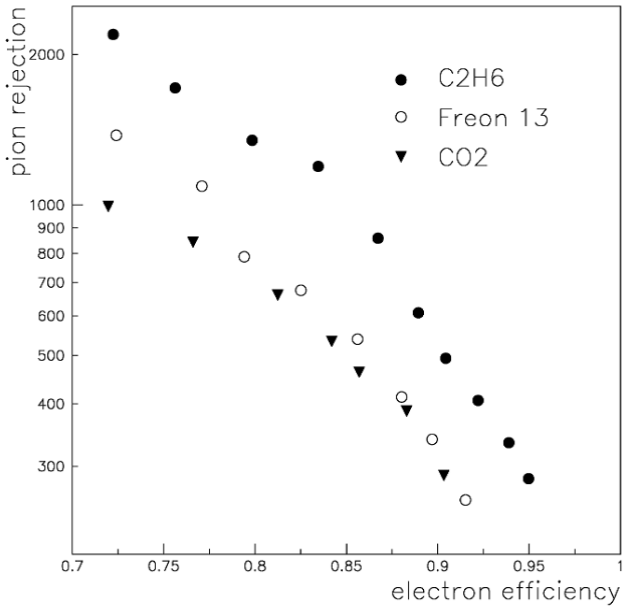

Figure 3.17: Simulated pion rejection factor vs electron efficiency for Ethane, Freon 13 and CO_2 [171].

alternating tiles of lead absorber and scintillator. These cells are connected by 36 longitudinally penetrating wavelength shifting fiber for light collection. Light is read out by 30 mm phototubes (FEU115M) at the back of the towers. Four towers are grouped into one module as shown in Fig.3.18. 36 modules are attached to a backbone and held together by welded stainless steel skins on the outside to form a rigid structure called a super module. 16 supper modules make a single sector.

The energy linearity, the energy resolution and the position resolution are measured with the electron beam from AGS (BNL) and SPS (CERN) [174]. They are evaluated as a function of incident energy of electrons in Fig.3.19. The energy resolution of PbSc is given by

$$\frac{\sigma_E}{E} = \frac{8.1\%}{\sqrt{E(\mathrm{GeV})}} \oplus 2.1\%. \tag{3.1}$$

The position resolution is evaluated with the logarithmic method [175] as follows,

$$\sigma_x\,(E) = \frac{5.9\,(\mathrm{mm})}{\sqrt{E(\mathrm{GeV})}} \oplus 1.4\,(\mathrm{mm})\,. \tag{3.2}$$

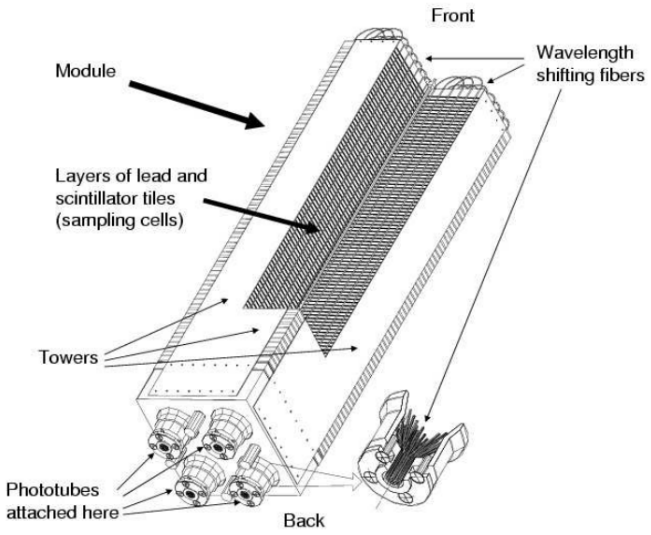

Figure 3.18: The Interior view of a Pb-scintillator calorimeter module showing a stack of scintillator and lead plates, wavelength shifting fiber readout and leaky fiber inserted in the central hole [173].

Lead-glass calorimeter

Lead-glass calorimeter (PbGl) is a Cherenkov detector with radiation length $X_0 = 2.8$ cm, Moliere radius $R_M = 3.7$ cm, nuclear interaction length $\lambda_I = 38$ cm and refractive index $n = 1.648$. PbGl comprises 192 supermodeules (SM) in an array of 16 SM wide by 12 SM high. Each SM consists of 24 modules in an array of 6 module wide by 4 module high. Figure 3.20 shows exploded view of a PbGl supermodule. The Cherenkov light emitted in the electromagnetic shower process is read out with the phototubes (FEU84) at the end of each module. Each PbGl crystal consists of 55 % PbO and 45 % SiO_2 with $4\times4\times40$ cm^2. Therefore the PbGl has 9216 read out channels in total.

The incident energy dependence of the measured energy resolution for positron showers is shown in Fig. 3.21. The energy resolution is expressed with the fit parameters as follows.

$$\frac{\sigma_E}{E} = \frac{6.0\%}{\sqrt{E(\mathrm{GeV})}} \oplus 0.8\%. \tag{3.3}$$

The position resolution can be fit with the parameterization and given by

$$\sigma_x\,(E) = \frac{8.4\,(\mathrm{mm})}{\sqrt{E\,(\mathrm{GeV})}} \oplus 0.2\,(\mathrm{mm})\,. \tag{3.4}$$

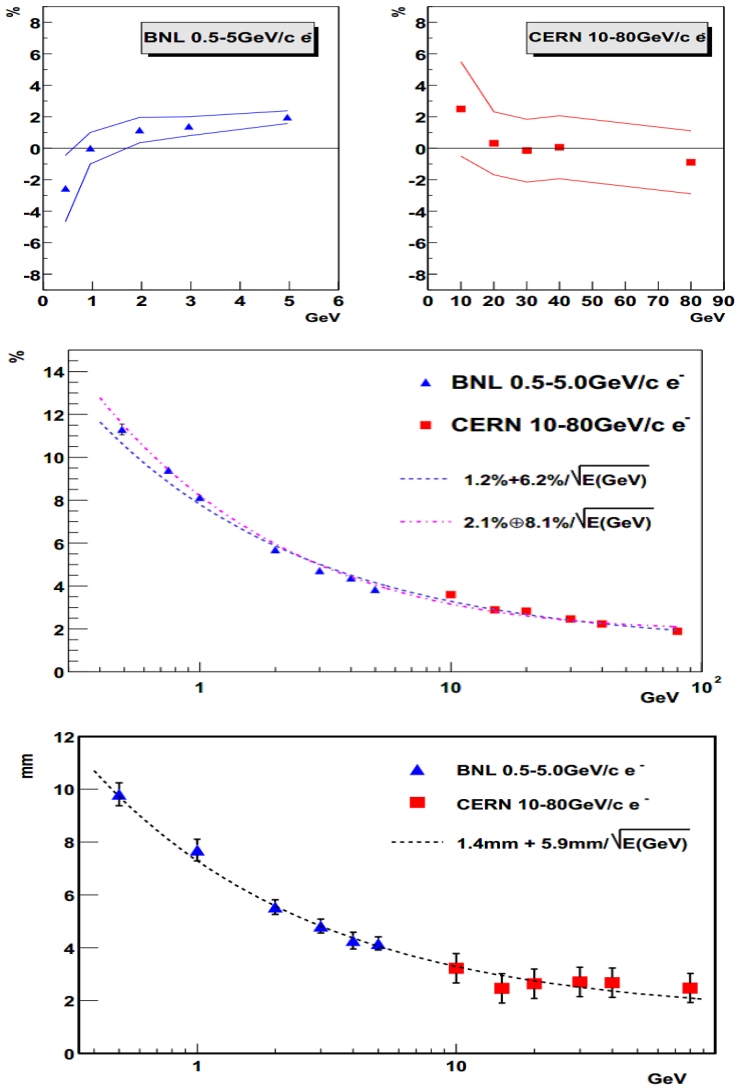

Figure 3.19: The energy linearity (top), energy resolution (middle) and position resolution (bottom) as a function of incident electron energy [173, 174].

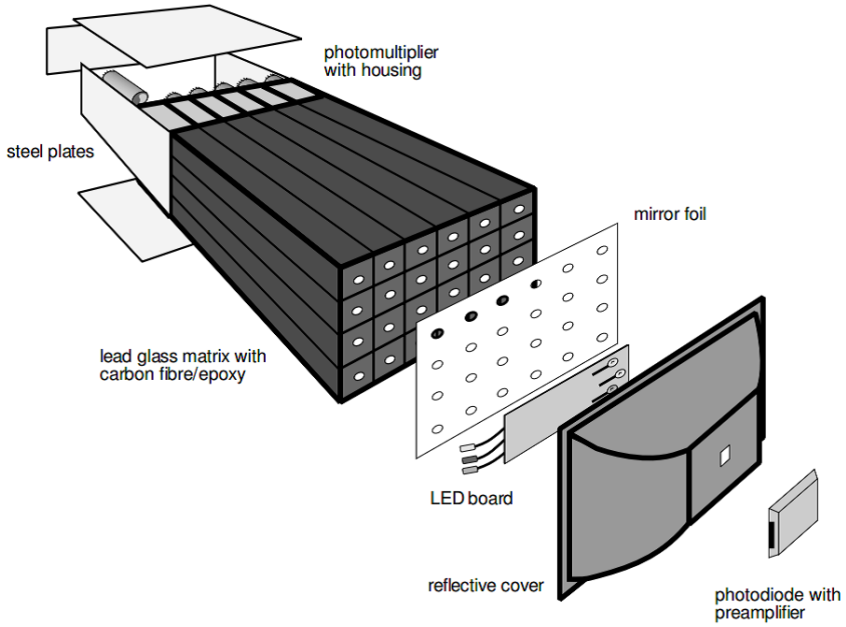

Figure 3.20: Exploded view of a lead-glass detector supermodule [173].

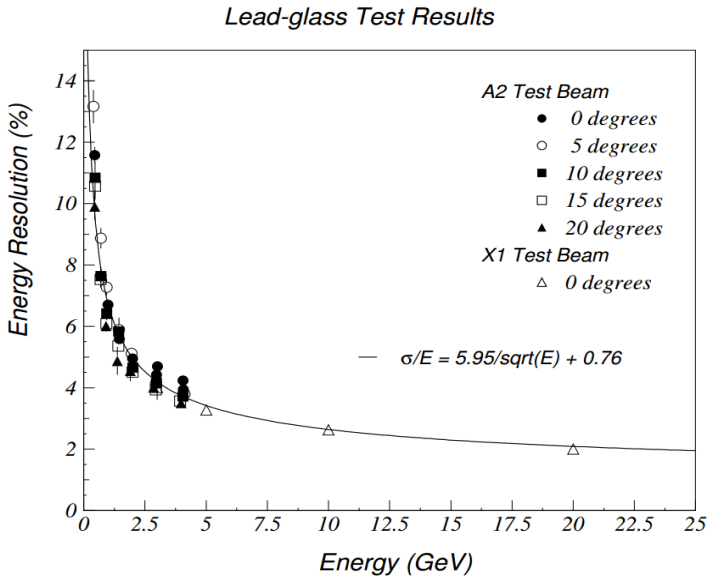

Figure 3.21: The energy resolution of the PbGl as a function of incident energy [173]

3.7 Data acquisition system

The PHENIX detectors have capabilities of measuring several kinds of particles simultaneously at various collision species. The occupancy in the PHENIX detectors is expected to be a few tracks in p+p collisions and 10 % of all detectors in central Au+Au collisions. The interaction rate at design luminosity varies from a few kHz in central Au+Au collisions to 500 kHz for minimum bias p+p collisions. In order to handle a variety of the event sizes and event rates, the PHENIX Data Acquisition (DAQ) systems have the pipelined and deadtimeless front-ends read outs and high-level triggers. The data recording rate of the DAQ system is typically $\sim$ 1 kHz for Au+Au collisions in Run4 (2004) and $\sim$ 5 KHz for p+p collisions in Run5 (2005), respectively. A schematic diagram of the data acquisition flow in shown in Fig.3.22.

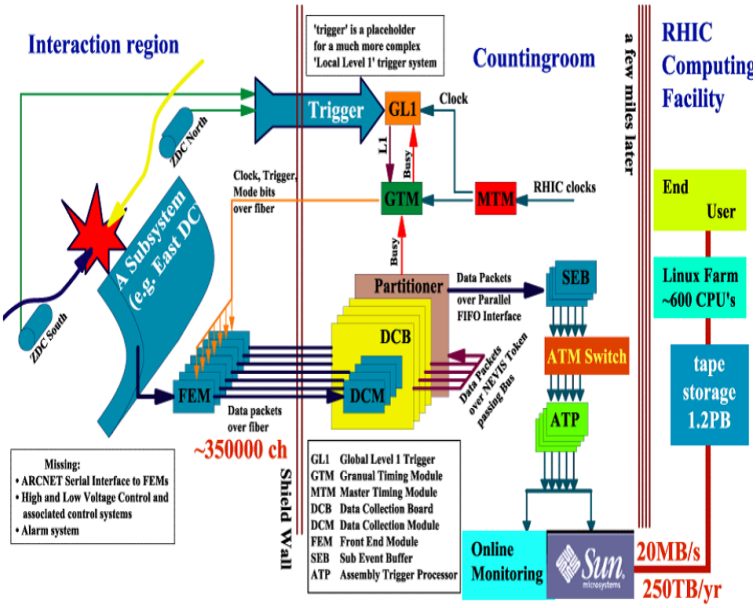

Figure 3.22: Schematic diagram of the data acquisition flow [176].

The DAQ system adopts the concepts of granule and partition. A granule has features of timing control and data collection for each detector subsystem. A partition is a combination of granules, sharing busy signals and accept signals. Therefore the DAQ system takes the data in desired combinations of subsystems.

The data acquisition flow has to be synchronized with the beam clock of 94 MHz in the RHIC. The beam clock is transferred to the Master Timing Module (MTM). The MTM distributes the clock to the Granule Timing

Modules, which are timing modules for individual detector, and the Global Level-1 (GL1). The GTM delivers the clock, the control command bits (Mode bits) and the Level-1 trigger accept signals to the Front End Modules (FEM). The GTM distributes the busy signal to GL1 from its internal busy state or the busy state of the Data Collection Module (DCM). In addition, the GTM equips a fine delay of 50 ps steps in order to compensate timing differences among the FEMs. The GL1 collect the Local Level-1 trigger signals and decide the event trigger.

A FEM can store the data for up to 40 bunch-crossings ($\sim 4.24\ \mu$s) to wait for the accept signal from the Local Level-1 (LL1) and converts the analog signals from the detectors into the digital data. There are two types of data processing methods in the FEMs. One is that the analog signal is digitized in every clock period. The other is that the analog signal is stored in Analog Memory Units and digitized after the event trigger is accepted by the LL1. The former is used for the BBC, ZDC, DC and PC. The latter is used for the RICH and EMCal. Figure 3.23 is an example of the data flow in the FEM.

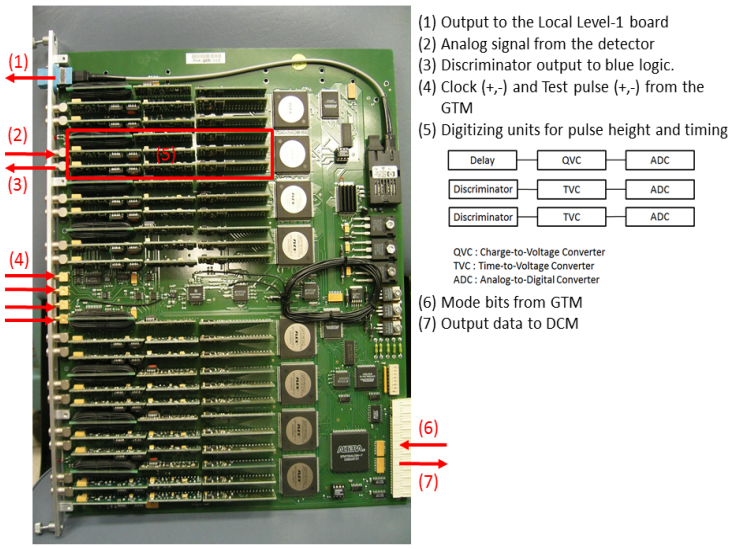

Figure 3.23: The photograph of the front-end module for BBC and the data flow diagram.

The digitized data in each FEM are collected in the DCM at over 100 G bytes per second via optical fiber cable. The DCM provides data buffering, performs zero suppression for all subsystem data, checks the errors, formats the data and outputs the compressed data to the Event Builder (EvB).

The EvB consists of 39 Sub Event Builders (SEBs), Asynchronous Transfer Mode (ATM) switches and 52 Assembly Trigger Processors (ATPs). A SEB communicates with a granule and transfers the data to the ATP via ATM, where the event assembly is performed. The data are combined in units of event and stored on disk with a maximum recording rate of 400 M bytes per second. The EvB architecture is shown in Fig.3.24. The format of the raw data is called "PHENIX Raw Data Format (PRDF)". These data are sent to the High Performance Storage System at thr RHIC Computing Facility (RCF) and converted into a useful format for the data analysis.

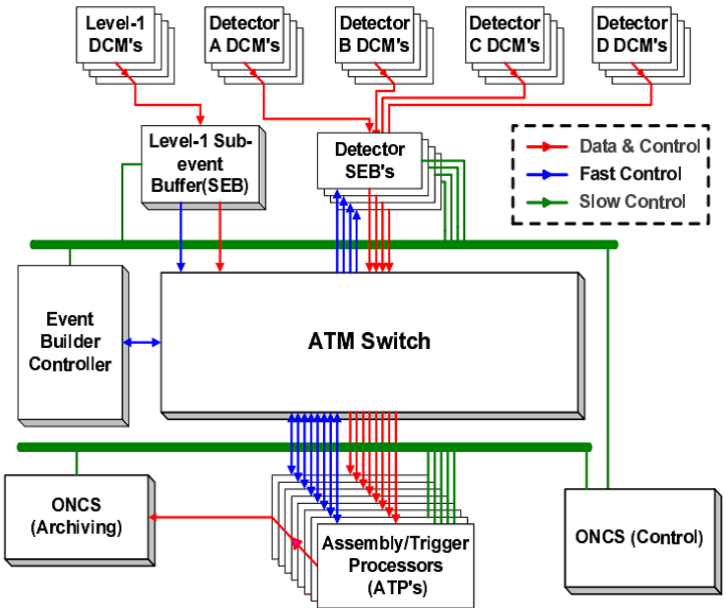

Figure 3.24: Block diagram of the event builder system [176].

Chapter 4

Analysis

4.1 Data set

4.1.1 Integrated luminosity and the number of events

Run4 Au+Au physics runs were performed from the beginning of Jan. 2004 to the middle of Mar. 2004. The integrated luminosity of 241 μb^{-1} was delivered to the PHENIX experiment. Figure 4.1 shows the integrated luminosity vs days during Au+Au runs. PHENIX has successfully recorded 1.5×10^9 "Minimum Bias (MB)" triggered events. The MB trigger fulfills the following requirements:

$$\mathrm{BBCN} \geq 2 \cap \mathrm{BBCS} \geq 2 \cap |bbcz| < 38.0\,\mathrm{cm}, \tag{4.1}$$

where BBCN and BBCS is the number of hits for the north-side BBC and the south-side BBC, respectively. *bbcz* is the measured collision vertex in z direction (beam axis). The relation between the integrated luminosity and the number of MB events is described by

$$\int Ldt = \frac{N_{\mathrm{MB}}}{\sigma_{\mathrm{AuAu}}\epsilon_{\mathrm{MB}}^{\mathrm{AuAu}}} = \frac{N_{\mathrm{MB}}}{\langle N_{\mathrm{coll}}^{\mathrm{MB}}\rangle \sigma_{\mathrm{pp}}\epsilon_{\mathrm{MB}}^{\mathrm{AuAu}}}, \tag{4.2}$$

where $\int Ldt$ is the integrated luminosity, N_{MB} is the number of MB events. $\epsilon_{\mathrm{MB}}^{\mathrm{AuAu}}$ is the MB trigger efficiency in Au+Au collisions. The MB trigger efficiency is

$$\epsilon_{\mathrm{MB}}^{\mathrm{AuAu}} = \epsilon_{\mathrm{BBC}} \times \epsilon_{\mathrm{ZDC}} = 92.2^{2.5}_{-3.0}\,\%, \tag{4.3}$$

where ϵ_{BBC} and ϵ_{ZDC} are the trigger efficiencies of BBC and ZDC, respectively. ϵ_{BBC} is $93.1 \pm 0.4 \pm 1.6$ % [179] and ϵ_{ZDC} is $99.0^{+1.0}_{-1.5}$ % [180]. The inelastic cross section of Au+Au collision is deduced by the inelastic cross section of p+p collision, $\sigma_{\mathrm{pp}} = 42\,\mathrm{mb}$ [181], and the number of binary collisions, $\langle N_{\mathrm{coll}}^{\mathrm{MB}}\rangle$.

$\langle N_{\rm coll}^{\rm MB} \rangle$ is calculated by the Glauber Monte Carlo simulation [50, 51]. In this study, 0.9×10^9 (880 M) events are analyzed with selecting good runs.

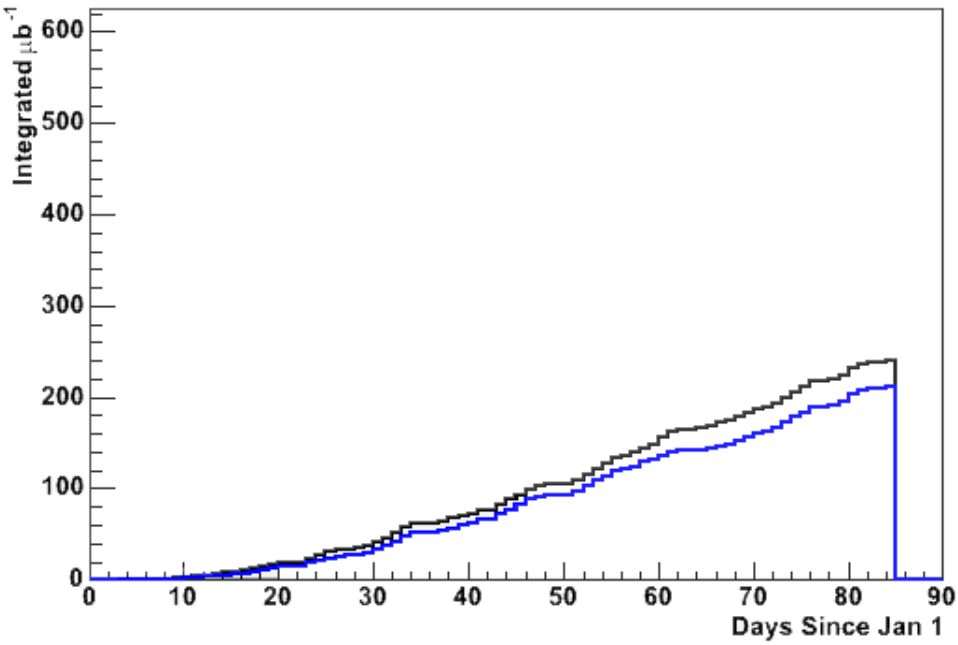

Figure 4.1: The integrated luminosity vs days during whole Au+Au runs (Run4) [178]. The black line is MB and the blue line is MB with Muon active.

4.2 Event classification

Heavy-ion collisions can be classified by the collision vertex and the collision geometry. The basic quantities for the event classification and the treatments in the data analysis are introduced.

4.2.1 Collision vertex

Collision vertex, *bbcz*, is determined by the timing measurement of BBCs as follows.

$$bbcz = \frac{T_{\rm south} - T_{\rm north}}{2} \times c + z_{\rm offset}, \tag{4.4}$$

where c is the speed of light ($c = 299792458$ m/s). $z_{\rm offset}$ is an intrinsic offset BBCs have. $T_{\rm south}$ and $T_{\rm north}$ are the arrival times of charged particle from a

collision for the south-side BBC and the north-side BBC, respectively. Figure 4.2 schematically shows the timing measurement with BBC. In this example, 3 hits are detected in the north side and 2 hits are detected in the south side.

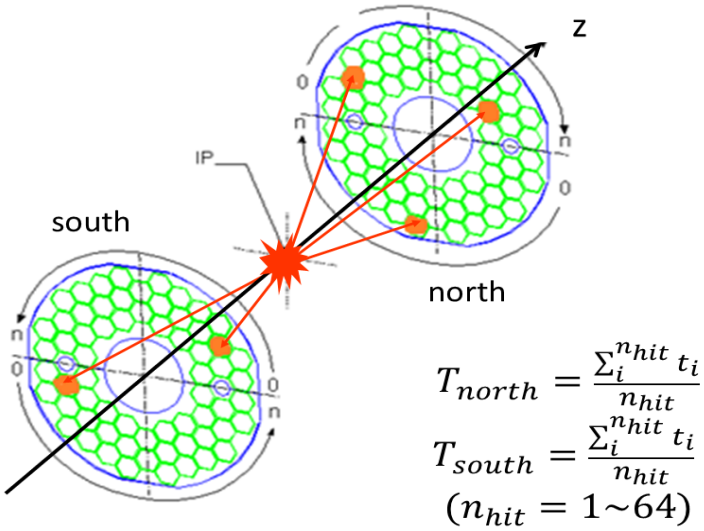

Figure 4.2: Schematic view of timing measurement for BBCs. Charged particles from a collision enter the BBC element.

Figure 4.3 shows the number of electrons as a function of $bbcz$. The enhancement in the vertex range, $|bbcz| < 5.0$ cm and $bbcz > 25$ cm, suggests the secondary producing electrons interacted with the detector materials in the central arm and the muon arm, respectively. In order to avoid the contamination from the muon arm, the events with $|bbcz| < 25$ cm are used in this analysis.

4.2.2 Collision geometry and centrality

In high-energy heavy-ion collisions, collision geometry is characterized by the number of binary collision, N_{coll} , the number of participant nucleons, N_{part}, and the impact parameter, b. The parameters are provided by the Glauber model.

Experimentally, collision geometry is measured as "Centrality". Centrality is determined by the correlation between the sum of charge for scattering particles and the energy for spectators (neutrons). Figure 4.4 shows the centrality classification and the correlation of the output between BBC and ZDC.

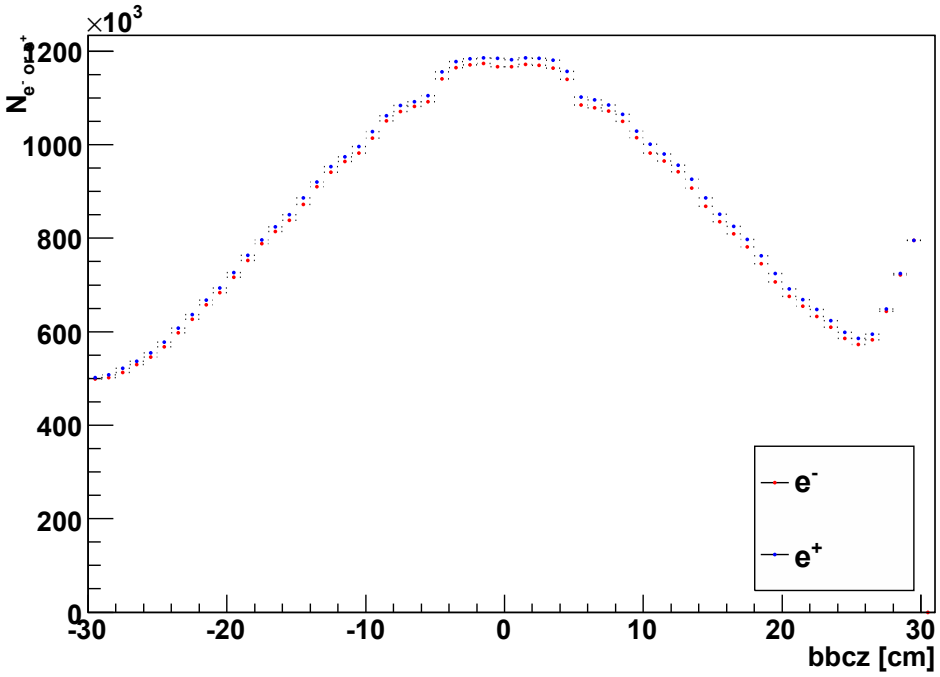

Figure 4.3: The number of electrons (red) and positrons (blue) vs bbcz

As a collision becomes central (i.e. centrality approaches 0%), more charged particles enter BBC but less neutrons go to ZDC. Figure 4.5 shows the measured correlation between the charge of particles by BBC and the energy of neutrons by ZDC. Negatively correlated distribution is seen from mid-central to central collisions. In peripheral collisions, however, the correlation is hardly seen due to the decline of the detection efficiency for BBC.

The measured centrality is often converted into N_{coll} and N_{part} in order to compare with the different data in different experiments. In addition, N_{coll} and N_{part} are often used as a kind of scaling parameter for comparing between nucleus-nucleus collisions and nucleon-nucleon collisions.

Table 4.1 is the results of the Glauber Monte Carlo simulation in Au+Au collisions at $\sqrt{s_{NN}} = 200$ GeV [51].

4.3 Run selection

The run-by-run stabilities of the detectors are checked over the entire run period. Table 4.2 shows period-by-period information for whole runs in Au+Au collisions. Au+Au runs are classified into eleven run groups (G1-G9, CV1-

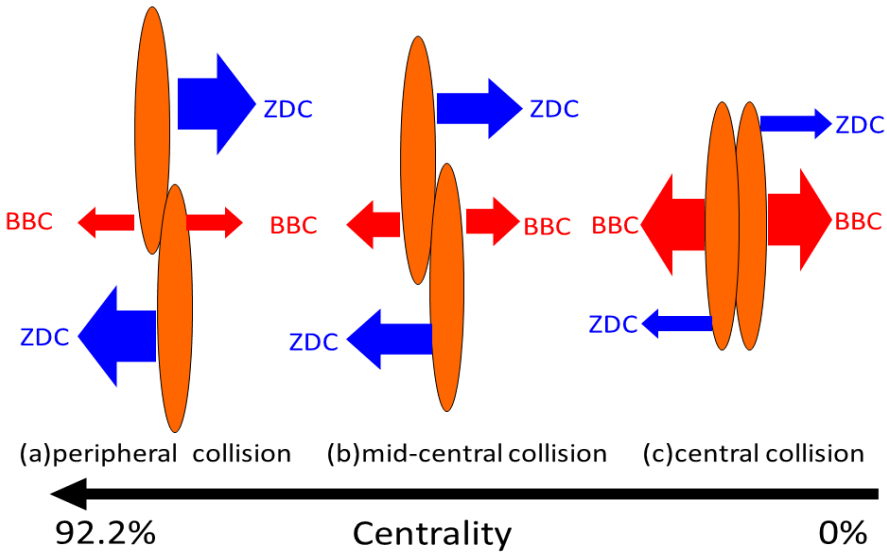

Figure 4.4: Centrality classification and the correlation of the output amplitude for BBC and ZDC.

Centrality	$\langle N_{part} \rangle$	sys. err.	$\langle N_{coll} \rangle$	sys. err.	T_{AB} (mb^{-1})	sys. err.	$\langle b \rangle$ (fm)	sys. err.
0-10 %	325.2	3.3	955.4	93.6	22.75	1.56	3.2	0.2
10-20 %	234.6	4.7	602.6	59.3	14.35	1.00	5.7	0.3
20-30 %	166.6	5.4	373.8	39.6	8.90	0.72	7.4	0.3
30-40 %	114.2	4.4	219.8	22.6	5.23	0.44	8.7	0.4
40-50 %	74.4	3.8	120.3	13.7	2.86	0.28	9.9	0.4
50-60 %	45.5	3.3	61.0	9.9	1.45	0.23	11.0	0.4
60-70 %	25.7	3.8	28.5	7.6	0.68	0.18	11.9	0.5
70-92.2 %	9.5	1.9	8.3	2.4	0.20	0.06	13.5	0.5
0-20 %	279.9	4.0	779.0	75.2	18.55	1.27	4.4	0.2
20-60 %	100.2	3.4	193.7	19.1	4.61	0.36	9.3	0.4
60-92.2 %	14.5	2.5	14.5	4.0	0.35	0.10	13.0	0.5
0-92.2 % (MB)	109.1	4.1	257.8	25.4	6.14	0.45	9.5	0.4

Table 4.1: The results of the Glauber Monte Carlo simulation for individual centrality divisions.

CV2) by the stabilities of main detectors and the detection efficiency of electrons.

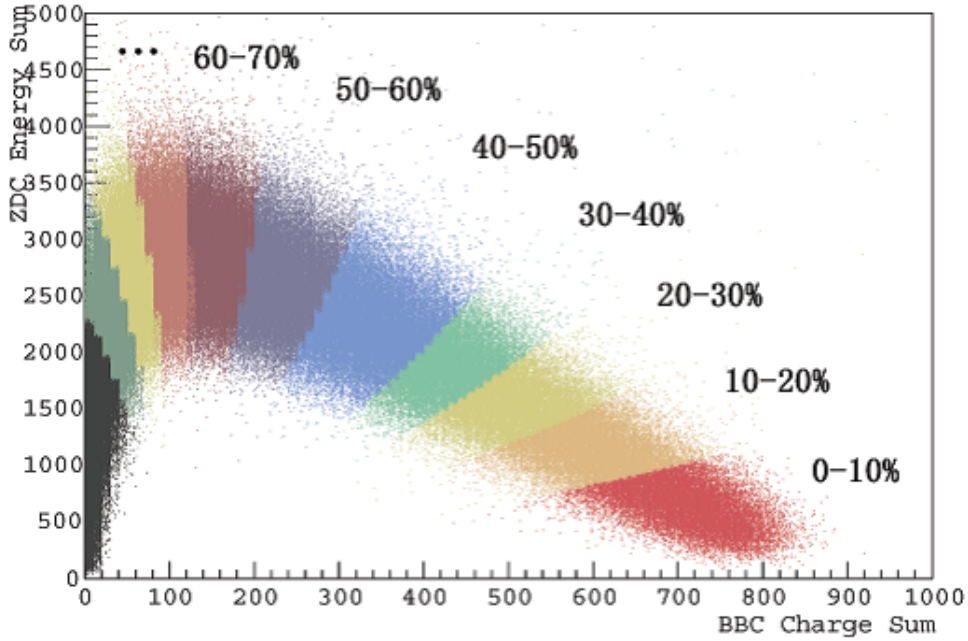

Figure 4.5: The sum of charge in BBC vs the sum of energy in ZDC. Centrality is determined by the fraction relative to all entries in the scattering plot.

The detector condition in the reference run (run 120496) is used for the simulation study. Therefore the fluctuations of each run with respect to the reference run group (G8) are important. Figure 4.6 is the number of electrons or positrons per event normalized by that of the reference run group G8. The data for electrons (red) and positrons (blue) are superimposed on Fig.4.6. The dotted line is the boundary between the magnetic field configurations of CM_{++} and CM_{--}. Since the polarities of the CM_{++} and CM_{--} are opposite, the detector acceptances of electrons and positrons become upside down. CV1 and CV2 are excluded due to the existence of many background electrons. G1-G3 groups are also excluded because there are large dead areas in the EMCal sector. In addition, the runs, whose efficiencies are within $\pm 2\sigma$ deviation from the mean efficiency of each run group, are selected as good runs.

Group	Run period	Magnet	Remarks
G1	108280-108714	CM_{--}	E0 and E1 off
G2	108769-110236	CM_{--}	E0 off
CV1	110237-111033	CM_{--}	E0 off, converter run
G3	111350-113528	CM_{--}	E0 off
G4	113529-114330	CM_{--}	
G5	114331-115780	CM_{--}	
G6	115979-116691	CM_{++}	
G7	116701-118110	CM_{++}	
G8	118110-120528	CM_{++}	include reference run (run 120496)
CV2	120845-121111	CM_{++}	converter run
G9	121113-122223	CM_{++}	

Table 4.2: The first column is the name of a run group. CV1 and CV2 are converter runs. In converter run period, the additional materials are implemented to study the amount of photon-conversion electrons. The second column shows run number which belongs to each group. The third column shows the polarities of two central magnet. The last column shows the remarks.

4.4 Track reconstruction and momentum measurement

4.4.1 Track reconstruction

The measurement of charged particles starts from the track reconstruction. The trajectory of a particle is determined by hit information on the tracking device. The PHENIX applies a track finding algorithm called "Combinatorial Hough Transform (CHT)" technique [183, 184]. In this technique, an arbitrary trajectory is reconstructed by combining hits on the plane (i.e. x-y plane or r-ϕ plane) perpendicular to the magnetic field. Each trajectory characterizes Hough transform parameters, ϕ_0 and α, where ϕ_0 is polar angle at the intersection of the tracks with a reference circle near the mid-point of DC and α is the inclination angle relative to the straight line from the interaction point. Hough transform parameters and an example of a reconstructed track in x-y plane are shown in the top figure in Fig.4.7. The bottom figure in Fig.4.7 shows a schematic view of a reconstructed track in r-z plane. Figure 4.8 shows an example of hits in a part of DC (left) and the corresponding hit distribution (right) in the Hough transform parameter space. The more details of the track reconstruction used in the PHENIX experiment are ex-

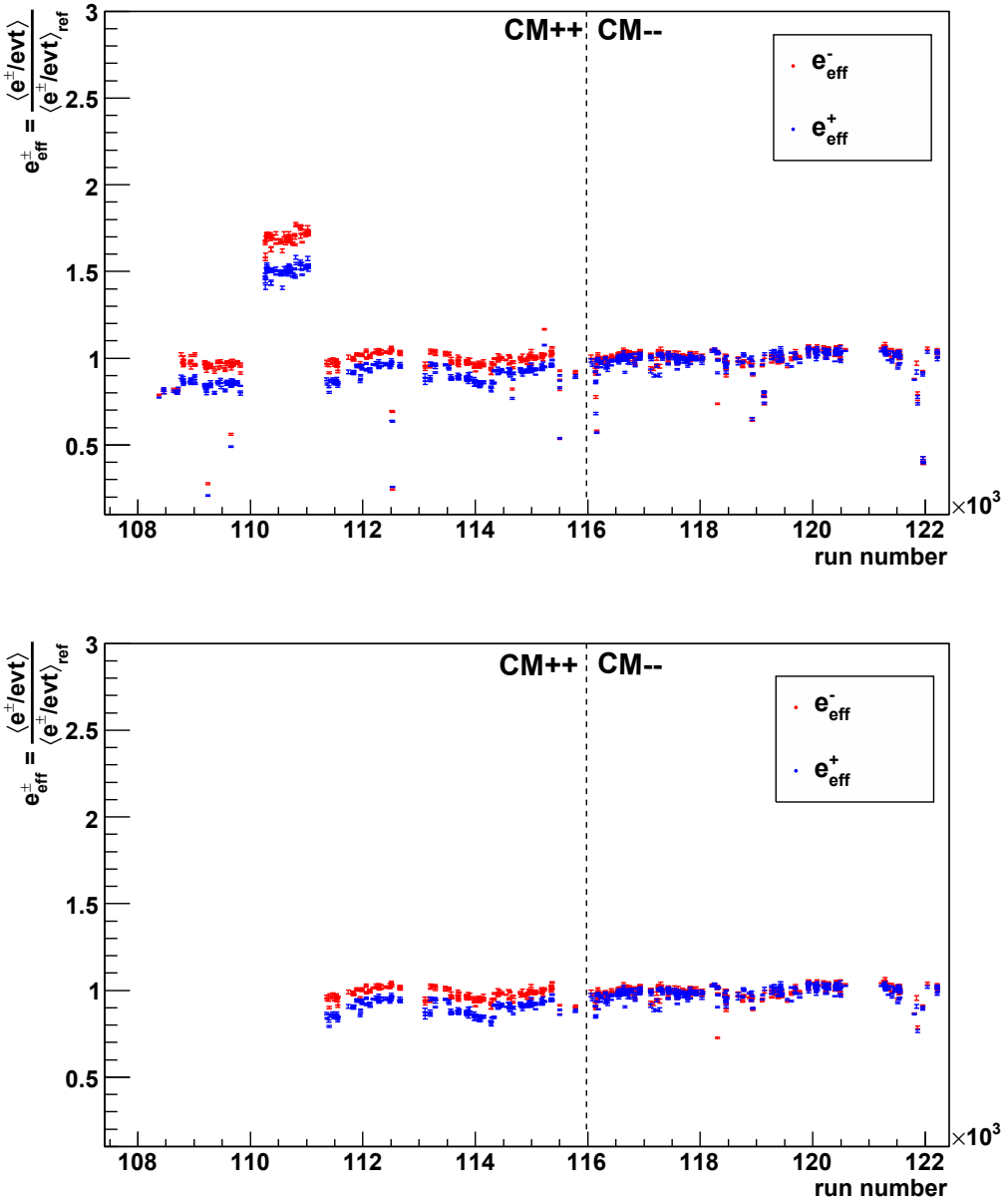

Figure 4.6: Relative efficiency of the number of electrons (red) and positrons (blue) per event with respect to the run group G8 without run selection (top) and after selecting good runs (bottom).

plained in the reference [182].

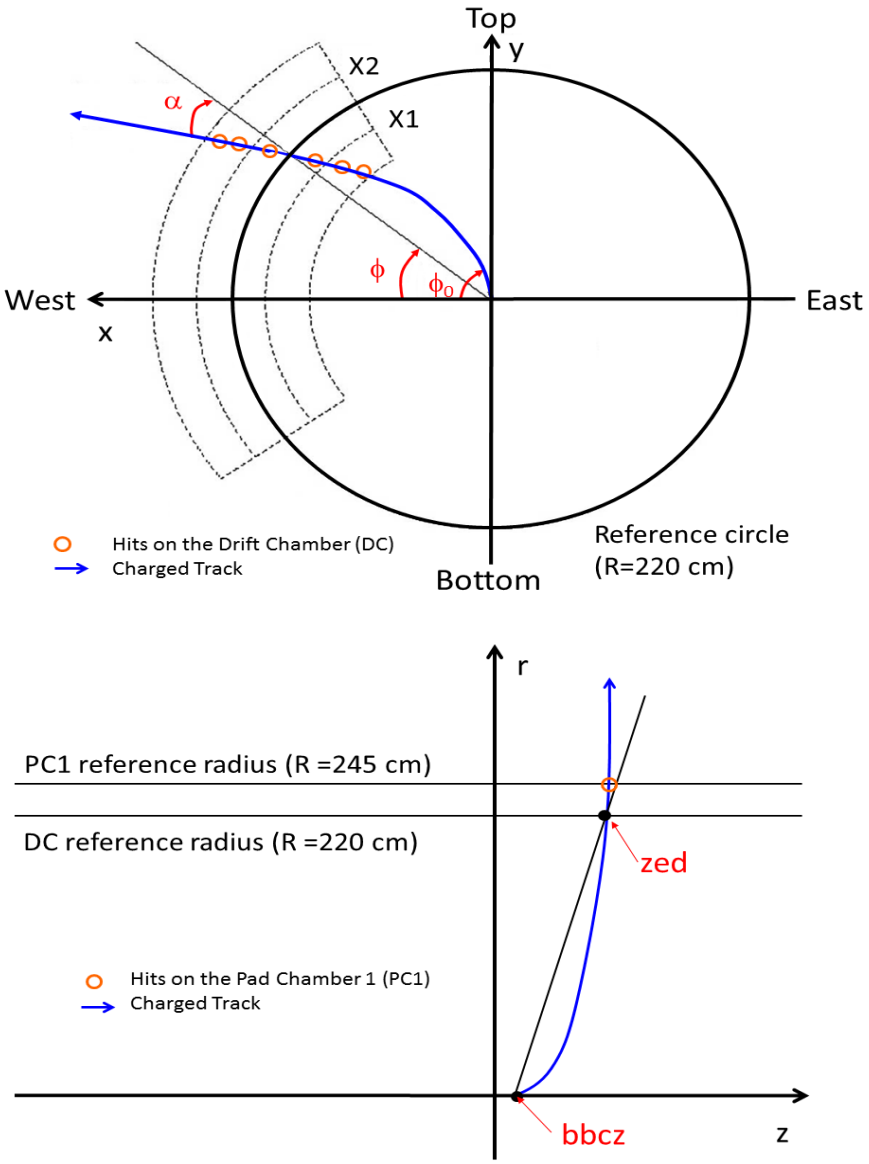

Figure 4.7: Schematic view of a reconstructed track by DC in x-y plane (top) and r-z plane (bottom). Hough transform parameters, ϕ and α, are shown on the top.

4.4.2 Track quality

The quality of a track is assured by requiring the hits on X wires (X1,X2) and stereo UV wires and associated clusters in PC1. The hit information is

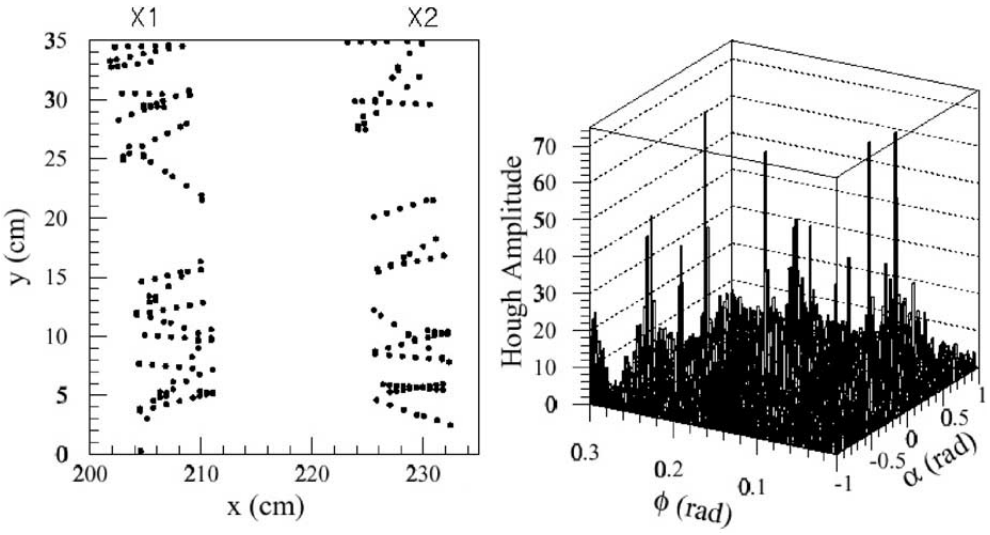

Figure 4.8: The track reconstruction by the CHT technique [182]. The hits on DC in x-y plane (left) and the hit distribution in the parameter space (ϕ, α) (right).

recorded as a bit, which is named "quality bit". Quality bit is defined as

$$quality\,bit = a \times 2^0 + b \times 2^1 + c \times 2^2 + d \times 2^3 + e \times 2^4 + f \times 2^5, \qquad (4.5)$$

The coefficients of quality bit are summarized in Table 4.3.

Track quality has an influence on the accuracy of the momentum measurement. In addition, track quality is related to the methods of electron identification, since some variables for electron identification often require the track projection. The highest track quality is *quality bit* = 63. In this case, both hits of X1 and X2, unique UV hit and unique PC1 hit are required. The second best one is *quality bit* = 31. In order to increase the statistics, not only the best case but also the second best one,

$$quality\,bit = 31 \cup 63, \qquad (4.6)$$

are used in this analysis. Figure 4.9 shows the distribution of *quality bit*. Filled bits in Fig.4.9 are selected in this analysis.

coefficients	bit	description
a	0	X1 hit is not used
	1	X1 hit is used
b	0	X2 hit is not used
	1	X2 hit is used
c	0	UV hit is not found
	1	UV hit is found
d	0	UV hit shares from other track
	1	UV hit is unique
f	0	PC1 hit is not used
	1	PC1 hit is used
f	0	PC1 hit shares from other track
	1	PC1 hit is unique

Table 4.3: The definition of quality bit.

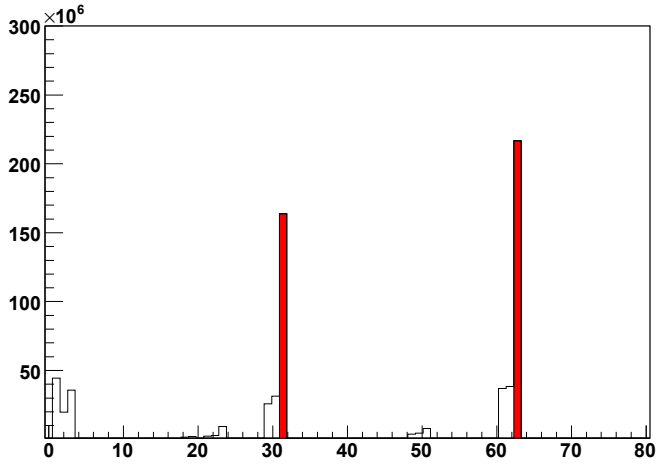

Figure 4.9: *quality bit* distribution. Filled bit patterns are used in this analysis.

4.4.3 Momentum measurement

Transverse momenta of charged tracks are determined by the effective magnetic field, K, and the measured Hough parameter, α as follows.

$$\begin{aligned} p_T &\sim \frac{K}{\alpha}, \\ K &= \frac{e}{R_{\rm DC}} \int lBdl, \end{aligned} \tag{4.7}$$

where e is the elementary charge (e=0.2998 GeV/c $T^{-1}m^{-1}$), R_{DC} is the reference radius of DC (R_{DC}=220 cm). The effective field integral K is 87 mrad GeV/c in the central arm. The momentum resolution is directly related to α resolution of DC [182, 185] as follows.

$$\frac{\delta p}{p} = \frac{\delta \alpha}{\alpha} = \frac{1}{K}\sqrt{\left(\frac{\sigma_{ms}}{\beta}\right)^2 + (\sigma_\alpha p)} \tag{4.8}$$

where $\delta\alpha$ is the measured angular spread, which depends on the multiple scattering deviation, σ_{ms}, and the intrinsic angular resolution, σ_α. The multiple scattering deviation σ_{ms} mainly contributes in the low momentum region. σ_α is 0.84±0.005 mrad $(GeV/c)^{-1}$, which is obtained by the data analysis in zero-field runs. Figure 4.10 shows the momentum resolution as a function of momentum [182]. At high momentum, σ_α is the dominating contribution,

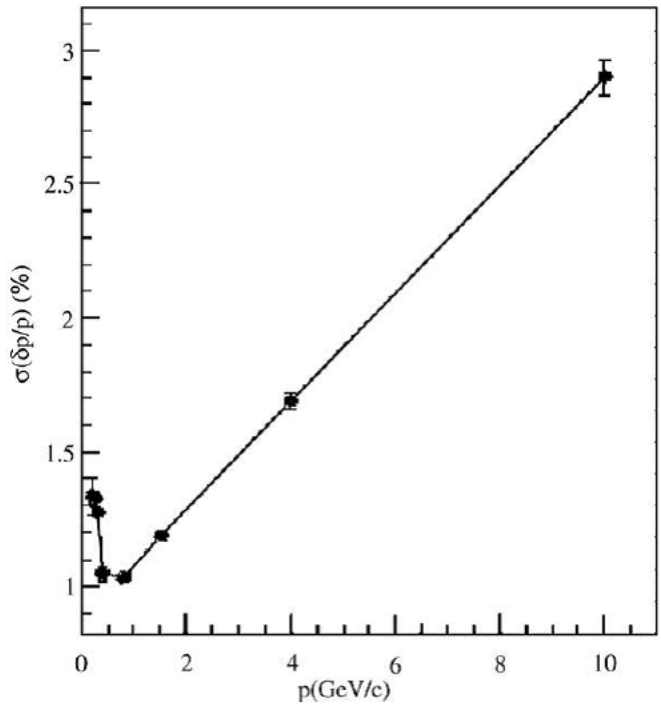

Figure 4.10: The momentum resolution as a function of momentum for DC [182].

that is, $\delta\alpha \sim \sigma_\alpha$. Finally,

$$\frac{\delta p}{p} \sim 0.7\,(\%) \oplus 1.0\,(\%) \times p\ (\mathrm{GeV/c}) \tag{4.9}$$

is obtained.

4.5 Electron identification

4.5.1 Electron identification by RICH

The reconstructed track is projected onto RICH as shown in Fig.4.11. If this track is an electron, conical light with a certain angle is radiated during passing though the radiator. Emitted Cherenkov lights are reflected on the spherical mirror and detected on the PMT array. Fired phototubes on the array are distributed around the nominal ring-shaped range with respect to the track projection point on the array.

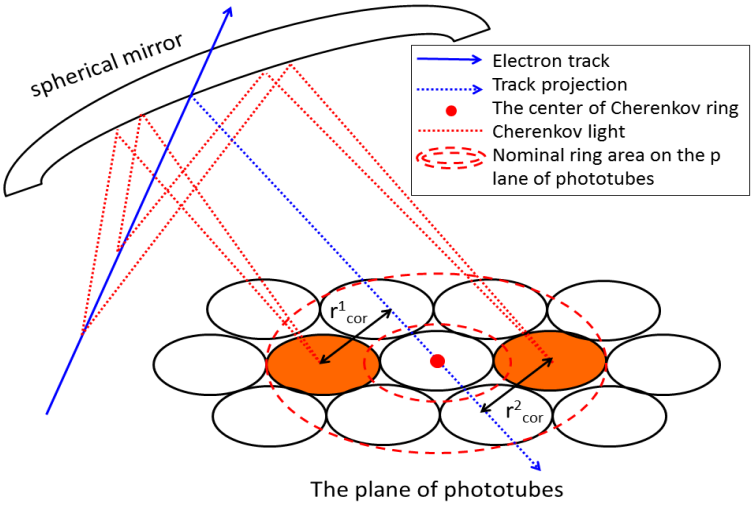

Figure 4.11: Electron detection in RICH.

The parameter r^i_{cor} is the distance between the center of a phototube and the projection point $R_{cross} = (z_{cross}, \phi_{crosss})$. The projection point is calculated by the extrapolation from the trajectory on DC and PC. Several variables for electron identification are defined on the basis of the projection points.

The variable n_0 is the number of fired phototubes found in the expected range from the nominal Cherenkov ring ($3.4 \leq r^i_{cor} \leq 8.4$ cm).

The variable $npe0$ is defined as

$$npe0 = \sum_{3.4 \leq r^i_{cor} \leq 8.4\,\mathrm{cm}} N_{p.e.}\,(i)\,, \tag{4.10}$$

where $N_{p.e.}$ is the number of the photoelectrons in i-th phototube in the expected range of $3.4 \leq r^i_{cor} \leq 8.4$ cm.

The variable *disp* is defined by the distance between the center of Cherenkov ring center R_{center} and the track projection point R_{cross}. R_{center} is calculated by the weighted average of the position of fired phototubes. Therefore,

$$R_{center} = \frac{\sum_{3.4 \leq r^i_{cor} \leq 8.4\,\mathrm{cm}} N_{p.e.}\,(i) \cdot R_i}{npe0}. \tag{4.11}$$

disp is expressed as

$$disp = \sqrt{(z_{cross} - z_{center})^2 + (\phi_{cross} - \phi_{center})^2}. \tag{4.12}$$

In other words, *disp* shows the consistency between the center of Cherenkov light calculated by fired phototubes in RICH and the projection point from DC and PC1.

The variable *chi*2 is obtained by the weighted average of deviation of fired phototubes from the ideal ring radius r_{ideal}(= 5.9 cm).

$$chi2 = \frac{\sum_{3.4 \leq r^i_{cor} \leq 8.4\,cm} N_{p.e.}\,(i) \cdot \left(r^i_{cor} - r_{ideal}\right)^2}{npe0} \tag{4.13}$$

z-flipped technique

Under high multiplicity environment produced by a Au+Au collision, charged hadron tracks are accidentally associated with the fired phototubes in RICH. "z-flipped" technique is used in order to estimate randomly associated backgrounds. The track projection point $R = (x, y, z)$ is flipped in the z direction and z-flipped point $R_s = (x, y, -z)$ is determined. $n0$, $npe0$, *disp* and *chi*2 of R correspond to $sn0$, $snpe0$, *sdisp* and *schi*2 of R_s, respectively. The net distributions of $n0$, $npe0$, *disp* and *chi*2 for electron candidates are obtained by subtracting the estimated distribution of randomly associated tracks from the raw distribution. Figure 4.12 is $n0$ distribution of electron (left) and positron (right) with the requirements of $disp < 4$ and $chi2 < 7$. The random associated distribution is obtained with the requirements of $sdisp < 4$ and $schi2 < 7$.

RICH misalignment

The array of phototubes in RICH is composed of four sectors as East South, East North, West South and West North. Thus sector-by-sector response to Cherenkov light should be checked and calibrated. Figure 4.13 shows *disp* distribution of electrons at the east-south sector (left) and west-south sector (right). Red filled points are the real data, blue open points are the simulation. The distribution of the real data is much different from that

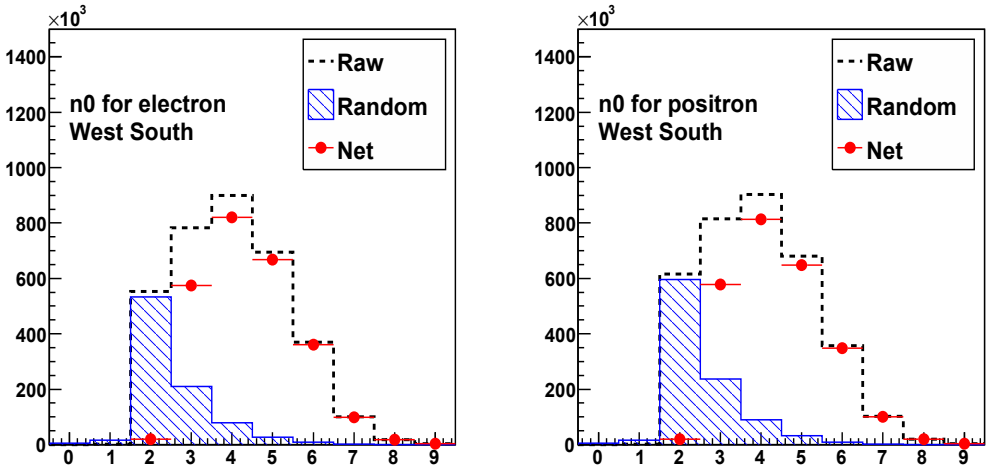

Figure 4.12: n0 distribution of the West-south sector for electron (left) and positron (right).

of the simulation at the east-south sector because of the misalignment of RICH. The biases caused by the RICH misalignment are taken into account by embedding the misalignment into the simulation. Figure 4.14 shows *disp* distribution with embedding the RICH misalignment into the simulation.

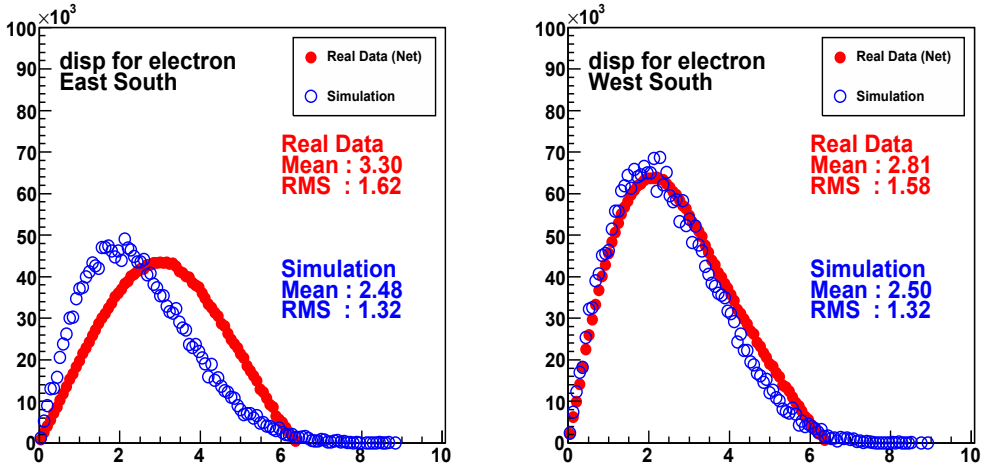

Figure 4.13: disp distribution of the east-south sector (left) and the west-south (left).

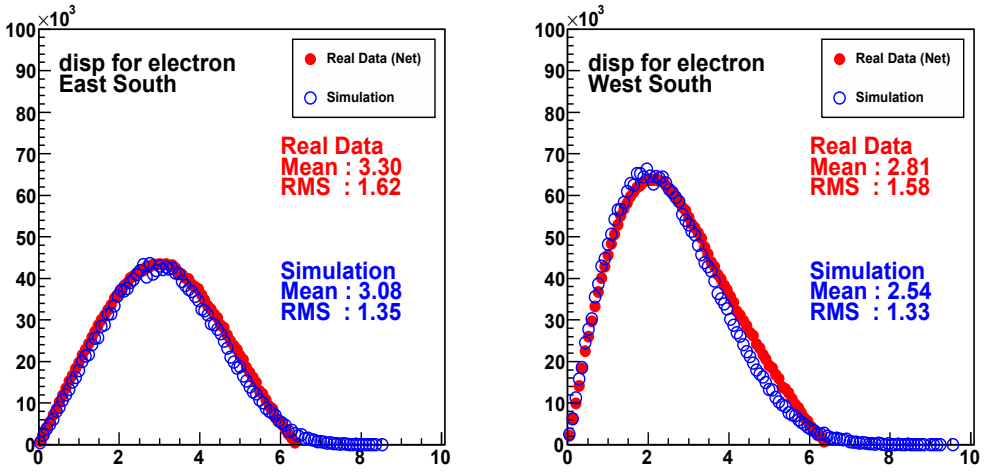

Figure 4.14: disp distribution of the east-south sector (left) and the west-south (left) after the biases of the RICH misalignment are embedded into the simulation.

Comparison between the real data and the simulation

The detector responses are studied by comparing the real data with the simulation. The contributions from randomly associated tracks are estimated in the real data analysis. The biases of the RICH misalignment are embedded into the simulation. Figure 4.15 shows sector-by-sector $n0$ distributions for electrons (top) and positrons (bottom). Figure 4.16 shows sector-by-sector *disp* distributions for electrons (top) and positrons (bottom). The distributions of the RICH variables are reasonably consistent between the real data and the simulation.

4.5.2 Electron identification by track matching

Track matching variable is defined by the displacement between the track projection point ($R_{pemc} = (pemcz, pemzphi)$) from DC and PC1 onto the backward EMCal surface and the energy centroid ($R_{emc} = (emcz, emcphi)$) of an electromagnetic shower developing in the EMCal. The z and ϕ components of the track matching are expressed by

$$emcdz = emcz - pemcz, \tag{4.14}$$

$$emcdphi = emcphi - pemcphi, \tag{4.15}$$

The definition of them is illustrated in Fig.4.17. *emcdz* and *emcdphi* dis-

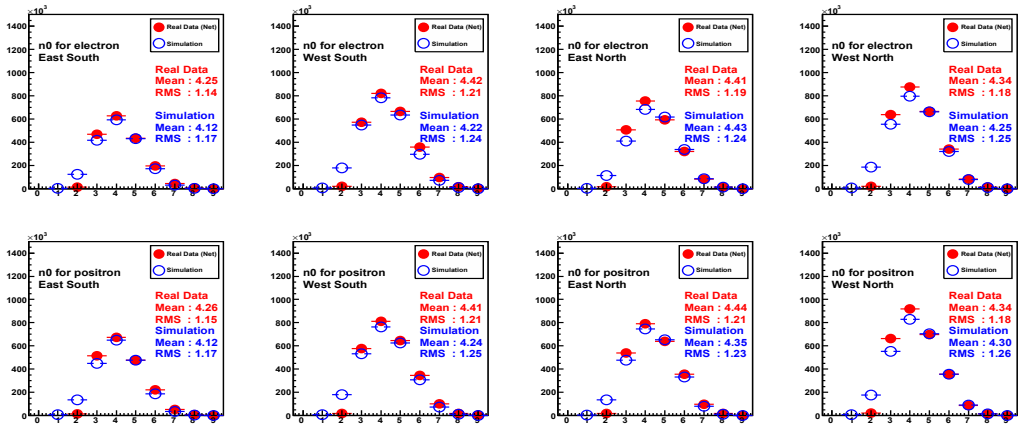

Figure 4.15: The comparison of the net distribution between the real data and the simulation, taking the RICH misalignment effect into account. The comparisons are shown for East-South, West-South, East-North and West-North. The top and bottom plots are $n0$ distribution for electrons and positrons, respectively.

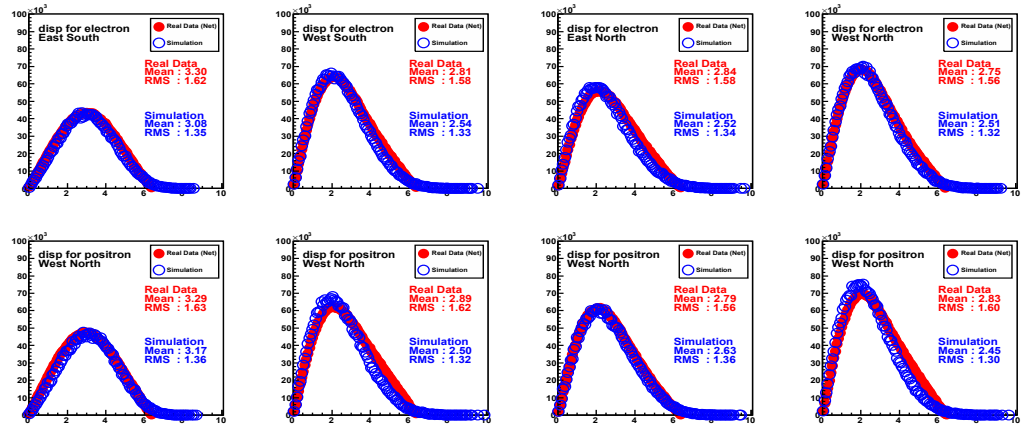

Figure 4.16: The comparison of the net distribution between the real data and the simulation, taking the RICH misalignment effect into account. The comparisons are shown for East-South, West-South, East-North and West-North. The top and bottom plots are *disp* distribution for electrons and positrons, respectively.

tribution is shown in the panel (a) of Fig.4.18 and Fig.4.20, respectively. The

dotted black points and the blue line in the panel (a) show the net distribution and the contribution from randomly associated tracks, respectively. The red points in the panel (b) show the net distribution after subtracting the distribution of the randomly associated tracks. The contribution from random associated tracks is estimated under the conditions of $sn0 > 2$, $schi2/snpe0 < 7$ and $sdisp < 4$.

In order to clarify the selecting criteria of electrons, the track mathing variables in units of radian and cm are normalized into the units of one standard deviation σ. The normalized matching variables, $emcsdphi_e$ and $emcsdz_e$, are defined by

$$emcsdz_e = \frac{emcdz - \langle emcdz \rangle}{\sigma_{emcdz}}, \tag{4.16}$$

$$emcsdphi_e = \frac{emcdphi - \langle emcdphi \rangle}{\sigma_{emcdphi}}, \tag{4.17}$$

where $\langle emcdz \rangle$ and $\langle emcdphi \rangle$ are the mean values of the net distribution of the track matching. σ_{emcdz} and $\sigma_{emcdphi}$ are the standard deviations.

Track matching calibration

The track matching variables depend on the momentum of a track, the EMCal sector, the bending direction and the incident position. These dependences are summarized in Table 4.4.

Variables	Dependences
$emcsdz_e$	The total momentum (mom) EMCal sector (sector and dcarm) Bending direction (sign of α) Incident polar angle (θ)
$emcsdphi_e$	The total momentum (mom) EMCal sector (sector and dcarm) Bending direction (sign of α) Incident position (zed)

Table 4.4: The dependences considered for the track matching calibration.

The track matching variables are calibrated for not only the real data but also the simulation. Figure 4.18 and Fig. 4.19 is an example to explain the procedure of the calibration. The panel (b) in the figure shows the net distribution after subtracting the randomly associated distribution from the

raw distribution. The fit with Gauss function is superimposed on the plot. The mean parameter, $\langle emcdz \rangle$ and the sigma parameter, σ_{emcdz} are extracted by the Gauss fit. $\langle emcdz \rangle$ and σ_{emcdz} as a function of the inverse momentum are shown in the panel (c) and (d), respectively. $\langle emcdz \rangle$ and σ_{emcdz} change linearly at low $1/p_T$ region (i.e. high p_T region) but non-linear tendencies are seen at high $1/p_T$ region (i.e. low p_T region). Therefore, the following function is used by this calibration.

$$f(x) = \sum_{i=1}^{3} a_i \sin\left(\frac{i\pi x}{L}\right) + a_4 + a_5 x, \tag{4.18}$$

where L is determined by the dynamic range of the data points. The summation term of Eq.(4.18) is introduced to take non-linear tendency and point-to-point fluctuation into account. In addition, this term has the good convergence at the edge of the data points, that is, it is preferable for the extrapolation out of the data points. Figure 4.19 is the normalized matching variable $emcsdz_e$, which is defined in Eq.(4.16), after the calibration. Mean parameter is distributed around 0 and sigma parameter is distributed around 1 σ independent of the inverse p_T and the bending direction α. The dependences on the sector (E0-E3, W0-W3) and incident position (θ) are also taken into account in the calibration. The results of the calibration are referred to Appendix D.

The calibration of *emcdphi* is performed in the same way of *emcdz*. The results are shown in Fig.4.20 and Fig.4.21.

The calibrations for the simulation are performed in the same procedure. The results are shown in Fig.4.22 to Fig.4.25.

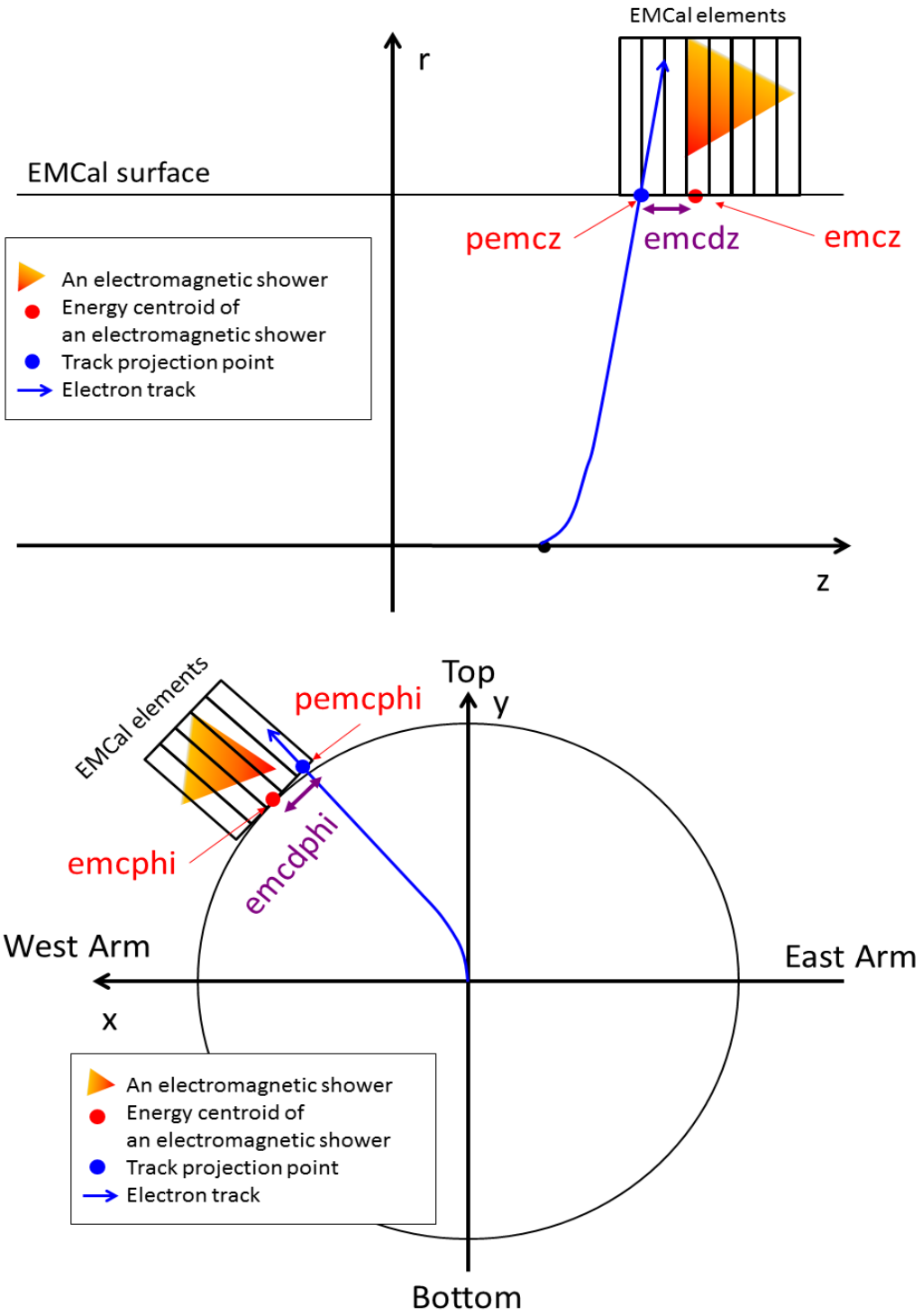

Figure 4.17: The definition of track matching, *emcdz* and *emcdphi*.

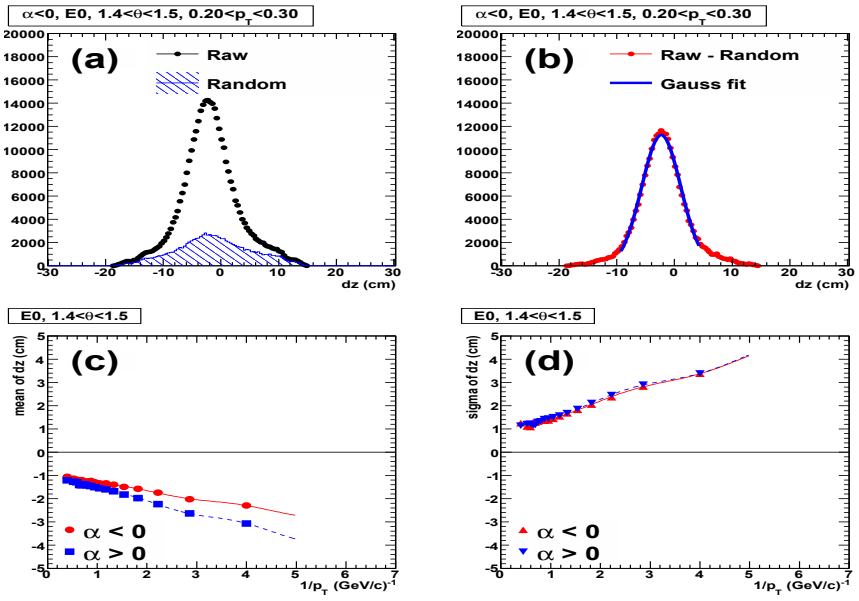

Figure 4.18: The track matching parameter *emcdz* of the real data before the calibration.

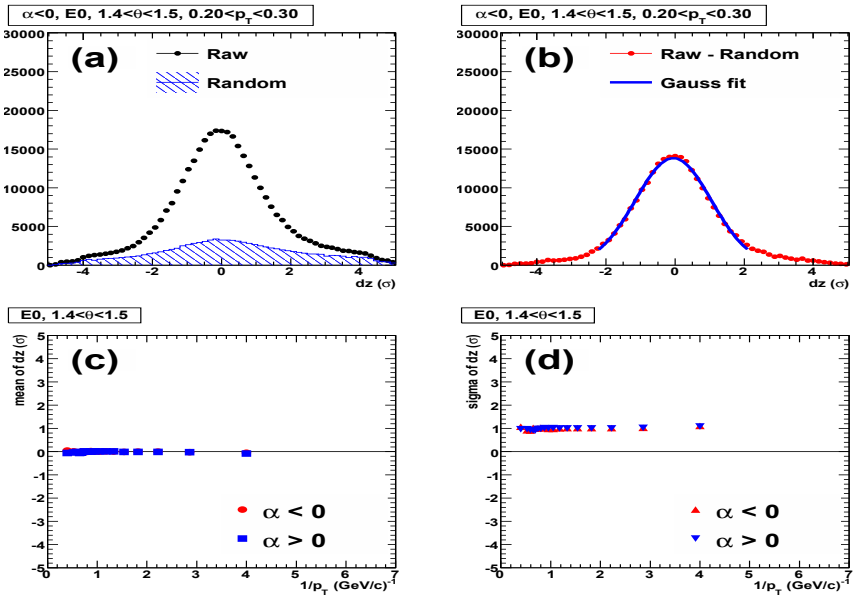

Figure 4.19: The normalized track matching parameter $emcsdz_e$ of the real data after the calibration.

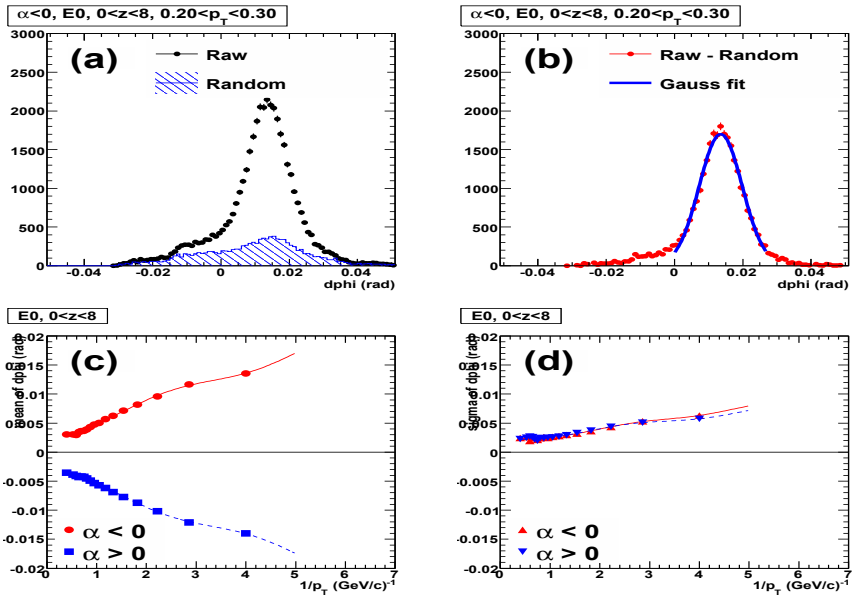

Figure 4.20: The track matching parameter *emcdphi* of the real data before the calibration.

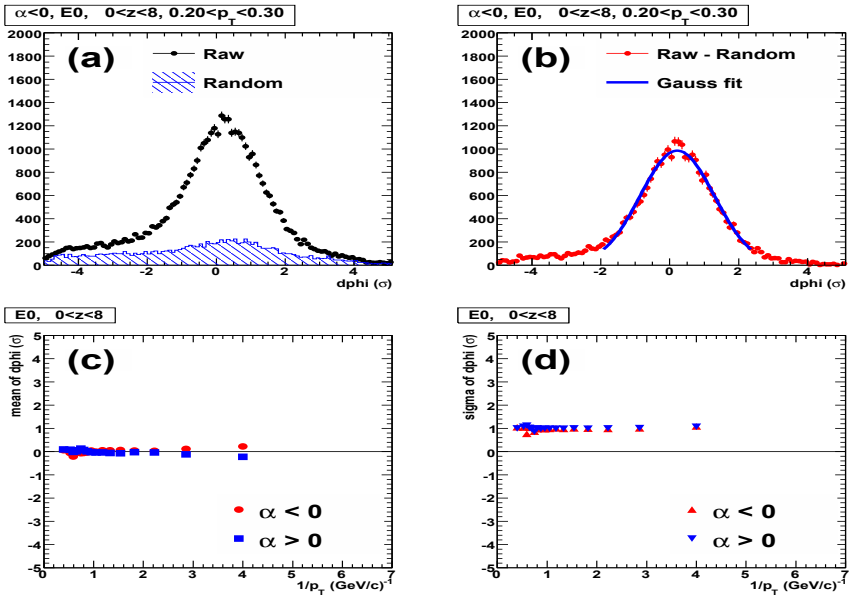

Figure 4.21: The normalized track matching parameter $emcsdphi_e$ of the real data after the calibration.

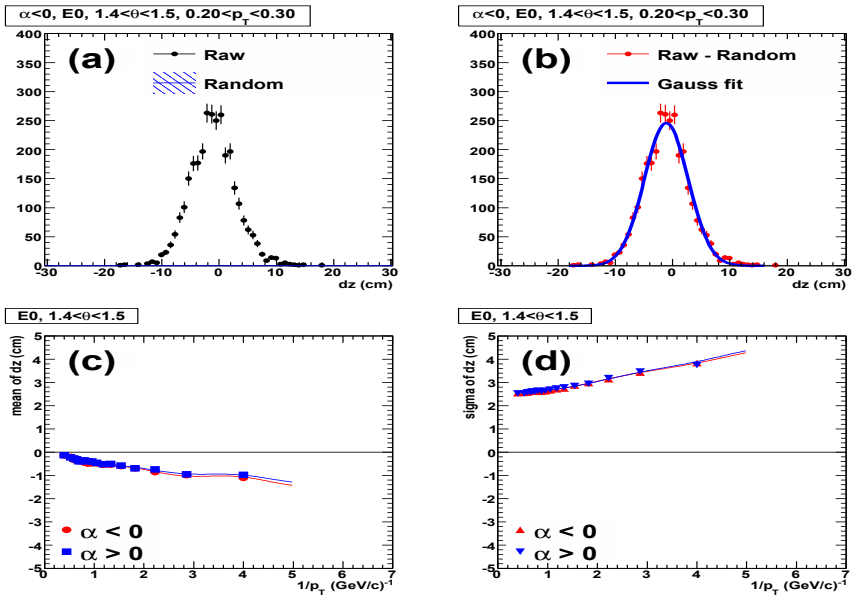

Figure 4.22: The track matching parameter *emcdz* of the simulation before the calibration.

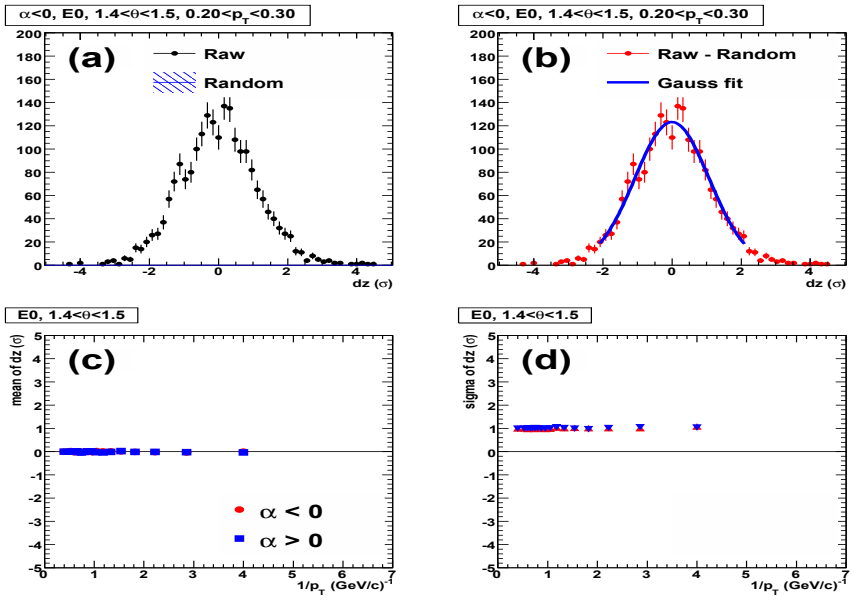

Figure 4.23: The normalized rack matching parameter $emcsdz_e$ of the simulation after the calibration.

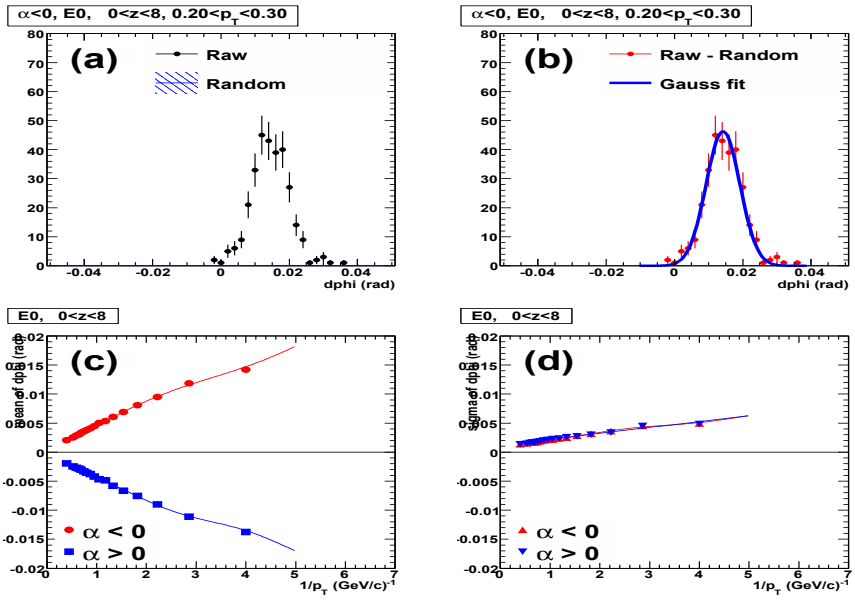

Figure 4.24: The track matching parameter *emcdphi* of the simulation before the calibration.

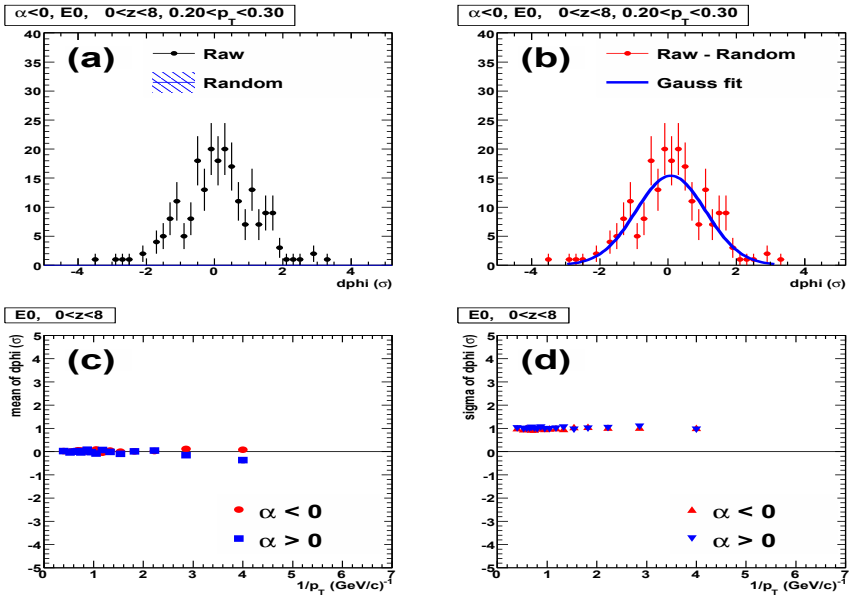

Figure 4.25: The normalized track matching parameter $emcsdphi_e$ of the simulation after the calibration.

4.5.3 Electron identification by energy-momentum matching

The Energy-momentum matching, E/p, is defined by the fraction between the energy deposit in the EMCal and the momentum measured by DC,

$$E/p = ecore/mom, \tag{4.19}$$

where *ecore* is the core energy of the energy deposit in the EMCal, *mom* is the measured momentum. In case of electrons, E/p should distribute around 1 since electrons mass (m_e=0.511 MeV/c^2) is negligible in comparison to measuring momentum scale of a few hundreds MeV to GeV (i.e. $E = \sqrt{p^2 + m_e^2} \approx p$). On the other hand, E/p of charged hadrons is much smaller because they deposit only the minimum ionization energy in EMCal[1]. The raw E/p distribution is shown in the panel (a) of Fig.4.26. The black points are the E/p with the requirements of $n0 > 2$, $chi2/npe0 < 7$ and $disp < 4$. The blue line is the distribution of the randomly associated tracks with $sn0 > 2$, $schi2/snpe0 < 7$ and $sdisp < 4$. The net distribution after subtracting the distribution of random associated tracks is shown in the panel (b).

In order to clarify the criterion of electron identification, the normalized energy-momentum variable *dep* is defined as

$$dep = \frac{E/p - 1}{\sigma_{E/p}}. \tag{4.20}$$

Energy-momentum matching calibration

The energy-momentum matching is not always distributed around 1.0 even in case of electrons. Because the nonlinearity response of the detector becomes apparent especially in the low momentum region due to the inhomogeneity of the material in the EMCal, the bremsstrahlung of electrons passing through the detector material and so on. In addition, photon-conversion electrons produced at the off-vertex point have higher momentum than the original one due to the biases of the tracking algorithm. The panel (c) and (d) in Fig.4.26 show the mean and standard deviation of the energy-momentum matching distribution. The non-linear behavior is remarkably seen at the low momentum region (i.e. high $1/p$ in the figures)

The energy-momentum calibration is performed dependent on the momentum, the bending direction and the EMCal sector. These dependences are summarized in Table 4.5

[1]Hadronic shower with high energy can be produced in nuclear reaction with a small probability.

Variables	Dependences
E/p	The total momentum (mom)
	Bending direction (sign of α)
	EMCal sector (sector and dcarm)

Table 4.5: The dependences considered for the energy-momentum matching calibration.

The calibrations are applied to not only the real data but also the simulation. Figure 4.26 is an example to explain the procedure of this calibration. The panel (b) shows the net distribution and the fitting results of the linear combination between the Gauss function and the exponential function. The exponential function is applied to estimate the residual backgrounds. The fitting parameters, $\langle E/p-1\rangle$ and $\sigma_{E/p-1}$, are extracted by the Gauss fit. The panel (c) and (d) show the parameters as a function of the inverse p. The fitting function in the panel (c) and (d) is

$$f(x) = \sum_{i=1}^{3} a_i \sin\left(\frac{i\pi x}{L}\right) + a_4 + a_5 x, \tag{4.21}$$

where L is determined by the dynamic range of the data points. The summation term of Eq.(4.21) is introduced to take non-linear tendency, point-to-point fluctuation and into account. The fitting results of Eq.(4.21) are used for calibration. Figure 4.27 is the normalized matching variable *dep* after the calibration. The mean parameter is distributed around 0 and sigma parameter is distributed around 1 σ independent of the inverse p. The dependences of the EMCal sector (E0-E3, W0-W3) are shown in Appendix D.

The calibrations for the simulation are performed in the same way above. The results are shown in Fig.4.28 and Fig.4.29

4.5.4 Summary of the electron identification variables

The definition of the variables for electron identification are summarized in Table 4.6.

The selection criteria in this data analysis are summarized in Table 4.7.

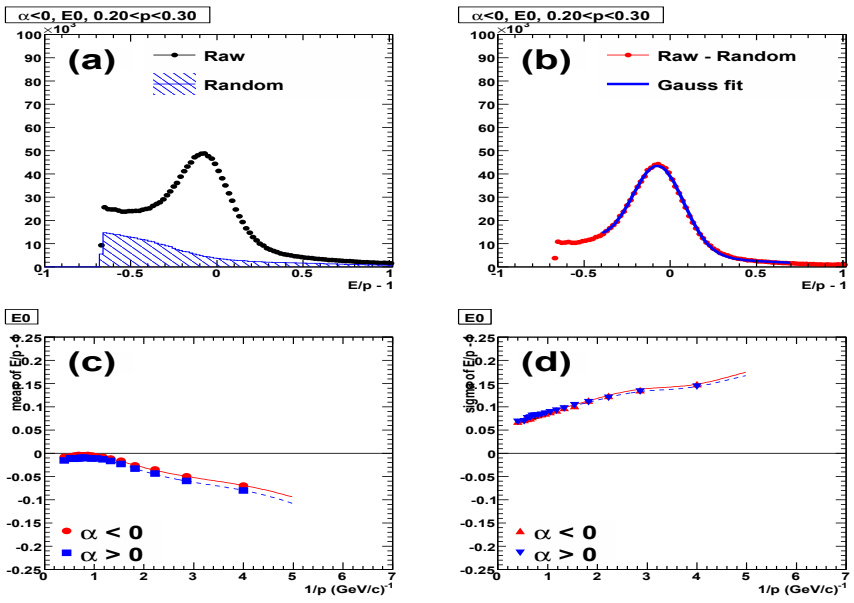

Figure 4.26: The energy-momentum matching parameter $E/p - 1$ of the real data before the calibration.

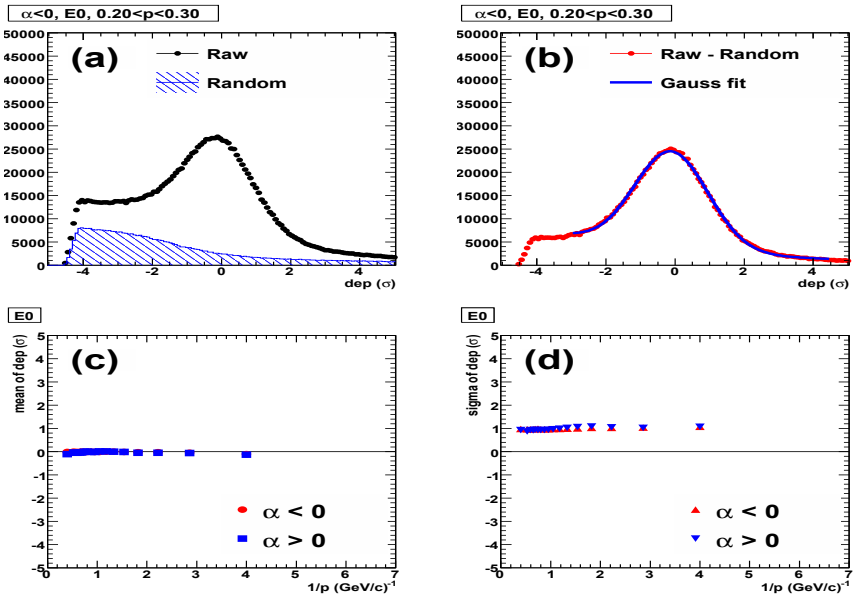

Figure 4.27: The normalized energy-momentum matching parameter *dep* of the real data after the calibration.

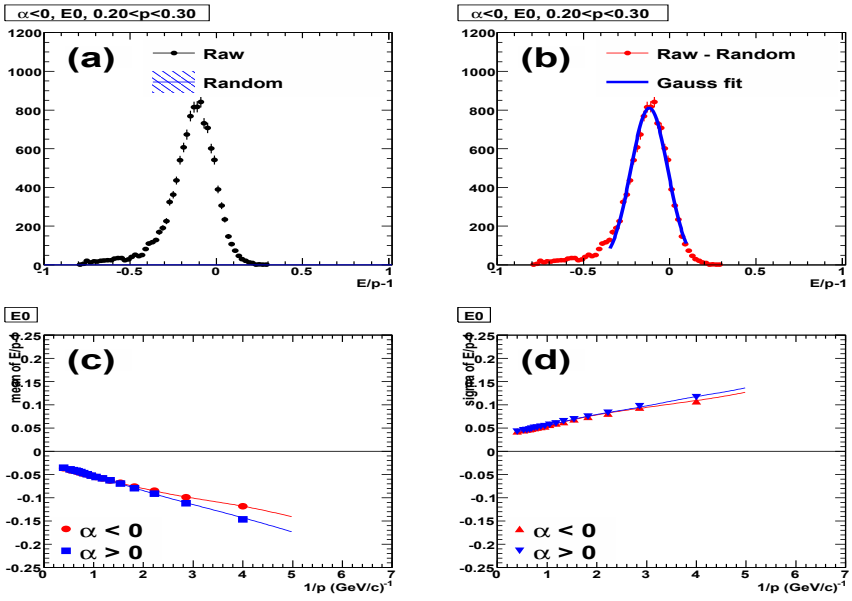

Figure 4.28: The energy-momentum matching parameter $E/p - 1$ of the simulation before the calibration.

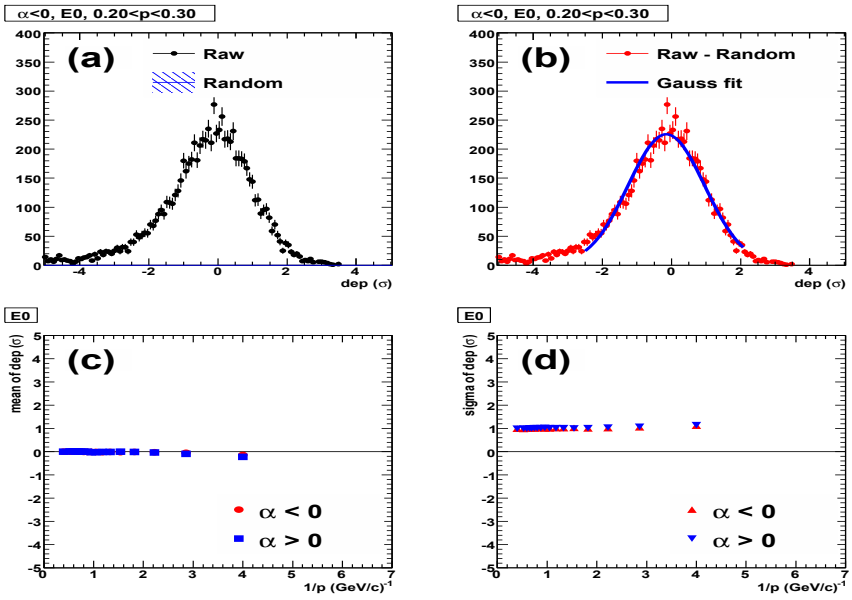

Figure 4.29: The normalized energy-momentum matching parameter *dep* of the simulation after the calibration.

Variables	Descriptions
$n0$	The number of fired phototubes in the nominal ring area ($3.8 \leq r \leq 8.0$ cm)
$npe0$	The number of photoelectrons detected in nominal ring radius
$disp$	Displacement between the projection point onto RICH PMT plane and the centroid of the fired phototubes
$chi2$	The weighted average of deviation for fired phototubes from the ideal ring radius ($r_{ideal} = 5.9$ cm).
$emcdz$	The difference of z between the track projection points and the centroid of the electromagnetic shower.
$emcdphi$	The difference of ϕ between the track projection points and the centroid of the electromagnetic shower.
$emcsdphi_e$	The track matching in ϕ direction normalized by σ_{emcdph}
$emcsdz_e$	The track matching in z direction normalized by σ_{emcdz}
mom	The measured momentum.
$ecore$	The core energy in the EMCal (summed up for 3 towers)
E/p	The ratio between $ecore$ and mom.
dep	The energy-momentum matching normalized by $\sigma_{E/p}$

Table 4.6: The definitions of the variables for electron identification

Variables	Selection criteria
Track quality bit	$31 \cup 63$
Number of fired PMT	$n0 > 2$
Ring quality	$chi2 < 10$
Track matching to RICH	$disp < 5$ cm
Track matching to EMCal	$\sqrt{emcsdphi_e^2 + emcsdz_e^2} < 3\ \sigma$
Energy-momentum matching	$\lvert dep \rvert < 2\ \sigma$

Table 4.7: The summary of the selection criteria in this analysis.

4.6 Fiducial area selection

In order to select fiducial area in the detector, low-efficiency or noisy regions to electrons are identified by the following hit informations.

- hit maps on cosθ vs *bbcz*
- hit maps on *charge/momentum* vs ϕ of the DC. (c/p vs ϕ)
- hit maps on z-ϕ plane projected to the PC1 plane ($ppc1z$ vs $ppc1phi$)
- hit maps on z-ϕ plane on the DC (*zed* vs *phi*)

The criteria of the track selection are as follows.

- track quality bit = 31 $\cup$ 63
- $n0$ >2,
- $chi2/npe0$ <10,
- $disp$ < 5 cm,
- $\sqrt{emcsdphi_e^2 + emcsdz_e^3} < 3\sigma$
- $|dep| < 2\sigma$.

The procedure to select fiducial area consists of three steps as follows.

Step(1) reject obviously dead area in the real data.

Step(2) compare the hit maps between the real data and the simulation.

Step(3) identify and reject the low-efficiency or noisy area with the relative amplitude between the real data and the simulation.

Figure 4.30 is an example of 2-dimensional hit maps. The top-left and bottom-left figures show the cosθ vs bbcz before and after selecting fiducial areas for the real data, respectively. The right two figures show cosθ vs bbcz for the simulation.

Figure 4.31 is the acceptance comparison between the real data and the simulation for *zed* and *phi*. The black points show the real data and the blue lines show the simulation. There is good agreement between the real data and the simulation after selecting fiducial area. Sector-by-sector comparisons are shown in Fig.4.32 and 4.33.

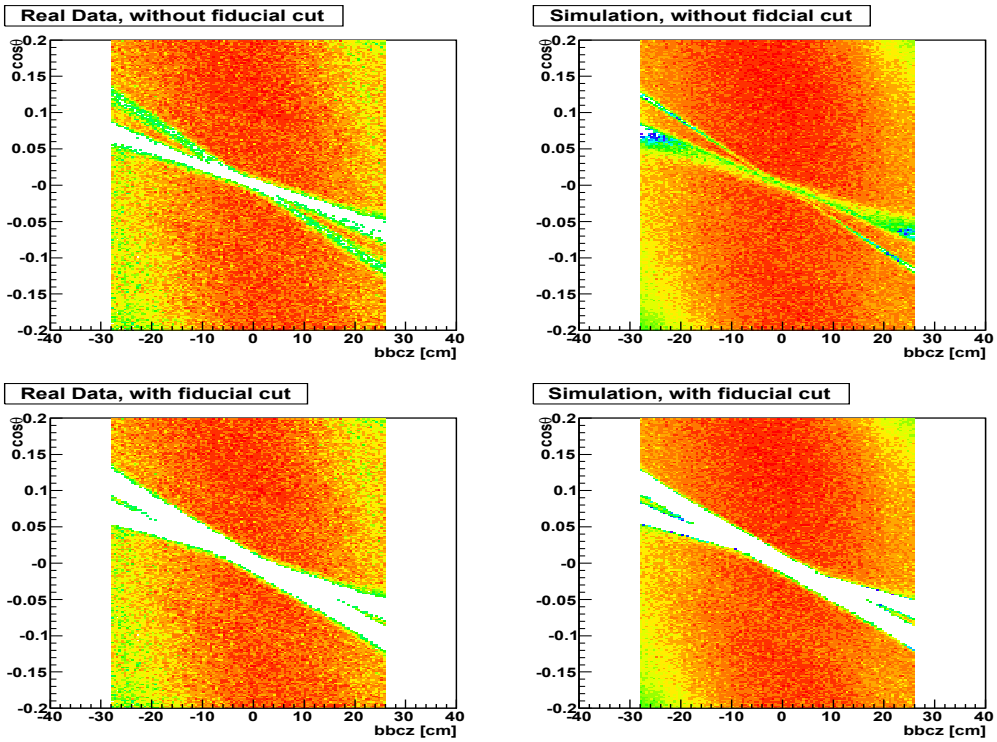

Figure 4.30: cosθ vs bbcz.

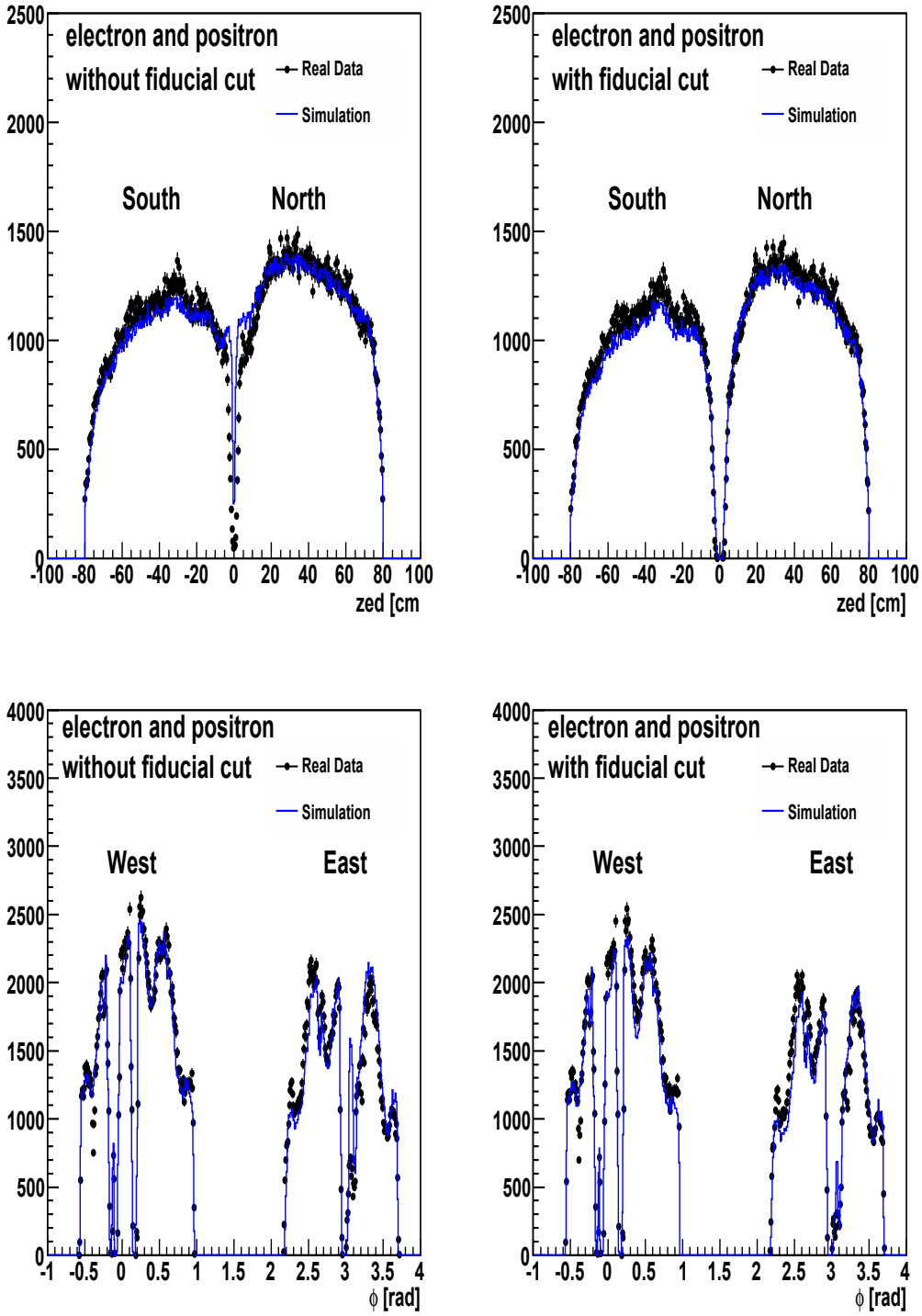

Figure 4.31: Acceptance comparison between the real data and the simulation before (left) and after selecting fiducial areas (right).

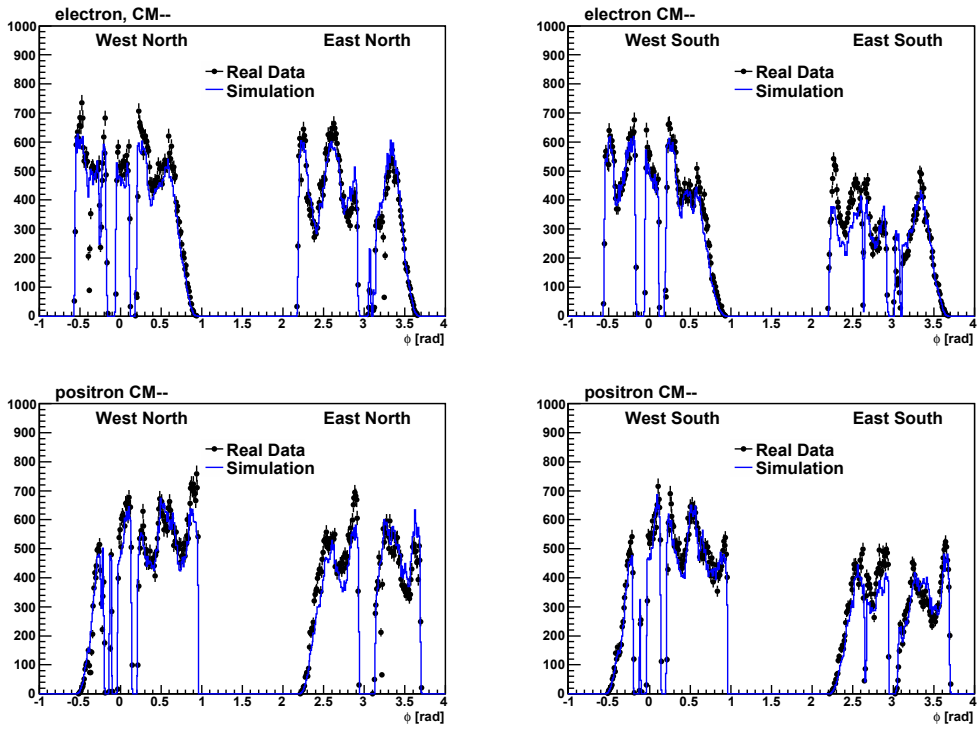

Figure 4.32: *phi* distribution of single electrons after selecting fiducial areas.

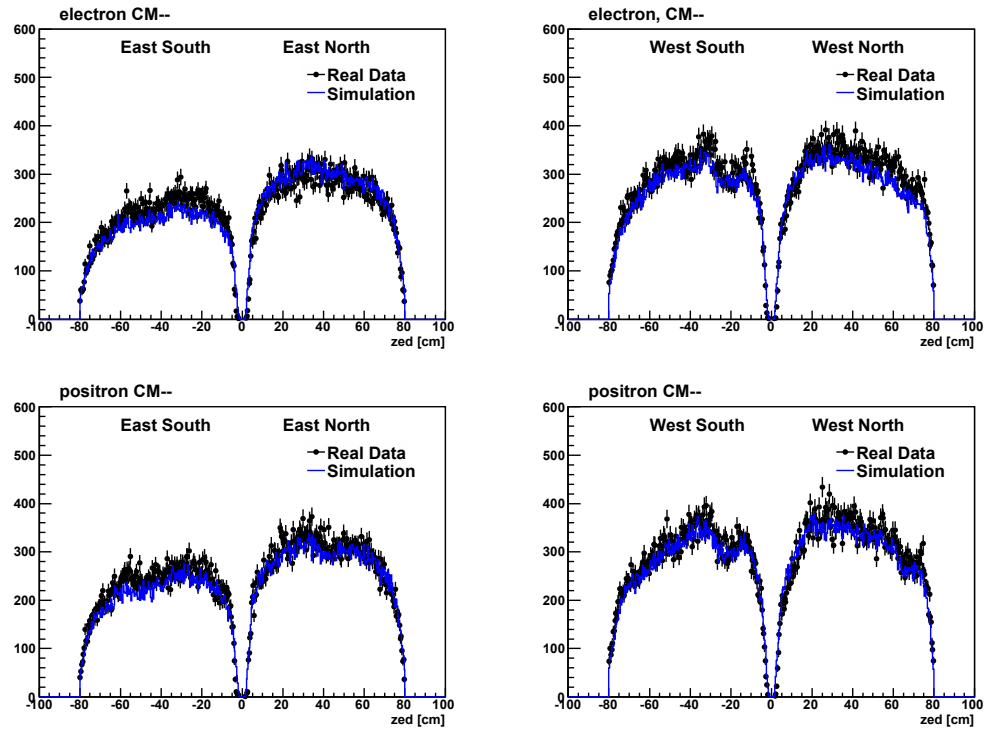

Figure 4.33: *zed* distribution after selecting fiducial areas.

4.7 Pair analysis

4.7.1 Pair reconstruction

Since the source of any particular electron and positron in an event cannot be known in advance, all possible electrons and positrons are combined into pairs. Therefore, the signal pairs, that is, the light vector mesons are identified by the invariant mass spectra of the di-electrons and found on the backgrounds pairs. The invariant mass is reconstructed by

$$\begin{aligned} M_{e^+e^-} &= \sqrt{\left(E_{e^+} + E_{e^-}\right)^2 - \left(\vec{p}_{e^+} + \vec{p}_{e^-}\right)^2}, \\ E_{e^\pm} &= \sqrt{m_{e^\pm}^2 + p_{e^\pm}^2}, \\ \vec{p}_{e^\pm} &= \left(p_{e^\pm x}, p_{e^\pm y}, p_{e^\pm z}\right), \end{aligned} \tag{4.22}$$

where $E_{e^\pm}$ is the energy of electrons and positrons. $\vec{p}_{e^\pm}$ is the momentum vector of them. The vector components of the momentum are expressed in

$$\left(p_x, p_y, p_z\right) = \left(p\sin\theta\cos\phi, p\sin\theta\sin\phi, p\cos\theta\right), \tag{4.23}$$

where θ and ϕ are polar angle with respect to the beam axis and azimuthal angle, respectively. The definition of the PHENIX coordinate system is explained in Chapter 3.

Figure 4.34 shows the invariant mass spectra of unlike-sign pairs changing the severity of the electron identification. The peak of J/ψ meson becomes clearer as more severely electrons are selected.

4.7.2 Backgrounds of electron-positron pairs

The invariant mass spectra are reconstructed by all combinations of electrons and positrons since the origin of any electron cannot be identified. Therefore the inclusive invariant mass spectrum consists of the signal pairs, the correlated background pairs and the combinatorial background pairs. The background pairs are mainly classified into the two types from experimental viewpoints. Background Type (i) is classified as follows.

(1) Overlapping pairs

(2) Photon-conversion pairs

They are basically identical in the pair-by-pair analysis. Background Type (ii) consists of

(3) Combinatorial background pairs,

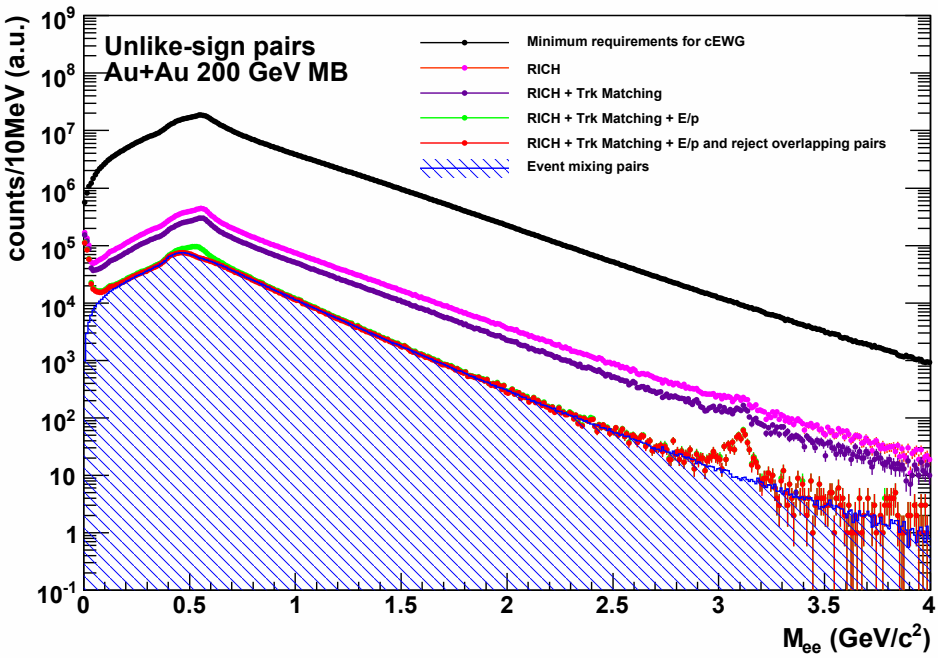

Figure 4.34: The invariant mass spectra of unlike-sign pairs. The severity of the electron identification is different for ea The filled distribution is obtained by the event-mixing pairs.

(4) Correlated background pairs from individual sources: Decaying di-electron pair originated from a meson, final-state di-electron pair from two hadron within a jet or in back-to-back jets and semi-leptonic decay from a hadron.

It is hard to remove these backgrounds in the pair-by-pair analysis, therefore, they are subtracted statistically.

Overlapping background pairs

Under high multiplicity environment produced in heavy-ion collisions, multiple particles enter RICH. When two tracks are parallel to each other, one is an electron and the other is a charged hadron at most cases, their track projection points onto the PMT array are same due to the feature of the reflecting mirrors. This effect is named "ring sharing effect" and illustrated in Fig.4.35. Since the angle of the ring sharing tracks are close to zero , these tracks produce strong angular correlation and make the undesirable peak structure on

the invariant mass distribution.

Strong angular correlations of the ring sharing pairs appears as the correlations between two track projection points on the PMT array. The difference of two projection points, (z_{cross},ϕ_{crosss}), on the PMT array is defined by

$$\begin{aligned} dcross\_z &= z_{cross_i} - z_{cross_j}, \\ dcross\_phi &= \phi_{cross_i} - \phi_{cross_j}, \end{aligned} \tag{4.24}$$

where $(z_{cross_i}, \phi_{cross_i})$ is the projection point on the PMT array for i-th track. Figure 4.36 shows the relative amplitude in the parameter space $(dcross\_z, dcross\_phi)$. The relative amplitude is defined as the ratio between the distribution in a same event and estimated ones with the event-mixing pairs[2]. The relative amplitude shows the strength of the correlation because the event-mixing pairs are uncorrelated. The strong correlations are clearly seen around $(dcross\_z, dcross\_phi) = (0, 0)$. Any two tracks which fulfill the following requirements are rejected in this analysis.

$$R_{RICH} = \sqrt{\left(\frac{dcross\_z}{7.5\,\mathrm{cm}}\right)^2 + \left(\frac{dcross\_phi}{0.02\,\mathrm{rad}}\right)^2} < 4.0\,\sigma \tag{4.25}$$

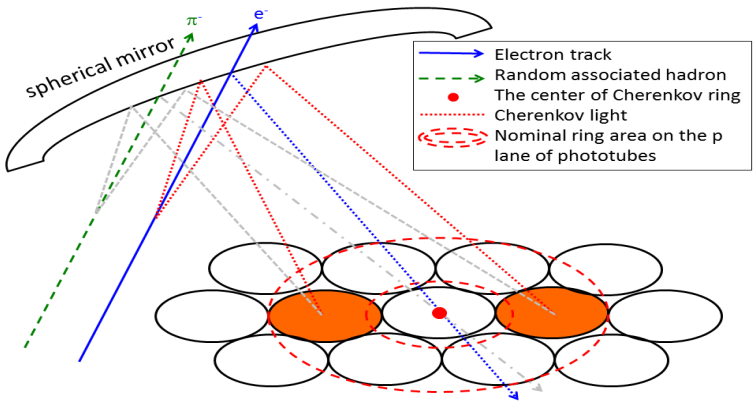

Figure 4.35: Schematic diagram of the ring sharing effect in RICH.

Similar overlapping effect appears in reconstructing the trajectory of the tracks. If two incident charged particles are close to each other in DC, multiple hits are discovered in neighborhood. In this case, multiple tracks are

[2]The distribution of the event-mixing pairs are made by the event mixing technique. The details of the event mixing technique are explained later

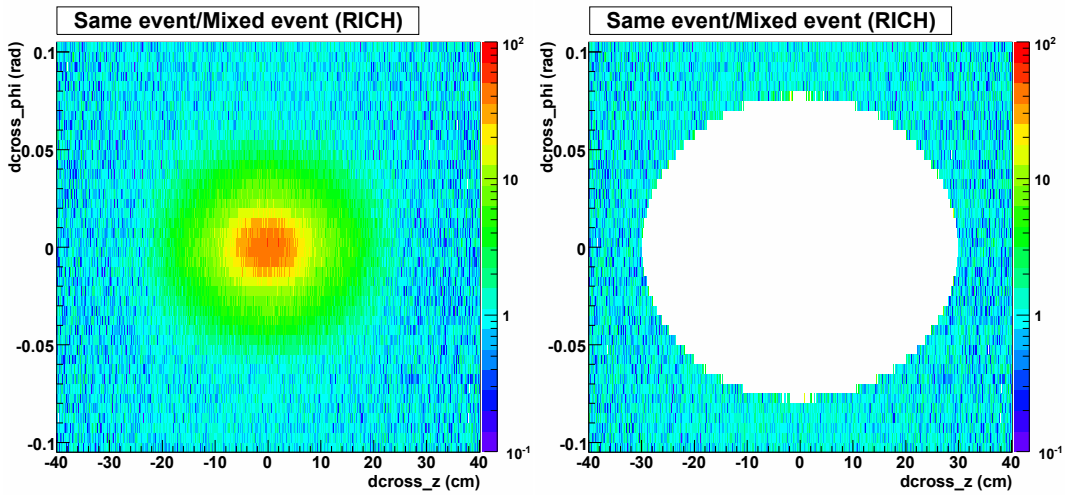

Figure 4.36: The relative amplitude of the pairs in the parameter space $(dcross\_z, dcross\_phi)$. The left and right plots show the relative amplitude before and after rejecting ring sharing tracks, respectively.

reconstructed as long as the combinations of the hit points look reasonable for a track finding algorithm. This effect is named "ghost track effect" and illustrated in Fig.4.37. For instance, if four hits are observed as shown in Fig.4.37, four probable trajectories of all ${}_4C_2$ combinations[3] are selected as real tracks. In this case, two true tracks and two fake ones are included.

These tracks are gathered around 0 in the parameter space of $(dzed, dphi)$. $dzed$ and $dphi$ are defined as the difference of the hit position, (zed, phi) in z direction and ϕ direction, respectively. The definitions are shown by

$$\begin{aligned} dzed &= zed_i - zed_j, \\ dphi &= \phi_i - \phi_j, \end{aligned} \tag{4.26}$$

where (zed_i, ϕ_i) is the hit point in DC for i-th track.

Figure 4.38 shows the relative amplitude in the parameter space $(dzed, dphi)$. In this analysis, any two tracks to fulfill the following requirements are rejected.

$$R_{DC} = \sqrt{\left(\frac{dzed}{0.2\ \mathrm{cm}}\right)^2 + \left(\frac{dphi}{0.01\ \mathrm{rad}}\right)^2} < 4.0\ \sigma. \tag{4.27}$$

[3]All combinations are not necessarily taken, but some of fake combinations can be selected.

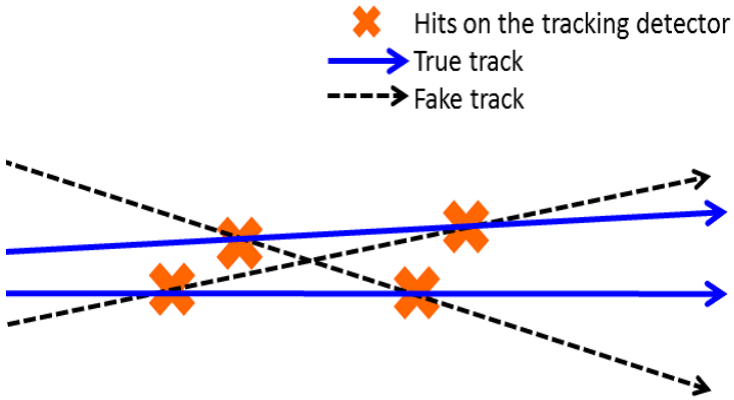

Figure 4.37: Schematic diagram of the ghost track effect in DC.

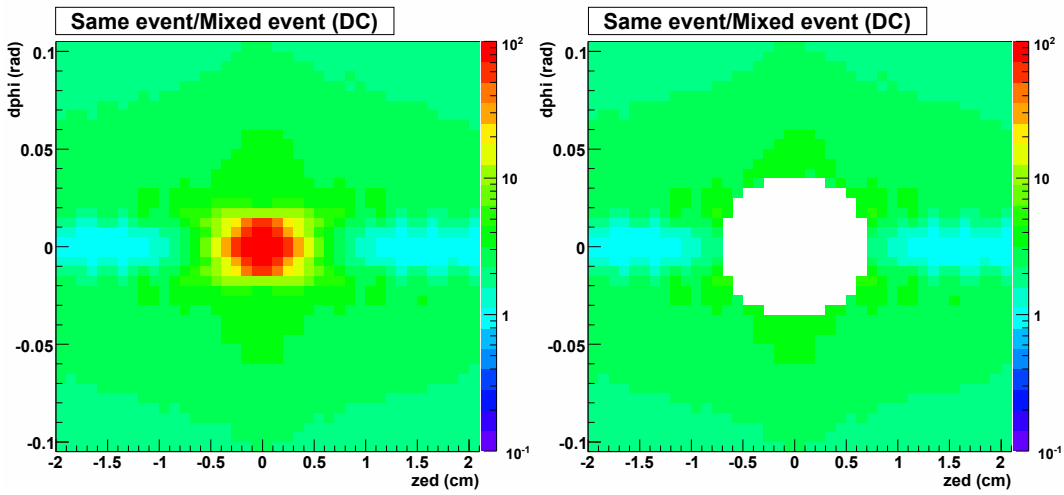

Figure 4.38: The relative amplitude of the pairs in the parameter space $(dzed, dphi)$. The left and right plots show the relative amplitude before and after rejecting ghost tracks, respectively.

Photon-conversion di-electron pairs

The pairs from photon-conversion process in the detector materials are reconstructed as backgrounds. The track reconstruction algorithm in PHENIX, which is based on the combinatorial Hough transform technique, assumes that all charged particles are produced at the collision vertex, that is, at azimuthal radial distance $R = 0$. Thus the produced pairs at the off-axis point are wrongly reconstructed and have higher momentum than the original ones. Figure 4.39 shows the relation between real tracks and wrongly reconstructed tracks. The wrongly reconstructed pairs have higher invariant mass than original one and the increase of invariant mass depends on the radial distance between the collision vertex and the photon-conversion point. The photon-conversion pairs at $R \leq R_{DC}$ mainly contribute to the backgrounds since the pairs at $R > R_{DC}$ can be removed by requiring track quality. The main detector materials at $R \leq R_{DC}$ and fake invariant masses are listed in Table 4.8.

Detector materials	Invariant mass (m_{ee})
The beam pipe at $R = 4$ cm	$m_{ee} \approx 20\,\mathrm{MeV/c^2}$
Detector support structure at $R = 25$ cm	$m_{ee} \approx 125\,\mathrm{MeV/c^2}$
Helium bags at $R < 200$ cm	$m_{ee} < 300\,\mathrm{MeV/c^2}$
The entrance window of the DC	$m_{ee} \approx 300\,\mathrm{MeV/c^2}$

Table 4.8: The main source of the photon conversion and the relation between the photon-conversion points and misreconstructed invariant masses.

The photon-conversion pairs have no intrinsic opening angle, that is, their opening angle is zero at the conversion point, due to zero mass of real photon. Thus the photon-conversion pairs can be bent in the azimuthal direction by only the magnetic field. The direction of the magnetic field is designed to be parallel with respect to the beam axis $\vec{z}$. A resultant unit momentum vector of the pairs, $\hat{\mu}$ and a normal unit vector with respect to the plane of the pair, $\hat{v}$, are defined by

$$\begin{aligned} \hat{\mu} &= \frac{\vec{p}_+ + \vec{p}_-}{|\vec{p}_+ + \vec{p}_-|}, \\ \hat{v} &= \hat{p}_+ \times \hat{p}_-, \end{aligned} \tag{4.28}$$

where $\hat{p}_\pm = \vec{p}_\pm / |\vec{p}_\pm|$ is the three momentum vector of the $e^\pm$. The orientation of the expected opening angle $\hat{\omega}_{exp}$ and that of the actual opening angle $\hat{\omega}_{act}$

are defined as

$$\hat{\omega}_{exp} = \hat{\mu} \times \hat{z},$$
$$\hat{\omega}_{act} = \hat{\mu} \times \hat{v}, \tag{4.29}$$

where $\hat{z}$ is the unit vector of the beam axis. The useful variable ϕ_V is defined by

$$\phi_V = \arccos\left(\hat{\omega}_{exp} \cdot \hat{\omega}_{act}\right). \tag{4.30}$$

The ϕ_V of photon-conversion pairs should be zero[4]. In other words, these pairs are gathering on the perpendicular plane to the beam axis. On the other hand, the di-electron pairs from hadron decays as well as the combinatorial pairs have no preferred orientation.

The reduction of the backgrounds with ϕ_V cut turned out to be a few percents in the mass region of the light vector mesons. This is because ϕ_V cut becomes effective in case the detector system has significantly large acceptance. The ϕ_V is not calculated until electrons and positrons are detected as a pair, unfortunately many of electrons are detected as a single track in the limited acceptance of the PHENIX[5].

Combinatorial backgrounds

The combinatorial pairs cannot be identified in the pair-by-pair analysis. Therefore the contributions from the combinatorial pairs are estimated by the statistical treatment.

The shape of combinatorial background spectrum is estimated by the event mixing technique [186, 187]. The event mixing technique is that an electron in an event and a positron in another event are mixed as shown in Fig.4.40. The similar event classes, in concrete, the similar centrality and collision vertex, are selected in mixing events to avoid the biases from the event topology in a collision. Any event-mixing pair is naturally uncorrelated because there is no correlation between events in principle. Therefore the event mixing technique has the advantage of estimating the shape of the uncorrelated distribution. The other advantage of the event mixing is that the statistical errors of the event mixing can be significantly small because the analyzed number of mixing events is selectable. Substantially the statistical errors from the residual distribution after subtracting the combinatorial distribution are determined by the distribution in the same event, that is, the error propagation of the event-mixing subtraction becomes negligible.

[4]The ϕ_V are calculated to avoid $\phi_v = \pi$ as a solution for photon conversion by ordering positive and negative tracks within the pair

[5]Even in such situation, ϕ_V is useful for the low-mass di-electron continuum analysis ($m_{ee} < 0.7\,\mathrm{GeV/c^2}$).

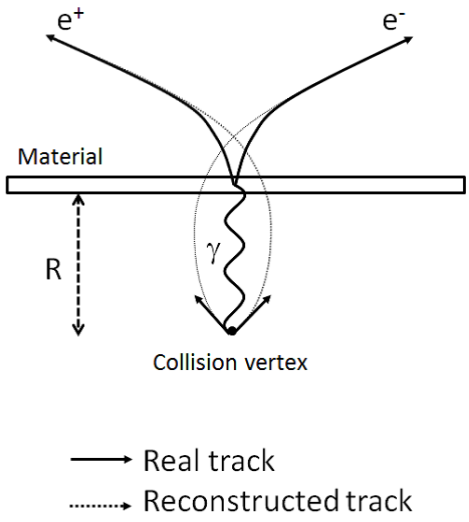

Figure 4.39: Schematic diagram of the photon conversion at the off-vertex point.

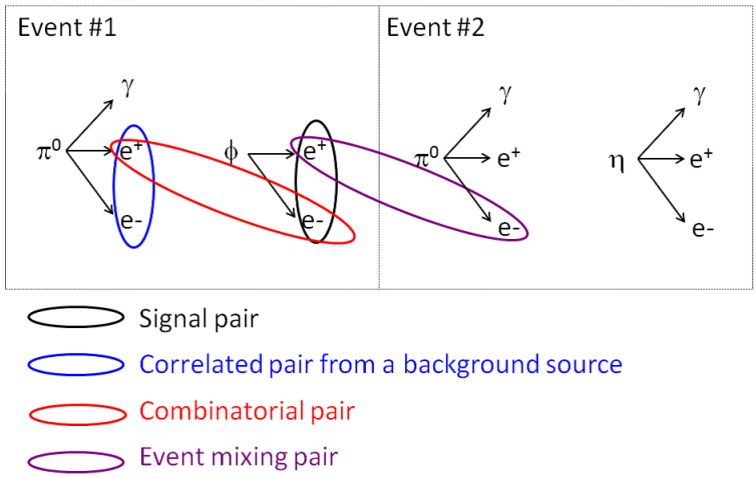

Figure 4.40: The definition of a signal pair, a background pair, a combinatorial pair and an event-mixing pair.

The combinatorial background distribution via the event mixing technique is needed to be normalized. The absolute yield of uncorrelated pairs in same events is estimated by the geometrical mean of the number of like-sign pairs $2\sqrt{N_{++}N_{--}}$, where N_{++} and N_{--} are the number of e^+e^+ and e^-e^- pairs, re-

spectively. This estimation is valid as long as e^+ and e^- with equal acceptance are usually produced as pairs. Counting the uncorrelated pairs in like-sign distribution is much easier than in unlike-sign distribution because there is no existence of e^+e^+ or e^-e^- decay from hadrons except for the following processes.

- The cross pairs from π^0/η, that is, $\pi^0/\eta \to \gamma_1\gamma_2$ or $e_1^+e_1^-\gamma_2 \to e_1^+e_1^-e_2^+e_2^-$
- The e^+e^+ or e^-e^- pairs in a jet

The left plot in Fig.4.41 shows the invariant mass spectra of the cross pairs estimated by the simulation[6]. The mass spectra of the cross pairs from π^0/η are radically dropped at the mass range of 0.1-0.2 GeC/c^2 and 0.5-0.6 GeV/c^2, respectively. The like-sign pairs in a jet has strong correlation in azimuth. The azimuthal angle difference between pairs are close to zero and such correlations make the mass peak at $m_{ee} \sim 0$ GeV/c^2. The right plot in Fig.4.41 is an example of the jet-like correlation of like-sign pairs when the pairs are found in a same jet or back-to-back jets[7]. The contributions from the jet pairs are much smaller than the cross pairs. Therefore the like-sign pairs are counted in the mass range of $m_{ee} > 0.6$ GeV/c^2 in order to minimize the effects from the correlated like-sign pairs.

The normalization factor is calculated in the following procedure. First, the integrated number of like-sign pairs, N'_{++} and N'_{--}, are defined as follows.

$$\begin{aligned} N'_{++} &= \int_0^\infty A_{++} \times B_{++}(m_{ee})\, dm_{ee}, \\ N'_{--} &= \int_0^\infty A_{--} \times B_{--}(m_{ee})\, dm_{ee}, \\ A_{++} &= \frac{\int_{N.R.} N_{++}(m_{ee})}{\int_{N.R.}^\infty B_{++}(m_{ee})} dm_{ee}, \\ A_{--} &= \frac{\int_{N.R.} N_{--}(m_{ee})}{\int_{N.R.}^\infty B_{--}(m_{ee})} dm_{ee}, \end{aligned} \tag{4.31}$$

[6] π^0 and η are singly generated based on the differential cross section in p+p 200 GeV. The geometrical acceptance and momentum resolution of the PHENIX detector system are taken into account. The p_T threshold sets 150 MeV/c, which is equivalent to minimum p_T in cEWG data file. The invariant mass distribution of η meson is scaled by the η/π^0 ratios in p+p 200 GeV.

[7] The four-momentum vector of an electron is generated based on the differential cross section of single electron in p+p 200 GeV and embedding azimuthal correlation. The azimuthal correlation is determined by the assumption that a jet has Gauss profile with the sigma of 0.25 rad and like-sign pairs are found in a same jet or back-to-back jet.

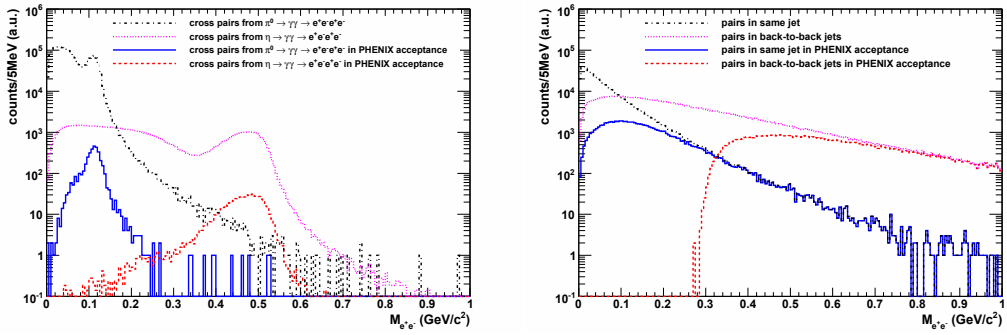

Figure 4.41: The left figure is the invariant mass spectra of the cross pairs from π^0/η. The spectra in case of ideal detector coverage and PHENIX acceptance are depicted as the different curves. The η spectra is scaled with the η/π^0 ratio based on the measured production cross section in p+p 200 GeV. The right figure is the invariant mass spectra when the pairs are found in a same jets or back-to-back jets. The case of ideal detector acceptance and the PHENIX acceptance are depicted as the different curves.

where $N_{\pm\pm}(m_{ee})$ is the number of like-sign pairs in the same events, $B_{\pm\pm}(m_{ee})$ is the number of like-sign pairs in the mixed events. N.R. is the chosen normalization region. The invariant mass range of $0.6 < M_{ee} < \infty$ are selected as the normalization region in this analysis in order to minimize the effect from the correlated like-sign pairs. Therefore the normalization factor, α, is estimated by the following equation.

$$\begin{aligned} \alpha &= \frac{2\sqrt{N'_{++}N'_{--}}}{B_{+-}} \\ &= \sqrt{\frac{\int_{m_{th}}^{\infty} N_{++}(m_{ee})\,dm_{ee} \times \int_{m_{th}}^{\infty} N_{--}(m_{ee})\,dm_{ee}}{\int_{m_{th}}^{\infty} B_{++}(m_{ee})\,dm_{ee} \times \int_{m_{th}}^{\infty} B_{--}(m_{ee})\,dm_{ee}}} \end{aligned} \tag{4.32}$$

where $m_{th} = 0.6$ GeV/c^2, B_{+-} is the integrated number of unlike-sign pairs in the mixed events.

The top two figures in Fig.4.42 show the invariant mass spectra of e^+e^+ and e^-e^-, respectively. The like-sign pairs in same events and the normalized like-sign pairs in mixed events are depicted on each plot. Both of them reasonably agree with each other at the accuracy of a few % in the mass region of $m_{ee} > 0.3$ GeV/c^2[8].

[8]The uncertainty of this normalization method is confirmed by the originally developed numerical simulation. The details of the simulation is explained in Chapter 6.

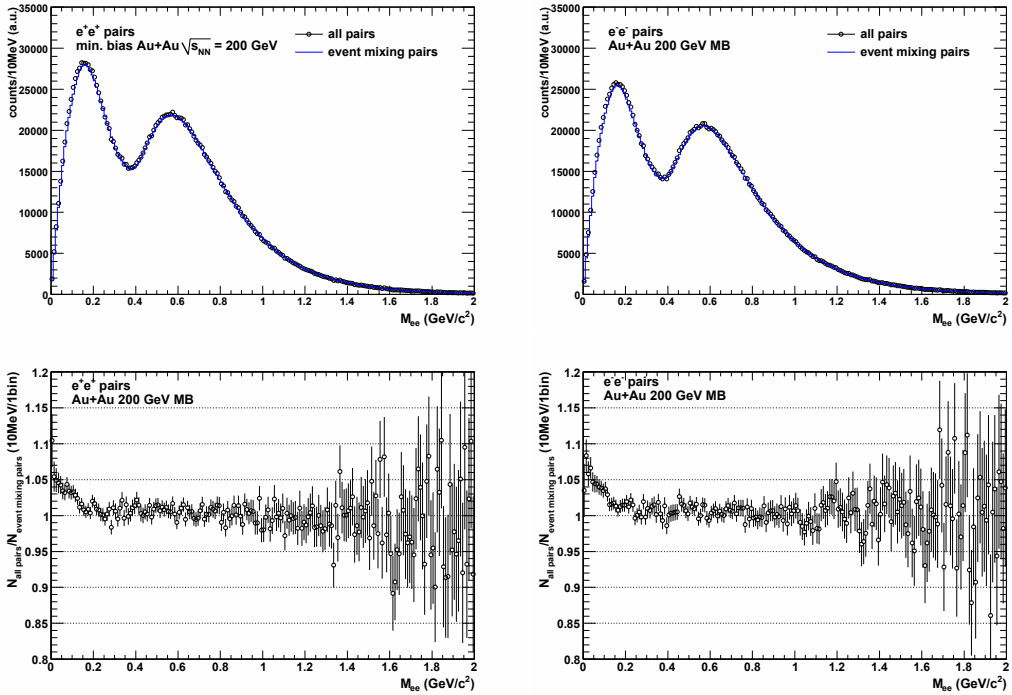

Figure 4.42: The invariant mass spectra of e^+e^+ pairs (top-left) and e^-e^- pairs (top-right). The ratio between the same-event mass spectrum and the normalized event-mixing mass spectrum for e^+e^+ pairs (bottom-left) and e^-e^- pairs (bottom-right).

Dalitz decay: $\pi^0/\eta \to \gamma e^+e^-$

The invariant mass spectrum of Dalitz decaying di-electrons reproduces Kroll-Wada formula as shown in Chapter 2. The mass spectrum has a character whose leading edge of the summation of masses of decay products (i.e. $2m_e = 1$ MeV/c^2) and the distribution continues up to their parent mass (i.e. $m_{\pi^0} = 135$ MeV/c^2 and $m_\eta = 548$ MeV/c^2). Therefore the tails of invariant mass does not affect in the mass region of light vector mesons.

Heavy flavor decay: $c\bar{c}\,(b\bar{b}) \to D\bar{D}\,(B\bar{B}) \to e^+e^-$

The mass shape of di-electrons from heavy quarks strongly depends on the heavy quark and anti-heavy quark production, the fragmentation process of hadrons and decays. Therefore the correlation between electrons and positrons are complicated since final-state electrons are produced bound for for many processes. Figure 4.43 shows the two extreme cases of these corre-

lations. One of them is the case di-electrons have no correlation. The other is the case di-electrons have the back-to-back correlation. The number of di-electrons between two cases vary by the factor of 2 to 3 in the mass region of light vector mesons (i.e. $0.6 < M_{ee} < 1.2$ GeV/c^2). In real data analysis, it is unknown how much the correlations exist. Therefore the contributions to the mass spectrum are estimated by the empirical fitting to the residual distribution after rejecting the combinatorial backgrounds.

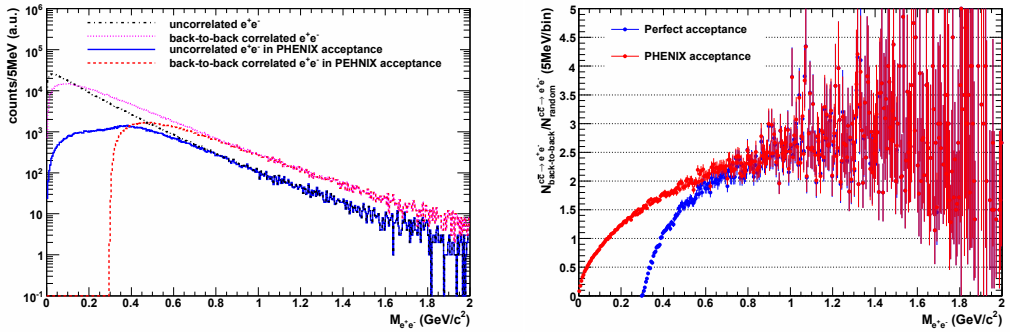

Figure 4.43: The invariant mass spectra of di-electrons originating from heavy flavor decays (left). Uncorrelated di-electrons and back-to-back correlations are assumed in case of the perfect acceptance and the PHENIX acceptance. The ratio of the mass spectra between the uncorrelated case and the back-to-back case (right).

$J/\psi \to e^+e^-$ and Drell-Yan process

The contributions from $J/\psi \to e^+e^-$ and Drell-Yan process are negligible due to the small productions[9] and the large gap from the masses of light vector mesons.

4.7.3 Inclusive invariant mass spectra of di-electrons

Figure 4.44 shows the invariant mass spectra of unlike-sign pairs (top) and like-sign pairs (bottom). The contributions from the overlapping background pairs are superimposed on the plots.

[9]According to the production cross section in p+p 200 GeV, the yield of the final-state di-electrons is about one-third of that for ϕ meson. In addition, J/ψ production is known to be suppressed in heavy-ion collisions. The yield of di-electrons from the Drell-Yan process are smaller than that of J/ψ meson.

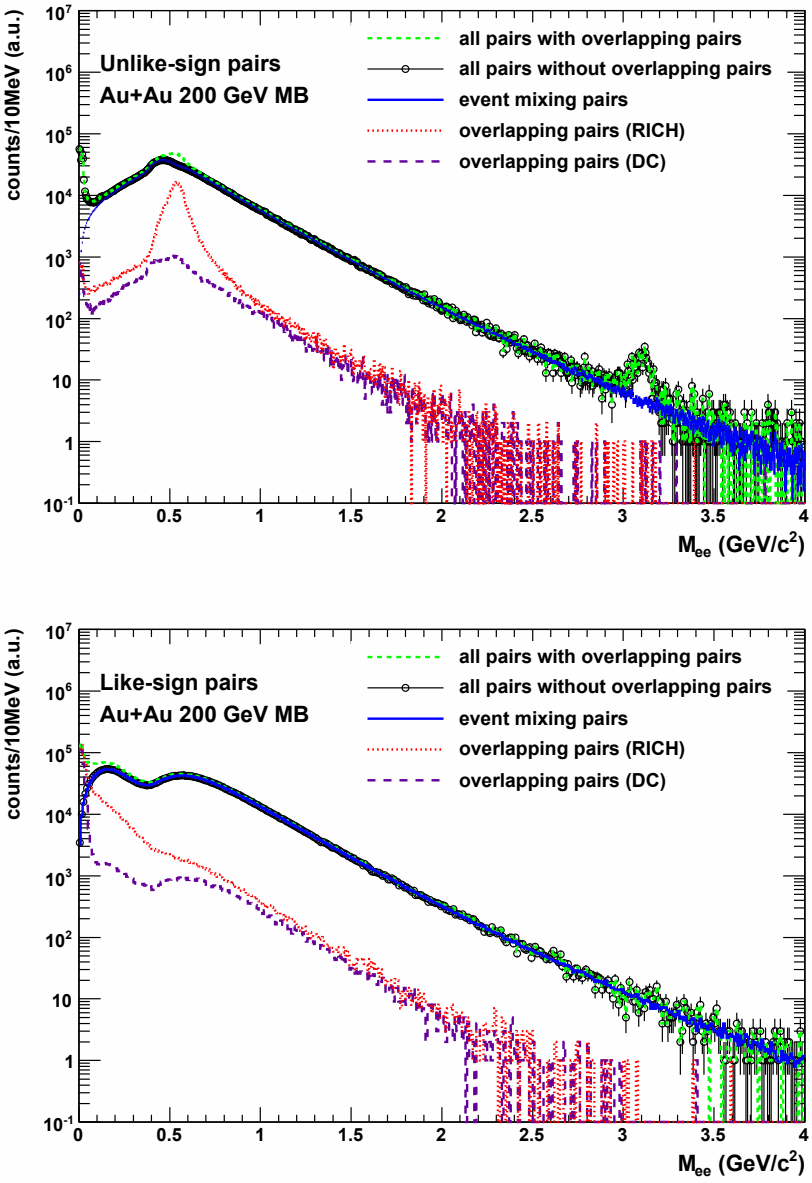

Figure 4.44: The invariant mass spectra of unlike-sign pairs (top) and like-sign pairs (bottom). The contributions from the overlapping pairs are superimposed on the plot.

4.7.4 Light vector mesons: $\phi/\omega/\rho \to e^+e^-$

The correlated components are extracted by subtracting the combinatorial backgrounds estimated by the event mixing technique. The signals of the

light vector mesons can be identified by their intrinsic masses [12]. The top plot in Fig.4.45 is the invariant mass spectrum focusing on the mass region of the light vector mesons. The bottom plot in Fig.4.45 is the invariant mass spectrum after subtracting the combinatorial backgrounds. The mass spectra of the light vector mesons are assumed to follow the Breit-Wigner function in this analysis, since the resonance peaks of the light vector mesons with short lifetime are known to follow the Breit-Wigner distribution. The mass resolution is expressed in the form of the Gauss function. The residual background shape, which dominates the correlated backgrounds, is estimated by a polynomial function. Therefore, the signals of the ϕ and ω are extracted by the fits with the linear combination between the Breit-Wigner function convoluted with the Gauss function and a polynomial function. In the mass range of ϕ meson, we use

$$\frac{dN_{e^+e^-}}{dM_{e^+e^-}} = A \int F_\phi\left(M'\right) G_{gauss}\left(M_{e^+e^-} - M'\right) dM' + H_{bg}\left(M_{e^+e^-}\right). \quad (4.33)$$

In the mass range of ω/ρ meson, two Breit-Wigner functions should be convoluted with the Gauss function.

$$\frac{dN_{e^+e^-}}{dM_{e^+e^-}} = B \int \left\{RF_\omega\left(M'\right) + \left(1-R\right) F_\rho\left(M'\right)\right\} G_{gauss}\left(M_{e^+e^-} - M'\right) dM' + H_{bg}\left(M_{e^+e^-}\right),$$

$$R = \frac{N_\omega BR\left(\omega \to e^+e^-\right)}{N_\omega BR\left(\omega \to e^+e^-\right) + N_\rho BR\left(\rho \to e^+e^-\right)}, \quad (4.34)$$

where N_ω and N_ρ are the inclusive yields of ω and ρ meson, respectively. The inclusive yield of the mesons are assumed to be as same as those in p+p 200 GeV[10]. This assumption is not realistic because ρ mesons are considered to be significantly melting in heavy-ion collisions. However, even in the case, this assumption provides the candles whether or not the yields of ω and ρ mesons change[11]. $BR\left(\omega \to e^+e^-\right)$ and $BR\left(\rho \to e^+e^-\right)$ are the branching ratios to a di-electron for ω and ρ meson, respectively. $F_{\phi,\omega,\rho}\left(M'\right)$ in Eq.(4.33) and (4.34) indicate the Breit-Wigner function describing the intrinsic mass spectra of the light vector mesons and $G_{gauss}\left(M_{e^+e^-} - M'\right)$ shows the Gauss function expressing the smearing effect caused by the transverse momentum resolution. The residual backgrounds are estimated by the empirical function, $H_{bg}\left(M_{e^+e^-}\right)$. These functions are expressed as

$$F_{\phi,\omega,\rho}\left(M'\right) = \frac{\Gamma_{\phi,\omega,\rho}/2\pi}{\left(M' - M_{\phi,\omega,\rho}\right)^2 + \left(\Gamma_{\phi,\omega,\rho}/2\right)^2}, \quad (4.35)$$

[10]The production cross sections are listed in Chapter 2.

[11]The uncertainty of the ρ yield are evaluated in the systematic study.

$$G_{gauss}\left(M_{e^+e^-} - M'\right) = \frac{1}{\sqrt{2\pi}\sigma} e^{-\left(M_{e^+e^-} - M'\right)^2/2\sigma^2}, \tag{4.36}$$

$$H_{bg}\left(M_{e^+e^-}\right) = C \tag{4.37}$$

where the mass center $M_{\phi,\omega,\rho}$ and the width $\Gamma_{\phi,\omega,\rho}$ of the light vector mesons are fixed to their intrinsic values [12]. The mass resolution σ is also fixed to the experimental resolution in PHENIX. A, B and C in the equations are normalization factors. The fitting ranges are from 0.9 to 1.2 GeV/c^2 for ϕ meson and from 0.6 to 0.9 GeV/c^2 for ω/ρ meson. The number of the light vector mesons is counted by the integration of the convolution function over the signal mass region.

The p_T dependent mass resolutions for ϕ/ω are summarized in Table 4.9.

p_T range	ϕ meson	ω meson
all p_T	6.9 MeV/c^2	5.6 MeV/c^2
$0.0 \leq p_T < 1.5$ GeV/c	5.4 MeV/c^2	4.5 MeV/c^2
$1.5 \leq p_T < 3.0$ GeV/c	7.3 MeV/c^2	4.9 MeV/c^2
$3.0 \leq p_T < 4.5$ GeV/c	8.6 MeV/c^2	6.9 MeV/c^2

Table 4.9: The p_T dependent mass resolutions for ϕ and ω mesons. The mass resolutions are calculated by the PISA simulation.

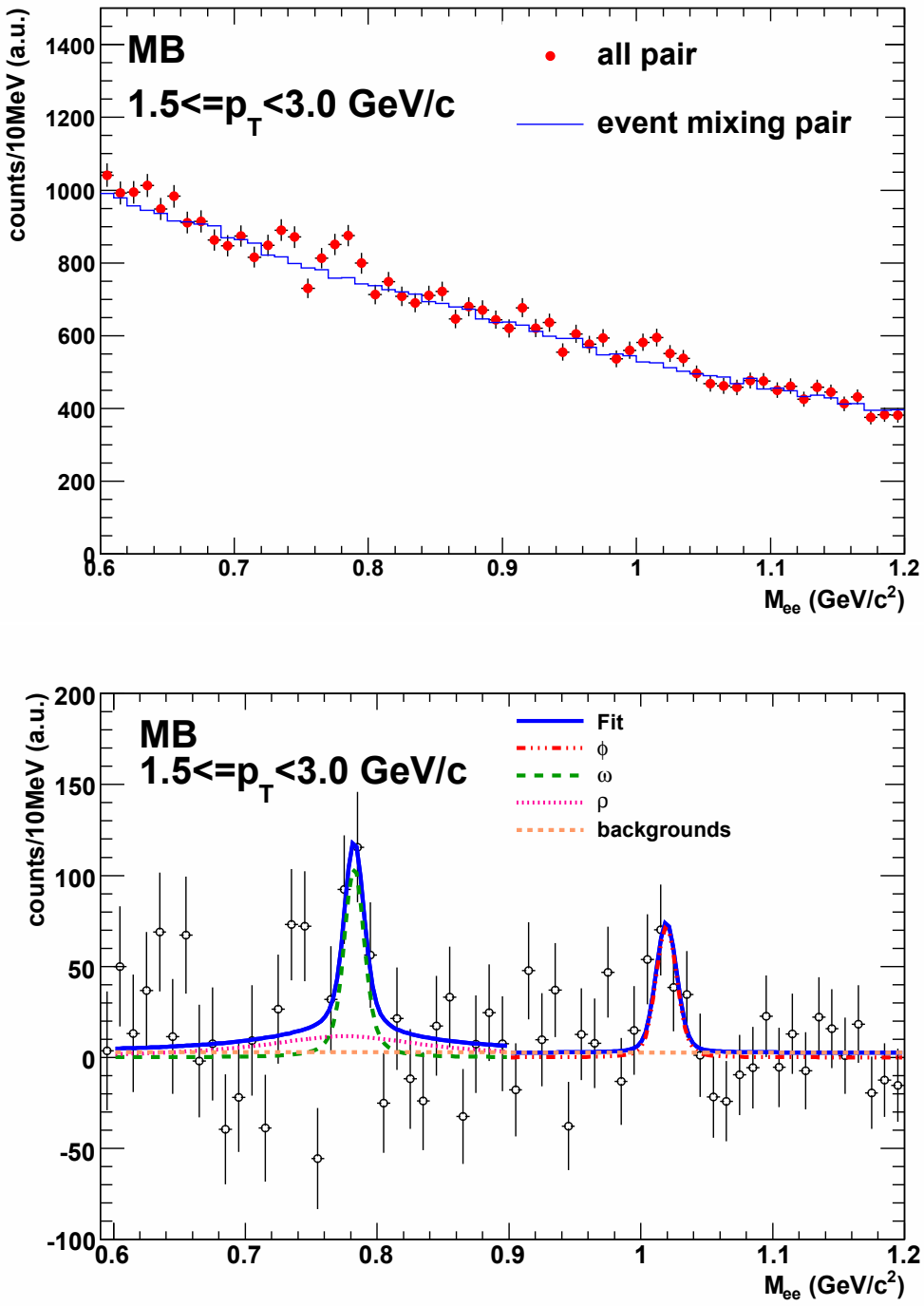

Figure 4.45: The invariant mass spectra of the di-electrons around the mass range of the light vector mesons (top). The invariant mass spectra of the di-electrons after subtracting the combinatorial backgrounds (bottom). The fitting results are superimposed in the plot.

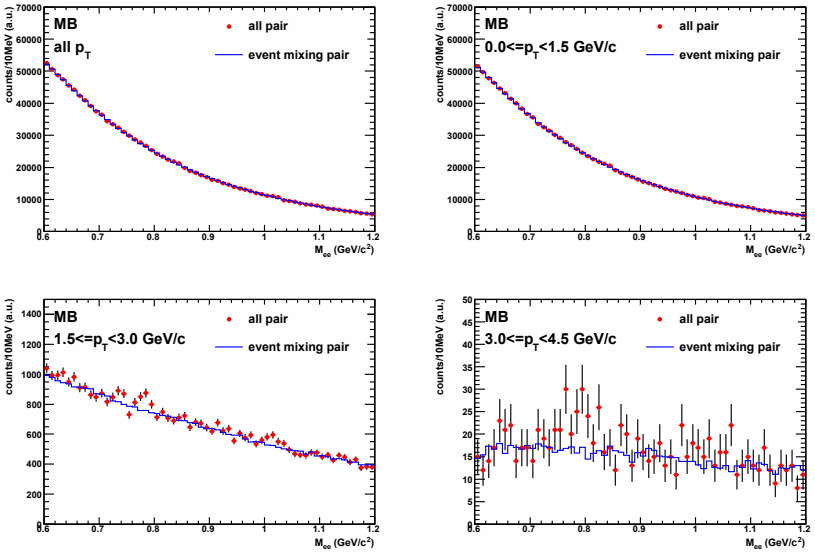

Figure 4.46: The invariant mass spectra of the di-electrons at the centrality class of 0-92.2% (MB).

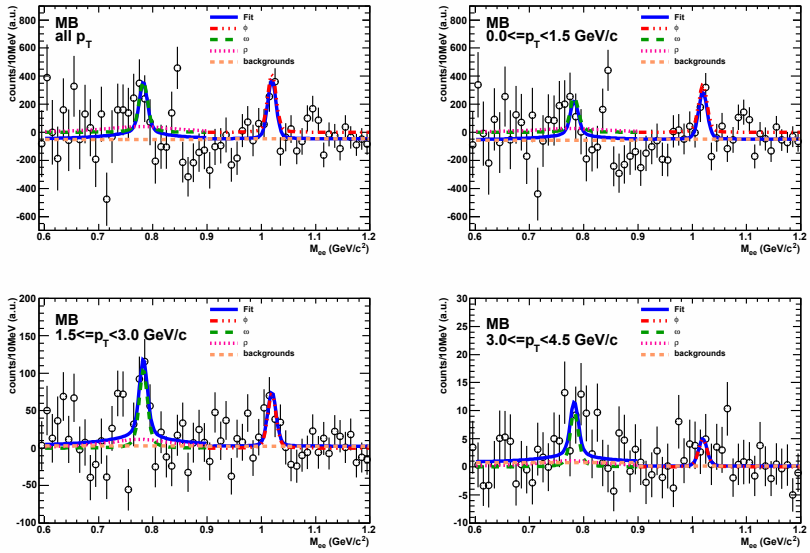

Figure 4.47: The invariant mass spectra of the di-electrons after subtracting the event mixing distribution at the centrality class of 0-92.2% (MB).

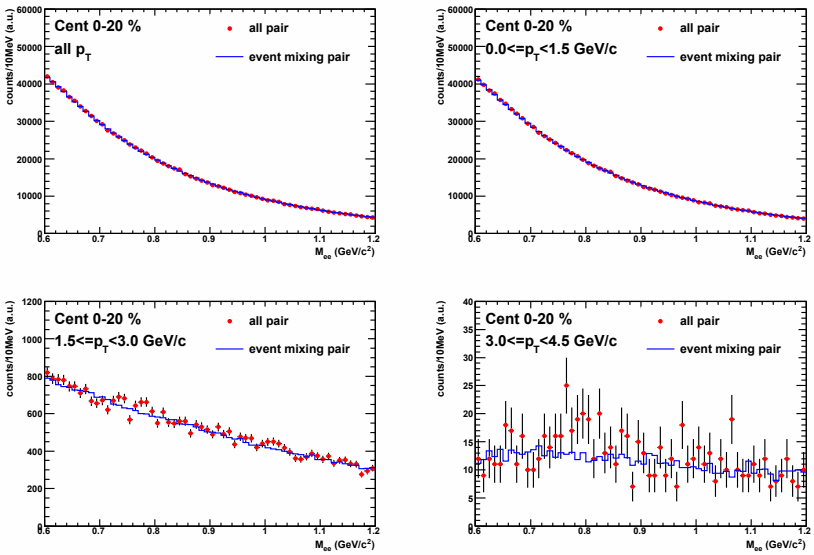

Figure 4.48: The invariant mass spectra of the di-electrons at the centrality class of 0-20%.

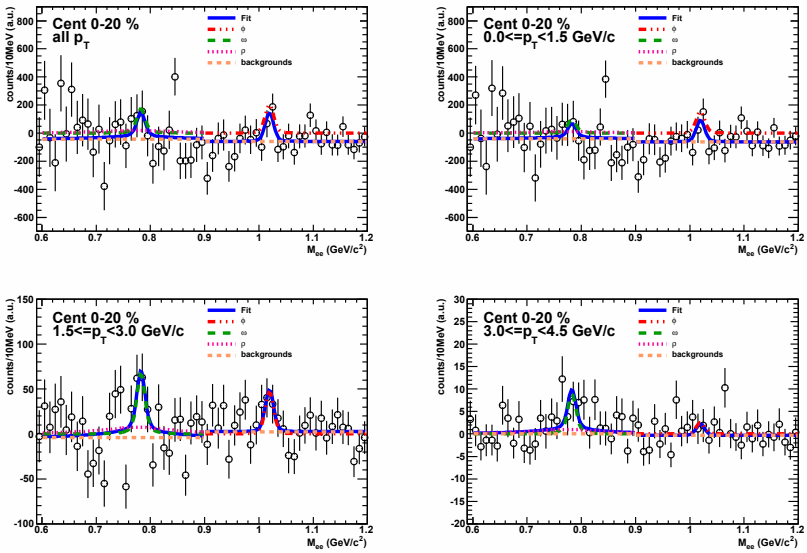

Figure 4.49: The invariant mass spectra of the di-electrons after subtracting the event mixing distribution at the centrality class of 0-20%

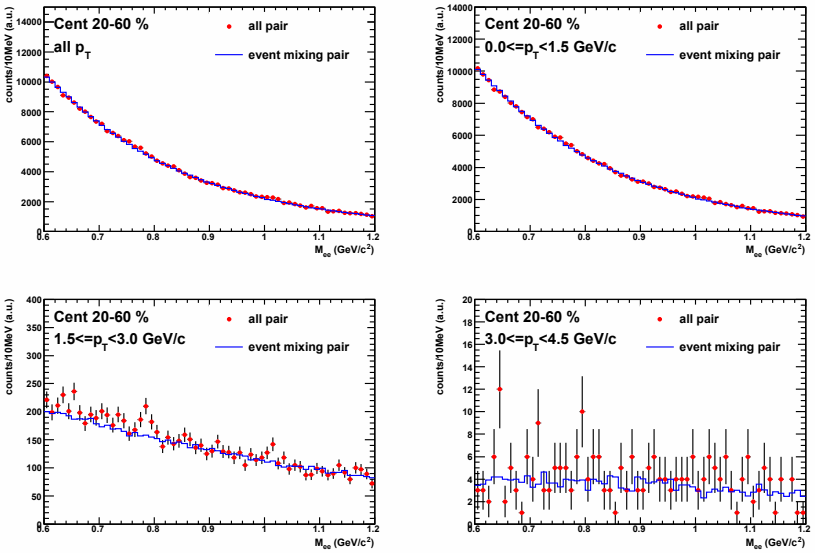

Figure 4.50: The invariant mass spectra of the di-electrons at the centrality class of 20-60%.

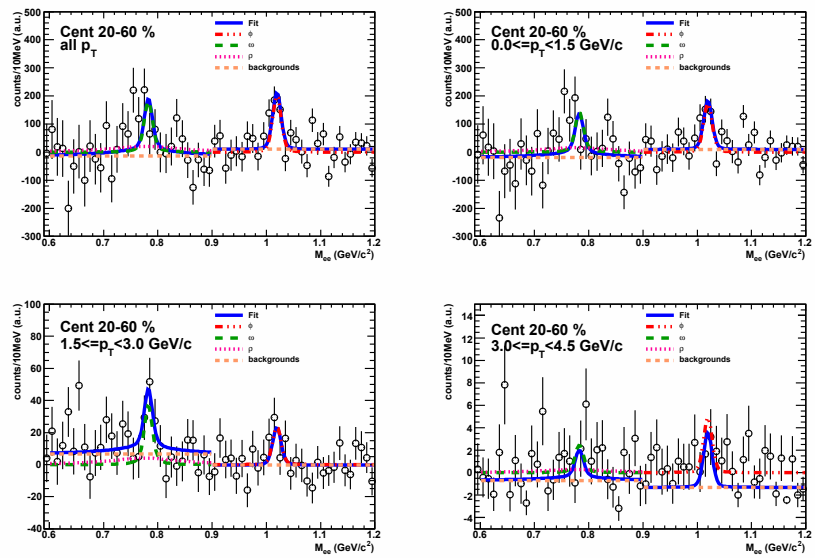

Figure 4.51: The invariant mass spectra of the di-electrons after subtracting the event mixing distribution at the centrality class of 20-60%

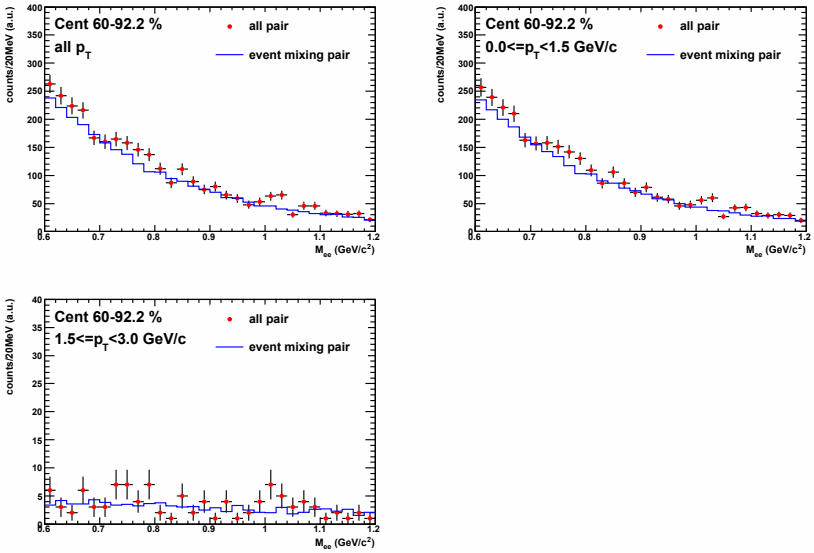

Figure 4.52: The invariant mass spectra of the di-electrons at the centrality class of 60-92.2%.

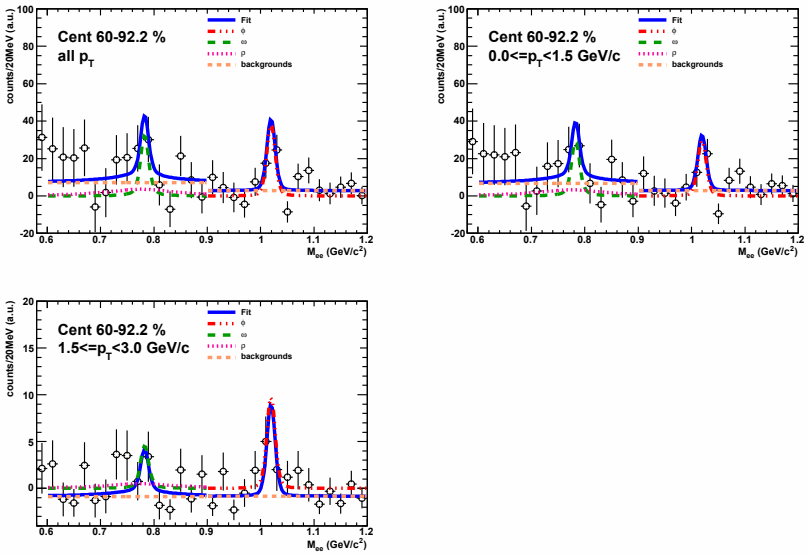

Figure 4.53: The invariant mass spectra of the di-electrons after subtracting event mixing distribution at the centrality class of 60-92.2%

4.7.5 Efficiency calculation

Monte Carlo simulation

The efficiency study is performed by the Monte Carlo simulation. The production and the decay kinematics are simulated by the single event generator called "EXODUS". The ω and ϕ mesons are singly generated and decay into e^+e^-. The parent particles are uniformly generated at the rapidity range of $|y| < 0.5$ and at the ZVertex of $|z| < 25$ cm. The azimuthal angle is isotropically distributed in $0 < \phi < 2\pi$. The input transverse momentum spectra are determined based on the Tsalis fit to the measured $\phi \to K^+K^-$ data [188, 189, 190] for ϕ mesons. The spectra of ω mesons are assumed to be the same shape in p+p 200 GeV [191, 192, 193, 194, 195]. The consistency between the spectrum shape by the fit and the $\omega \to \pi^0\gamma$ data [196, 197] in Au+Au 200 GeV is confirmed. They are shown in Fig.4.54. The particle generation is performed at $0 < p_T < 5$ GeV/c, which covers measurable p_T range in analyzed luminosity.

The simulation of the PHENIX detection system is performed with the PISA (PHENIX Integrated Simulation Application), which is based on the GEANT code. The PISA simulation simulates the interaction between the generating particles and the materials of the concrete detector system, and traces all physics processes. The real detector performance such as spacial and energy resolution, active area, track reconstruction and so forth are implemented in the simulation. The real detector conditions in the reference run (i.e. run 120496 in run group G8) are implemented in the simulation. Therefore, the PISA simulation is essentially equivalent to the real experiment.

Pair detection efficiency

The pair detection efficiency of light vector mesons is defined by

$$\epsilon_{pair}\left(p_T\right) = \epsilon_{geo}\left(p_T\right) \cdot \epsilon_{rec}\left(p_T\right) \cdot \epsilon_{trk}\left(p_T\right), \tag{4.38}$$

where $\epsilon_{geo}\left(p_T\right)$, $\epsilon_{rec}\left(p_T\right)$, $\epsilon_{trk}\left(p_T\right)$ are the geometrical acceptance, the reconstruction efficiency of di-electrons, the efficiency of track selection. The efficiency of track selection includes the requirement of the track quality and electron identification. The pair detection efficiency is calculated by the PISA simulation. The left plot in Fig 4.55 shows the generating p_T spectra (tagged as "input") and the reconstructed p_T spectra (tagged as "output"). The right plot in Fig.4.55 shows the pair detection efficiency.

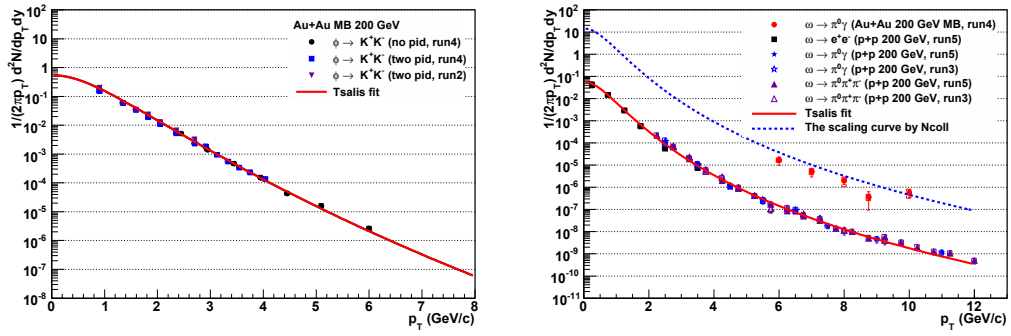

Figure 4.54: The input p_T spectrum for ϕ meson (left) and for ω meson (right). The p_T spectrum of ϕ meson is determined by directly fitting with Tsalis function to the $\phi \rightarrow K^+K^-$ data [188, 189, 190]. For ω mesons, the spectrum shape is determined by the fit to the data in p+p 200 GeV [191, 192, 193, 194, 195]. The fitting curve is scaled by the N_{coll} and the consistency between the scaling curve and the $\omega \rightarrow \pi^0\gamma$ data in Au+Au 200 GeV [196, 197] can be confirmed in the plot.

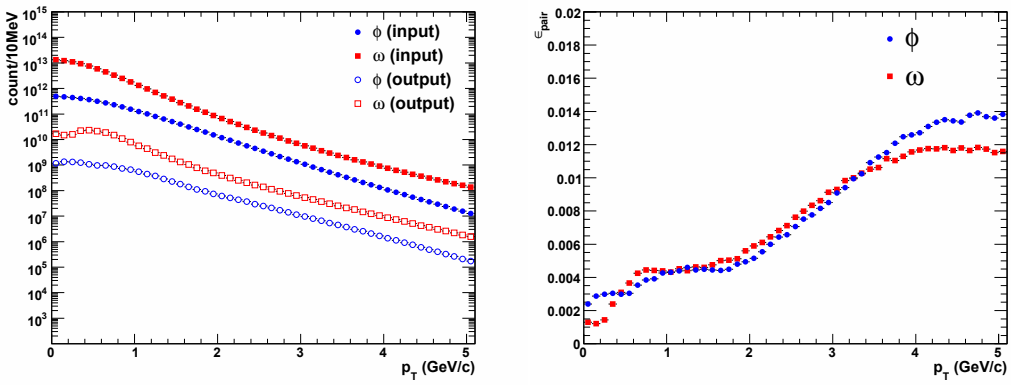

Figure 4.55: The left figure shows the input and output p_T spectra for ϕ and ω mesons. The input spectra are consistent with the Tsalis curve shown in Fig.4.54. The output spectra are obtained by considering the PHENIX geometrical coverage, the reconstruction efficiency, the requirements of track quality and electron identification. The right figure is the pair detection efficiency for ϕ and ω meson as a function of pair p_T.

Multiplicity dependent efficiency

The mass shape for di-electrons is smeared by multiply entering the detector even if there is no mass shift from the physics process. Its effect results in

inefficiency of di-electron pairs in the signal mass region. The multiplicity dependent efficiency is calculated by the embedding simulation, which is performed by embedding simulated signal di-electron pairs (i.e. $\phi/\omega \to e^+e^-$) into the real data. Table 4.10 is the results of multiplicity dependent efficiencies for ϕ mesons.

Centrality	ϵ_{e^+}	ϵ_{e^-}	$\epsilon_{e^+e^-}$
MB	0.9099 ± 0.0172	0.9099 ± 0.0172	0.8360 ± 0.0220
0-10	0.8700 ± 0.0482	0.8712 ± 0.0509	0.7577 ± 0.0611
10-20	0.8722 ± 0.0492	0.8914 ± 0.0512	0.7775 ± 0.0626
20-30	0.9661 ± 0.0541	0.8545 ± 0.0493	0.8255 ± 0.0663
30-40	0.9038 ± 0.0516	0.9512 ± 0.0548	0.8598 ± 0.0698
40-50	0.9172 ± 0.0505	0.9124 ± 0.0518	0.8369 ± 0.0661
50-60	0.9269 ± 0.0521	0.9365 ± 0.0537	0.8680 ± 0.0696
60-70	0.9382 ± 0.0529	0.9343 ± 0.0538	0.8766 ± 0.0707
70-80	0.9283 ± 0.0546	0.8982 ± 0.0571	0.8339 ± 0.0686
80-94	0.9432 ± 0.0252	0.9361 ± 0.0089	0.8950 ± 0.0223

Table 4.10: The multiplicity dependent efficiencies for di-electrons for ϕ mesons.

4.7.6 The invariant yield of ϕ and ω meson

The invariant yield as a function of p_T for a given p_T bin at a given centrality class for ϕ and ω meson is obtained by

$$\begin{aligned} \frac{1}{2\pi p_T}\frac{d^2N\left(\text{cent}\right)}{dydp_T} &= \frac{1}{2\pi p_T N_{event}\left(\text{cent}\right)}\frac{1}{BR}\frac{1}{\epsilon\left(p_T,\text{cent}\right)}\frac{N\left(\Delta p_T,\text{cent}\right)}{\Delta y\Delta p_T}, \\ \epsilon\left(p_T,\text{cent}\right) &= \epsilon_{pair}\left(p_T\right)\cdot\epsilon_{mul}\left(\text{cent}\right)\cdot CF_{run}, \end{aligned} \tag{4.39}$$

where $N_{event}\left(\text{cent}\right)$ is the number of events for the given centrality class. BR is the branching ratios to di-electron decay for ϕ mesons and ω mesons. $\epsilon_{pair}\left(p_T\right)$ is the pair detection efficiency including acceptance, pair reconstruction and track selection. $\epsilon_{mul}\left(\text{cent}\right)$ is the multiplicity dependent efficiency. CF_{run} is the correction factor of the run-by-run pair fluctuation with respect to the reference run[12].

[12]The detector condition in the reference run is applied to the PISA simulation. Therefore the additional correction is applied to the results.

Bin shift correction

The extracted yield of a given finite p_T bin at the bin center introduces a wrong result in case the spectra is not flat such as exponentially falling spectra. Therefore the data points should be shifted to the correct points. There are two possibilities to get the true p_T spectra.

Method (A) move the data point vertically by fixing the p_T of the data point.
Step(1) Fit the uncorrected data points with the function $f(p_T)$.
Step(2) Calculate the ratio r between the average yield in this p_T bin and the value of the function at the bin center p_T^c as follows.

$$r = \frac{\int_{p_T^c-\Delta/2}^{p_T^c+\Delta/2} f(p_T)\, dp_T}{\Delta \cdot f(p_T)} \tag{4.40}$$

where Δ is the bin width.
Step(3) Calculate the corrected yield via the ratio r.

$$\left.\frac{dN}{dp_T}\right|_{corrected} = \frac{1}{r}\left.\frac{dN}{dp_T}\right|_{uncorrected} \tag{4.41}$$

Method (B) move the data point along the p_T axis by fixing.
Step(1) Fit the uncorrected data points with the function $f(p_T)$.
Step(2) Take the value $f(\bar{p_T})$ to correspond to the average yield in the bin, that is,

$$f(\bar{p}_T) = \frac{1}{\Delta}\int_{p_T^c-\Delta/2}^{p_T^c+\Delta/2} f(p_T)\, dp_T \tag{4.42}$$

where $\bar{p}_T$ is correct p_T, which is the weighted average p_T in a p_T bin.
Step(3) Calculate correct p_T.
If $f(p_T)$ is an exponential function, that is, $f(p_T) \propto \exp(-p_T/T)$, the solution is

$$\bar{p}_T = p_T^c - \frac{1}{24}\frac{\Delta^2}{T} \tag{4.43}$$

In this analysis, we applied the method (A) for the bin shift correction. The bin shift correction is performed with the following fitting function.

$$f(m_T) = \mathrm{N}\exp(-m_T/T), \tag{4.44}$$

where N and T are the parameters. The total energy of a particle is approximately equal to m_T at mid-rapidity. The exponential behavior is seen as a

function of m_T rather than p_T. That is why m_T instead of p_T is applied to the bin shift correction in this analysis. Figure 4.56 and 4.57 are the comparisons between the uncorrected spectra and the corrected ones for ϕ and ω meson, respectively. The correction is iteratively performed. The correction is clearly converged after a few tries in both figures.

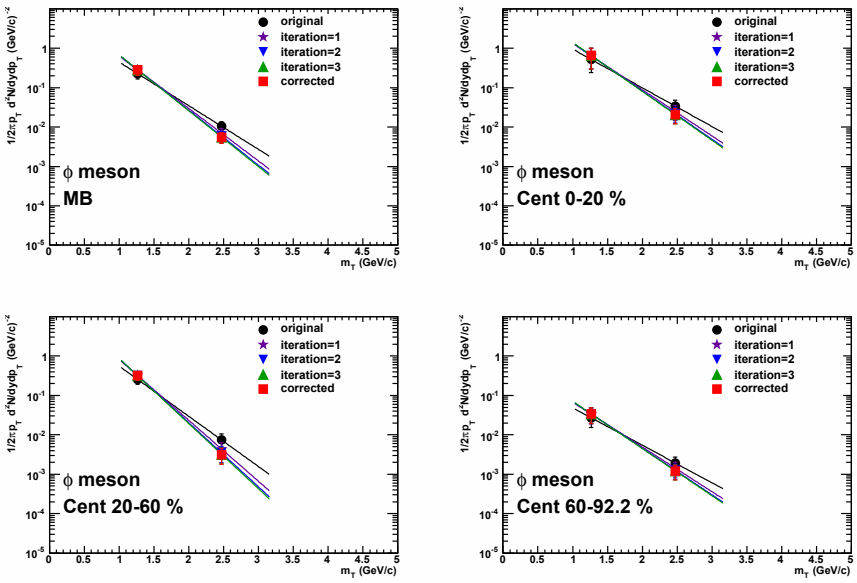

Figure 4.56: Bin shift correction for ϕ meson.

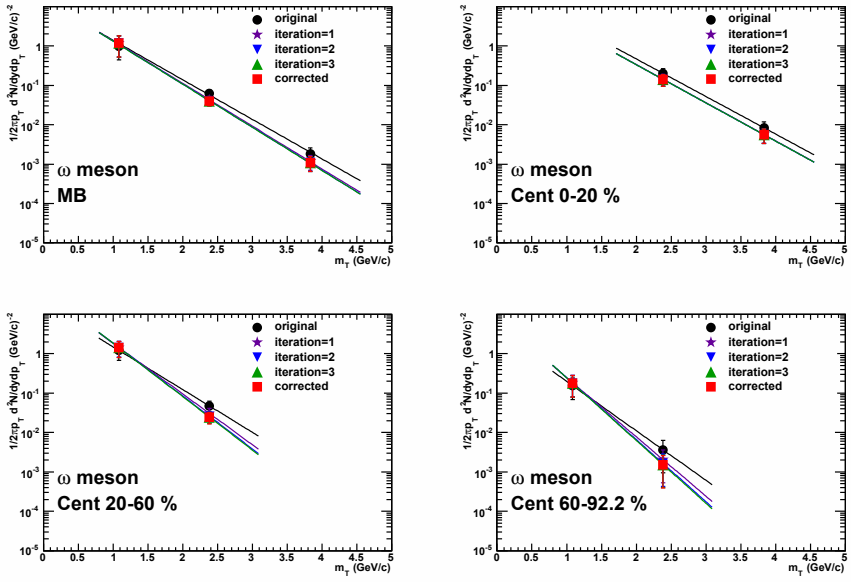

Figure 4.57: Bin shift correction for ω meson.

4.8 Systematic study

The systematic error is defined by

$$\text{Sys.Err.} = \frac{2 \times D_{\max}}{\sqrt{12}}, \tag{4.45}$$

where $D_{\max}$ is the largest deviation in all possible cases. This definition is based on the standard deviation suppose the distribution follows the uniform function. Each deviation is defined by the difference between the result given in the basic analysis procedure and that in an arbitrary case. This assumption gives a conservative consequence as a systematic error but it is reasonable if the number of possible cases is very limited. The classification and the evaluation for each systematic study are listed below.

Run-by-run fluctuation

The uncertainty of the run-by-run pair efficiency is estimated by the fluctuation of the each run group with respect to the reference run group G8[13]. The systematic error of the run-by-run pair efficiency is 10.1%.

Acceptance

The difference of the acceptance between the real data and the simulation should be taken into account. The systematic error from the acceptance mismatch comes from the uncertainty of the normalization between the real data and the simulation. The normalization is performed by the integration in six kinds of ϕ ranges: $-0.54 < \phi < -0.40$ rad, $0.30 < \phi < 0.21$ rad, $0.0 < \phi < 0.1$ rad, $0.48 < \phi < 0.57$ rad, $2.52 < \phi < 2.61$ rad and $3.26 < \phi < 3.41$ rad. The systematic error from the acceptance mismatch is 5.2%.

eID

The systematic errors of the eID parameters are well studied by the single electron analysis. The systematic errors for the eID parameters are summarized in Table 4.11.

Input p_T spectra of the simulation

The uncertainty of the input p_T spectra for the efficiency calculation is estimated by the two types of the functions. The Tsallis function and the flat distribution are assumed. The systematic errors are shown in Table 4.12.

[13]The definition of the run group are explained in Chaper 3

n_0	$chi2/npe0$	$disp$	$emcsdz_e \oplus emcsdphi_e$	dep	Total
7 %	1 %	5 %	1.4 %	1 %	8.8 %

Table 4.11: The systematic errors from the electron identification [198].

p_T range	ω meson	ϕ meson
$0 < p_T \leq 1.5$ GeV/c	12.7 %	3.7 %
$1.5 < p_T \leq 3.0$ GeV/c	6.5 %	6.4 %
$3.0 < p_T \leq 4.5$ GeV/c	3.5 %	1.8 %

Table 4.12: The systematic errors from the uncertainty of the input p_T spectra.

Normalization

The uncertainty of the normalization is estimated by the numerical simulation [14]. The difference between the true combinatorial backgrounds and the estimated event-mixing ones with the normalization factor of $2\sqrt{N_{++}N_{--}}/N_{+-}^{mix}$ is distributed to 0.05 to 0.30 % in central Au+Au collisions, depending on the detector conditions such as the amount of the detector materials and the purity of electrons. Therefore the uncertainty of 0.3% is assumed for the evaluation of the systematic error. The systematic errors of the normalization factor are summarized in Table 4.13.

Residual background shape

The correlated backgrounds such as $c\bar{c} \to e^+e^-$ are estimated by the empirical fits. The uncertainty of the correlated background shape is evaluated under the assumption that the residual background shape is constant, the first-order polynomial function and the exponential functions. The systematic errors are summarized in Table 4.14.

Signal extraction

The systematic errors are evaluated by fitting the Breit-Wigner function, fitting the relativistic Breit-Wigner function and directly counting the data. The yield of the correlated backgrounds is estimated by the fits. The estimated background level is used in counting the signals. The systematic errors are in Table 4.15.

[14]The simulation can estimate the true combinatorial backgrounds under consideration of the detector performance. The details of the simulation are explained in Chapter 5.

Centrality	p_T range	ω meson	ϕ meson
MB	all p_T	2.1 %	1.2 %
	$0 < p_T \leq 1.5$ GeV/c	3.0 %	1.4 %
	$1.5 < p_T \leq 3.0$ GeV/c	< 1.0 %	< 1.0 %
	$3.0 < p_T \leq 4.5$ GeV/c	< 1.0 %	-
0-20 %	all p_T	3.6 %	1.9 %
	$0 < p_T \leq 1.5$ GeV/c	-	2.5 %
	$1.5 < p_T \leq 3.0$ GeV/c	< 1.0 %	< 1.0 %
	$3.0 < p_T \leq 4.5$ GeV/c	< 1.0 %	-
20-60 %	all p_T	1.0 %	< 1.0 %
	$0 < p_T \leq 1.5$ GeV/c	1.0 %	1.0 %
	$1.5 < p_T \leq 3.0$ GeV/c	< 1.0 %	< 1.0 %
60-92.2 %	all p_T	< 1.0 %	< 1.0 %
	$0 < p_T \leq 1.5$ GeV/c	< 1.0 %	< 1.0 %
	$1.5 < p_T \leq 3.0$ GeV/c	< 1.0 %	< 1.0 %

Table 4.13: The systematic errors from the uncertainty of the normalization factor for ω and ϕ meson.

Centrality	p_T range	ω meson	ϕ meson
MB	all p_T	5.8 %	2.7 %
	$0 < p_T \leq 1.5$ GeV/c	11.8 %	4.6 %
	$1.5 < p_T \leq 3.0$ GeV/c	2.7 %	3.4 %
	$3.0 < p_T \leq 4.5$ GeV/c	4.2 %	-
0-20 %	all p_T	3.0 %	8.1 %
	$0 < p_T \leq 1.5$ GeV/c	-	13.2 %
	$1.5 < p_T \leq 3.0$ GeV/c	1.4 %	5.1 %
	$3.0 < p_T \leq 4.5$ GeV/c	4.2 %	-
20-60 %	all p_T	4.7 %	2.6 %
	$0 < p_T \leq 1.5$ GeV/c	11.0 %	2.7 %
	$1.5 < p_T \leq 3.0$ GeV/c	1.3 %	1.0 %
60-92.2 %	all p_T	12.8 %	1.2 %
	$0 < p_T \leq 1.5$ GeV/c	12.8 %	2.8 %
	$1.5 < p_T \leq 3.0$ GeV/c	4.5 %	1.0 %

Table 4.14: The systematic errors from the uncertainty from the residual background shape for ω and ϕ meson.

The uncertainty of the ρ yield

The uncertainty of the yield for ρ mesons is estimated by assuming three cases: $\rho/\omega = 0.9$, $\rho/\omega = 0.5$ and $\rho/\omega = 0.0$ (i.e. there is no ρ meson.). The

Centrality	p_T range	ω meson	ϕ meson
MB	all p_T	4.0 %	7.4 %
	$0 < p_T \leq 1.5$ GeV/c	1.1 %	16.2 %
	$1.5 < p_T \leq 3.0$ GeV/c	18.0 %	16.2 %
	$3.0 < p_T \leq 4.5$ GeV/c	47.0 %	-
0-20 %	all p_T	33.3 %	27.2 %
	$0 < p_T \leq 1.5$ GeV/c	-	50.0 %
	$1.5 < p_T \leq 3.0$ GeV/c	17.5 %	15.2 %
	$3.0 < p_T \leq 4.5$ GeV/c	36.2 %	-
20-60 %	all p_T	22.7 %	12.3 %
	$0 < p_T \leq 1.5$ GeV/c	34.1 %	12.9 %
	$1.5 < p_T \leq 3.0$ GeV/c	15.8 %	19.6 %
60-92.2 %	all p_T	12.4 %	10.3 %
	$0 < p_T \leq 1.5$ GeV/c	14.5 %	14.6 %
	$1.5 < p_T \leq 3.0$ GeV/c	12.2 %	8.9 %

Table 4.15: The systematic errors from the uncertainty from signal counting for ω and ϕ meson.

case of $\rho/\omega = 0.9$[15] is the baseline to calculate the ω yield. The systematic errors are summarized in Table 4.16.

Bin shift correction

The systematic errors of the fitting function for the binshift correction are evaluated by assuming two types of function: the exponential function and the Tsalis function. The results are shown in Table 4.17

Total systematic errors

Total systematic errors are obtained by the quadratic sum of the errors above and summarized in Table 4.18.

[15]This value is obtained by the production cross section in p+p 200 GeV and the branching ratio to di-electron.

Centrality	p_T range	ω meson
MB	all p_T	3.2 %
	$0 < p_T \leq 1.5$ GeV/c	1.8 %
	$1.5 < p_T \leq 3.0$ GeV/c	8.0 %
	$3.0 < p_T \leq 4.5$ GeV/c	1.0 %
0-20 %	all p_T	9.1 %
	$0 < p_T \leq 1.5$ GeV/c	-
	$1.5 < p_T \leq 3.0$ GeV/c	8.3 %
	$3.0 < p_T \leq 4.5$ GeV/c	1.0 %
20-60 %	all p_T	2.3 %
	$0 < p_T \leq 1.5$ GeV/c	4.8%
	$1.5 < p_T \leq 3.0$ GeV/c	7.6 %
60-92.2 %	all p_T	8.4 %
	$0 < p_T \leq 1.5$ GeV/c	7.9 %
	$1.5 < p_T \leq 3.0$ GeV/c	13.6 %

Table 4.16: The systematic errors from the uncertainty from ρ yield for ω meson.

Centrality	p_T range	ω meson	ϕ meson
MB	$0 < p_T \leq 1.5$ GeV/c	< 1.0 %	< 1.0 %
	$1.5 < p_T \leq 3.0$ GeV/c	1.0 %	2.2 %
	$3.0 < p_T \leq 4.5$ GeV/c	6.0 %	-
0-20 %	$0 < p_T \leq 1.5$ GeV/c	-	< 1.0 %
	$1.5 < p_T \leq 3.0$ GeV/c	2.7 %	1.2 %
	$3.0 < p_T \leq 4.5$ GeV/c	2.6 %	-
20-60 %	$0 < p_T \leq 1.5$ GeV/c	1.3 %	< 1.0 %
	$1.5 < p_T \leq 3.0$ GeV/c	5.6 %	1.8 %
60-92.2 %	$0 < p_T \leq 1.5$ GeV/c	6.1 %	1.2 %
	$1.5 < p_T \leq 3.0$ GeV/c	21.0 %	6.7 %

Table 4.17: The systematic errors from the fitting function for the binshift correction for ω and ϕ meson.

Centrality	p_T range	ω meson	ϕ meson
MB	all p_T	16.5 %	16.4 %
	$0 < p_T \leq 1.5$ GeV/c	22.8 %	22.5 %
	$1.5 < p_T \leq 3.0$ GeV/c	25.4 %	22.9 %
	$3.0 < p_T \leq 4.5$ GeV/c	49.8 %	-
0-20 %	all p_T	37.7 %	31.9 %
	$0 < p_T \leq 1.5$ GeV/c	-	53.9 %
	$1.5 < p_T \leq 3.0$ GeV/c	25.2 %	22.5 %
	$3.0 < p_T \leq 4.5$ GeV/c	39.4 %	-
20-60 %	all p_T	27.4 %	19.1 %
	$0 < p_T \leq 1.5$ GeV/c	41.0 %	19.9 %
	$1.5 < p_T \leq 3.0$ GeV/c	24.3 %	25.2 %
60-92.2 %	all p_T	24.4 %	17.7 %
	$0 < p_T \leq 1.5$ GeV/c	29.0 %	21.0 %
	$1.5 < p_T \leq 3.0$ GeV/c	32.3 %	19.3 %

Table 4.18: The total systematic errors for a given centrality in p_T bins for ϕ meson and ω meson.

Chapter 5

Results of the data analysis

5.1 The invariant transverse momentum spectra and the particle production

The underlying physics in heavy-ion collisions are different from the momentum range of particles. According to the pQCD, the particle production in the high p_T region is described by the power-law function. The modified power-law function, which has good agreement with the production of ϕ and ω mesons in p+p collisions at $\sqrt{s} = 200$ GeV, is described as

$$\frac{1}{2\pi p_T}\frac{d^2N}{dydp_T} = N\left(1+\frac{p_T}{b}\right)^{-n}, \tag{5.1}$$

where N is a normalization factor. b and n are the parameters of this function.

On the other hand, the particle production in the low p_T region is dominantly caused by thermal or thermal-like processes. Therefore, the data are well described by an exponential function as follows.

$$\frac{1}{2\pi p_T}\frac{d^2N}{dydp_T} = \frac{1}{2\pi T^2}\frac{dN}{dy}\exp\left(-p_T/T\right), \tag{5.2}$$

where T is the inverse slope parameter of the function.

The Tsallis function [135] is widely used for explaining the properties of the particle production. At midrapidity, the total energy of each particle is approximately represented by transverse mass, $m_T = \sqrt{p_T^2 + m_0^2}$ (m_0 is rest mass of a particle). The Tsallis function is formulated as a function of m_T as follows.

$$\frac{1}{2\pi p_T}\frac{d^2N}{dydp_T} = \frac{1}{2\pi}\frac{dN}{dy}\frac{(n-1)(n-2)}{(nT+m_0(n-1))(nT+m_0)}\left(\frac{nT+m_T}{nT+m_0}\right)^{-n}, \tag{5.3}$$

where $n = -1/(1-q)$, and dN/dy is the inclusive yield over all p_T range at midrapidity. Equation (5.3) simultaneously represents the power-law behavior at high p_T and the exponential behavior at low p_T by the two parameters q and T.

In the limit of $m_0 \to 0$, Eq.(5.3) becomes

$$\frac{1}{2\pi p_T}\frac{d^2N}{dydp_T} = \frac{1}{2\pi}\frac{dN}{dy}\frac{(n-1)(n-2)}{(nT)^2}\left(1+\frac{p_T}{nT}\right)^{-n}. \tag{5.4}$$

Equation (5.4) is essentially equivalent to the modified power-law function in Eq.(5.1).

In the limit of $m_0 \to 0$ and $q \to 1$ (i.e. $n \to -\infty$), Eq. (5.3) becomes

$$\frac{1}{2\pi p_T}\frac{d^2N}{dydp_T} = N\exp\left(-p_T/T\right), \tag{5.5}$$

where N is a normalization factor. Equation (5.5) is similar to Eq.(5.2). The slope parameter T characterizes the thermal-like production of the particles.

Figure 5.1-5.8 are the invariant yield of ϕ and ω meson as a function of transverse momentum at the centrality class of 0-92.2% (MB), 0-20%, 20-60% and 60-92.2%. The spectrum shape is characterized by the parameters of three types of the fitting function: The modified power-law function, the exponential function and the Tsallis function. The fitting parameters are summarized in Table 5.1 to 5.4.

The inclusive yields of the light vector mesons at midrapidity, dN/dy, are estimated by three methods: the direct count of the signals, the estimation with Tsallis fit and the estimation with exponential fit. The results are summarized in Table 5.5.

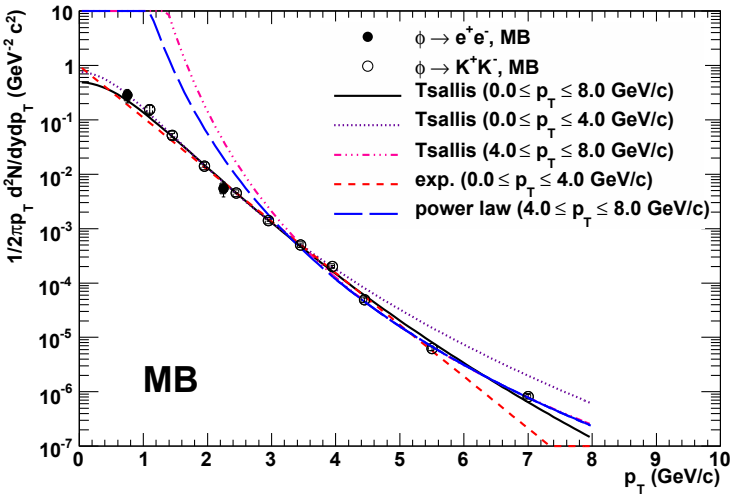

Figure 5.1: The invariant yield as a function of transverse momentum for ϕ meson at the centrality class of 0-92.2 % (MB). The error bars and the brackets in the figure show the statistical errors and systematic errors, respectively. The data points of $\phi \to K^+K^-$ are cited from the reference [132].

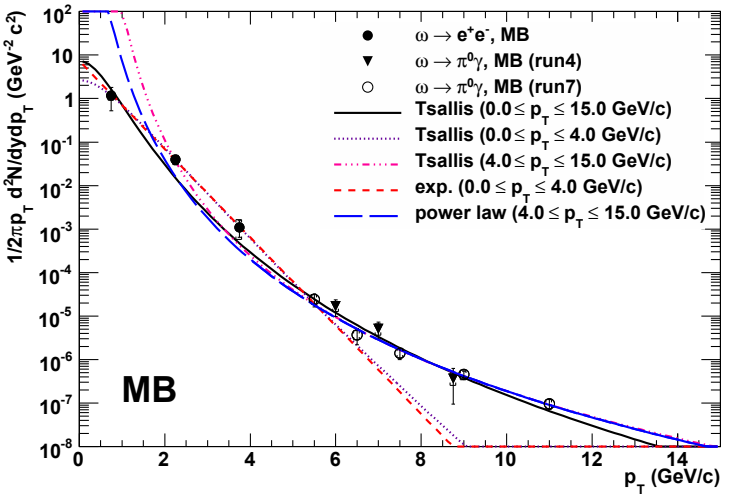

Figure 5.2: The invariant yield as a function of transverse momentum for ω meson at the centrality class of 0-92.2 % (MB). The error bars and the brackets in the figure show the statistical errors and systematic errors, respectively. The data points of $\omega \to \pi^0\gamma$ are cited from the reference [133].

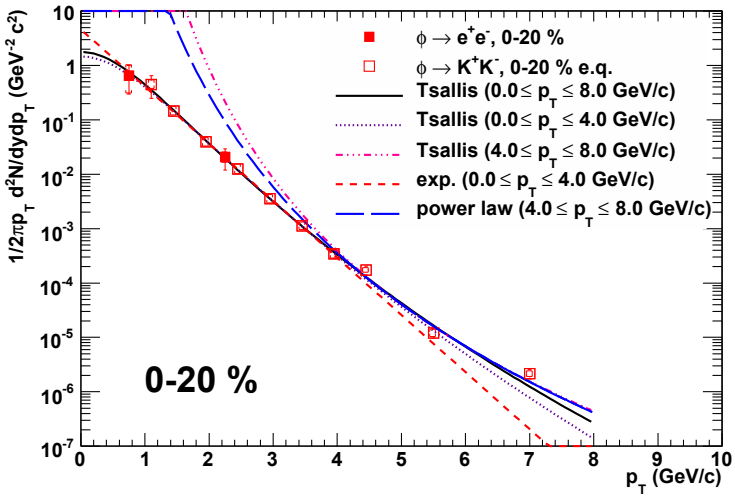

Figure 5.3: The invariant yield as a function of transverse momentum for ϕ meson at the centrality class of 0-20 %. The error bars and the brackets in the figure show the statistical errors and systematic errors, respectively. The data points of $\phi \to K^+K^-$ are cited from the reference [132].

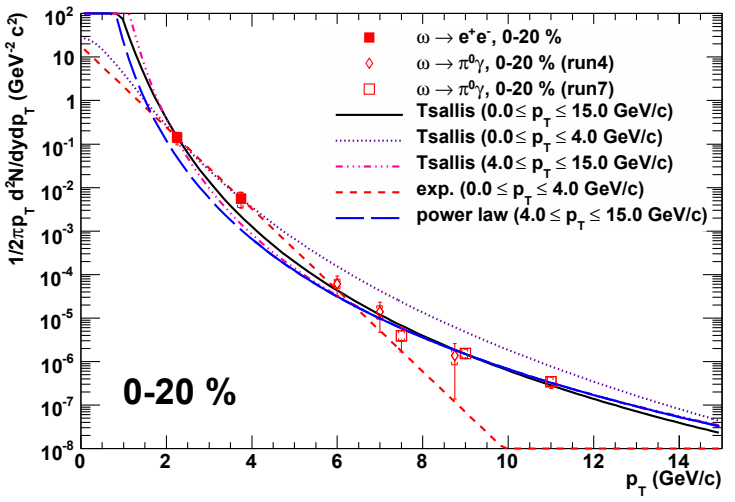

Figure 5.4: The invariant yield as a function of transverse momentum for ω meson at the centrality class of 0-20 %. The error bars and the brackets in the figure show the statistical errors and systematic errors, respectively. The data points of $\omega \to \pi^0\gamma$ are cited from the reference [133].

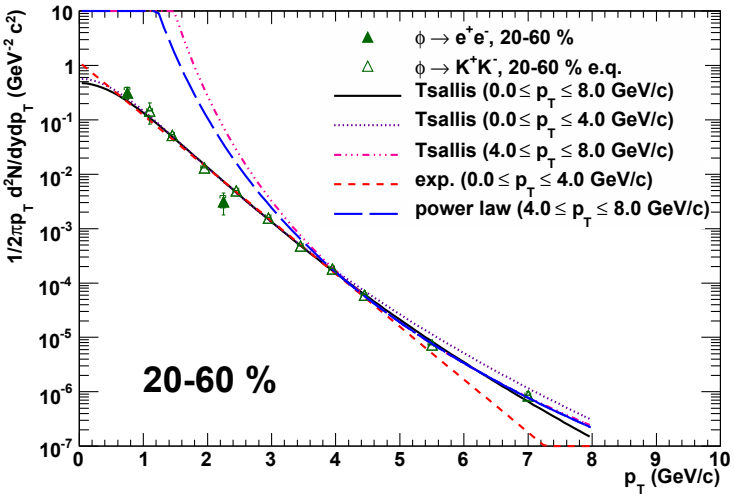

Figure 5.5: The invariant yield as a function of transverse momentum for ϕ meson at the centrality class of 20-60 %. The error bars and the brackets in the figure show the statistical errors and systematic errors, respectively. The data points of $\phi \to K^+K^-$ are cited from the reference [132].

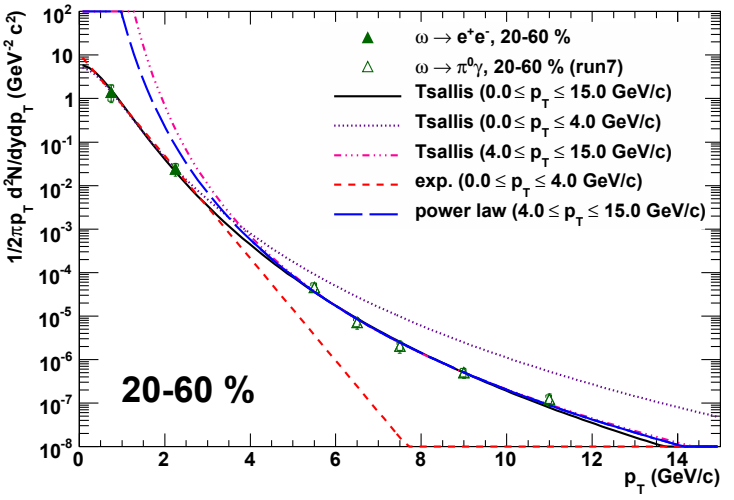

Figure 5.6: The invariant yield as a function of transverse momentum for ω meson at the centrality class of 20-60 %. The error bars and the brackets in the figure show the statistical errors and systematic errors, respectively. The data points of $\omega \to \pi^0\gamma$ are cited from the reference [133].

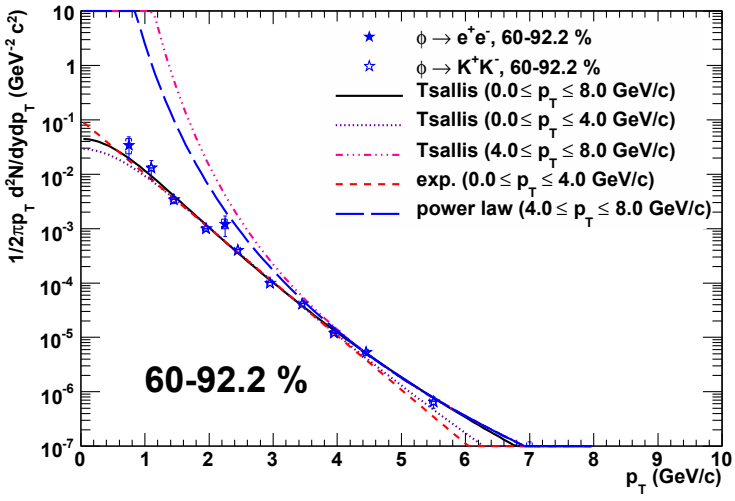

Figure 5.7: The invariant yield as a function of transverse momentum for ϕ meson at the centrality class of 60-92.2 %. The error bars and the brackets in the figure show the statistical errors and systematic errors, respectively. The data points of $\phi \to K^+K^-$ are cited from the reference [132].

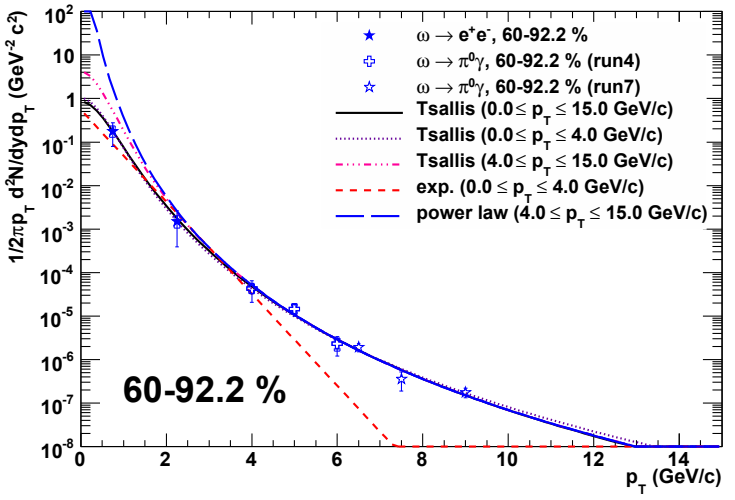

Figure 5.8: The invariant yield as a function of transverse momentum for ω meson at the centrality class of 60-92.2 %. The error bars and the brackets in the figure show the statistical errors and systematic errors, respectively. The data points of $\omega \to \pi^0\gamma$ are cited from the reference [133].

Particle	Function	Fitting range	T (GeV)	n
ϕ meson	Tsallis	$0.0 \leq p_T \leq 4.0$ GeV/c	0.158 ± 0.028	-
		$4.0 \leq p_T \leq 8.0$ GeV/c	-	7.65 ± 0.24
	Exponential	$0.0 \leq p_T \leq 4.0$ GeV/c	0.456 ± 0.004	-
	Power-law	$4.0 \leq p_T \leq 8.0$ GeV/c	-	9.06 ± 0.30
ω meson	Tsallis	$4.0 \leq p_T \leq 15.0$ GeV/c	-	6.97 ± 0.53
	Exponential	$0.0 \leq p_T \leq 4.0$ GeV/c	0.427 ± 0.050	-
	Power-law	$4.0 \leq p_T \leq 15.0$ GeV/c	-	7.65 ± 0.59

Table 5.1: The comparison of the parameters among Tsallis fit, exponential fit and power-low fit at the centrality class of 0-92.2 % (MB).

Particle	Function	Fitting range	T (GeV)	n
ϕ meson	Tsallis	$0.0 \leq p_T \leq 4.0$ GeV/c	0.268 ± 0.072	-
		$4.0 \leq p_T \leq 8.0$ GeV/c	-	8.31 ± 1.10
	Exponential	$0.0 \leq p_T \leq 4.0$ GeV/c	0.413 ± 0.012	-
	Power-law	$4.0 \leq p_T \leq 8.0$ GeV/c	-	9.87 ± 1.04
ω meson	Tsallis	$4.0 \leq p_T \leq 15.0$ GeV/c	-	6.94 ± 0.78
	Exponential	$0.0 \leq p_T \leq 4.0$ GeV/c	0.464 ± 0.067	-
	Power-law	$4.0 \leq p_T \leq 15.0$ GeV/c	-	7.53 ± 1.15

Table 5.2: The comparison of the parameters among Tsallis fit, exponential fit and power-low fit at the centrality class of 0-20 % (Central).

Particle	Function	Fitting range	T (GeV)	n
ϕ meson	Tsallis	$0.0 \leq p_T \leq 4.0$ GeV/c	0.215 ± 0.052	-
		$4.0 \leq p_T \leq 8.0$ GeV/c	-	8.07 ± 0.51
	Exponential	$0.0 \leq p_T \leq 4.0$ GeV/c	0.447 ± 0.007	-
	Power-law	$4.0 \leq p_T \leq 8.0$ GeV/c	-	7.86 ± 0.62
ω meson	Tsallis	$4.0 \leq p_T \leq 15.0$ GeV/c	-	9.61 ± 0.60
	Exponential	$0.0 \leq p_T \leq 4.0$ GeV/c	0.369 ± 0.050	-
	Power-law	$4.0 \leq p_T \leq 15.0$ GeV/c	-	8.69 ± 0.67

Table 5.3: The comparison of the parameters among Tsallis fit, exponential fit and power-low fit at the centrality class of 20-60 % (Semi-central).

5.2 Conclusions for the mass modification of the light vector mesons

The mass modification is discussed from the viewpoints of the mass spectrum shape and the branching ratio. The change of the mass spectrum shape is

Particle	Function	Fitting range	T (GeV)	n
ϕ meson	Tsallis	$0.0 \leq p_T \leq 4.0$ GeV/c	0.320 ± 0.058	-
		$4.0 \leq p_T \leq 8.0$ GeV/c	-	7.55± 0.49
	Exponential	$0.0 \leq p_T \leq 4.0$ GeV/c	0.438 ± 0.006	-
	Power-law	$4.0 \leq p_T \leq 8.0$ GeV/c	-	7.54 ± 0.69
ω meson	Tsallis	$4.0 \leq p_T \leq 15.0$ GeV/c	-	8.98 ± 0.59
	Exponential	$0.0 \leq p_T \leq 4.0$ GeV/c	0.411 ± 0.074	-
	Power-law	$4.0 \leq p_T \leq 15.0$ GeV/c	-	7.66 ± 0.46

Table 5.4: The comparison of the parameters among Tsallis fit, exponential fit and power-low fit at the centrality class of 60-92.2 % (Peripheral).

Particle	Centrality	Method	dN/dy
ϕ meson	MB	Direct counting	1.43 ± 0.33 ± 0.23
		Tsallis ($0.0 \leq p_T \leq 4.0$ GeV/c)	1.72 ± 0.20
		Exponential ($0.5 \leq p_T \leq 4.0$ GeV/c)	1.28 ± 0.05
	0-20 %	Direct counting	3.53 ± 1.47 ± 1.13
		Tsallis ($0.0 \leq p_T \leq 4.0$ GeV/c)	4.02 ± 0.88
		Exponential ($0.5 \leq p_T \leq 4.0$ GeV/c)	4.94 ± 0.60
	20-60 %	Direct counting	1.51 ± 0.32 ± 0.29
		Tsallis ($0.0 \leq p_T \leq 4.0$ GeV/c)	1.48 ± 0.25
		Exponential ($0.5 \leq p_T \leq 4.0$ GeV/c)	1.43 ± 0.10
	60-92.2 %	Direct counting	0.18 ± 0.06 ± 0.03
		Tsallis ($0.0 \leq p_T \leq 4.0$ GeV/c)	0.09 ± 0.02
		Exponential ($0.0 \leq p_T \leq 4.0$ GeV/c)	0.12 ± 0.01
ω meson	MB	Direct counting	5.55 ± 2.12 ± 0.92
		Exponential ($0.0 \leq p_T \leq 4.0$ GeV/c)	8.35 ± 3.11
	0-20 %	Direct counting	13.1 ± 9.6 ± 4.9
		Exponential ($0.0 \leq p_T \leq 4.0$ GeV/c)	24.3 ± 15.6
	20-60 %	Direct counting	6.06 ± 2.06 ± 1.66
		Exponential ($0.0 \leq p_T \leq 4.0$ GeV/c)	9.29 ± 4.10
	60-92.2 %	Direct counting	0.66 ± 0.34 ± 0.16
		Exponential ($0.0 \leq p_T \leq 4.0$ GeV/c)	0.58 ± 0.46

Table 5.5: The inclusive yield at midrapidity for ϕ and ω meson.

a direct signature of the mass modification. The mass spectra are shown in Fig.4.46 to Fig.4.53 in the previous chapter. As a result, the characteristics of the mass spectra are not extracted from the data due to the poverty of the signal-to-background ratios and the statistical significances. So far any clear statement is not made about the mass modification. The signal-to-background ratios and the statistical significances are evaluated at the mass range of $M_{center} \pm 3 \times \sqrt{\Gamma^2 + \sigma_{reso}^2}$ for the centrality class of 0-92.2 % (MB),

0-20 % (Central), 20-60 % (Semi-central) and 60-92.2 % (Peripheral). They are listed in Table 5.6 and Table 5.7.

Centrality	p_T range	ω meson	ϕ meson
MB	all p_T	4.2×10^{-3}	1.3×10^{-2}
	$0 < p_T \leq 1.5$ GeV/c	3.0×10^{-3}	1.1×10^{-2}
	$1.5 < p_T \leq 3.0$ GeV/c	4.2×10^{-2}	4.6×10^{-2}
	$3.0 < p_T \leq 4.5$ GeV/c	1.2×10^{-1}	1.1×10^{-1}
0-20 %	all p_T	2.5×10^{-3}	8.2×10^{-3}
	$0 < p_T \leq 1.5$ GeV/c	1.4×10^{-3}	6.4×10^{-3}
	$1.5 < p_T \leq 3.0$ GeV/c	3.4×10^{-2}	3.7×10^{-2}
	$3.0 < p_T \leq 4.5$ GeV/c	1.5×10^{-1}	5.0×10^{-2}
20-60 %	all p_T	1.1×10^{-2}	3.3×10^{-2}
	$0 < p_T \leq 1.5$ GeV/c	8.5×10^{-3}	3.0×10^{-2}
	$1.5 < p_T \leq 3.0$ GeV/c	6.9×10^{-2}	7.2×10^{-2}
	$3.0 < p_T \leq 4.5$ GeV/c	1.3×10^{-1}	5.7×10^{-1}
60-92.2 %	all p_T	6.7×10^{-2}	2.3×10^{-1}
	$0 < p_T \leq 1.5$ GeV/c	6.2×10^{-2}	1.9×10^{-1}
	$1.5 < p_T \leq 3.0$ GeV/c	3.2×10^{-1}	1.1×10^{-1}

Table 5.6: The signal-to-background ratios for ω and ϕ meson. The number of signals is obtained by the fits. The signal-to-background ratios are evaluated in the mass range of $M_{center} \pm 3 \times \sqrt{\Gamma^2 + \sigma^2_{reso}}$.

The yield fraction between different decay channels indirectly provides the information about the mass modification. Especially the comparison between the yield of $\phi \to e^+e^-$ and $\phi \to K^+K^-$ is important since the branch of $\phi \to K^+K^-$ is expected to be suppressed even in the case of small mass modification due to small Q value, $Q = (M_\phi - 2 \times M_K) \sim 30$ MeV. The change of the branching ratios can be observed as the inconsistency of the yield among difference decay channels, since the invariant yield, which is shown in Fig.5.1 to Fig.5.8, is calculated under the assumption that the branching ratios are the same in vacuum [12]. The results suggest that the invariant yield of $\phi \to e^+e^-$ and $\phi \to K^+K^-$ are consistent with each other within the errors.

In conclusion, any symptom for the mass modifications is not observed in Au+Au collisions at $\sqrt{s_{NN}} = 200$ GeV in current data set. The main origins of the poor signal-to-background ratios and the statistical significances are the residual backgrounds from photon-conversion process and Dalitz-decay process. These backgrounds are removable in the data analysis only if final-state di-electrons are detected as pairs. In most cases, however, one of a pair is out of the PHENIX acceptance and the other is detected. Typical two cases are illustrated in Fig.5.9. The detection efficiency of the background

Centrality	p_T range	ω meson	ϕ meson
MB	all p_T	1.8 σ	3.4 σ
	$0 < p_T \leq 1.5$ GeV/c	1.3 σ	2.8 σ
	$1.5 < p_T \leq 3.0$ GeV/c	3.0 σ	2.5 σ
	$3.0 < p_T \leq 4.5$ GeV/c	1.6 σ	1.0 σ
0-20 %	all p_T	1.0 σ	1.8 σ
	$0 < p_T \leq 1.5$ GeV/c	0.5 σ	1.4 σ
	$1.5 < p_T \leq 3.0$ GeV/c	2.2 σ	1.9 σ
	$3.0 < p_T \leq 4.5$ GeV/c	1.7 σ	0.6 σ
20-60 %	all p_T	2.1 σ	3.6 σ
	$0 < p_T \leq 1.5$ GeV/c	1.6 σ	3.2 σ
	$1.5 < p_T \leq 3.0$ GeV/c	2.3 σ	1.8 σ
	$3.0 < p_T \leq 4.5$ GeV/c	0.8 σ	1.9 σ
60-92.2 %	all p_T	1.5 σ	2.7 σ
	$0 < p_T \leq 1.5$ GeV/c	1.4 σ	2.2 σ
	$1.5 < p_T \leq 3.0$ GeV/c	1.2 σ	2.3 σ

Table 5.7: The statistical significances for ω and ϕ meson. The statistical significances are evaluated in the mass range of $M_{center} \pm 3 \times \sqrt{\Gamma^2 + \sigma^2_{reso}}$.

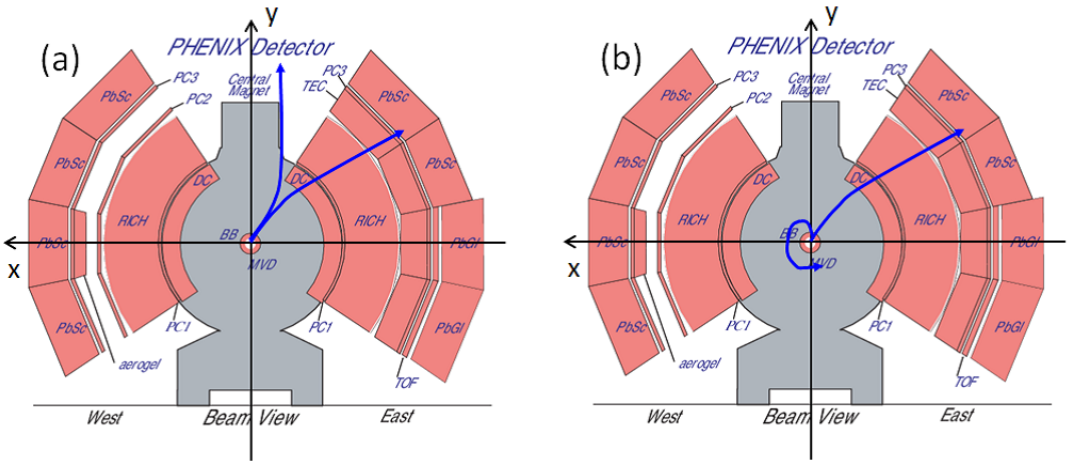

Figure 5.9: (a) One of a pair is going out of the PHENIX acceptance. (b) One of a pair is curling up in a magnetic field.

pairs depends on the coverage of the detection system and a magnetic field. Therefore the detection system should be upgraded to identify the background pairs for the improvement of the signal-to-background ratio.

5.3 Centrality dependence on the particle production

In order to compare the inclusive yield in different collision geometries, the normalization with the number of participant pairs, $0.5 \times N_{part}$ is often used. Since the number of participant pairs is strongly related to participant nucleon density in a nucleus per a collision, this normalization clarifies the linear or nonlinear relation between the data points and the initial-state nuclear effect in a collision. Figure 5.10 shows the inclusive yield normalized by $0.5 \times N_{part}$ for ϕ (top) and ω meson (bottom). The results suggest that the inclusive yield is scaled with the number of participant pairs independent of centrality within the errors.

5.4 Comparisons with p+p collisions at $\sqrt{s} =$ 200 GeV

The inclusive yield as a function of transverse momentum in Au+Au collisions can be compared with those in p+p collisions by scaling with the number of binary collisions, N_{coll}. N_{coll} is a useful indicator whether or not the particle production in a nucleus-nucleus collision is explained by the superposition of a reaction in a nucleon-nucleon collision. Figure 5.11 shows the transverse momentum spectra of ϕ and ω meson at the centrality class of 0-92.2% (MB), 0-20%, 20-60% and 60-92.2%. The scaling curves with N_{coll} are superimposed on the figure. The ratios between the data points and the scaling curves are shown in Fig.5.12 (ϕ meson) and Fig.5.13 (ω meson).

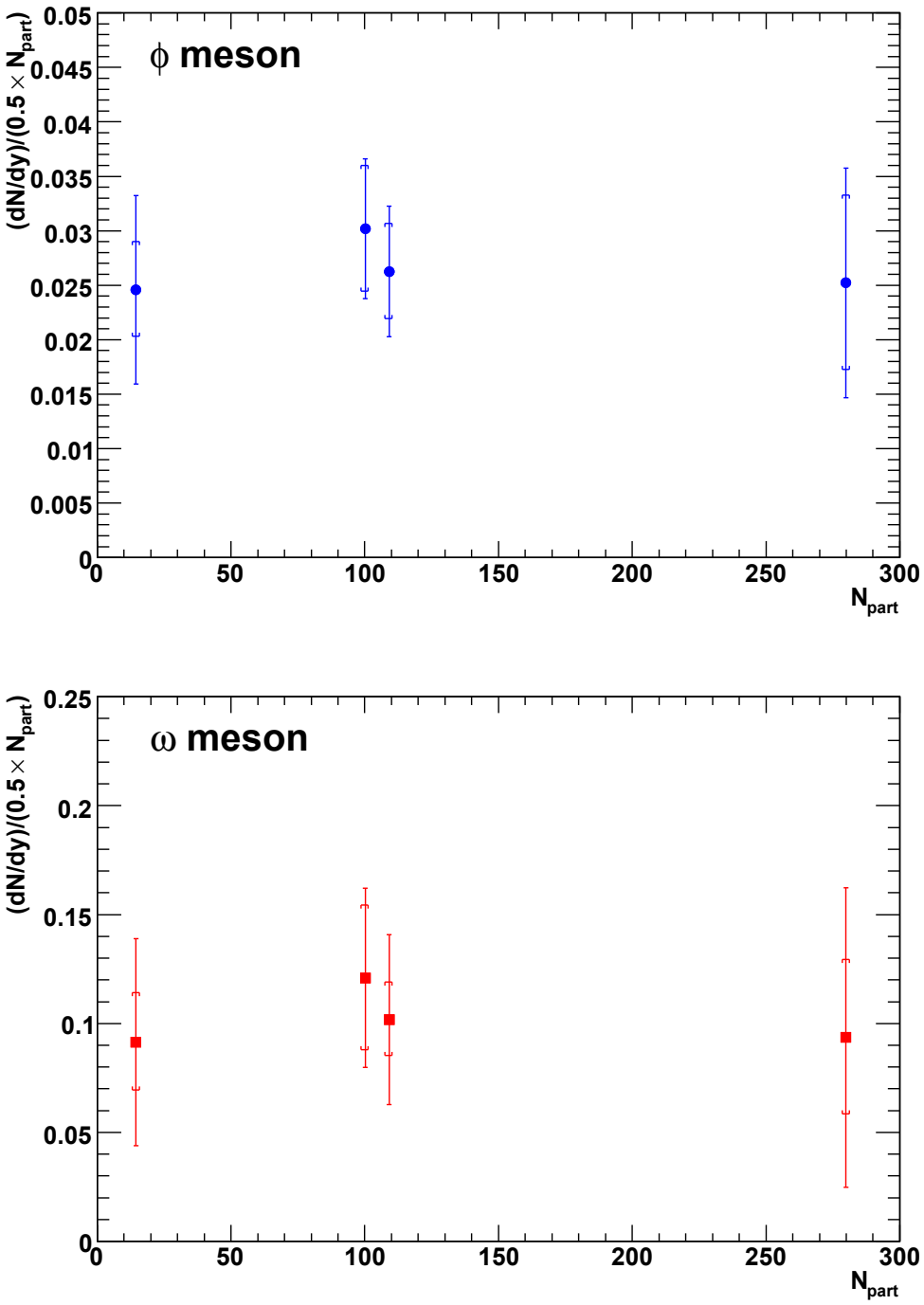

Figure 5.10: The ratio between the data points and the scaling lines with the number of participant nucleon pair, $0.5 \times N_{part}$, for ϕ (top) and ω meson (bottom). The error bars and the brackets in the figure show the statistical errors and systematic errors, respectively.

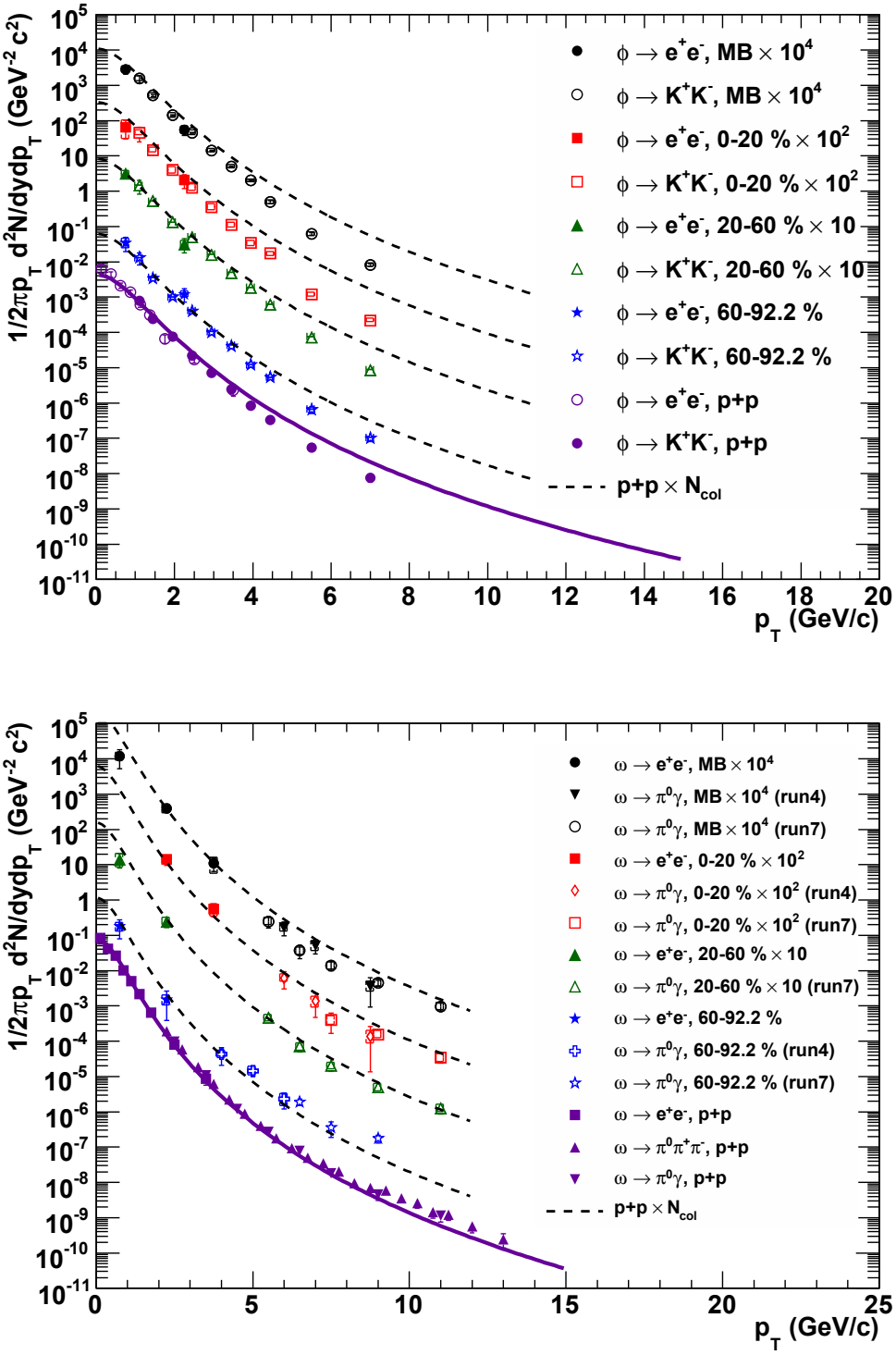

Figure 5.11: The comparison between the invariant transverse momentum spectra and the scaling curves via N_{coll} for ϕ (top) and ω meson (bottom). The scaling curves show the dotted lines. The shape of the curves are obtained from the fitting result to the p+p data [122] (solid line). The error bars and the brackets in the figure show the statistical errors and systematic errors, respectively. The data points of $\phi \to K^+K^-$ and $\omega \to \pi^0\gamma$ are cited from the references [132, 133].

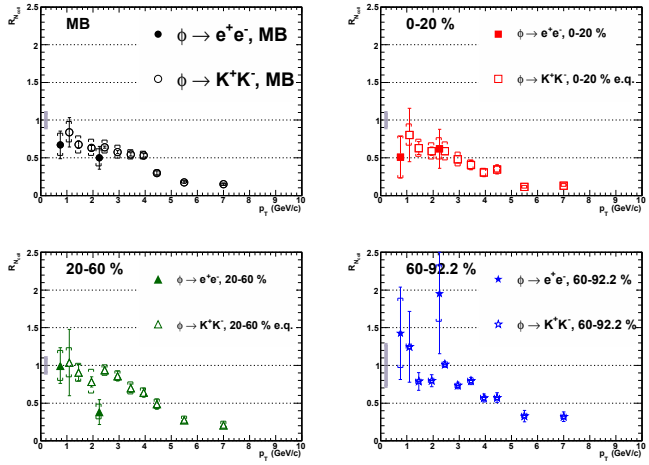

Figure 5.12: The ratios between the data points and the scaling lines of the number of binary collisions, N_{col}, for ϕ mesons. The error bars and the brackets in the figure show the statistical errors and systematic errors, respectively. The data points of $\phi \to K^+K^-$ are cited from the reference [132].

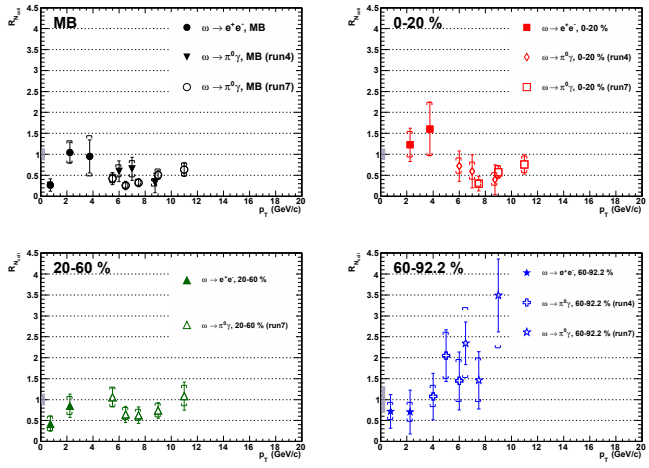

Figure 5.13: The ratios between the data points and the scaling lines of the number of binary collisions, N_{col}, for ω mesons. The error bars and the brackets in the figure show the statistical errors and systematic errors, respectively. The data points of $\omega \to \pi^0\gamma$ are cited from the reference [133].

Chapter 6

Numerical simulation for the feasibility study of di-electron measurement

The numerical simulation has been developed to search the experimental parameter ranges for di-electron measurement in heavy-ion collisions. This simulation takes key issues relevant to the di-electron measurement into account. In this chapter, the framework of the numerical simulation are explained.

6.1 The framework of the numerical simulation

The numerical simulation is developed to estimate the signal-to-background ratios and the statistical significance of light vector mesons via di-electron decays in heavy-ion collisions. Instead of directly simulating the multi-particle production with detailed dynamics in heavy-ion collisions, high multiplicity states are first represented by the form of the total pion multiplicity, $dN_{\pi^0+\pi^\pm}/dy$. The production of the relevant particles other than pions is determined based on the individual production cross sections relative to that of pions as a function of the transverse momentum, p_T. They are evaluated by the measured data points, or the extrapolation via the proper scaling for missing data points. In addition, the key experimental parameters for the di-electron measurement are set as the inputs. As the idealized baseline parameters on the experimental conditions, we choose the following set of parameters:

1. photon conversion probability P_{cnv}: 1%,

2. rejection factor of charged pions $R_{\pi^{\pm}}$, which is defined by the inverse of the probability that charged pions are identified as electrons: 500,
3. geometrical acceptance ϵ_{acc}: 100%,
4. electron tagging efficiency ϵ_{tag}: 100%,
5. transverse momentum threshold p_T^{th}: 0.1 GeV/c,
6. transverse momentum resolution $\sigma_{p_T}^{ref}$ (we quote the ALICE-TPC resolution [200]): $\sqrt{(0.01 \cdot p_T)^2 + (0.0056)^2}$ GeV/c.

Figure 6.1 shows the flowchart of the numerical simulation. The step (1) sets the input parameters above. In the step (2), primary particles are generated with the weights of the invariant p_T spectra. The p_T spectra are provided by the experimental data and the proper scaling for missing data. The details of the input p_T spectra are explained later. Rapidity y of a particle is uniformly generated in $|y| \leq 0.5$ [46, 201]. Primary particles branch into subsequent decay processes according to their branching ratios. The branching ratios are summarized in Table 2.2 of Chapter 2. ϕ, ω and ρ mesons decay into di-electrons through the two-body decay process in the step (3). The phase space of di-electrons from the light vector mesons is determined by the Gounaris-Sakurai model [202]. π^0 and η mesons branch into 2γ or the Dalitz decay process ($\gamma e^+ e^-$) in the step (3) or (4). The decaying γ's are subsequently converted into di-electrons with the given photon-conversion probability in the step (5). Kinematics of di-electron in the photon-conversion process, that is, energy and scattering angle, are simulated by the well-established GEANT algorithm [142, 143, 144]. All photon-conversion points are fixed to the primary vertex points[1]. The phase space of Dalitz decaying di-electrons is determined by the Kroll-Wada formula [136, 137]. The detailed formula is expressed in Chapter 2. Charged kaons decay into electrons through the three-body decay process in the step (6). In the step (7), electrons and positrons from open charms are directly generated to be consistent with the input p_T spectra of single electrons[2] as shown in Fig.6.2. They are randomly generated in azimuth with the branching ratio of 9.5% [127]. A di-electron pair

[1]The contribution to the di-electron background shape depends on where the photon conversion takes place, in other words, depends on the arrangement of the detector materials. They should be considered in association with the track reconstruction algorithms.

[2]The p_T spectrum of single electrons originates from not only charm quarks but also bottom quarks. The contributions from them are calculated by the fixed-order-plus-next-to-leading-log perturbative QCD calculation (FONLL) [203] and its calculation is compared to the measurements [204, 205, 206]. The results suggest that $N_{b\to e}/(N_{c\to e} + N_{b\to e})$ is smaller than 0.2 at $p_T \leq 2.0$ GeV/c in p+p 200 GeV and $N_{b\to e}/N_{c\to e}$ are smaller than 0.3 at $p_T \leq 2.0$ GeV/c in p+p 7 TeV, where $N_{b\to e}$ and $N_{c\to e}$ is the number of electrons from

originating from the open charm production is assumed to be uncorrelated in this simulation. The effect on the correlation is discussed later. Charged pions are identified as electrons with the given probability corresponding to the rejection factor of charge pions in the step (8). At the final stage of the simulation, final-state electrons are filtered by the geometrical acceptance, the electron tagging efficiency and p_T threshold in the step (9).

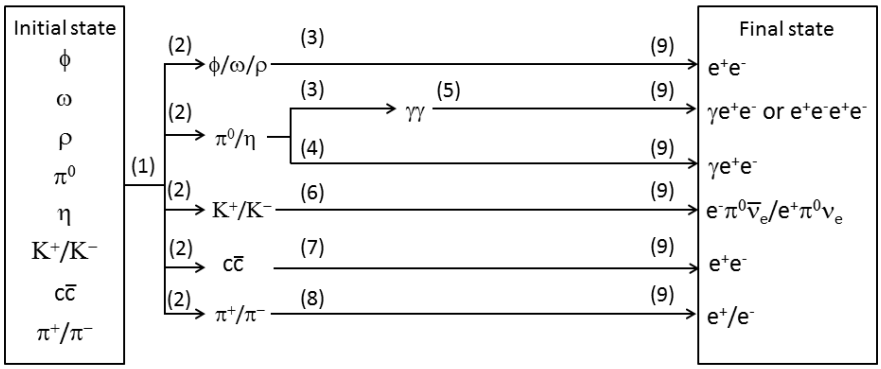

(1) Input parameters : $dN_{\pi^0+\pi^\pm}/dy$, collision specie and energy, the range of rapidity and p_T and experimental parameters (P_{cnv}, $R_{\pi^\pm}$, ε_{acc}, ε_{tag} , p_T^{th} and $\sigma_{p_T}^{ref}$)
(2) Primary particle selection (weighted by the production cross sections and the p_T spectra)
(3) Branching ratio and two-body decay
(4) Branching ratio and Dalitz decay
(5) Photon-conversion process (with the probability of P_{cnv})
(6) Branching ratio and three-body decay
(7) Branching ratio and single electron generation
(8) Electron misidentification (filtered by $R_{\pi^\pm}$)
(9) Acceptance, efficiency and p_T cutoff (filtered by ε_{acc}, ε_{tag} and p_T^{th})

Figure 6.1: The flowchart of the numerical simulation.

The $dN_{\pi^0+\pi^\pm}/dy$ and the invariant p_T spectra are applied to the simulation taking the given collision species and energies into account. The input $dN_{\pi^0+\pi^\pm}/dy$ is estimated by the measured dN_{ch}/dy [46, 47]. $dN_{\pi^0+\pi^\pm}/dy = 6$ is set for the simulation of p+p 7 TeV. The simulated results in p+p 7 TeV are shown as the reference. For central Pb+Pb 5.5 TeV collisions, the $dN_{\pi^0+\pi^\pm}/dy$ is estimated by the extrapolation of the scaling curve as a function of collision energy [47]. The extrapolated $dN_{\pi^0+\pi^\pm}/dy$ corresponds to 2700.

Figure 6.2 shows the invariant p_T spectra in p+p 7 TeV. The p_T spectra of pions, η mesons, ϕ mesons and single electrons are determined by the data

bottom quarks and charm quarks, respectively. These ratios tend to drop rapidly as the p_T reduces. Therefore we neglect the contributions from bottom quarks in the calculation of particle production and decay kinematics in this simulation.

points and the fits. The dotted curves show the p_T spectra of the other hadrons. The spectrum shape is estimated by the m_T scaling based on the π^0 data points, where $m_T = \sqrt{p_T^2 + m_0^2}$ and m_0 is the rest mass of a particle. Their absolute production cross sections are estimated by the inclusive ratios between pions and the other hadrons in p+p 200 GeV. The production cross sections are summarized in the table of Chapter 2. The invariant p_T spectra in p+p 7 TeV are commonly used for the simulations of p+p 7 TeV and Pb+Pb 5.5 TeV, since the relative production cross sections between pions and the other hadrons are expected to be common for both collision systems, as long as the particle production between 7 TeV and 5.5 TeV has little dependence on the collision energy.

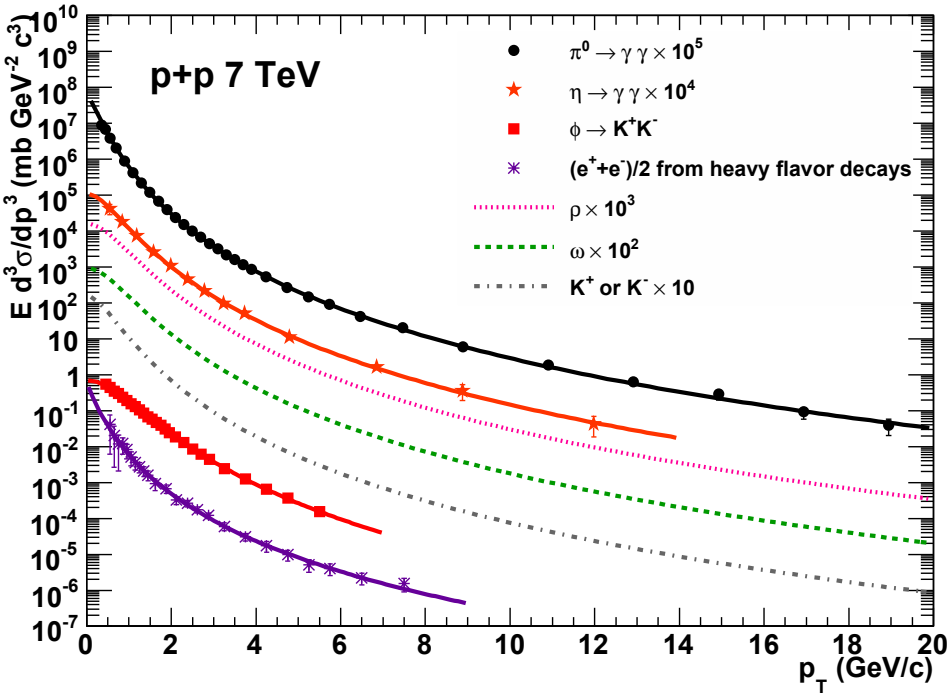

Figure 6.2: The differential cross section in p+p 7 TeV. The data points of π^0/η [207], ϕ [208] and single electrons from heavy flavor decays [209] are shown in this figure. Tsallis fitting curves are depicted as the solid curves. The dotted curves of ρ, ω and $K^{\pm}$ are obtained by assuming the same spectrum shape of π^0 and normalizing the individual production ratios with respect to pions in p+p 200 GeV.

Chapter 7

Measurability of light vector mesons via di-electron in central Pb+Pb collisions at $\sqrt{s_{NN}} = 5.5$ TeV

Feasibility study of the light vector mesons vi di-electron in central Pb+Pb collisions at $\sqrt{s_{NN}} = 5.5$ TeV is performed with the numerical simulation introduced in the previous chapter. The expected transverse momentum spectra of the final-state electrons and the invariant mass spectra for individual sources are shown in Section 7.1 and 7.2. They are simulated for the idealized detection system, that is, the baseline experimental parameters are applied to the simulation. In the Section 7.3, the results of the feasibility study are shown in the forms of the signal-to-backgrounds ratios and the statistical significance for the light vector mesons. At the end of this chapter, the non-trivial effects are discussed.

7.1 The transverse momentum spectra of the final-state electrons with the baseline experimental parameters

Figure 7.1 shows the simulated results of the p_T spectra for the final-state electrons from individual sources with the baseline parameter set in p+p collisions at $\sqrt{s} = 7$ TeV ($dN_{\pi^0+\pi^\pm}/dy = 6$) and central Pb+Pb collisions at $\sqrt{s_{NN}} = 5.5$ TeV ($dN_{\pi^0+\pi^\pm}/dy = 2700$), separately. The parents of electrons are all indicated with different symbols specified inside the plot.

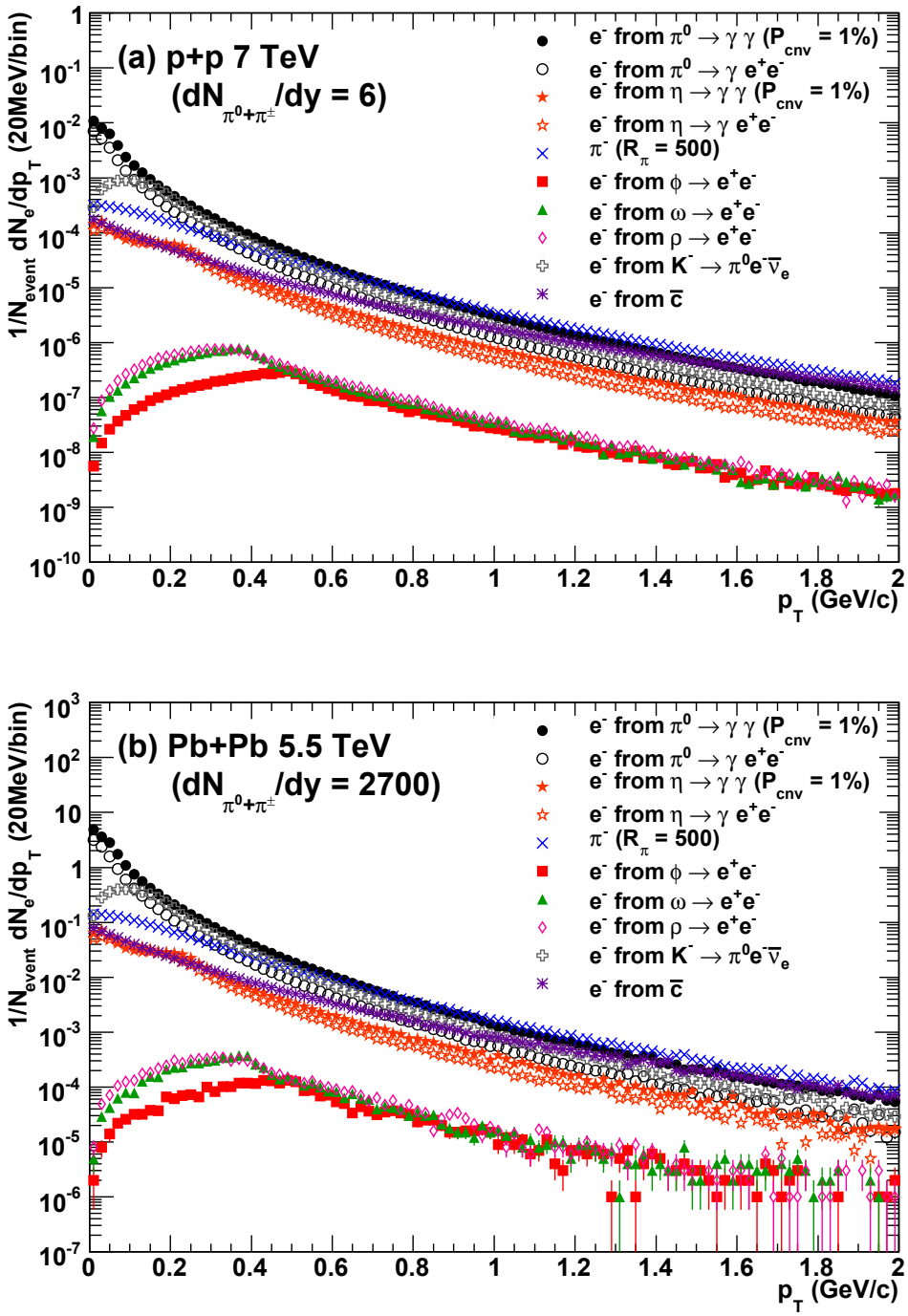

Figure 7.1: The transverse momentum spectra of final-state electrons and misidentified charged pions from individual sources at the pion multiplicities, $dN_{\pi^0+\pi^\pm}/dy = 6$ (panel (a)) and 2700 (panel (b)) with the baseline parameters: $P_{cnv} = 1$ %, $R_{\pi^\pm} = 500$, $\epsilon_{acc} = 100$ %, $\epsilon_{tag} = 100$ %, $\sigma^{ref}_{p_T} = \sqrt{(0.01 \cdot p_T)^2 + (0.0056)^2}$ GeV/c and without p_T cutoff.

7.2 The invariant mass spectra of di-electrons with the baseline experimental parameters

The panel (a) and (b) in Fig.7.2 show the invariant mass distributions of di-electron pairs in p+p collisions at $\sqrt{s} = 7$ TeV ($dN_{\pi^0+\pi^\pm}/dy = 6$) and central Pb+Pb collisions at $\sqrt{s_{NN}} = 5.5$ TeV ($dN_{\pi^0+\pi^\pm}/dy = 2700$), respectively. The components from individual di-electron sources are indicated with different types of curves in the figure. The mass shapes of ϕ, ω and ρ characterize their short lifetimes and show Breit-Wigner resonance peaks. The invariant mass spectrum of photon-conversion pairs obeys dynamics of the pair-creation process in materials. The invariant mass spectrum of Dalitz decaying pairs has a character whose leading edge is the summation of masses of decay products and the distribution continues up to their parent masses. The mass spectrum of $c\bar{c} \to e^+e^-$ is reconstructed by randomly pairing di-electrons in azimuth.

The panel (a) and (b) in Fig.7.3 show the inclusive invariant mass spectra of di-electrons in p+p collisions at $\sqrt{s} = 7$ TeV ($dN_{\pi^0+\pi^\pm}/dy = 6$) and central Pb+Pb collisions at $\sqrt{s_{NN}} = 5.5$ TeV ($dN_{\pi^0+\pi^\pm}/dy = 2700$), respectively. The component of signal pairs, combinatorial background pairs and all background pairs is superimposed in the figures. The peaks of the light vector mesons are clearly seen at the multiplicities in p+p collisions, but hardly seen in Pb+Pb collisions, though the statistical significance is not necessarily small. The quantitative evaluations of the signal-to-background ratios and the statistical significance are discussed in the next section.

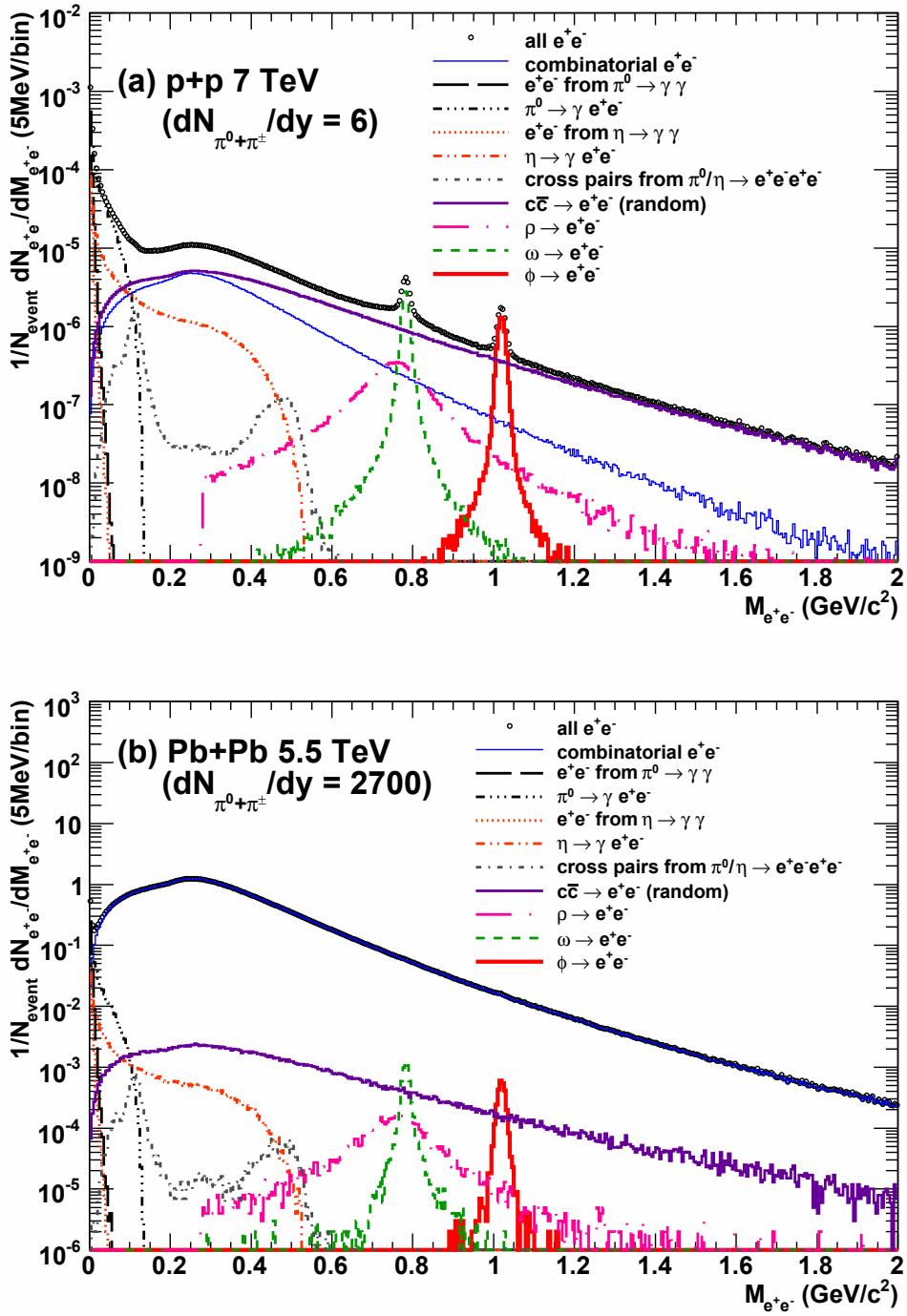

Figure 7.2: The invariant mass spectra of di-electrons from individual sources at the pion multiplicities, $dN_{\pi^0+\pi^\pm}/dy = 6$ (panel (a)) and 2700 (panel (b)) with the baseline experimental parameters: $P_{cnv} = 1$ %, $R_{\pi^\pm} = 500$, $\epsilon_{acc} = 100$ %, $\epsilon_{tag} = 100$ %, $p_T^{th} = 0.1$ GeV/c and $\sigma_{p_T}^{ref} = \sqrt{(0.01 \cdot p_T)^2 + (0.0056)^2}$ GeV/c. The mass spectra from individual origins are shown with different curves specified inside the plot. The curves of the combinatorial pairs are reconstructed by all combinations between electrons and positrons but only true combinations are excluded.

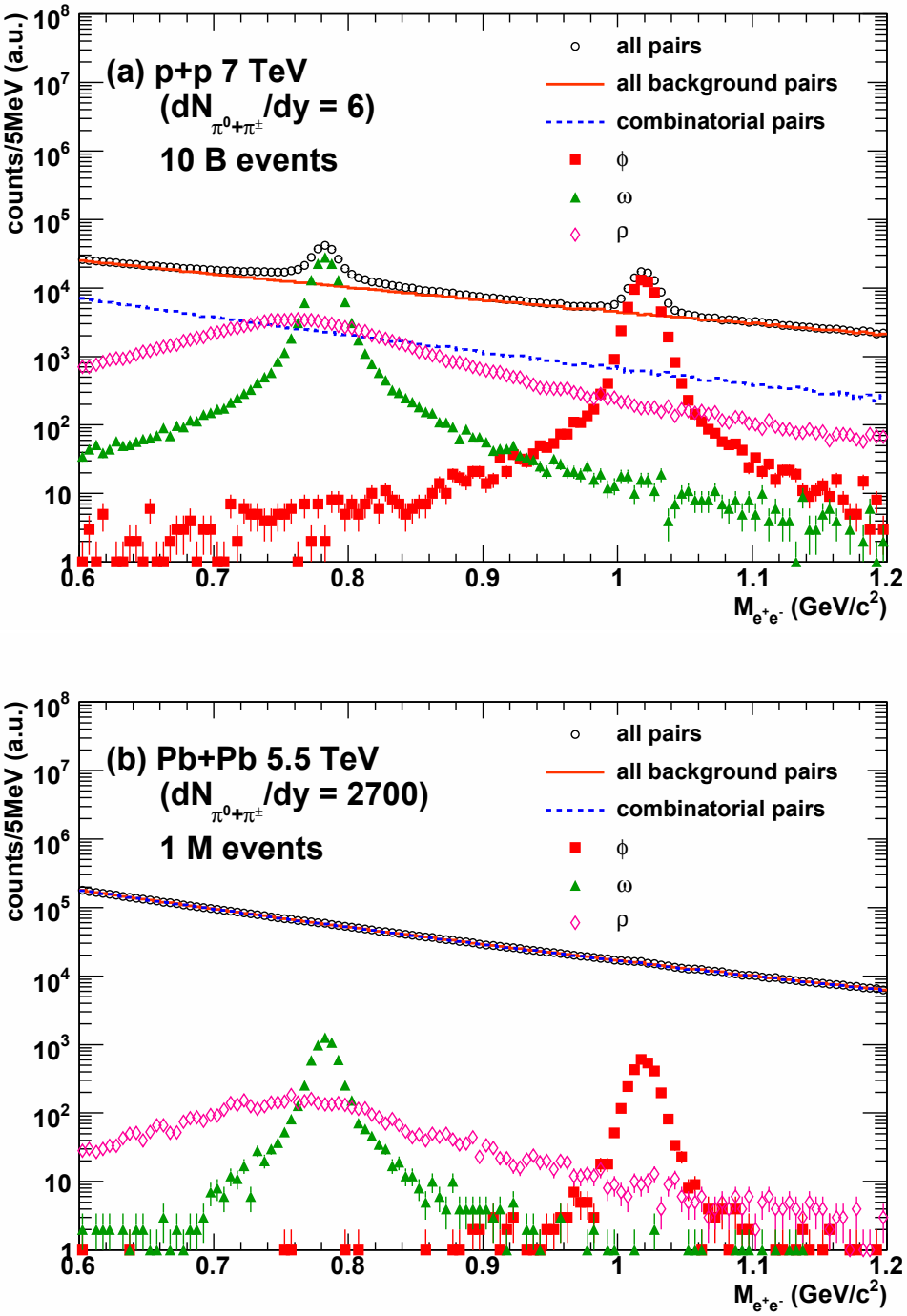

Figure 7.3: The inclusive mass spectra compared to the components of signal pairs, all background pairs and combinatorial background pairs at the pion multiplicities, $dN_{\pi^0+\pi^\pm}/dy$ = 6 (panel (a)) and 2700 (panel (b)) with the baseline experimental parameters: P_{cnv} = 1 %, $R_{\pi^\pm}$ = 500, ϵ_{acc} = 100 %, ϵ_{tag} = 100 %, p_T^{th} = 0.1 GeV/c and $\sigma_{p_T}^{ref} = \sqrt{(0.01 \cdot p_T)^2 + (0.0056)^2}$ GeV/c. The simulated number of events for each collision system is shown inside the plot.

7.3 Signal-to-background ratios and the statistical significance for light vector mesons

The feasibility to measure $\phi/\omega/\rho \rightarrow e^+e^-$ is evaluated by the signal-to-background ratios and the statistical significance in the signal mass region. The signal mass region for each meson is defined as the invariant mass range of $M_{\phi,\omega,\rho} \pm 3 \times \sqrt{\Gamma^2_{\phi,\omega,\rho} + \sigma^2_{\phi,\omega,\rho}}$, where $M_{\phi,\omega,\rho}$ is the mass center and $\Gamma_{\phi,\omega,\rho}$ is the decay width. $M_{\phi,\omega,\rho}$ and $\Gamma_{\phi,\omega,\rho}$ are cited from the particle data group [12]. The mass resolutions $\sigma_{\phi,\omega,\rho}$ are calculated by the single particle simulation[1] and result in 7.6, 5.7 and 5.6 MeV/c^2 for ϕ, ω and ρ mesons, respectively.

Figure 7.4 shows the signal-to-background ratios S/B as a function of the experimental parameters in central Pb+Pb collisions at $\sqrt{s_{NN}}$ = 5.5 TeV ($dN_{\pi^0+\pi^\pm}/dy$ = 2700). Only one parameter is changed by fixing the other parameters at the baseline values: P_{cnv} = 1 %, $R_{\pi^\pm}$ = 500, ϵ_{acc} = 100 %, ϵ_{tag} = 100 %, p_T^{th} = 0.1 GeV/c and $\sigma_{p_T}^{ref} = \sqrt{(0.01 \cdot p_T)^2 + (0.0056)^2}$ GeV/c. The top figure shows the S/B as a function of photon-conversion probability P_{cnv}. The minimum amount of detector materials typically corresponds to P_{cnv} = 1-2 %, because photon conversions from the beam pipe and the first layer of the innermost detector are unavoidable in any detector system, even though electron trajectories coming from the off-axis point are rejected by tracking algorithm. Thus the tendency below P_{cnv} = 10 % is important for the detector system with typical amount of the materials.

The dependence on the rejection factor of charged pions $R_{\pi^\pm}$ is shown in the middle plot of Fig. 7.4. Typical devices for the electron identification have the rejection factor of a few hundreds in the stand-alone operation [153, 154, 155, 156], although it varies by the principle of detection. Therefore, the information in the range of $R_{\pi^\pm}$ = 100-1000 are useful. The S/B can be changed by a factor of 3-5 for ϕ/ω meson in this range.

The bottom figure shows the S/B as a function of the azimuthal acceptance ϵ_{acc}. The S/B depends on decay kinematics of the signal particles and the backgrounds. Therefore the geometrical configuration in azimuthal coverage as well as the absolute acceptance in azimuth should be taken into account. Two types of geometrical configurations are considered in this simulation. Type I simply covers the azimuthal range of $0 \leq \phi \leq \phi_1$. Type II covers two separated domains which are symmetrically arranged in azimuth

[1]The mass resolutions are calculated as follows. ϕ, ω and ρ mesons are singly generated under the condition that their mass widths are set at zero, respectively. The mass distributions fluctuate around individual mass centers due to only the transverse momentum resolution $\sigma_{p_T}^{ref}$. The mass resolutions $\sigma_{\phi,\omega,\rho}$ are estimated by the fits with the Gauss function.

with respect to the collision point, that is, the coverage is set to $0 \leq \phi \leq \frac{\phi_1}{2}$ and $\pi \leq \phi \leq \pi + \frac{\phi_1}{2}$. Both of them have the same total acceptance in azimuth with different geometry. The difference between the two geometrical configurations increases in the case of the imperfect coverage. If ϵ_{acc} is 40 %, for instance, the S/B differs by a factor of 3-4 for ϕ/ω meson depending on the detector geometry.

The statistical significance $S/\sqrt{S+B}$ depends on the square root of the number of events, in other words, depends on available luminosity in experiments. Figure 7.5-7.7 show the statistical significance as a function of the experimental parameters in central Pb+Pb collisions at $\sqrt{s_{NN}} = 5.5$ TeV ($dN_{\pi^0+\pi^\pm}/dy = 2700$) for ϕ, ω and ρ meson, separately. The data points and the empirical curves are shown as filled symbols and the solid curves in the figures. The number of simulated events for central Pb+Pb collisions corresponds to 1M events. The other dotted curves show the scaled curves with the square root of the expected number of events with the highest centrality selection. The two horizontal lines indicate $S/\sqrt{S+B} = 3$ and 5. The S/B is independent of the electron tagging efficiency ϵ_{tag}, whereas the $S/\sqrt{S+B}$ scales with the square root of the statistics. Therefore we added the dependence on the ϵ_{tag} to the bottom figure for the discussion on the statistical significance. Depending on the available statistics in the specific collision centrality and the detector conditions, The results provide a guideline to evaluate whether or not a detection system is able to measure the light vector mesons with a reasonable statistical significance.

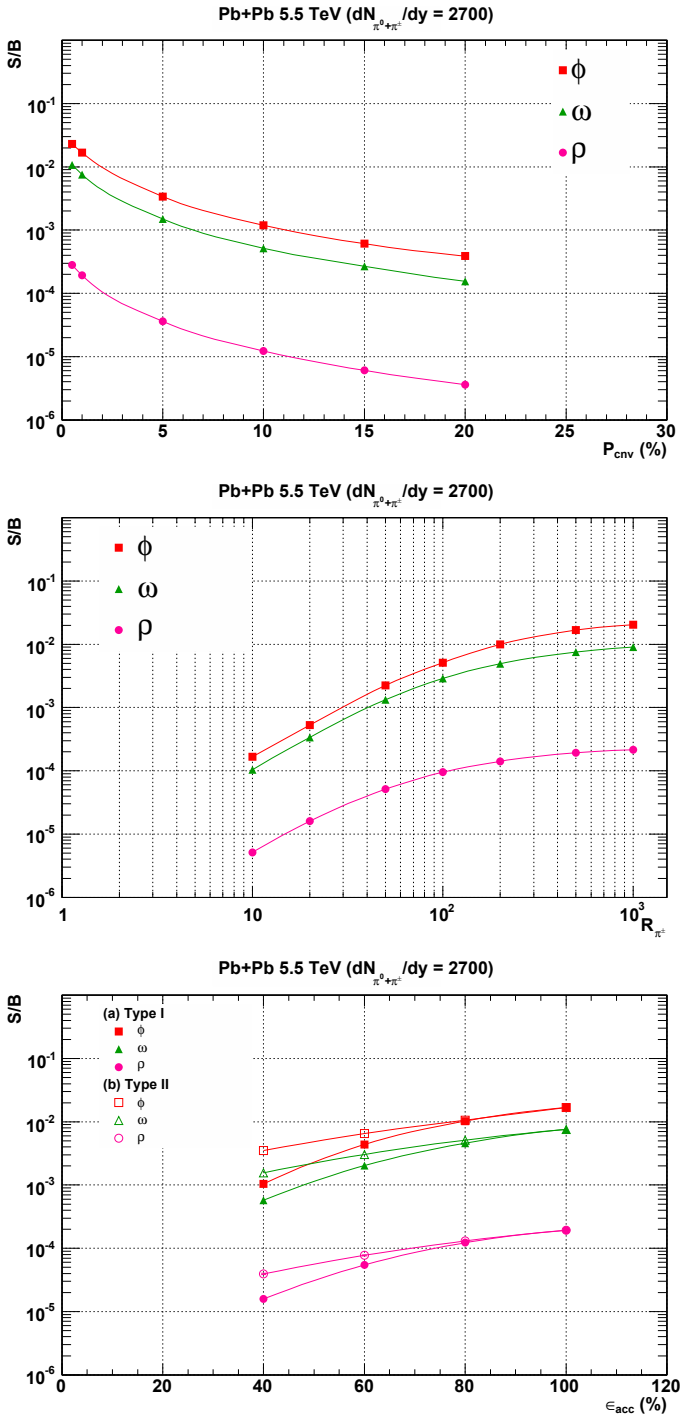

Figure 7.4: The signal-to-background ratio S/B of ϕ, ω and ρ meson as a function of the experimental parameters P_{cnv}, $R_{\pi^\pm}$ and ϵ_{acc} in central Pb+Pb collisions at $\sqrt{s_{NN}} = 5.5$ TeV ($dN_{\pi^0+\pi^\pm}/dy = 2700$). Only one parameter is changed by fixing the other parameters at the baseline values for each plot. Type I of the bottom figure shows the azimuthal coverage of $0 \leq \phi \leq \phi_1$. Type II shows two separated coverages of $0 \leq \phi \leq \frac{\phi_1}{2}$ and $\pi \leq \phi \leq \pi + \frac{\phi_1}{2}$.

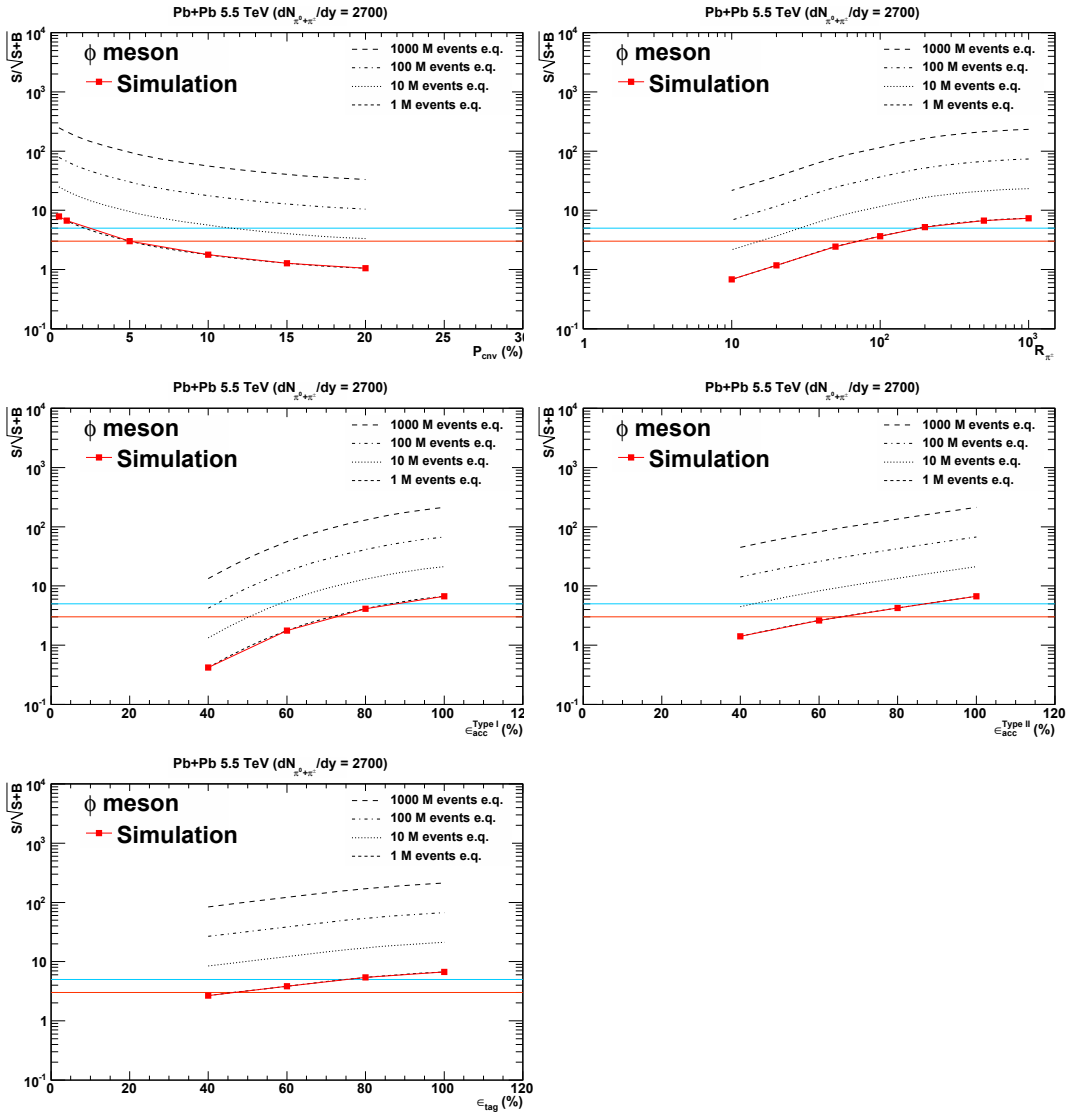

Figure 7.5: The statistical significance $S/\sqrt{S+B}$ of ϕ mesons as a function of the experimental parameters P_{cnv}, $R_{\pi^{\pm}}$, ϵ_{acc} and ϵ_{tag} in central Pb+Pb collisions at $\sqrt{s_{NN}} = 5.5$ TeV ($dN_{\pi^0+\pi^{\pm}}/dy = 2700$). Only one parameter is changed by fixing the other parameters at the baseline values for each plot. The results of the simulation are shown as the symbols and the empirical curves are superimposed on the data points as the solid curves. The other dotted curves are the scaled curves with the square root of the expected number of events found in the highest centrality class. Two horizontal lines indicate $S/\sqrt{S+B} = 3$ and 5.

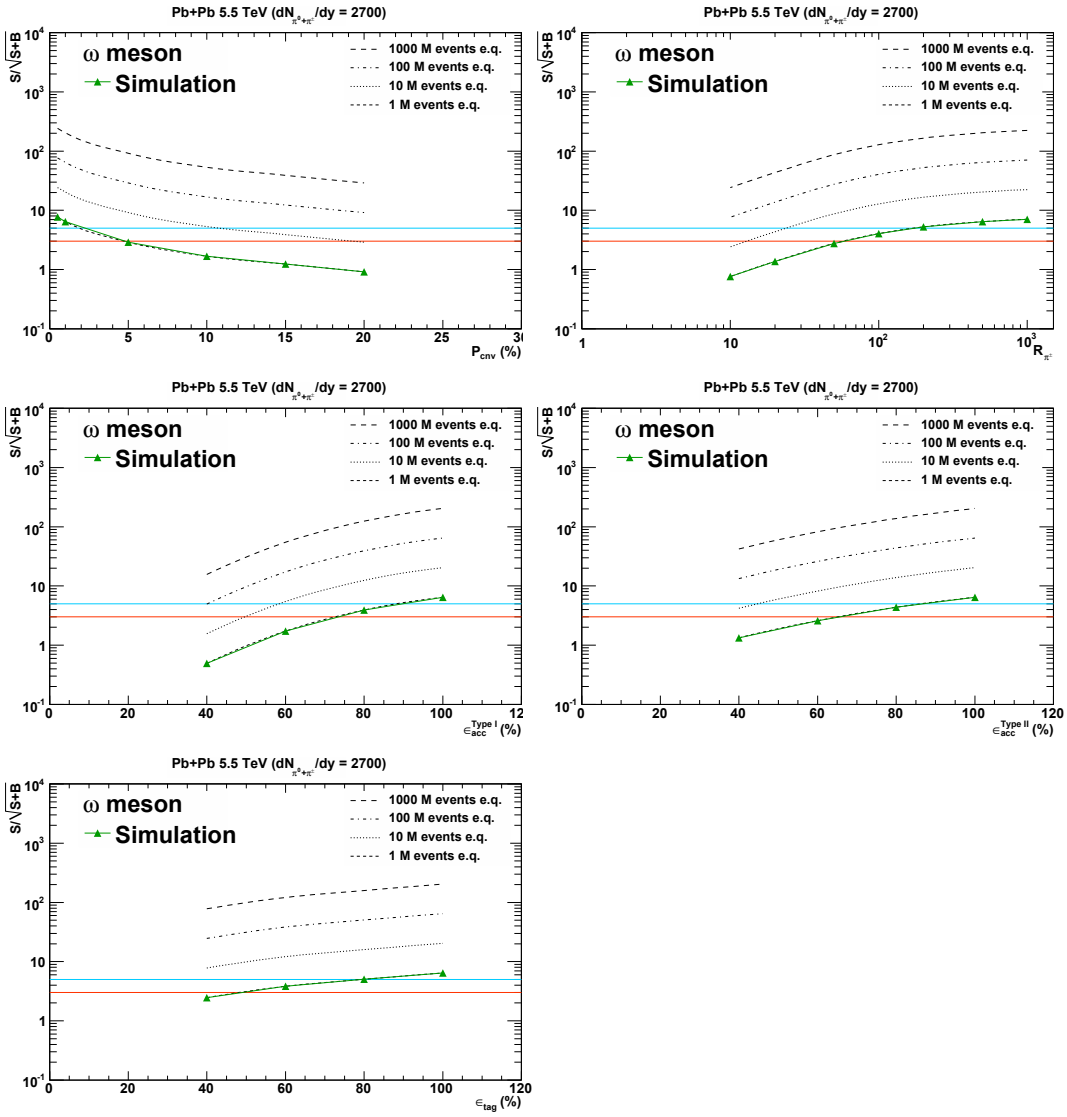

Figure 7.6: The statistical significance $S/\sqrt{S+B}$ of ω mesons as a function of the experimental parameters P_{cnv}, $R_{\pi^\pm}$, ϵ_{acc} and ϵ_{tag} in central Pb+Pb collisions at $\sqrt{s_{NN}} = 5.5$ TeV ($dN_{\pi^0+\pi^\pm}/dy = 2700$). Only one parameter is changed by fixing the other parameters at the baseline values for each plot. The results of the simulation are shown as the symbols and the empirical curves are superimposed on the data points as the solid curves. The other dotted curves are the scaled curves with the square root of the expected number of events found in the highest centrality class. Two horizontal lines indicate $S/\sqrt{S+B} = 3$ and 5.

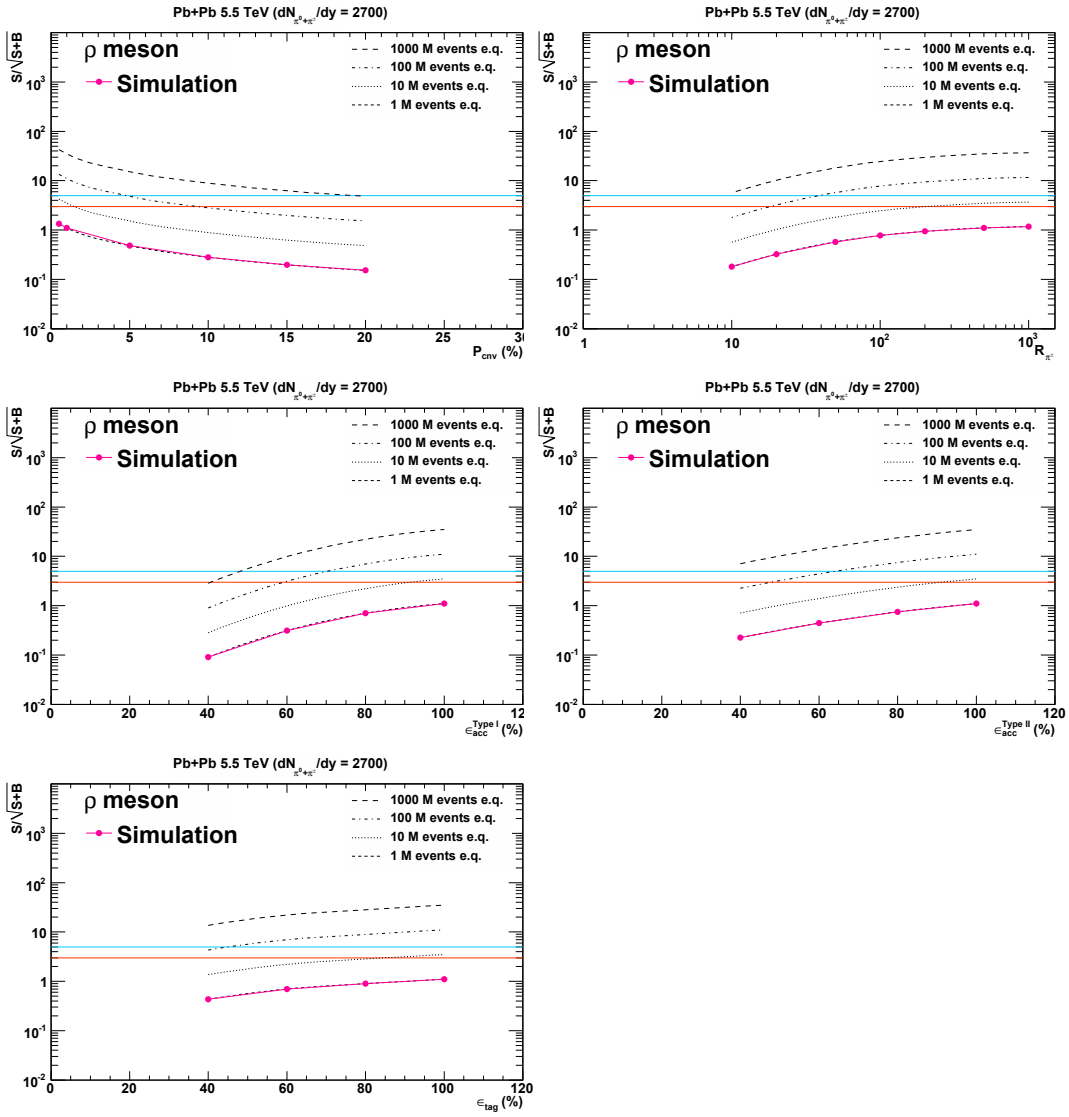

Figure 7.7: The statistical significance $S/\sqrt{S+B}$ of ρ mesons as a function of the experimental parameters P_{cnv}, $R_{\pi^\pm}$, ϵ_{acc} and ϵ_{tag} in central Pb+Pb collisions at $\sqrt{s_{NN}} = 5.5$ TeV ($dN_{\pi^0+\pi^\pm}/dy = 2700$). Only one parameter is changed by fixing the other parameters at the baseline values for each plot. The results of the simulation are shown as the symbols and the empirical curves are superimposed on the data points as the solid curves. The other dotted curves are the scaled curves with the square root of the expected number of events found in the highest centrality class. Two horizontal lines indicate $S/\sqrt{S+B} = 3$ and 5.

7.4 Uncertainties of the simulation study

The signal-to-background ratios and the statistical significance of the light vector mesons are evaluated with the idealized detection system so far. In this section, we discuss the non-trivial aspects originating from the real data analysis and the correlations in the open charm production. As the other issues beyond the scope of the numerical simulation, we mention the track reconstruction algorithm bias, the correlation between the electron identification and the rejection of charged hadrons, the fiducial effect on the acceptance to charged particles in the magnetic field, and unproved physics processes. The studies of this section are performed by simulating 5 M events in Pb+Pb 5.5 TeV with the baseline parameters set: $P_{cnv} = 1$ %, $R_{\pi^{\pm}} = 500$, $\epsilon_{acc} = 100$ %, $\epsilon_{tag} = 100$ %, $p_T^{th} = 0.1$ GeV/c and $\sigma_{p_T}^{ref} = \sqrt{(0.01 \cdot p_T)^2 + (0.0056)^2}$ GeV/c.

7.4.1 The uncertainty from signal extraction procedures

The numerical simulation so far is performed under the assumption that we know the exact number of signals and backgrounds. In the real data analysis, however, the source of any electron cannot be identified. Therefore all electrons and positrons are combined into pairs and reconstructed into the invariant mass. The mass distribution of pairs from one source ("true pairs") is extracted by subtracting that of pairs from different source ("combinatorial pairs") statistically. The mass shape of combinatorial pairs is estimated by mixing an electron in an event and a positron in another event ("event mixing"). The mass distribution of event-mixing pairs is normalized by $2\sqrt{N_{++}N_{--}}/N_{+-}^{mix}$, where N_{++}, N_{--} and N_{+-}^{mix} are the numbers of positron-positron pairs, electron-electron pairs and event-mixing electron-positron pairs, respectively. A series of procedures is equivalent to the real data analysis explained in Chapter 4.

The mass distribution of true pairs includes the light vector mesons and the other sources. The contributions from the light vector mesons and the background sources are separately estimated by the fits based on the linear combination between the Breit-Wigner function convoluted with the Gauss function and an empirical function. We apply a series of procedures used in the real data analysis to the simulated data and evaluate how much the signal-to-background ratios change by applying these procedures. The top panel of Fig.7.8 shows the invariant mass spectra assuming central Pb+Pb collisions at $\sqrt{s_{NN}} = 5.5$ TeV ($dN_{\pi^0+\pi^{\pm}}/dy = 2700$). The component of all reconstructed pairs (open symbols), the combinatorial pairs (closed circles) and the event-mixing pairs (solid curve) are superimposed on the top panel

in Fig.7.8. The middle panel in Fig.7.8 shows the ratio between the number of combinatorial pairs and that of event-mixing ones. The ratio is close to unity within a few % of statistical fluctuations below the mass of 1.0 GeV/c^2. Therefore the event-mixing pairs in the real data analysis can provide the reliable baseline representing the combinatorial pairs which is known only at the simulation study[2]. The bottom panel in Fig.7.8 shows the invariant mass distribution after subtracting the event-mixing distribution. The solid curves are the fitting results by the linear combination of the Breit-Wigner function convoluted with the Gauss function and a first-order polynomial function. In the mass range of ϕ meson,

$$\frac{dN_{e^+e^-}}{dM_{e^+e^-}} = A \int F_\phi\left(M'\right) G_{gauss}\left(M_{e^+e^-} - M'\right) dM' + H_{bg}\left(M_{e^+e^-}\right), \qquad (7.1)$$

In the mass range of ω/ρ meson,

$$\frac{dN_{e^+e^-}}{dM_{e^+e^-}} = A \int \left\{RF_\omega\left(M'\right) + \left(1-R\right) F_\rho\left(M'\right)\right\} G_{gauss}\left(M_{e^+e^-} - M'\right) dM' + H_{bg}\left(M_{e^+e^-}\right),$$

$$R = \frac{N_\omega BR\left(\omega \to e^+e^-\right)}{N_\omega BR\left(\omega \to e^+e^-\right) + N_\rho BR\left(\rho \to e^+e^-\right)}, \qquad (7.2)$$

where N_ω and N_ρ are the inclusive yields of ω and ρ meson, respectively. The absolute values of the inclusive yields are fixed to the measured values listed in Table 2.1 of Chapter 2. $BR\left(\omega \to e^+e^-\right)$ and $BR\left(\rho \to e^+e^-\right)$ are the branching ratios to a di-electron for ω and ρ meson, respectively. $F_{\phi,\omega,\rho}\left(M'\right)$ in Eq.(7.1) and (7.2) indicate the Breit-Wigner function describing the intrinsic mass spectra of the light vector mesons and $G_{gauss}\left(M_{e^+e^-} - M'\right)$ shows the Gauss function expressing the smearing effect caused by the transverse momentum resolution. The residual backgrounds are assumed to follow a first-order polynomial function $H_{bg}\left(M_{e^+e^-}\right)$. These functions are expressed as

$$F_{\phi,\omega,\rho}\left(M'\right) = \frac{\Gamma_{\phi,\omega,\rho}/2\pi}{\left(M' - M_{\phi,\omega,\rho}\right)^2 + \left(\Gamma_{\phi,\omega,\rho}/2\right)^2}, \qquad (7.3)$$

$$G_{gauss}\left(M_{e^+e^-} - M'\right) = \frac{1}{\sqrt{2\pi}\sigma} e^{-\left(M_{e^+e^-} - M'\right)^2/2\sigma^2}, \qquad (7.4)$$

[2]The normalization factor of $2\sqrt{N_{++}N_{--}}/N_{+-}^{mix}$ overestimates the combinatorial backgrounds by 0.05-0.3 %. For instance, if a detection system has large amount of materials (i.e. P_{cnv} is high) or has a poor capability of hadron rejection (i.e. $R_{\pi^\pm}$ is low), this estimation excessively subtracts the backgrounds.

$$H_{bg}\left(M_{e^+e^-}\right) = BM_{e^+e^-} + C, \tag{7.5}$$

where the mass center $M_{\phi,\omega,\rho}$ and the width $\Gamma_{\phi,\omega,\rho}$ of the light vector mesons are fixed to their intrinsic values [12], whereas the mass resolution σ is a free parameter. A, B and C in the equations are normalization factors. The fitting ranges are from 0.9 to 1.2 GeV/c^2 for ϕ meson and from 0.6 to 0.9 GeV/c^2 for ω/ρ meson. Each dotted curve in the bottom plot of Fig. 7.8 is obtained by the fitting results and shows the components of the light vector mesons and the residual background sources. The squares, triangles and diamonds show the invariant mass of the true di-electron pairs decaying from the light vector mesons.

The number of the light vector mesons is counted by the integration of the convolution function in the mass range of $M_{\phi,\omega,\rho} \pm 3 \times \sqrt{\Gamma^2_{\phi,\omega,\rho} + \sigma^2_{\phi,\omega,\rho}}$. The signal-to-background ratios are 1.7×10^{-2}, 6.7×10^{-3} and 1.7×10^{-4} for ϕ, ω and ρ mesons, respectively, in central Pb+Pb collisions at $\sqrt{s_{NN}} = 5.5$ TeV ($dN_{\pi^0+\pi^\pm}/dy = 2700$). They correspond to 3.2%, 12.1% and 14.3% differences with respect to the case of the simple counting of the simulated true pairs. The differences depend on the experimental parameters. It is unlikely for them to exceed 50% at a realistic range of the experimental parameters[3].

[3]The differences of the signal-to-background ratios between the estimation with the fit and the counting of the simulated true pairs originate from the background shape mainly depending on the subtraction of the combinatorial background. The differences are studied at the experimental parameter range of $1 < P_{cnv} < 5\,\%$ or $100 < R_{\pi^\pm} < 500$, and result in $\sim 20\%$ for the three mesons.

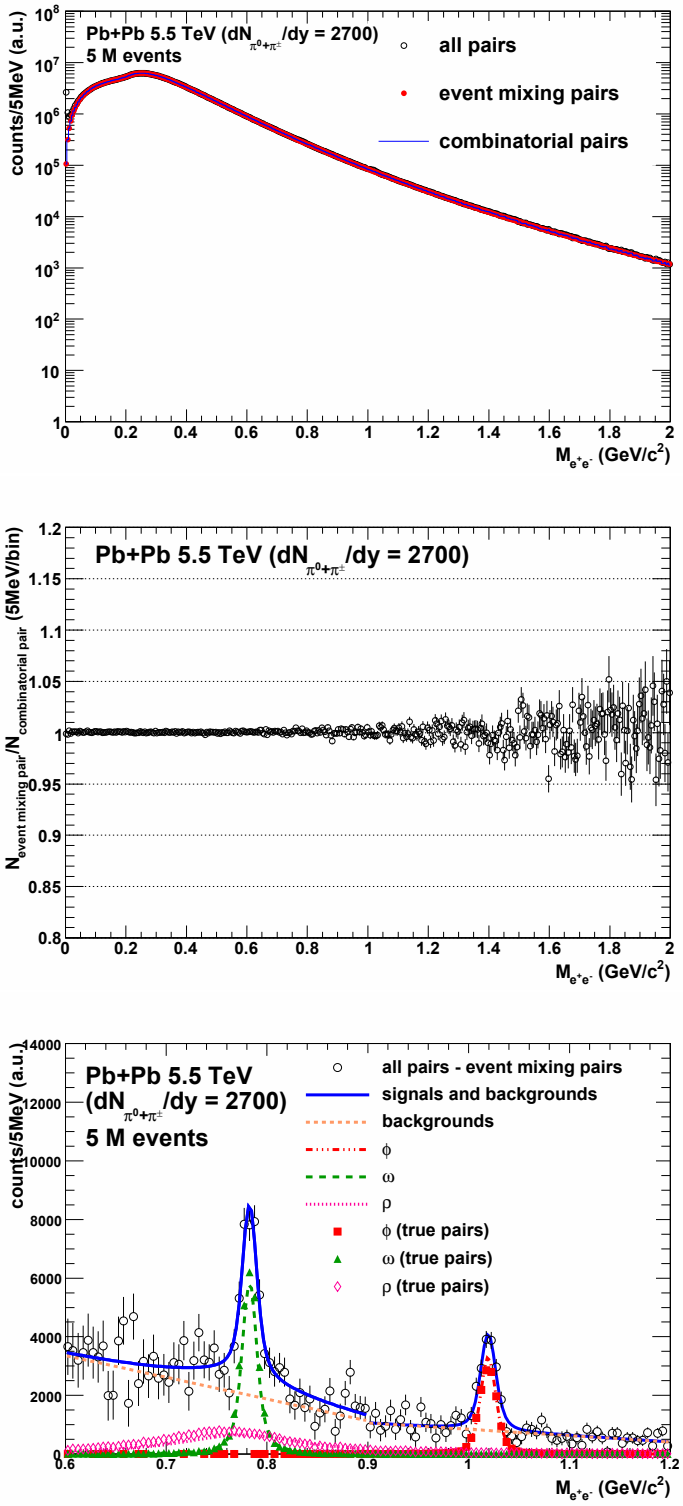

Figure 7.8: The invariant mass spectra in central Pb+Pb collisions at $\sqrt{s_{NN}}$ = 5.5 TeV ($dN_{\pi^0+\pi^\pm}/dy = 2700$) with the baseline experimental parameters: P_{cnv} = 1 %, $R_{\pi^\pm}$ = 500, ϵ_{acc} = 100 %, ϵ_{tag} = 100 %, p_T^{th} = 0.1 GeV/c and $\sigma_{p_T}^{ref} = \sqrt{(0.01 \cdot p_T)^2 + (0.0056)^2}$ GeV/c.

7.4.2 The uncertainty from the correlation of $c\bar{c}$ production

Electrons and positrons from open charms are randomly generated and combined into pairs in this simulation. These pairs are, in fact, azimuthally correlated at midrapidity, because they originate from the jets due to the large mass of charm quarks. We assume the back-to-back e^+e^- correlation in azimuth as the extreme case of the open charm production. Realistic correlations would exist between the random pairing case and the back-to-back correlated case. The top plot in Fig.7.9 shows the invariant mass spectra of all true pairs, combinatorial pairs and $c\bar{c} \to e^+e^-$, respectively. The distributions of the random di-electron pairs and the back-to-back correlated ones in azimuth are superimposed in the same plot. The middle plot in Fig.7.9 shows the ratio of the number of $c\bar{c} \to e^+e^-$ as a function of the invariant mass. The denominator is the number of di-electrons with random pairing and the numerator is the number of di-electrons with the back-to-back correlation. This ratio varies by a factor of 1.5 to 3 around the mass range of the light vector mesons. The ratio between the number of combinatorial pairs in the random pairing case and in the back-to-back correlated case is consistent within a few % as shown in the bottom plot in Fig.7.9 The correlation of the $c\bar{c}$ production has little influence on the signal-to-background ratios of the light vector mesons.

7.4.3 Residual uncertainties

Track reconstruction algorithms bias

Track reconstruction algorithms can bias momentum measurement of charged particles. For example, the algorithm based on the combinatorial Hough transform technique [183, 184] reconstructs higher momentum than true one, especially for a charged particle producing from the off-axis point. The photon-conversion electrons at the off-axis point contribute to the background shape in the relatively higher mass region. In addition, especially under a high multiplicity environment, fake tracks are reconstructed by chance depending on the algorithms. These tracks can contribute as the additional backgrounds.

Correlation between the tagging efficiency of electrons and the rejection factor of charged hadrons

The correlation between electron tagging efficiency and the rejection factor of charged hadrons depends on the method of particle identification. For

instance, if particles are identified by dE/dx, the correlation has a trade-off relation. Another example is the degradation in the situation where a number of particles simultaneously pass through the detector. If a hadron and an electron enter the same area of the electron identification device, either or both of them can be wrongly identified. In the more general case, complicated correlations may appear, since particles are identified with a combination of multiple devices.

Fiducial effect in the magnetic field

This simulation considers the detector acceptance under the assumption that di-electron kinematics is completely reconstructed. In real experiments, charged particles are bent in the magnetic field and entered into the imperfect coverage of the detectors. The fiducial effect becomes apparent at the edge of the acceptance. Therefore the inefficiency of the electron detection should be taken into account as a function of the magnetic field, the detector positions from the collision point and the detector configurations.

Unproved physics processes

The possible but unproved processes such as thermal di-electron radiation, mini-jet production and the in-medium modification of ρ mesons in heavy-ion collisions, are not implemented into the simulations. They can affect on the feasibility of the light vector meson.

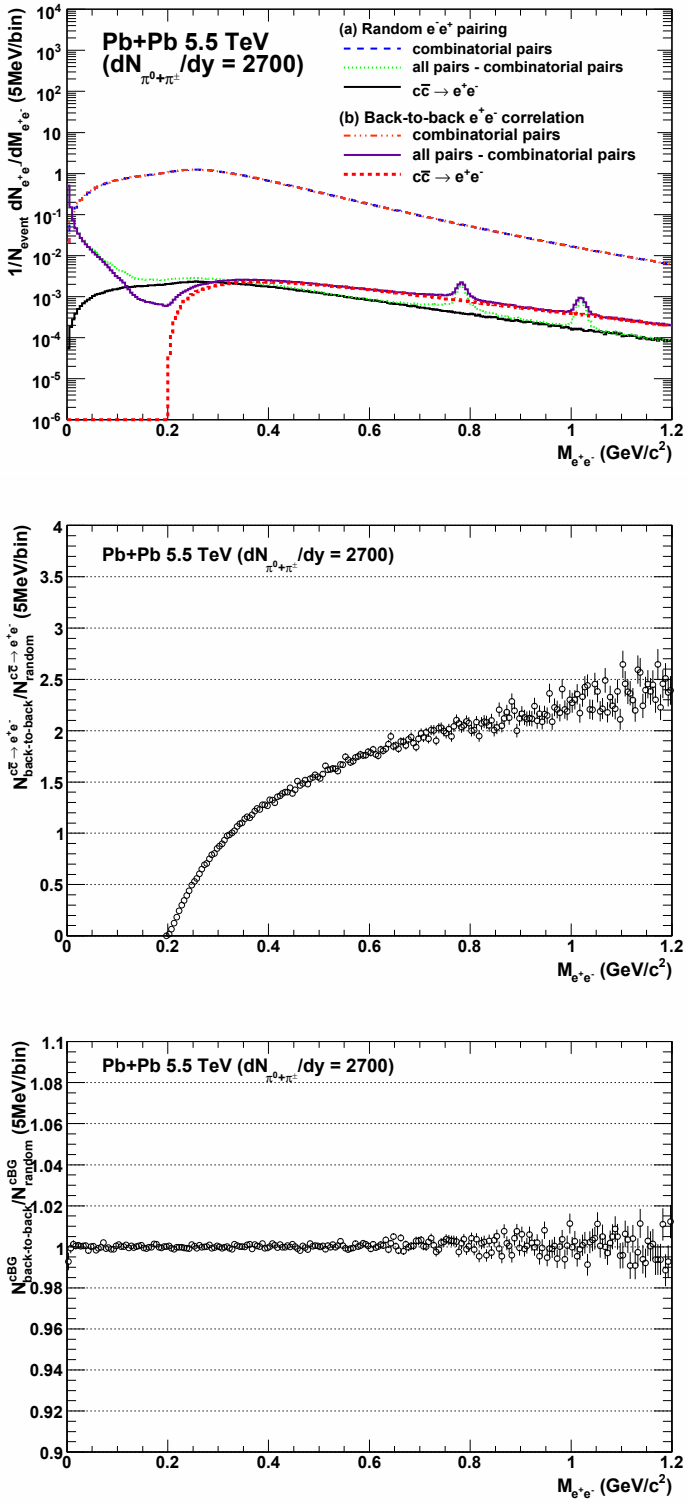

Figure 7.9: The comparison of the invariant mass spectra for different correlations of di-electrons from charm quarks (top). The ratio between the number of $c\bar{c} \to e^+e^-$ in the random pairing case and in the back-to-back correlated one (middle). The ratio between the number of combinatorial pairs in the random pairing case and in the back-to-back correlated one (bottom).

Chapter 8

Summary and conclusion

The production of ϕ and ω mesons in Au+Au collisions at $\sqrt{s_{NN}} = 200$ GeV has been studied at the centrality class of 0-92.2% (MB), 0-20% (Central), 20-60% (Semi-central) and 60-92.2% (Peripheral) with 9.0 $\times 10^8$ Minimum Bias events in the PHENIX experiment. The invariant yield as a function of transverse momentum with the range of $0 < p_T < 3$ GeV/c has been measured, and the data covers $0 < p_T < 8$ GeV/c for ϕ mesons and $0 < p_T < 20$ GeV/c for ω mesons by combining with different decay channels. The characteristics of the spectrum shape are systematically investigated by semi-empirical functions: the Tsallis function, the exponential function and the modified power-law function. The power parameter n and the inverse slope parameter T have little dependence of centrality. The inclusive yields of ϕ and ω mesons have been measured. The results suggest that the inclusive yield is scaled with the number of participant pairs independent of centrality within the errors. In addition, the transverse momentum spectra in Au+Au collisions at $\sqrt{s_{NN}} = 200$ GeV are compared with those in p+p collisions at $\sqrt{s} = 200$ GeV via the number of binary collisions.

The mass modification is discussed from the viewpoints of the mass spectrum shape and the branching ratio. The signature of the mass modification cannot be extracted from the mass spectrum shape of the light vector mesons due to the poverty of the signal-to-background ratio and the statistical significance. The yield fraction between $\phi \to e^+e^-$ and $\phi \to K^+K^-$ is studied. As a result, there is consistency between different decay channels. In conclusion, any symptom of the mass modification is not observed in Au+Au collisions at $\sqrt{s_{NN}} = 200$ GeV.

The numerical simulation has been developed for di-electron measurement in heavy-ion collisions. The feasibility of the light vector meson measurement via di-electrons in central Pb+Pb collisions at $\sqrt{s_{NN}} = 5.5$ TeV is studied via the numerical simulation. The simulation takes the key aspects of heavy-ion

collisions and experimental issues relevant to di-electron measurement into account, and provides a guideline to be applicable to a concrete detector design with the wide range of experimental parameters. The results of the simulation study suggest that there are realistic parameter ranges to measure light vector mesons via di-electrons with the reasonable significance level in realizable luminosity in central Pb+Pb collisions at $\sqrt{s_{NN}} = 5.5$ TeV.

Acknowledgement

I would like to express my sincere gratitude to my supervisor Prof. T. Sugitate for his continuous guidances and constructive efforts for promoting the experiment as the leader of our laboratory at Hiroshima University. I'm deeply grateful to Assist. Prof. K. Homma for discussing on the numerical simulation study. I could not have published the paper without his collaboration. I deeply acknowledge Dr. Y. Akiba, Assoc. Prof. K. Ozawa, Assoc. Prof. K. Shigaki, Mr. Y. Tsuchimoto and Dr. K. Kijima for their encourages and helpful advices for my di-electron analysis.

I would like to acknowledge all PHENIX collaboration. I have had a lot of supports for making progress on the analysis and driving the experiment. I also express gratitude to Dr. J. S Haggerty, Dr. C. Y. Chi, Dr. S. Stoll, Dr. M. Chiu, Dr. C. Pinkenburg, Dr. E. Desmond, Prof. J. Lajoie, Assist. Prof. M. Kaneta, Dr. K. Okada for their thoughtful help for the operation of the Beam-Beam counter. I could not stably operate the BBC without their help. I would like to thank Dr. T. Nakamura, Dr. M. Ouchida, Mr. D. Watanabe, Dr. H. Harada, Mr. K. Haruna, Mr. H. Sakata, Mr. M. Nihashi, Mr. Y Iwanaga and Mr. K. Yamaura for working together for the BBC operation. I would also like to thank Dr. K. Nakano, Dr. K. Sakashita, Dr. T. Kanesue, Mr. K. Shoji, Dr. Y. Fukao, Assist. Prof. M. Togawa, Assist. Prof. K. Aoki, Dr. S. Dairaku, Dr. K. Karatsu, Dr. I. Nakagawa, Dr. A. Taketani, Assoc. Prof. S. Esumi, Assoc. Prof. M. Inaba, Dr. T. Chujo, Dr. M. Konno, Dr. M. Shimomura, Mr. M. Oka, Dr. K. Miki, Mr. Y. Ikeda, Dr. F. Kajihara, Assist. Prof. T. Gunji, Dr. T. Isobe, Mr. N. Kurihara, Assist. Prof. S. Oda, Dr. Y. Morino, Dr. Y. Aramaki and Dr. Y. Yamaguchi for the great time we spent together at Brookhaven National Laboratory.

I would also like to thank relevant people of quark physics laboratory at Hiroshima University: Assist. Prof. T. Miyoshi, Dr. H. Torii, Project Assoc. Prof. T. Horaguchi, Dr. T. Hachiya, Assist. Prof. A. Enokizono, Mr. R. Kohara, Mr. K. Hirashita, Mr. D. Toyoda, Mr. K. Hosokawa, Mr. K. Kubo, Mr. T. Narita, Mr. K. Kadowaki, Mr. K. Mizoguchi, Mr. Y. Okada, Mr. Y. Maruyama, Mr. F. Chuman, Ms. A. Hiei, Mr. T. Iwasaki, Mr. H. Sakaguchi,

Mr. M. Saka, Ms. T. Yamamoto, Mr. T. Takata, Mr. J. Midori, Mr. H. Obayashi, Mr. T. Hiasa, Mr. S. Yano, Mr. T. Hoshino, Mr. S. Sakurai, Mr. K. Kume, Mr. D. Sato, Mr. T. Hasebe, Ms. A. Tuji, Mr. T. Okubo, Mr. Y. Oya, Mr. T. Ichima, Mr. D. Sekihata, Mr. K. Nagashima, Mr. T. Yuasa, Mr. Y. Nakazato, Ms. R. Tanizaki, Mr. S. Egawa, Mr. K. Tarunaga, Mr. Y. Ueda, Ms. K. Matsuura and Mr. Y. Miyazaki.

Finally, I wish to express my deepest gratitude to my parents, Yoshinobu and Yukiko, for their support and understanding of continuing my work. I could not have finishes this work without their long-time help.

Appendix A

Natural units

In high-energy heavy-ion domains, natural units are usually used. Natural units are composed by taking $\hbar = c = 1$, that is,

$$\begin{aligned} \hbar &\equiv \frac{h}{2\pi} = 6.5821 \times 10^{-25}\mathrm{GeV\,s} = 1, \\ c &= 2.9979 \times 10^{8}\mathrm{m\,s^{-1}} = 1. \end{aligned} \tag{A.1}$$

In natural units system, the dimensions of mass, momentum and energy are shown as GeV, and time and length are shown in GeV^{-1}. These results are obtained by dimension analysis as follows. Suppose that the dimensions of mass, momentum, energy, time and length are expressed as [m], [p], [E], [T] and [L] respectively,

$$[c] = [L]\,[T]^{-1}\,, \tag{A.2}$$

$$[\hbar] = [E]\,[T]\,. \tag{A.3}$$

These relations and energy the conservation law $E^2 = p^2c^2 + m^2c^4$ result in

$$[T] = [L]\,, \tag{A.4}$$

$$[E] = [m] = [p]\,, \tag{A.5}$$

$$[E] = [m] = [T]^{-1} = [L]^{-1} \tag{A.6}$$

The fine structure constant in the quantum electrodynamics α is defined as

$$\alpha = \frac{e^2}{4\pi\hbar c} = \frac{e^2}{4\pi} \sim \frac{1}{137.04}. \tag{A.7}$$

The pion Compton wavelength is given by

$$\lambda_\pi = \frac{\hbar}{m_\pi c} \sim \frac{1}{140}\,\mathrm{MeV}^{-1} \sim 1.41\,\mathrm{fm}, \tag{A.8}$$

where 1 fm $= 1 \times 10^{-15}$ m. A typical hadronic cross section is obtained by the pion Compton wavelength as follows.

$$\sigma \sim \lambda_\pi^2 \sim 2\,\mathrm{fm}^2 = 20\,\mathrm{mb} \tag{A.9}$$

where 1 b (barn) $= 10^{-28}$ m$^2 = 100$ fm^2. The Boltzmann constant k_B is often treated as $k_B = 1$ in studying relativistic thermodynamics as follows.

$$k_B = 8.6173 \times 10^{-14}\,\mathrm{GeV\,K^{-1}} = 1. \tag{A.10}$$

Table A.1 is transformation among different units in $\hbar = c = k_B = 1$.

	[J]	[MeV]	[g]	[cm^{-1}]	[K]
1 J	1	6.2415×10^{12}	1.1127×10^{14}	3.1630×10^{23}	7.2430×10^{22}
1 MeV	1.6022×10^{-13}	1	1.7830×10^{-27}	5.0677×10^{10}	1.1605×10^{10}
1 g	8.9876×10^{13}	5.6096×10^{26}	1	2.8428×10^{37}	6.5096×10^{36}
1 cm^{-1}	3.1615×10^{-24}	1.9733×10^{-11}	3.5177×10^{-38}	1	2.2290×10^{-1}
1 K	1.3807×10^{-23}	8.6173×10^{-11}	1.5362×10^{-37}	4.3670	1

Table A.1: Transformation among different units in $\hbar = c = k_B = 1$.

Appendix B

Relativistic kinematics and variables

B.1 Laboratory frame and center-of-mass frame

Initially a two-body reaction is assumed as follows.

$$a + b \to c + d + \cdots, \tag{B.1}$$

where a and b are the projectile and the target particle, respectively. In the laboratory frame, the projectile particle hits the target one, which is at rest, with am energy-momentum (E^{lab}, $\boldsymbol{p}^{lab}$). After the collision, final-state paricles are usually moving. In the center-of-mass frame, the sum of the momentum vectors of all particles in the initial state is zero, consequently the sum of the momentum vectors of final-state particles vanish. The features of both frames are summarized as follows.
Laboratory frame:

$$\boldsymbol{p}_b^{lab} = \mathbf{0},\ E_b^{lab} = m_b, \tag{B.2}$$

Center-of-mass frame:

$$\boldsymbol{p}_a^{cm} + \boldsymbol{p}_b^{cm} = \boldsymbol{p}_c^{cm} + \boldsymbol{p}_d^{cm} + \cdots = \mathbf{0}, \tag{B.3}$$

where $m_{B_{tar}}$ is the rest mass of the target particle.

In order to obtain the relation between the energies in laboratory and center-of-mass frame, Lorentz invariant quantity s, which is one of Mandelstam variables, is introduced:

$$s \equiv (p_a + p_b)^2 \equiv (p_a + p_b)_\mu (p_a + p_b)^\mu, \tag{B.4}$$

where p_a and p_b is the four momentum of particle a and b. By definition, s is the same in all coordinate systems.

Consider a relativistic collision between two particles with the same rest mass m (e.g. p+p collision). The following formula are obtained by Eq (B.2)-(B.4):
Laboratory frame:

$$\begin{aligned} p_a^{lab} &= \left(E^{lab}, \boldsymbol{p}^{lab}\right), \\ p_b^{lab} &= (m, \mathbf{0}), \\ s &= \left(p_a^{lab} + p_b^{lab}\right)^2 \\ &= \left(E^{lab} + m\right)^2 - \left(\boldsymbol{p}^{lab}\right)^2 \\ &= 2mE^{lab} + 2m^2. \end{aligned} \tag{B.5}$$

Center-of-mass frame:

$$\begin{aligned} p_a^{cm} &= (E^{cm}/2, \boldsymbol{p}^{cm}), \\ p_b^{cm} &= (E^{cm}/2, -\boldsymbol{p}^{cm}), \\ s &= (p_a^{cm} + p_b^{cm})^2 \\ &= (E^{cm})^2. \end{aligned} \tag{B.6}$$

Therefore,

$$E^{lab} = \frac{(E^{cm})^2}{2m} - m. \tag{B.7}$$

In the extreme limit of relativistic collision, that is, $E^{lab} \gg m$,

$$\sqrt{s} = E^{cm} \sim \sqrt{2mE^{lab}}. \tag{B.8}$$

The center-of-mass energy increases only as the square root of the laboratory energy.

B.2 Rapidity and pseud-rapidity

At the relativistic limit, the addition law of the velocities is non-linear.

$$v = \frac{v_1 + v_2}{1 + \frac{v_1 v_2}{c^2}} \text{ or } \beta = \frac{\beta_1 + \beta_2}{1 + \beta_1 \beta_2}, \tag{B.9}$$

where $\beta \equiv v/c = v$. In order to fulfill the addition law, a new variable y, which is so-called rapidity, as a function of β is introduced:

$$y \equiv \tanh^{-1}\beta = \frac{1}{2}\ln\frac{1+\beta}{1-\beta}. \tag{B.10}$$

At the non-relativistic limit, y is approximately equal to β. It means the rapidity is relativistic analogue of the velocity. Since $\beta = p_z/E$, Eq.(B.10) is expressed by

$$y = \frac{1}{2}\ln\frac{E+p_z}{E-p_z}, \tag{B.11}$$

where p_z is the momentum component of z axis. Equation (B.10) and (B.11) fulfill the addition law:

$$y_1 \pm y_2 = \tanh^{-1}\beta_1 \pm \tanh^{-1}\beta_2 = \tanh^{-1}\frac{\beta_1+\beta_2}{1\pm\beta_2\beta_2}. \tag{B.12}$$

Therefore a Lorentz boost along the z axis from a frame S to a new frame S' changes the rapidity in a simple additive way:

$$y' = y + \tanh^{-1}\beta', \tag{B.13}$$

where β' is the velocity of the S' frame with respect to the S frame.

If the particle masses are negligible, that is, $E^2 = \boldsymbol{p}^2 + m^2 \sim \boldsymbol{p}^2$, pseudo-rapidity η can be used instead of the rapidity y.

$$\begin{aligned} y &\simeq \frac{1}{2}\ln\frac{p+p_z}{p-p_z} = \frac{1}{2}\ln\frac{1+\cos\theta}{1-\cos\theta} \\ &= -\ln\left(\tan\frac{\theta}{2}\right) \\ &\equiv \eta \end{aligned} \tag{B.14}$$

The pseudo-rapidity η is useful because it can be directly determined from the particle production angle θ, where θ is measured angle with respect of the z axis (beam axis) in experiments.

B.3 Four-momentum in center-of-mass colliding system

The transverse momentum p_T and the longitudinal momentum p_z of a particle with the rest mass m and momentum vector $\boldsymbol{p} = (p_x, p_y, p_z)$ are given by

$$\begin{aligned} p_T = \sqrt{p_x^2 + p_y^2} &= |\boldsymbol{p}|\sin\theta, \\ p_z &= |\boldsymbol{p}|\cos\theta, \end{aligned} \tag{B.15}$$

where θ is the polar angle of the vector $\boldsymbol{p}$ with respect to the longitudinal axis (beam axis). Then transverse mass m_T is defined by

$$\begin{aligned} m_T &= \sqrt{p_T^2 + m^2} \\ &= \sqrt{E^2 - p_z^2}. \end{aligned} \tag{B.16}$$

The rapidity y can be rewritten by,

$$y = \ln \frac{E + p_z}{m_T}. \tag{B.17}$$

Therefore the four momentum p^μ are parameterized as

$$\begin{aligned} p^\mu &= (E,\, p_x,\, p_y,\, p_z) \\ &= (m_T \cosh y,\, p_T \cos\phi,\, p_T \sin\phi,\, m_T \,\mathrm{simh}\, y)\,. \end{aligned} \tag{B.18}$$

where ϕ is azimuthal angle in the perpendicular plane to the longitudinal axis (beam axis).

B.4 Lorentz-invariant cross section

A transformation of a four momentum $(E,\, p_x,\, p_y,\, p_z)$ in the S frame to a four momentum $\left(E',\, p'_x,\, p'_y,\, p'_z\right)$ in the S$'$ frame moving with β along the z axis with respect to S is

$$\begin{aligned} \begin{pmatrix} E' \\ p'_x \\ p'_y \\ p'_z \end{pmatrix} &= \begin{pmatrix} \gamma & 0 & 0 & -\beta\gamma \\ 0 & 1 & 0 & 0 \\ 0 & 0 & 1 & 0 \\ -\beta\gamma & 0 & 0 & \gamma \end{pmatrix} \begin{pmatrix} E \\ p_x \\ p_y \\ p_z \end{pmatrix} \\ &= \begin{pmatrix} \gamma\,(E - \beta p_z) \\ p_x \\ p_y \\ \gamma\,(p_z - \beta E) \end{pmatrix}, \end{aligned} \tag{B.19}$$

where $\gamma = \sqrt{1-\beta^2} = E/m$ is the Lorentz factor. If p_x and p_y are fixed, $p_z dp_z = EdE$ are obtained by $E^2 - p_x^2 - p_y^2 - p_z^2 = m^2$. Therefore

$$\begin{aligned} dp'_x &= dp_x, \\ dp'_y &= dp_y, \\ \frac{dp'_z}{E'} &= \frac{\gamma\,(dp_z - \beta dE)}{\gamma\left(1 - \beta\frac{p_z}{E}\right)E} = \frac{dp_z}{E}. \end{aligned} \tag{B.20}$$

Therefore,

$$\frac{d^3p'}{E'} \equiv \frac{dp'_x dp'_y dp'_z}{E'} = \frac{dp_x dp_y dp_z}{E} \equiv \frac{d^3p}{E}. \tag{B.21}$$

The Lorentz-invariant differential cross section for a particle with momentum $\boldsymbol{p}$ lying in the phase-space element d^3p and energy E is given by

$E\,(d^3\sigma/d^3p)$. The transverse momentum, p_T, the azimuthal angle, ϕ, and the rapidity, y, of the produced particle are related to $\boldsymbol{p}$ as follows.

$$\begin{aligned} dp_x dp_y &= d\phi p_T dp_T, \\ dy &= \frac{dp_z}{E}. \end{aligned} \tag{B.22}$$

Therefore Lorentz-invariant differential cross section is expressed by

$$E\frac{d^3\sigma}{dp^3} = E\frac{d^3\sigma}{dp_x dp_y dp_z} = \frac{d^3\sigma}{p_T dp_T d\phi dy} = \frac{d^3\sigma}{m_T dm_T d\phi dy}. \tag{B.23}$$

Appendix C

RICH variables

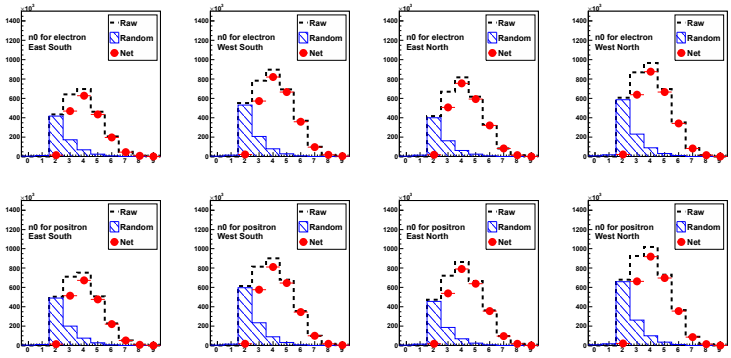

Figure C.1: Sector-by-sector $n0$ distribution for electron and positron.

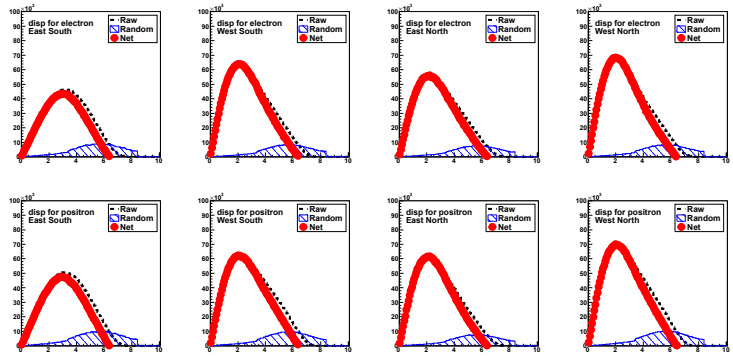

Figure C.2: Sector-by-sector *disp* distribution for electron and positron.

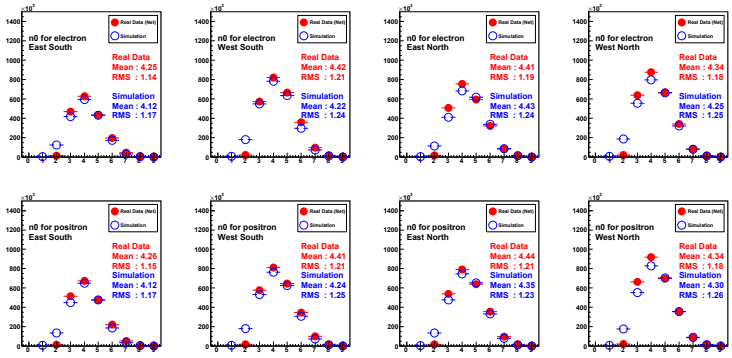

Figure C.3: The comparison of the net distribution between the real data and the simulation, taking the RICH misalignment effect into account. The comparisons are shown for East-South, West-South, East-North and West-North. The top and bottom plots are $n0$ distribution for electrons and positrons, respectively.

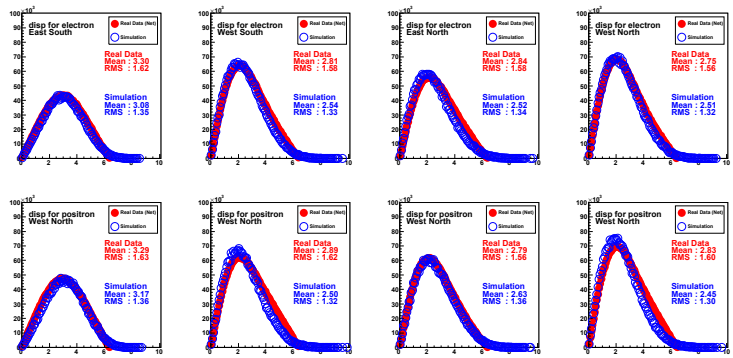

Figure C.4: The comparison of the net distribution between the real data and the simulation, taking the RICH misalignment effect into account. The comparisons are shown for East-South, West-South, East-North and West-North. The top and bottom plots are *disp* distribution for electrons and positrons, respectively.

Appendix D

Track matching calibration

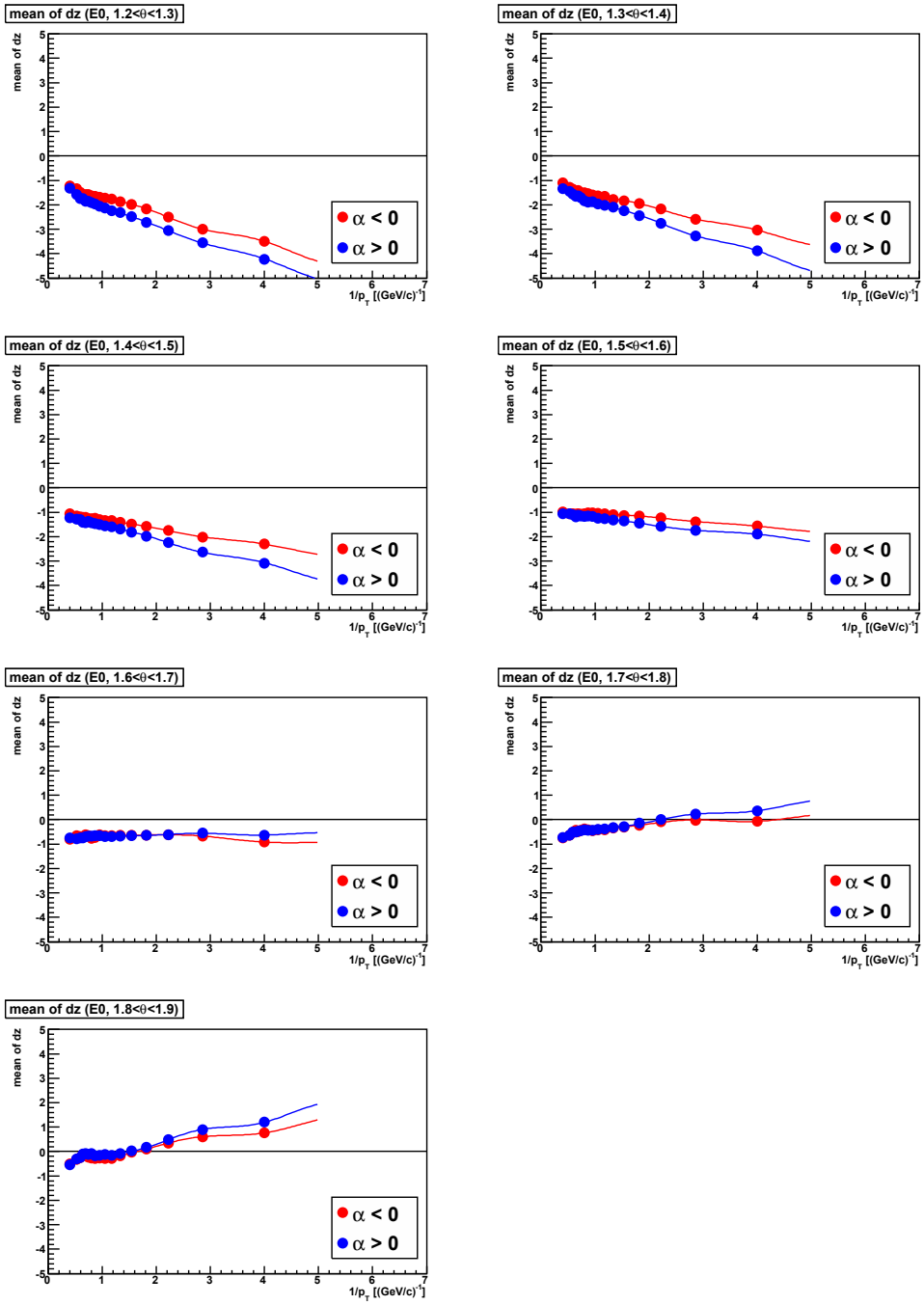

Figure D.1: The mean of dz before calibration for sector E0 (Real data).

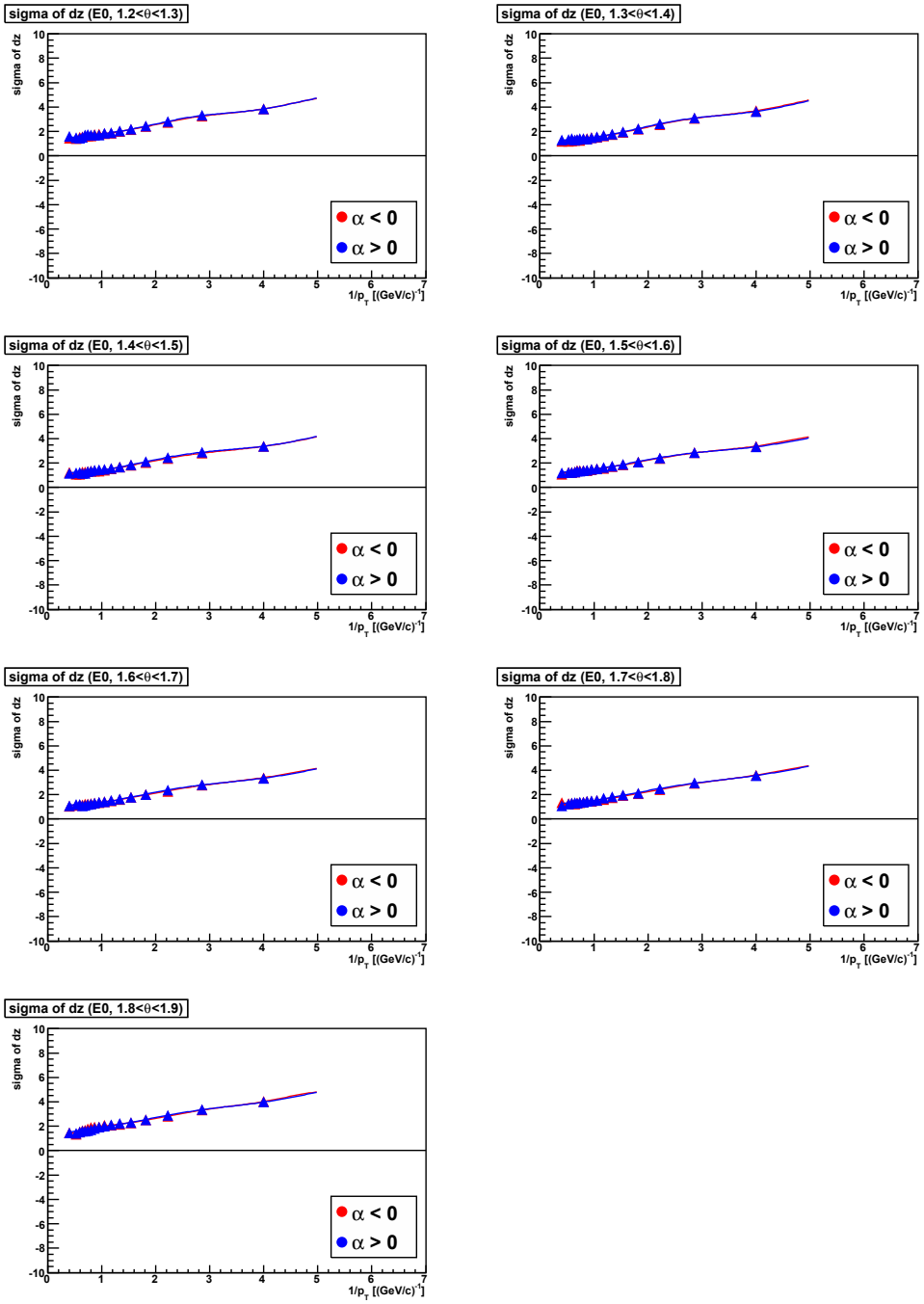

Figure D.2: The sigma of dz before calibration for sector E0 (Real data).

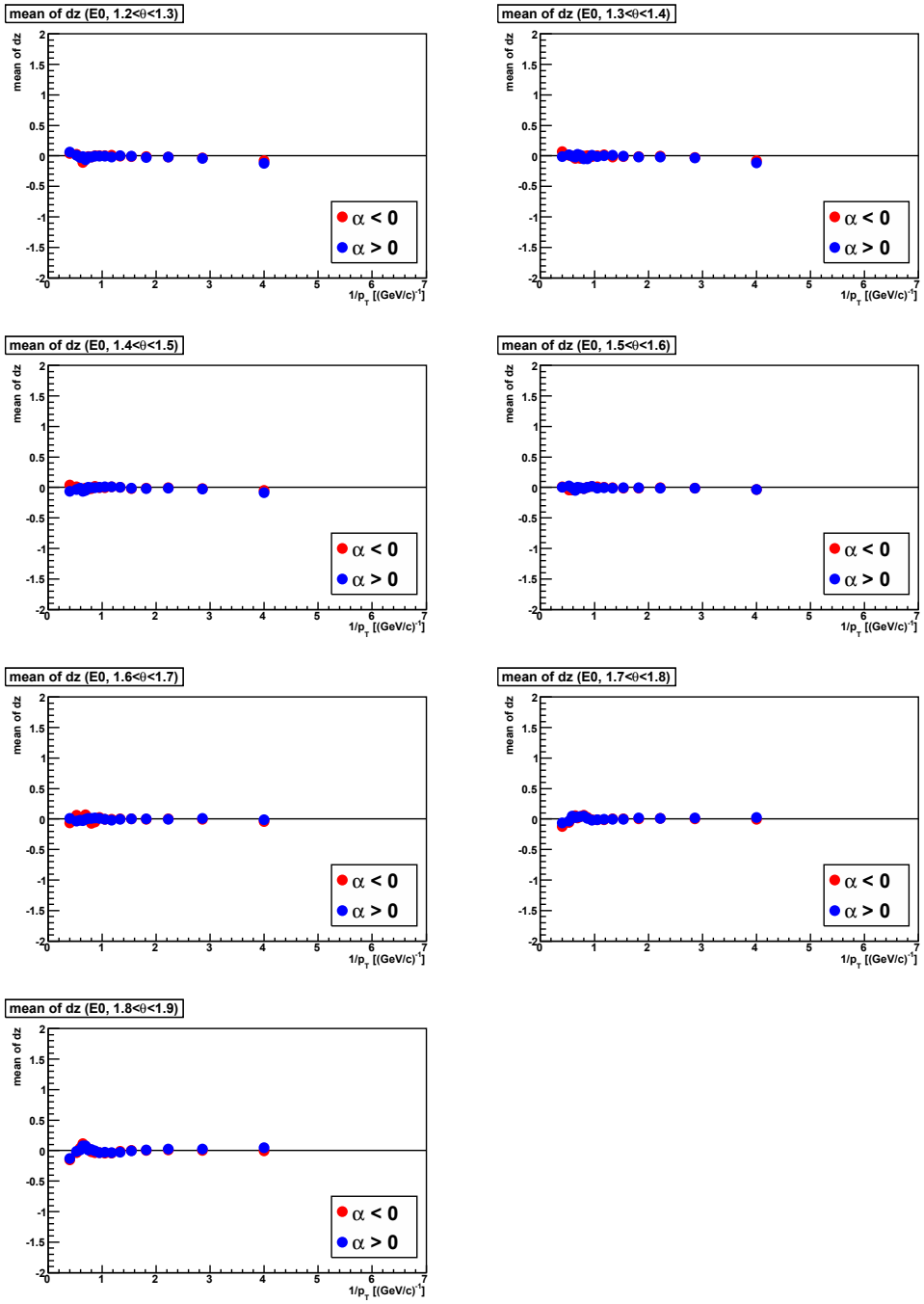

Figure D.3: The mean of dz after calibration for sector E0 (Real data).

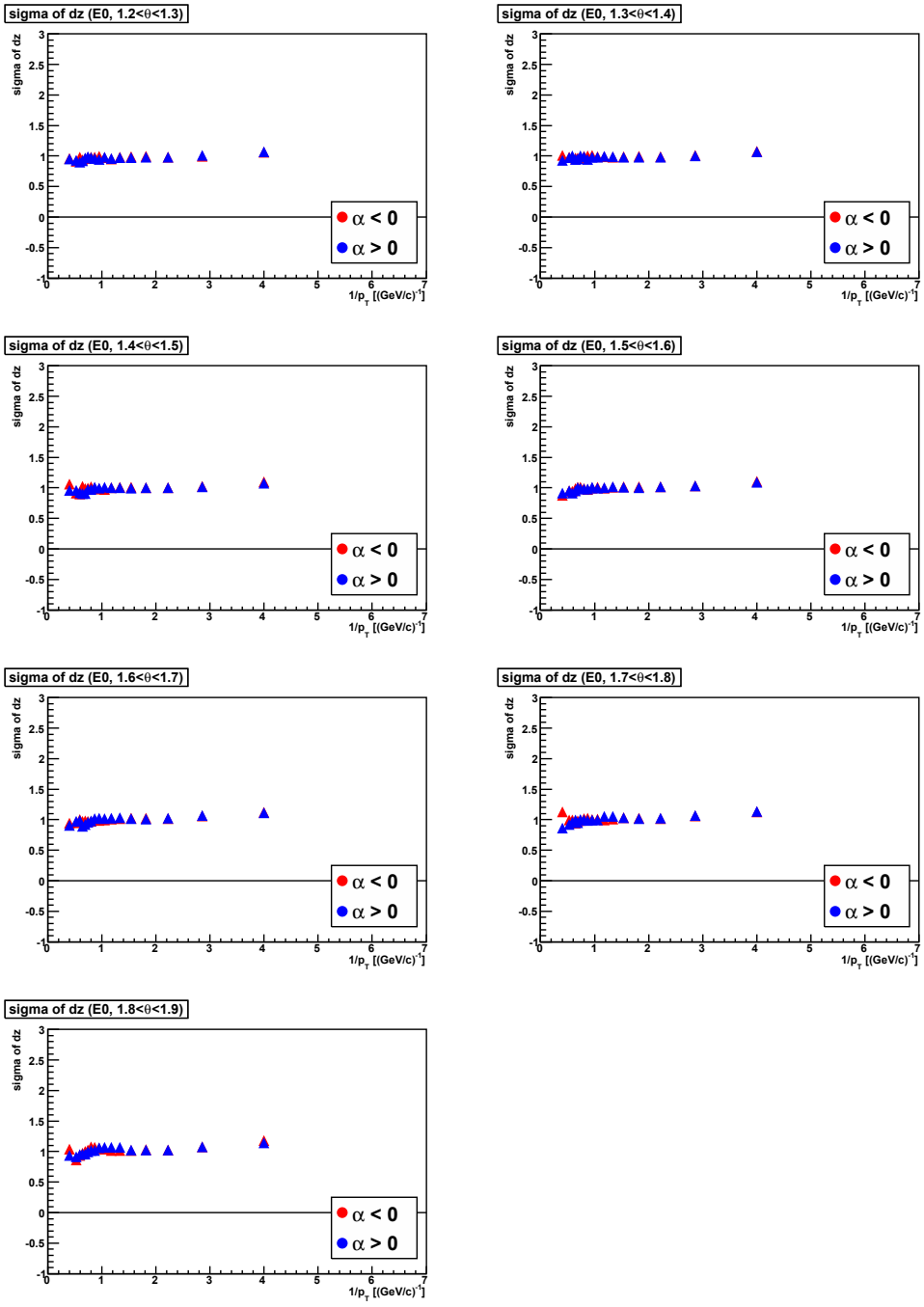

Figure D.4: The sigma of dz after calibration for sector E0 (Real data).

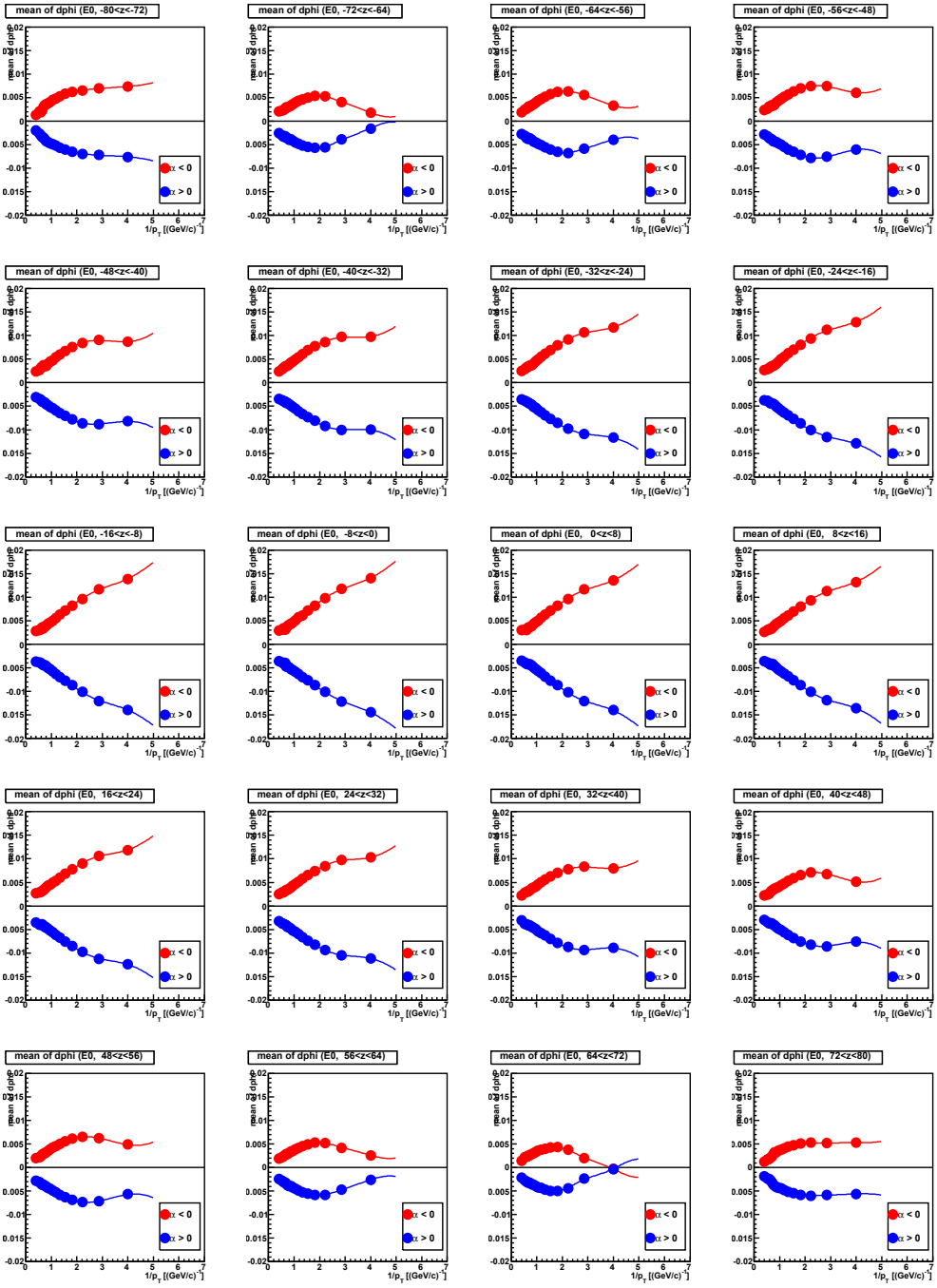

Figure D.5: The mean of *dphi* before calibration for sector E0 (Real data).

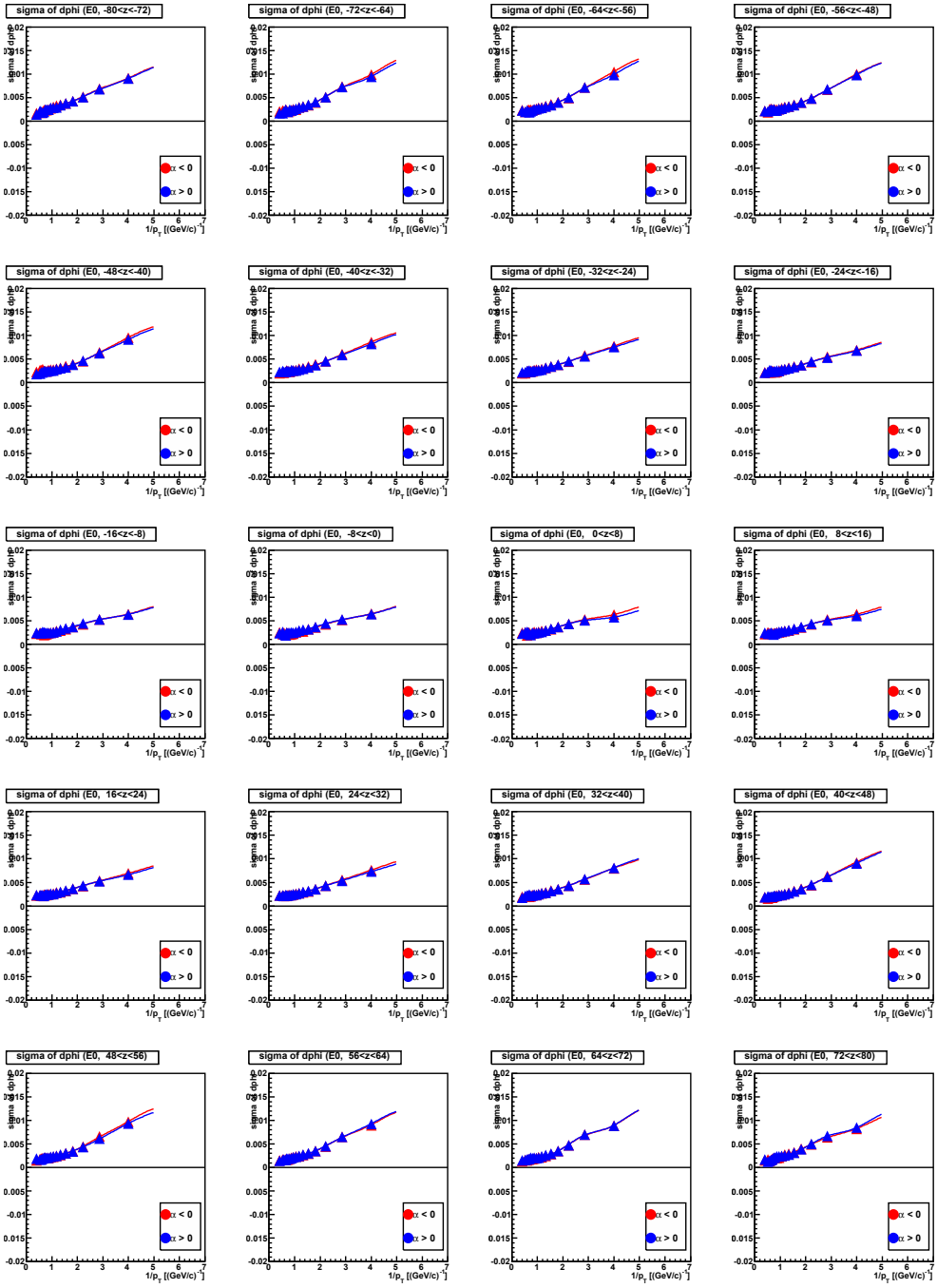

Figure D.6: The sigma of *dphi* before calibration for sector E0 (Real data).

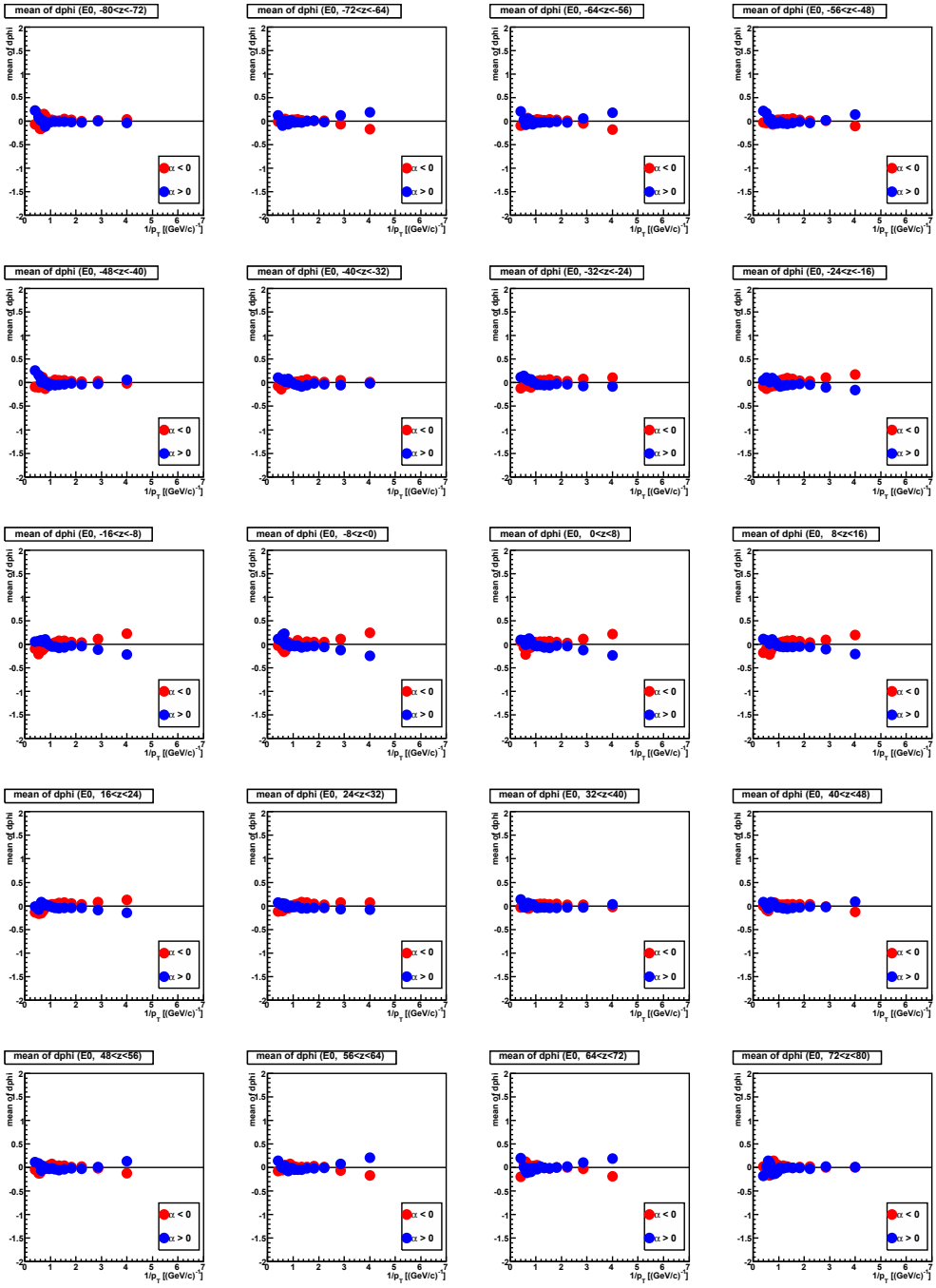

Figure D.7: The mean of *dphi* after calibration for sector E0 (Real data).

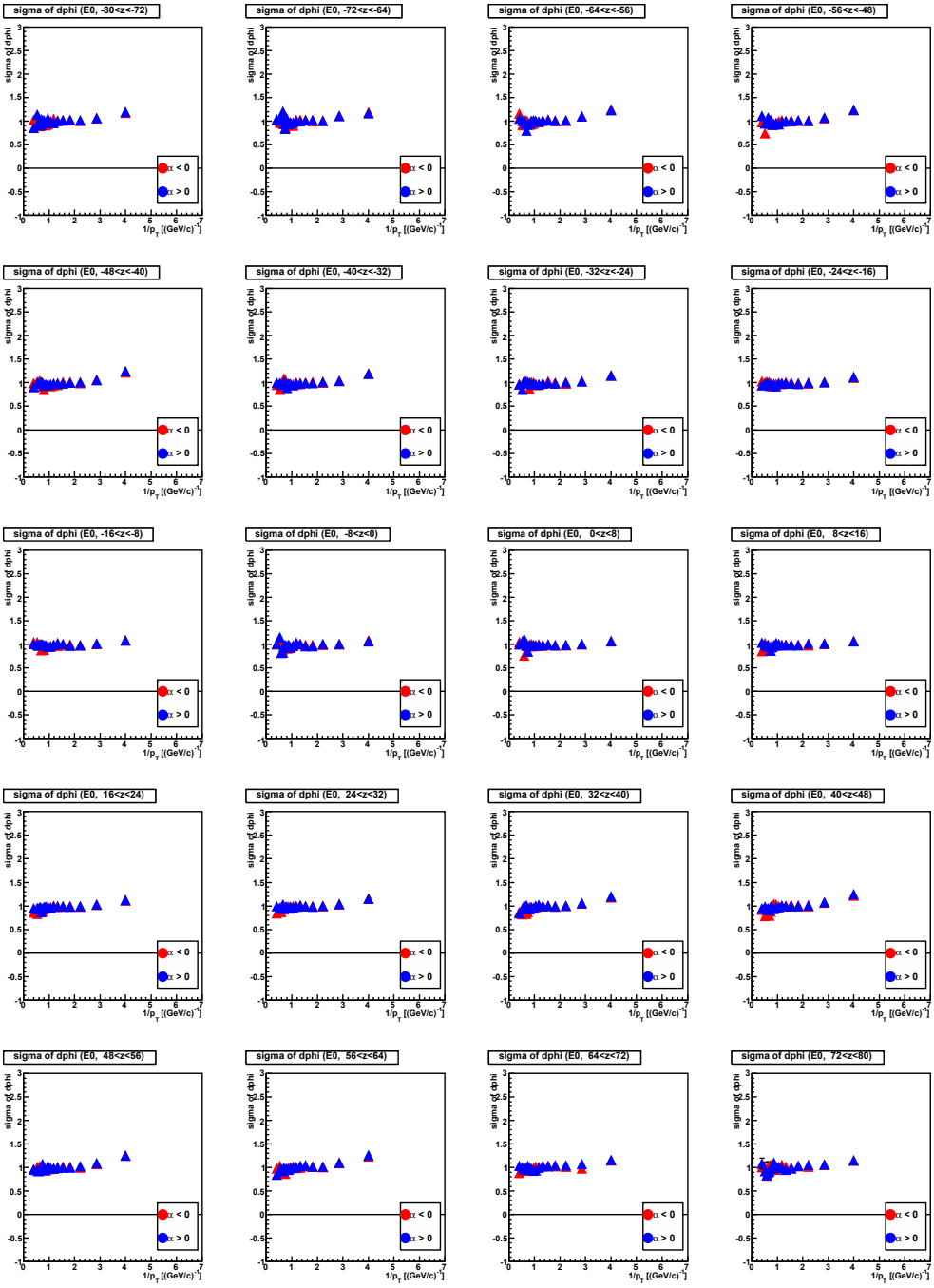

Figure D.8: The sigma of *dphi* after calibration for sector E0 (Real data).

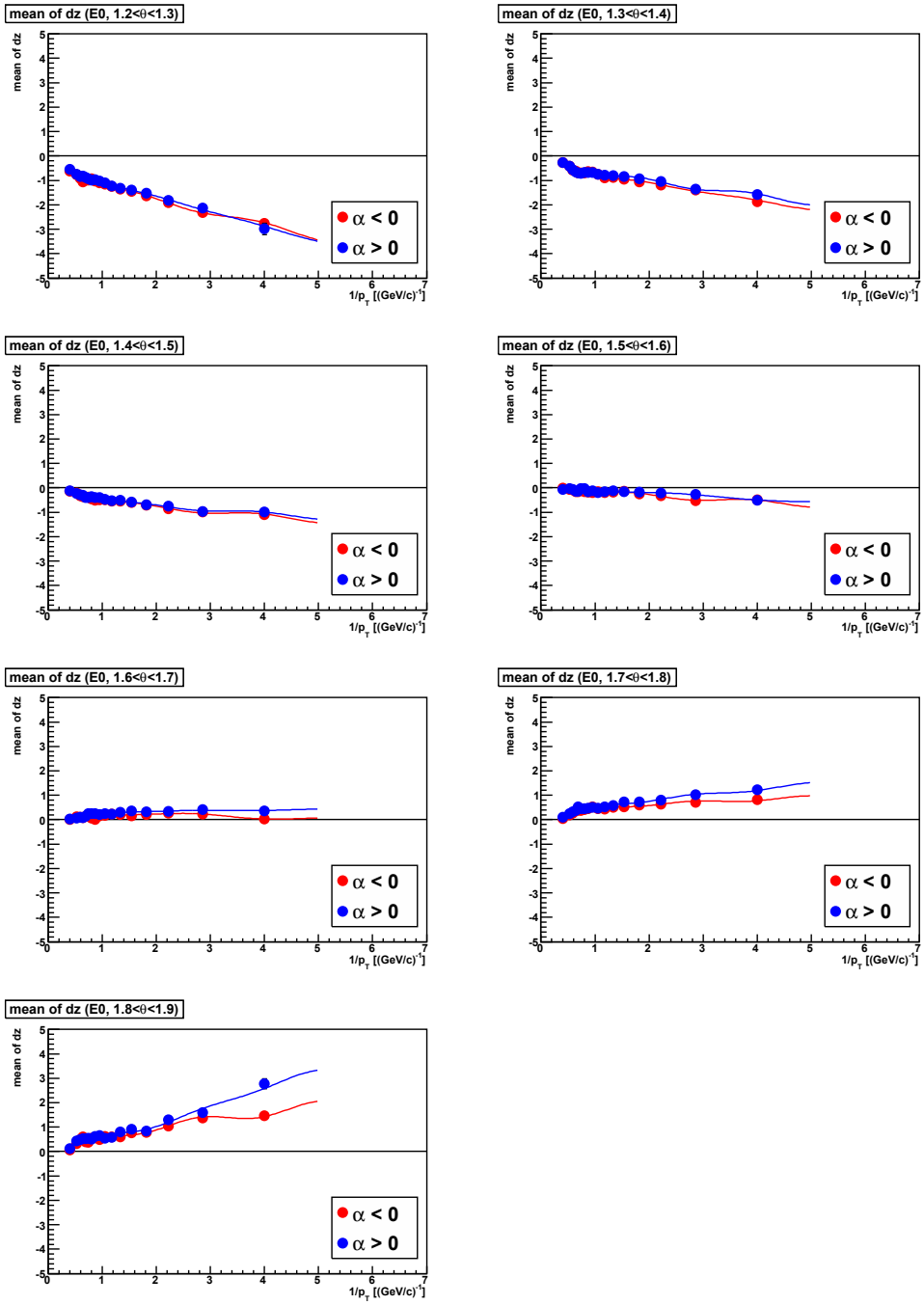

Figure D.9: The mean of dz before calibration for sector E0 (Simulation).

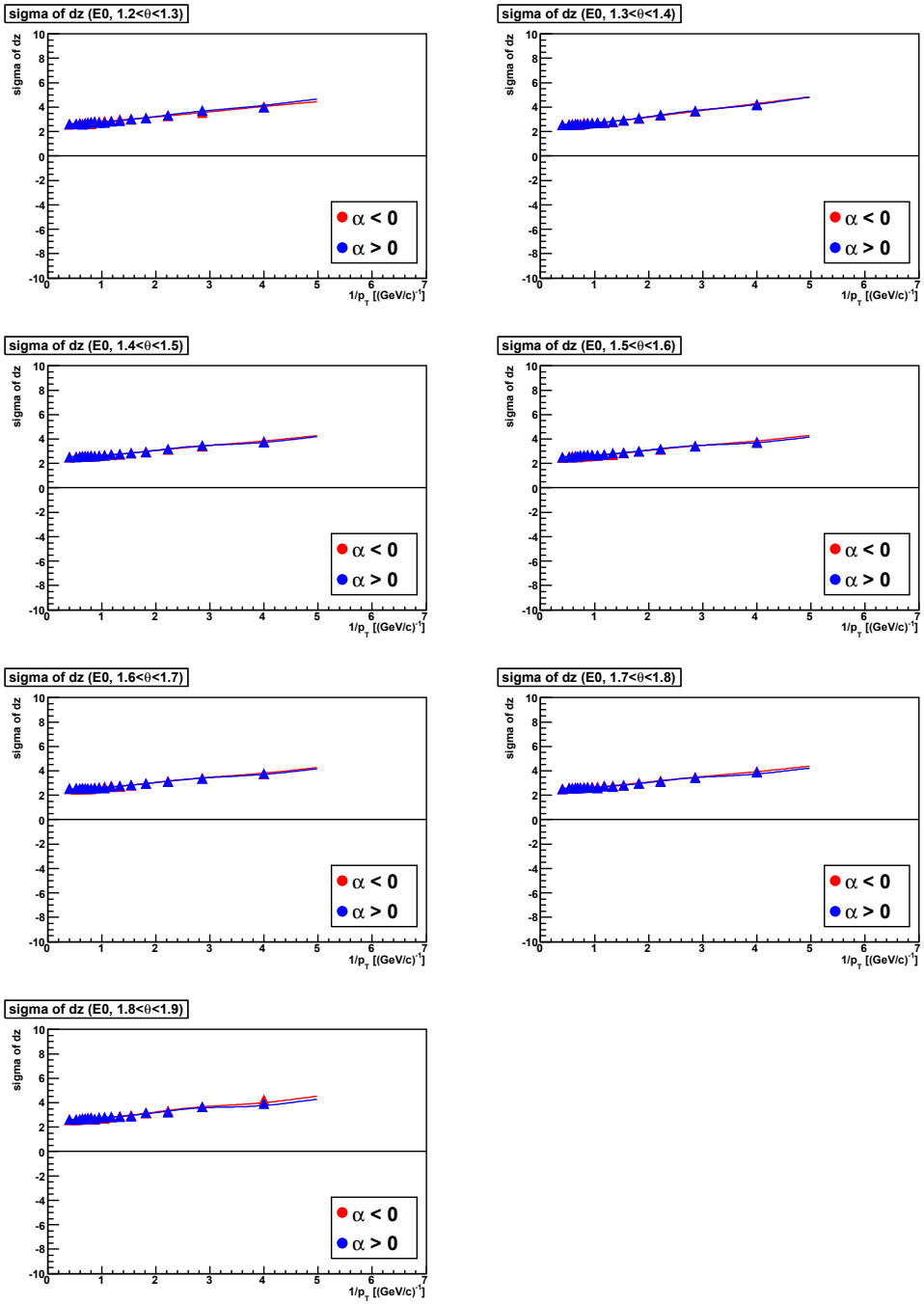

Figure D.10: The sigma of dz before calibration for sector E0 (Simulation).

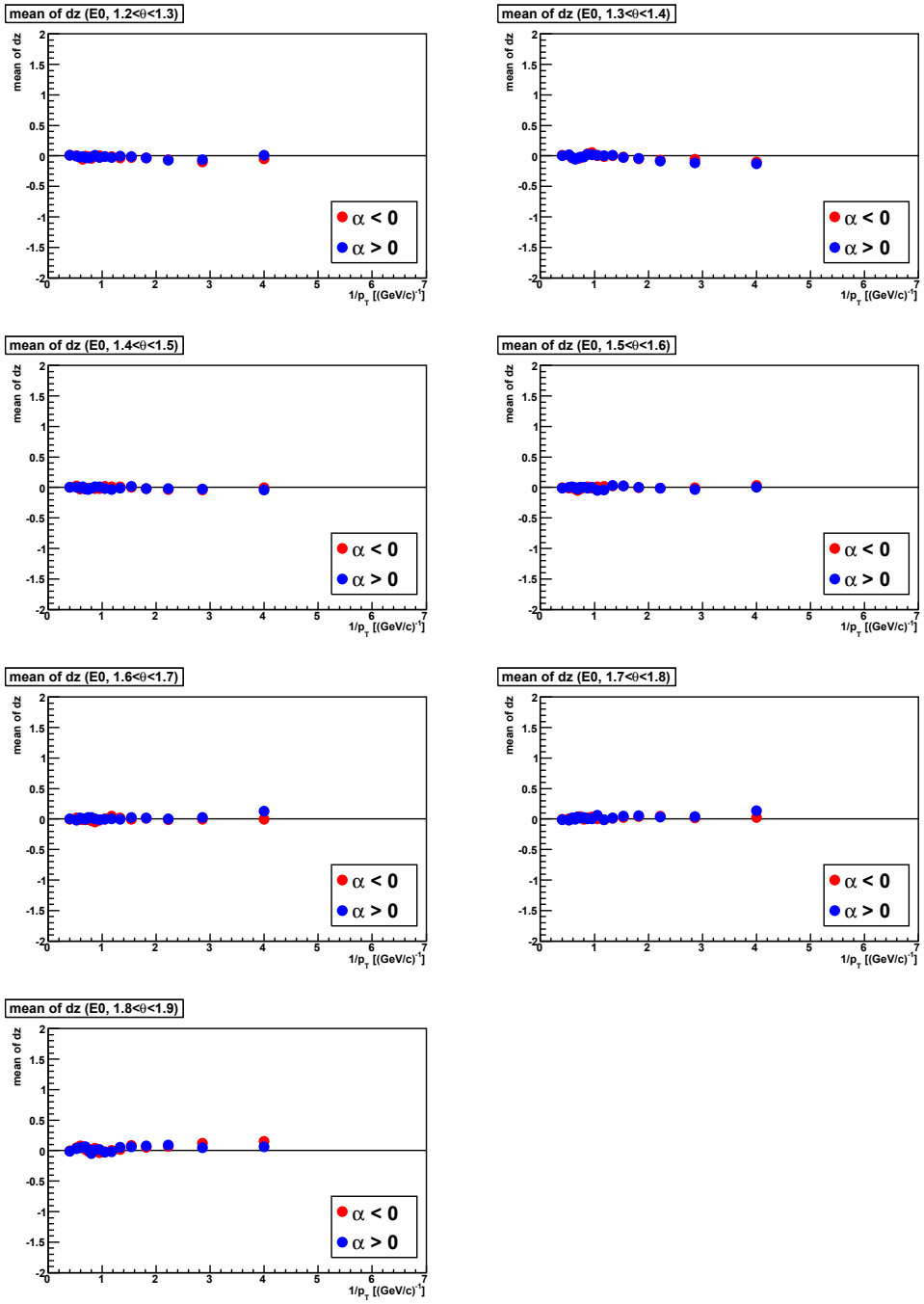

Figure D.11: The mean of dz after calibration for sector E0 (Simulation).

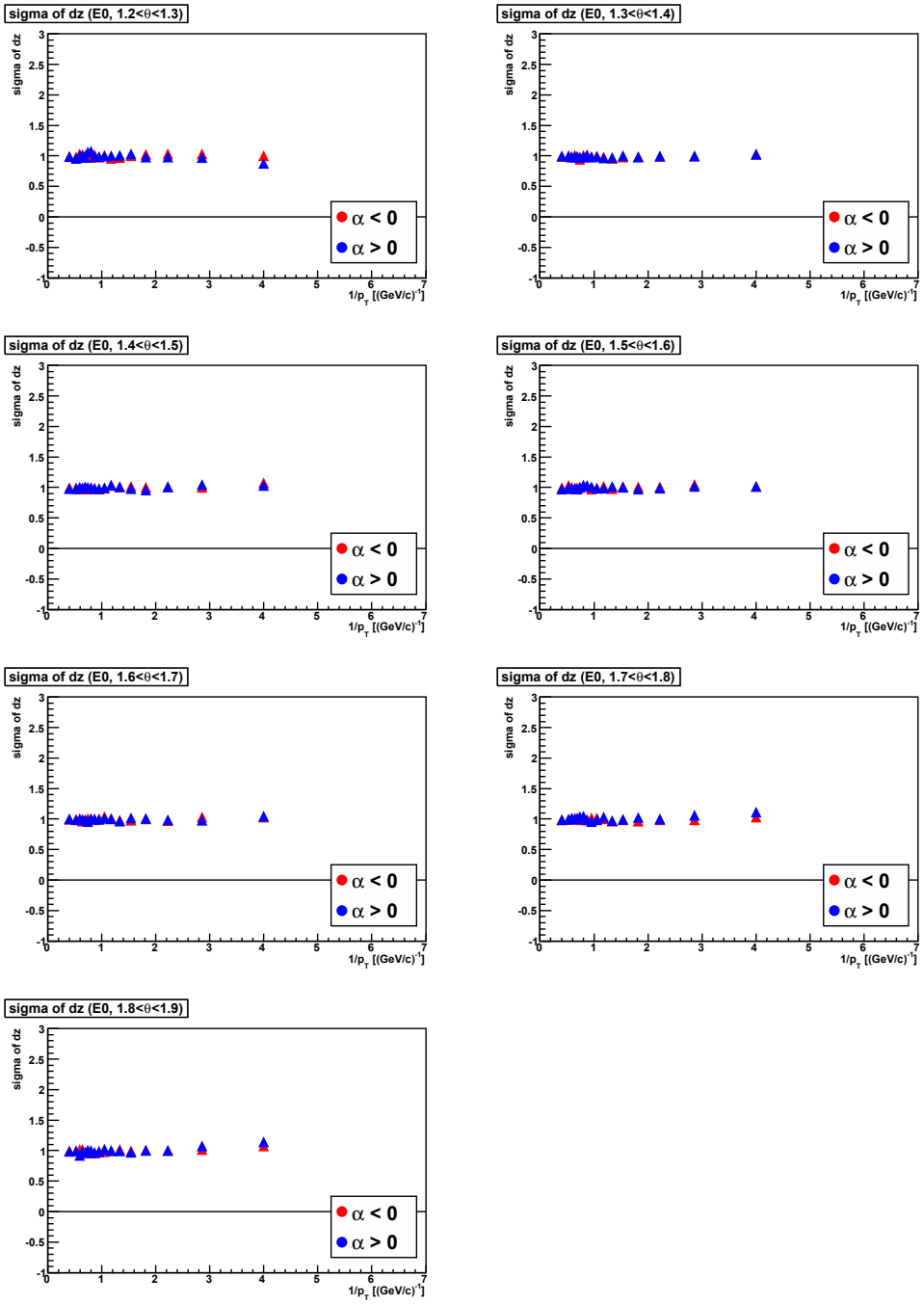

Figure D.12: The sigma of dz after calibration for sector E0 (Simulation).

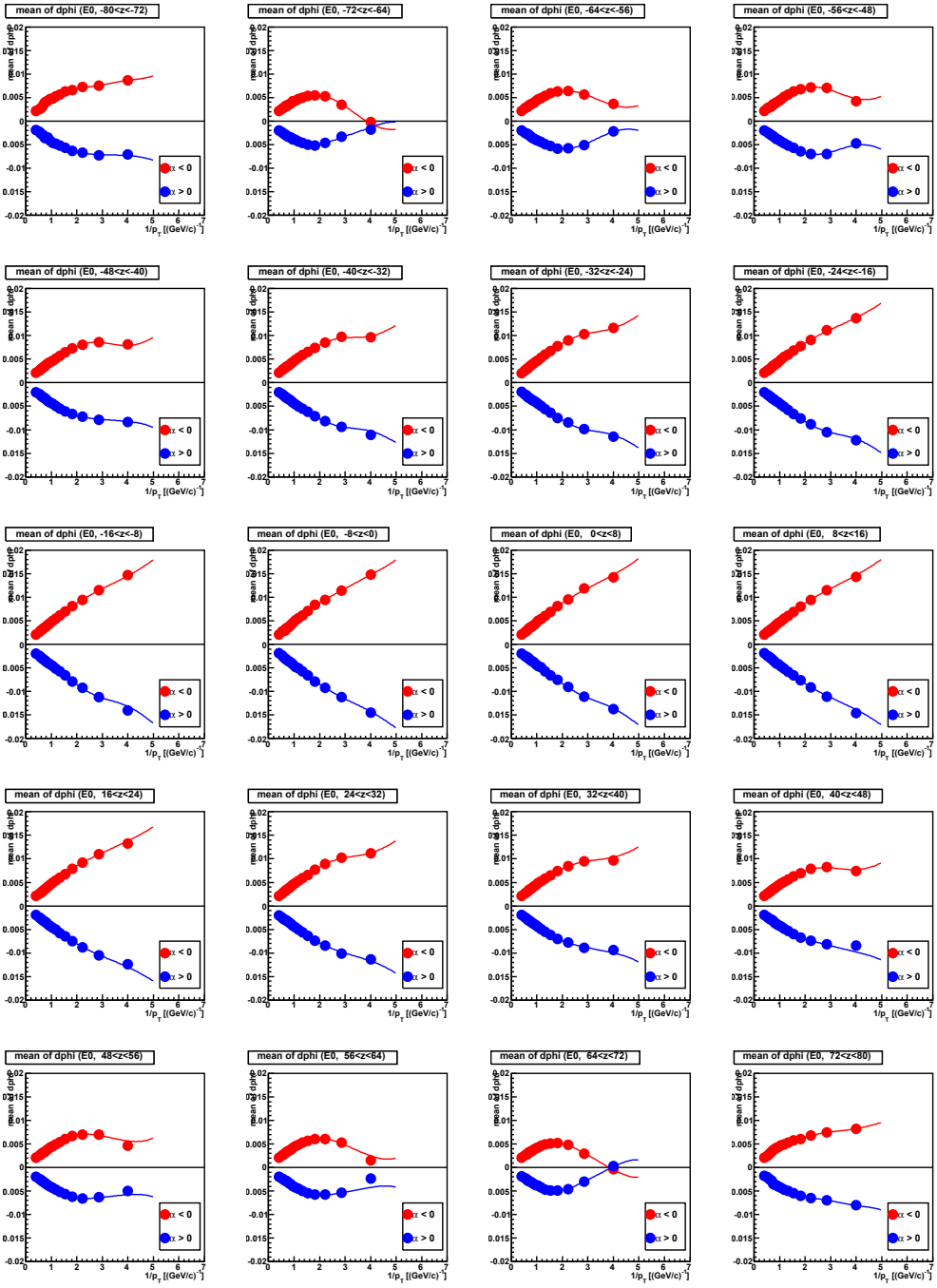

Figure D.13: The mean of *dphi* before calibration for sector E0 (Simulation).

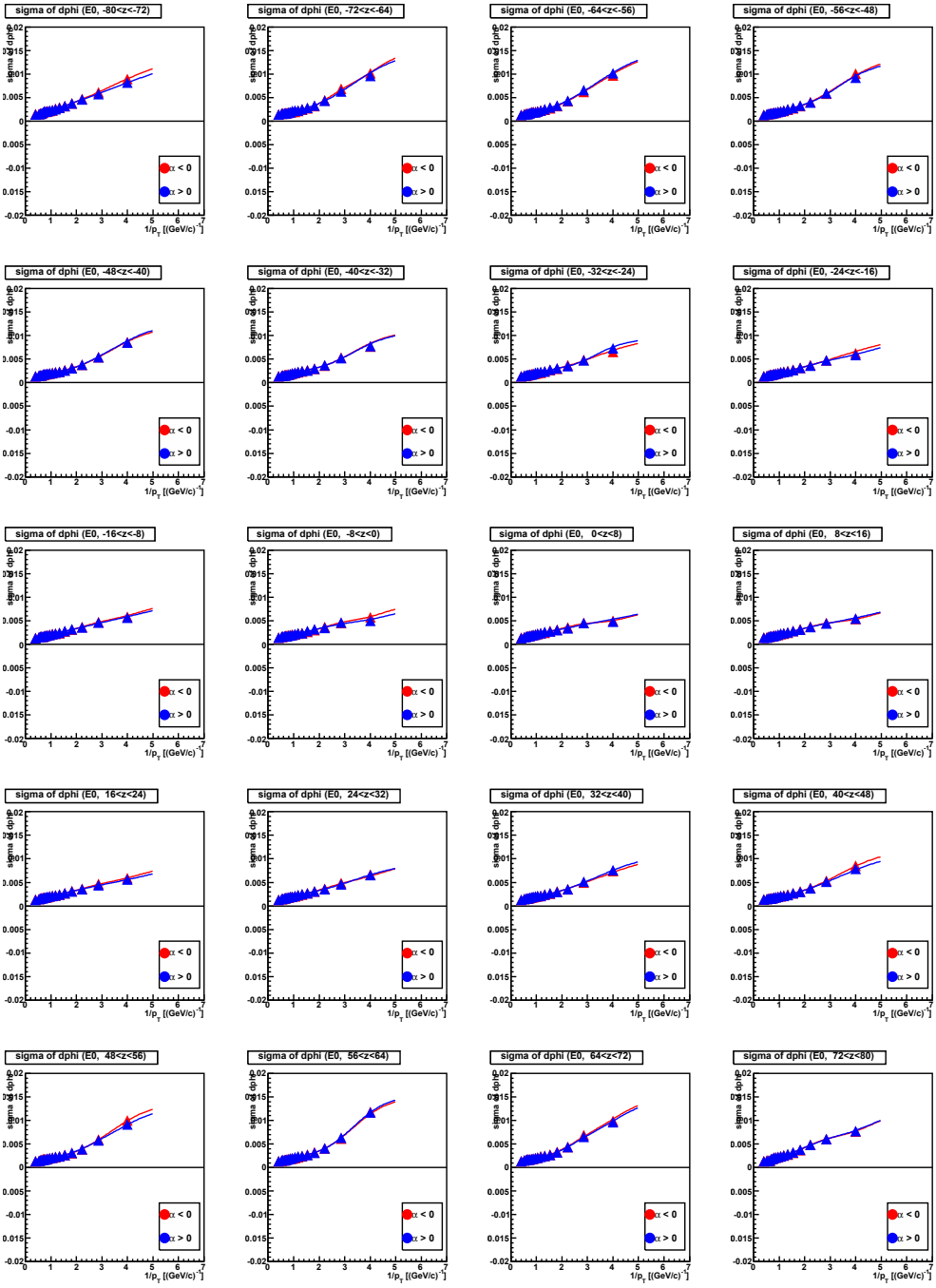

Figure D.14: The sigma of *dphi* before calibration for sector E0 (Simulation).

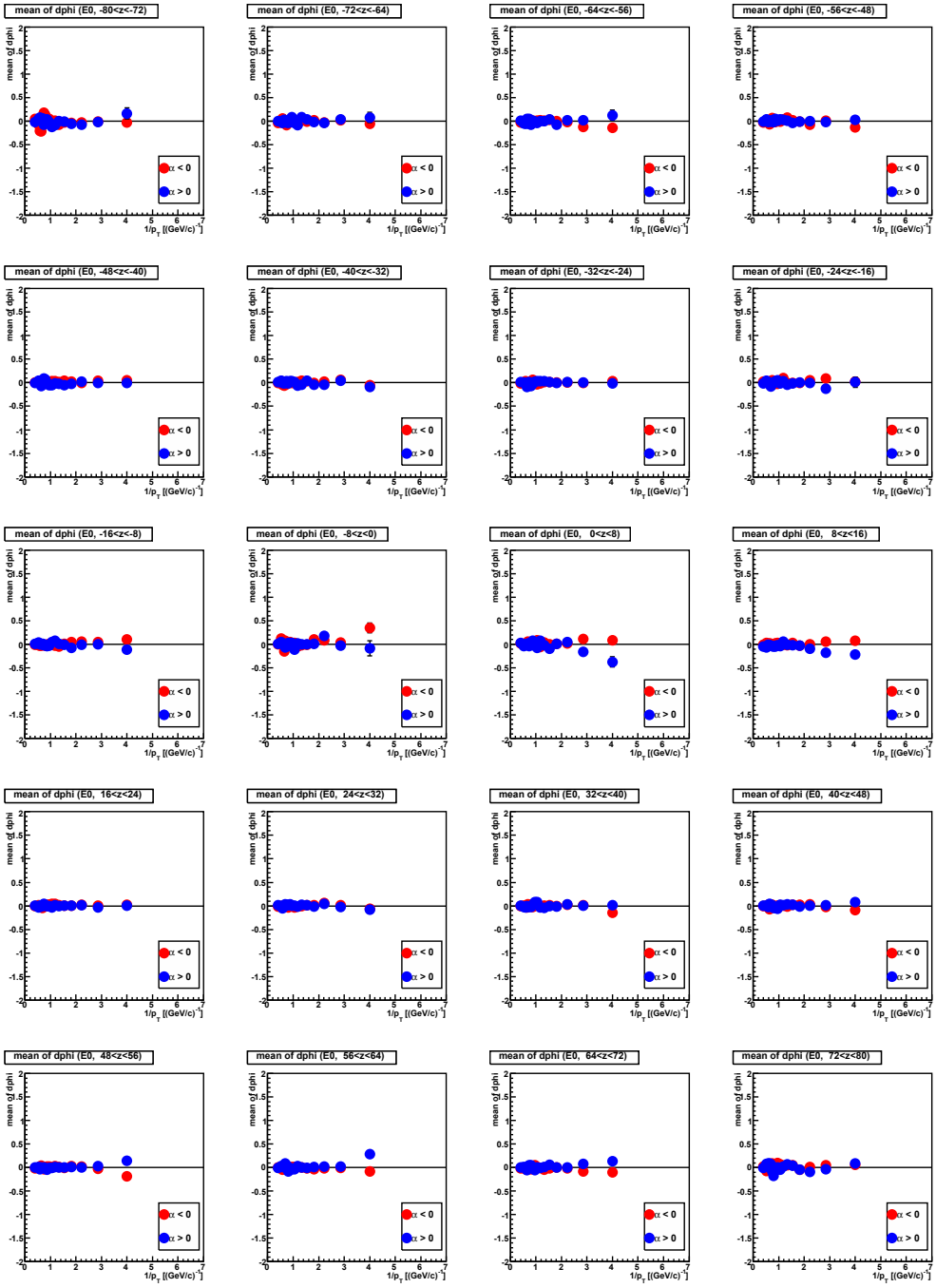

Figure D.15: The mean of *dphi* after calibration for sector E0 (Simulation).

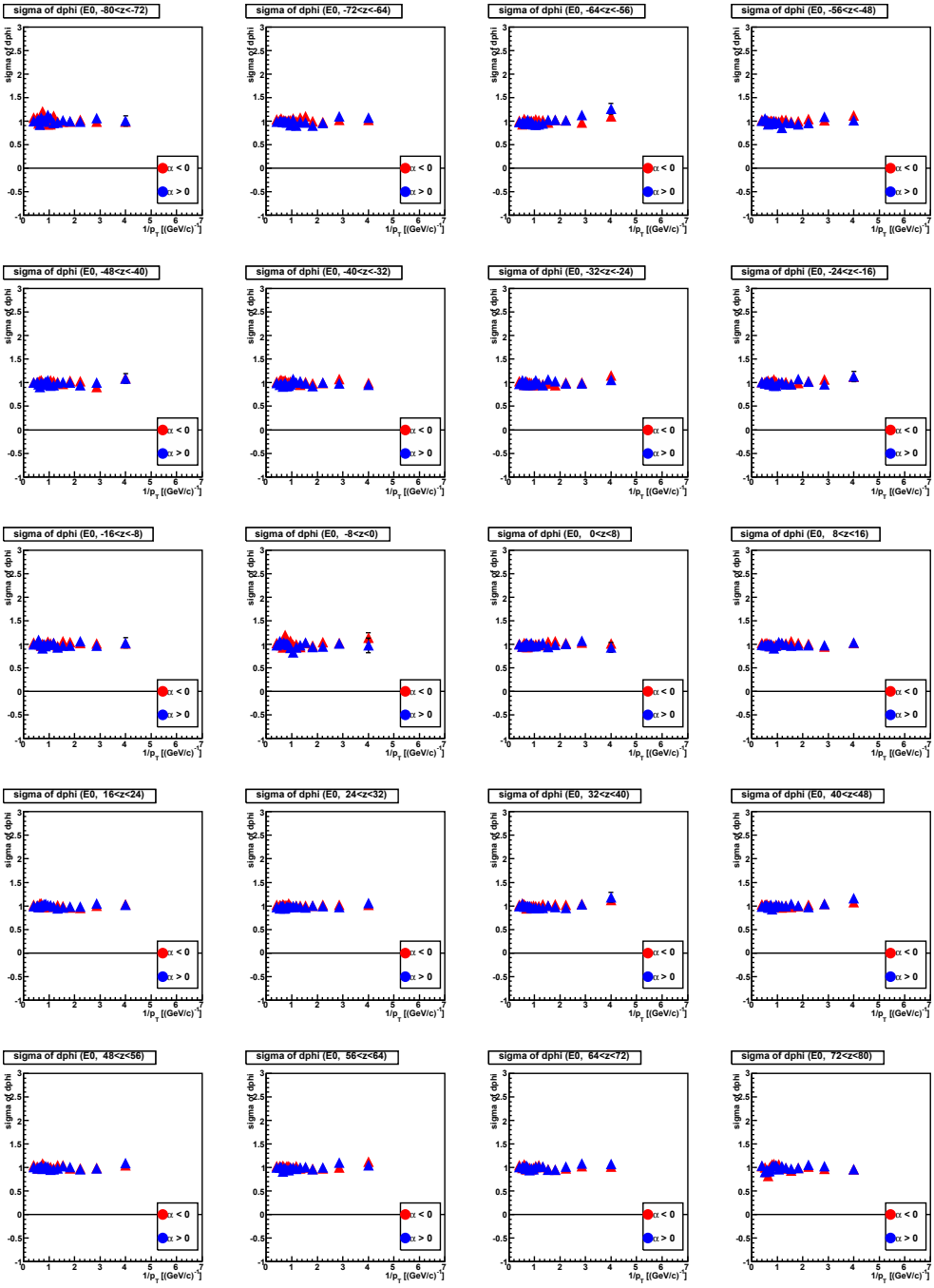

Figure D.16: The sigma of *dphi* after calibration for sector E0 (Simulation).

Appendix E

Energy-momentum matching calibration

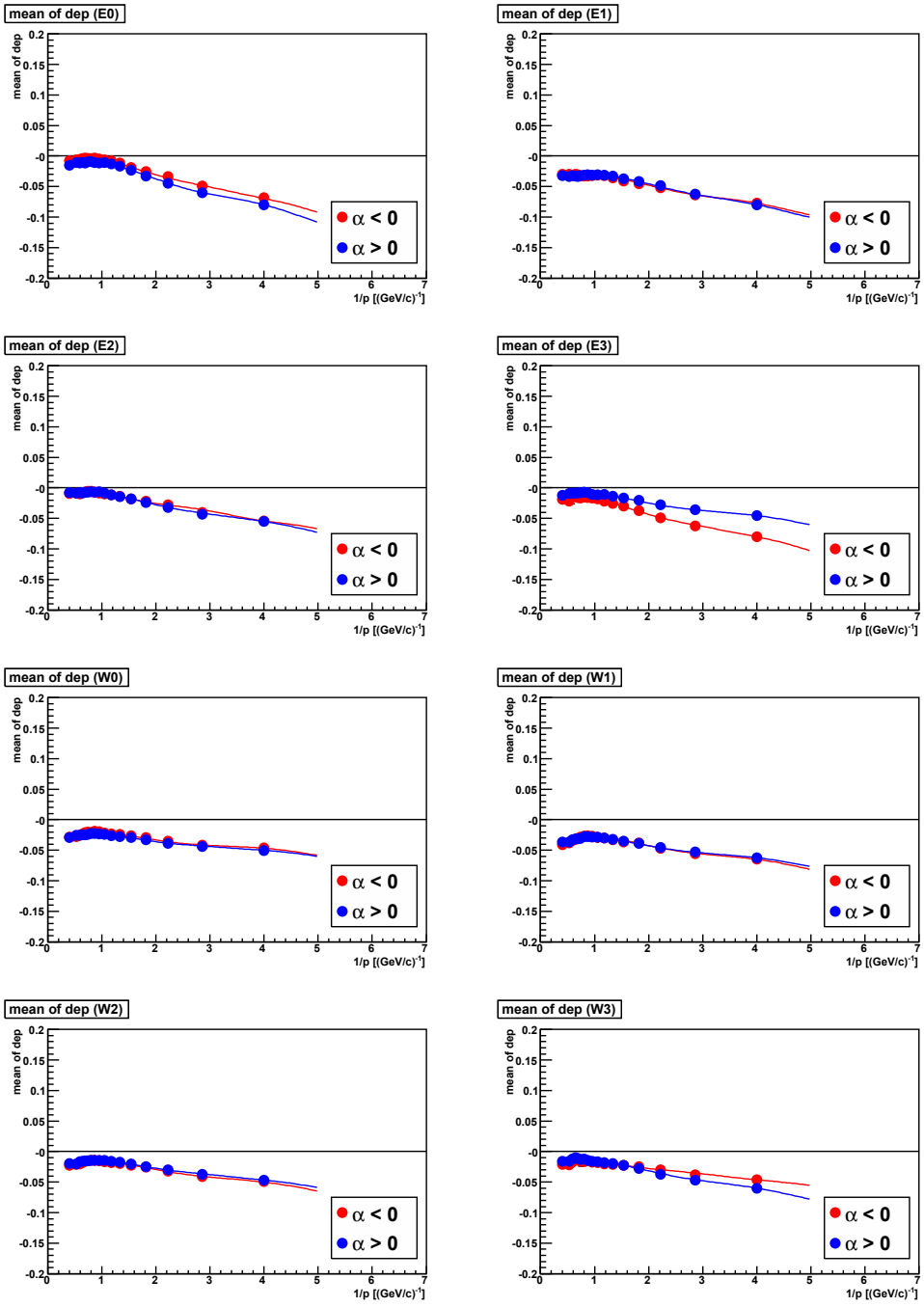

Figure E.1: The mean of $E/p-1$ before calibration for sector E0 (Real data).

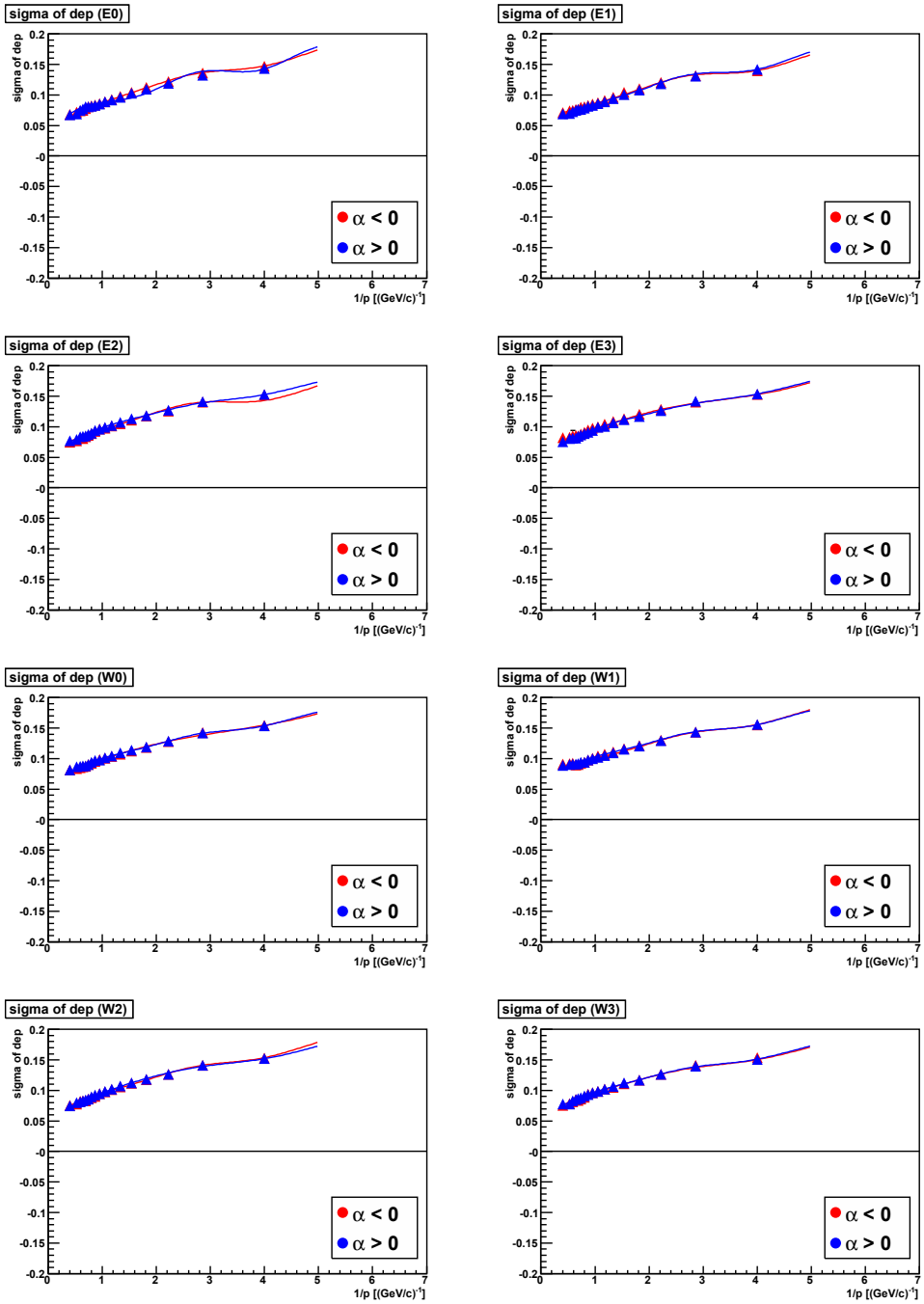

Figure E.2: The sigma of $E/p-1$ before calibration for sector E0 (Real data).

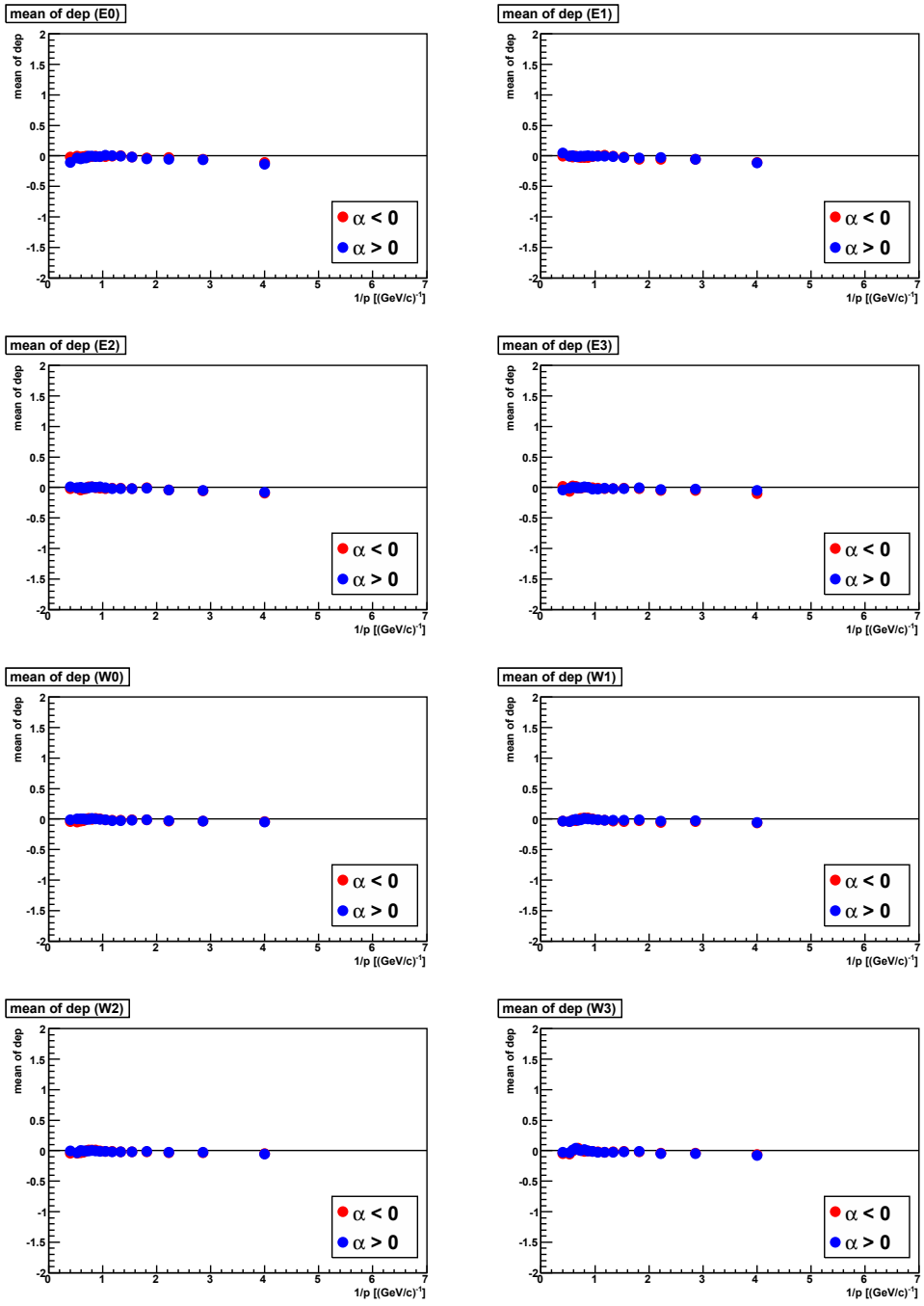

Figure E.3: The mean of $E/p - 1$ after calibration for sector E0 (Real data).

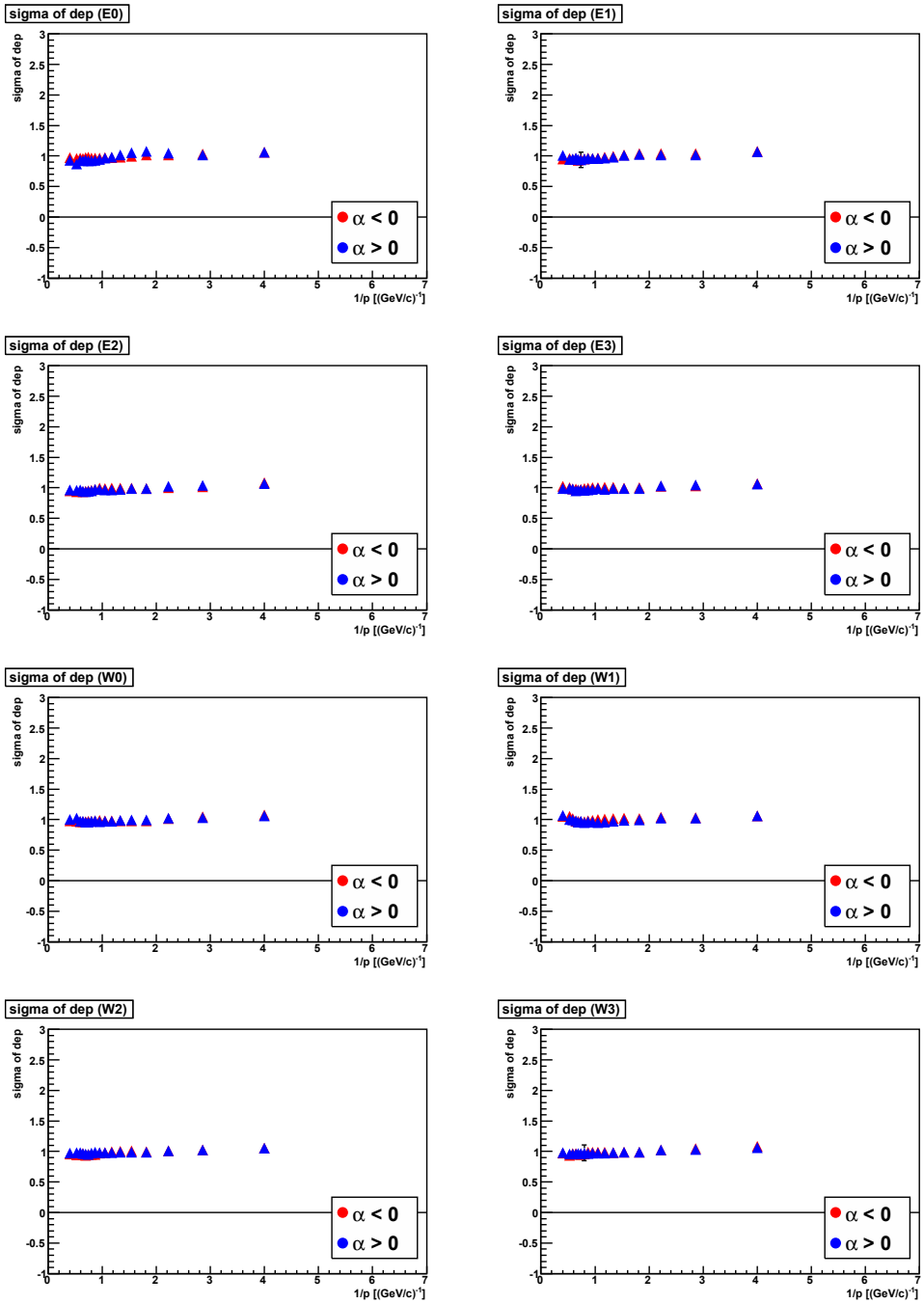

Figure E.4: The sigma of $E/p - 1$ after calibration for sector E0 (Real data).

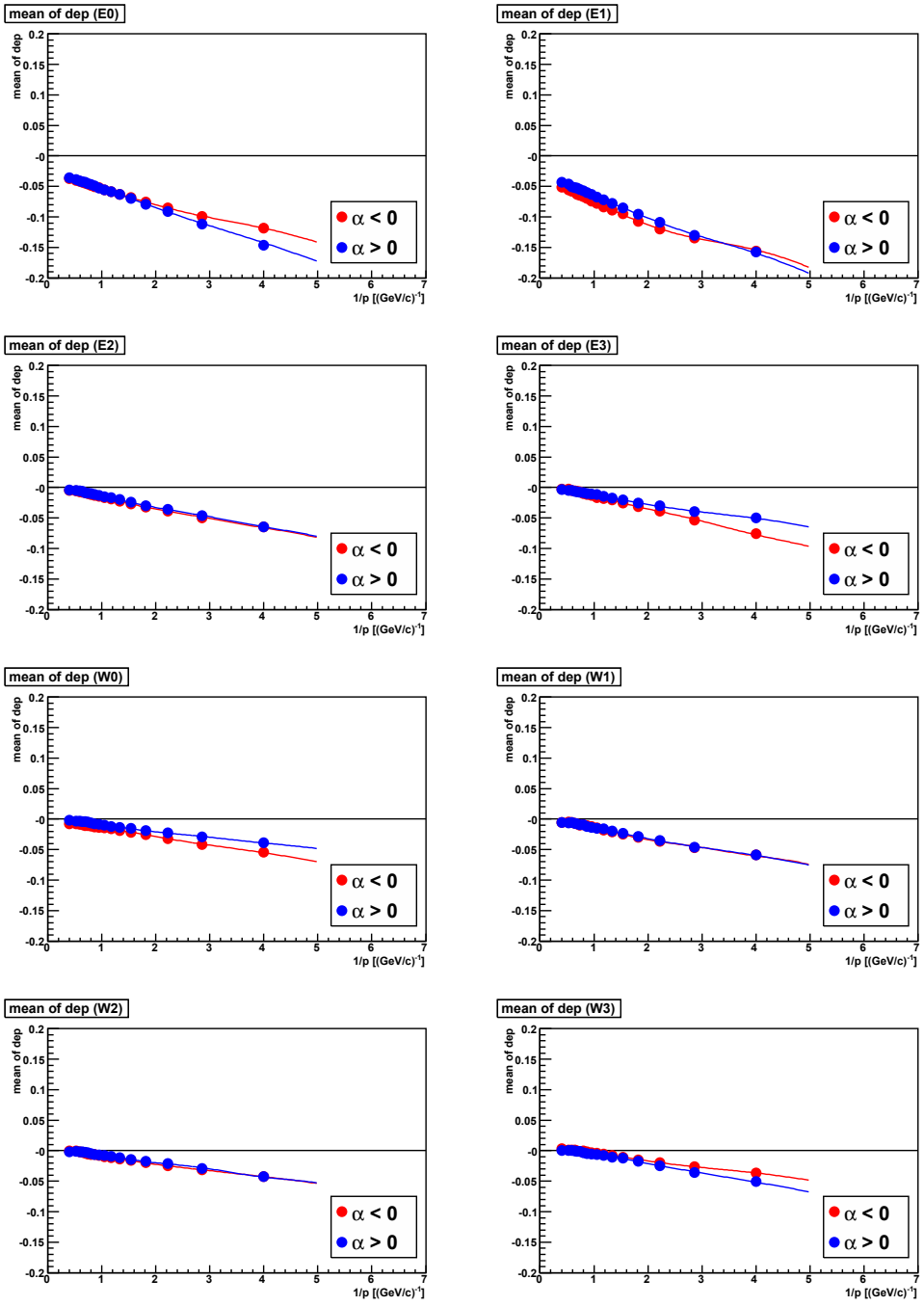

Figure E.5: The mean of *dep* before calibration for sector E0 (Simulation).

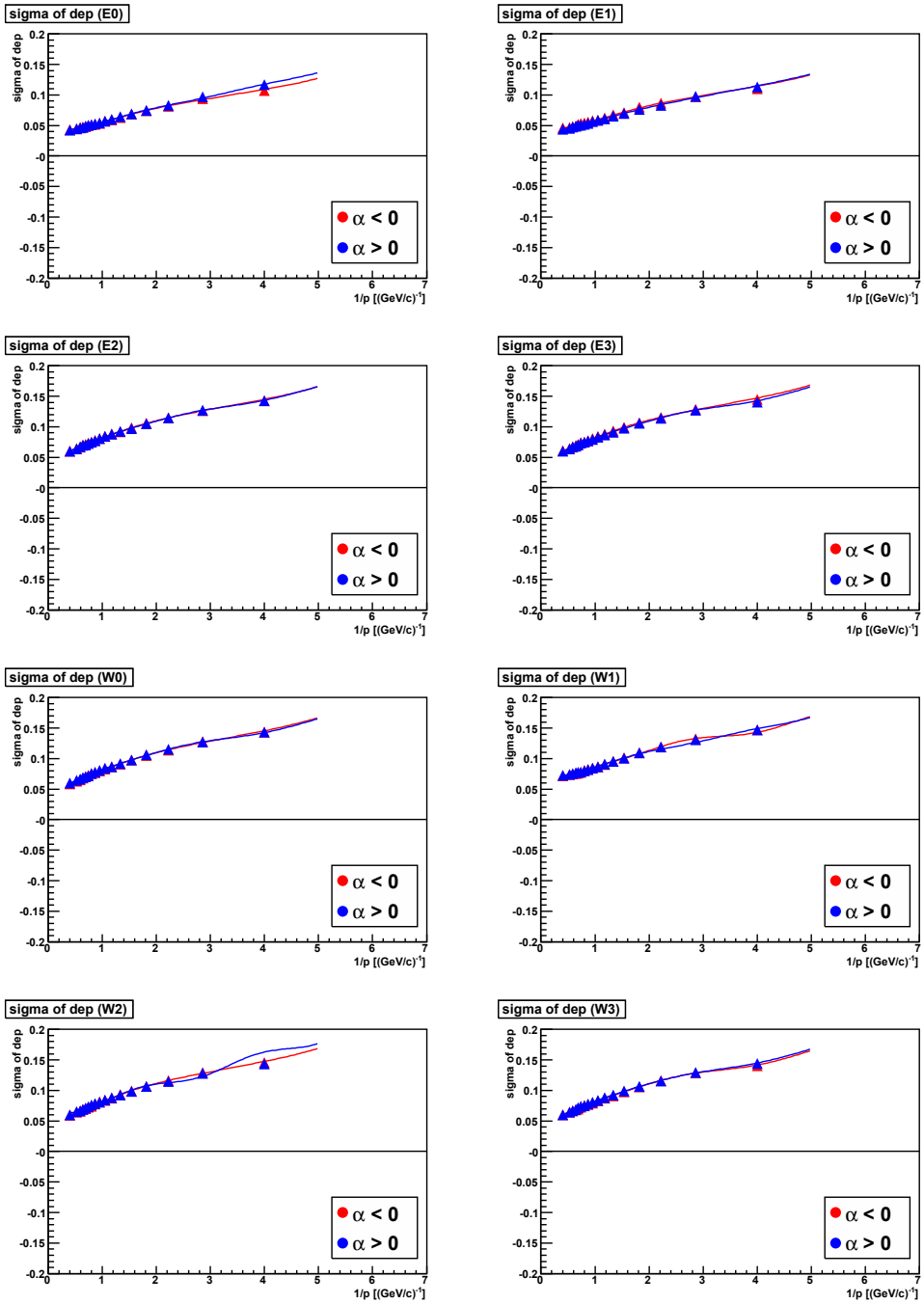

Figure E.6: The sigma of *dep* before calibration for sector E0 (Simulation).

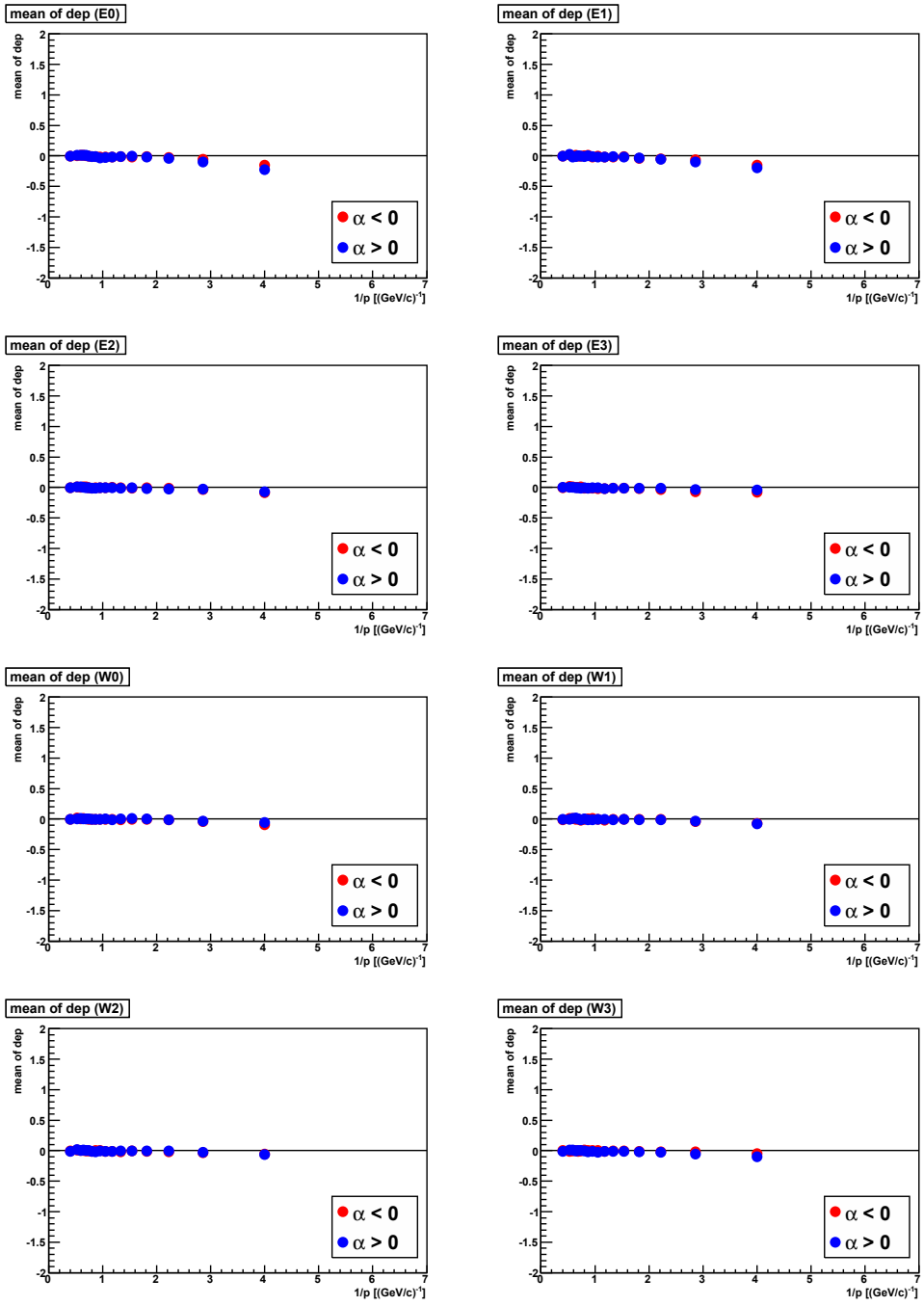

Figure E.7: The mean of *dep* after calibration for sector E0 (Simulation).

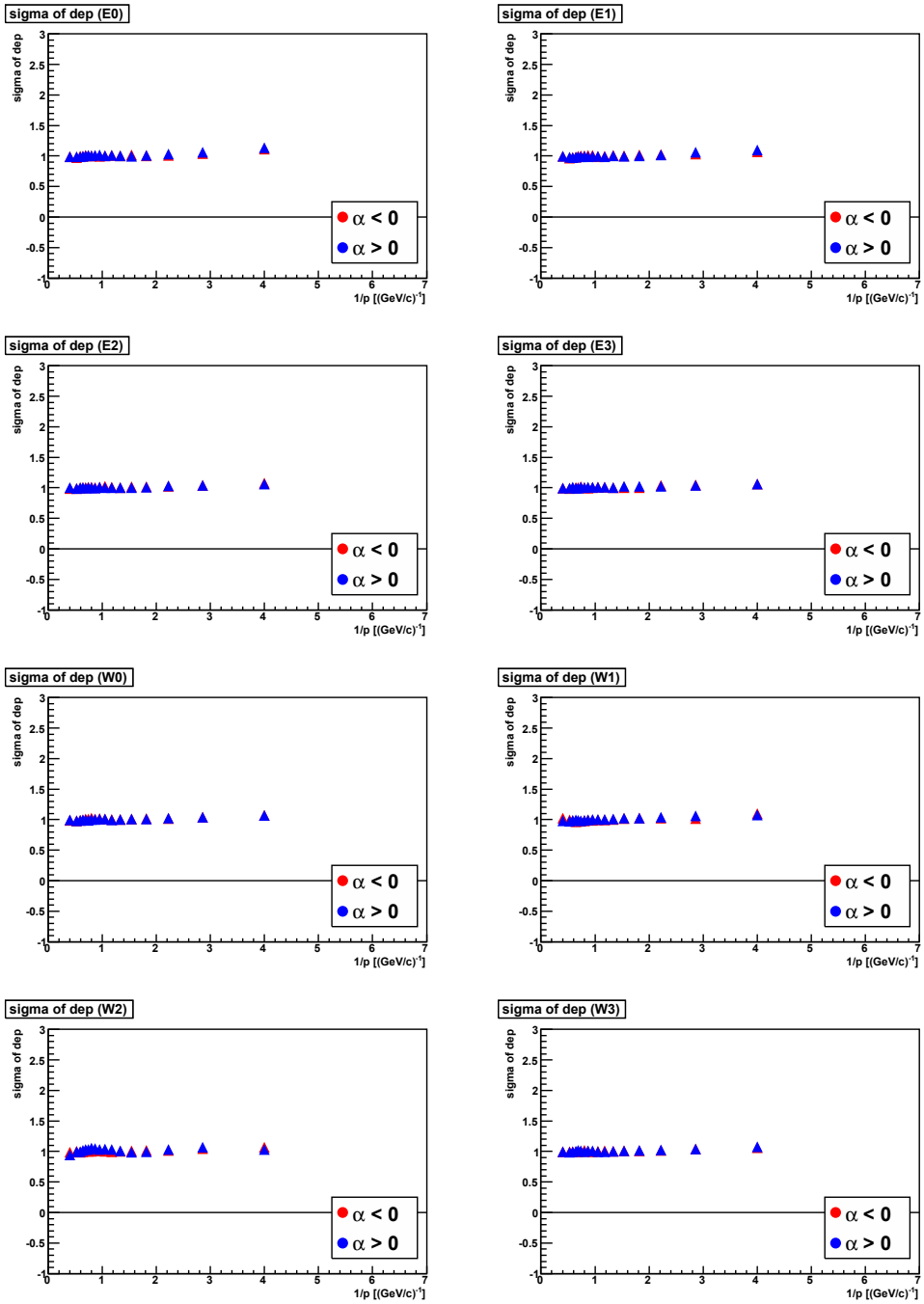

Figure E.8: The sigma of *dep* after calibration for sector E0 (Simulation).

Bibliography

[1] D. J. Gross and F. Wilczek, Phys. Rev. Lett. **30**, 1343 (1973).

[2] H. D. Politzer, Phys. Rev. Lett. **30**, 1346 (1973).

[3] S. Bethke, Eur. Phys. J. C **64**, 689 (2009).

[4] M. Gell-Mann, Phys. Lett. **8**, 214 (1964).

[5] G. Zweig, CERN-TH-401 (1964).

[6] G. Zweig, CERN-TH-412 (1964).

[7] M. Y. Han and Y. Nambu, Phys. Rev. **139**, B1006 (1965).

[8] O. W. Greenberg, Phys. Rev. Lett. **13**, 598 (1964).

[9] M. Gell-Mann, Il Nuovo Cimento **4**, 848 (1956).

[10] K. Nishijima, Prog. Theor. Phys. **13**, 285 (1955).

[11] T. Nakano and K.Nishijima, Prog. Theor. Phys. **10**, 581 (1953).

[12] K. Nakamura *et al.*, J. Phys. G **37**, 075021 (2010).

[13] C. Adloff *et. al*, Eur. Phys. J. C **21**, 33 (2001).

[14] C. Adloff *et. al*, Eur. Phys. J. C **30**, 1 (2003).

[15] S. Chekanov *et. al*, Eur. Phys. J. C **21**, 443 (2001).

[16] S. Chekanov *et. al*, Phys. Rev. D **70**, 052001 (2004).

[17] L. W. Whitlow *et. al*, Phys. Lett. B **282**, 475 (1992).

[18] A. C. Benvenuti *et. al*, Phys. Lett. B **223**, 485 (1989).

[19] M. R. Adams *et. al*, Phys. Rev. D **54**, 3006 (1996).

[20] M. Arneodo *et. al*, Nucl. Phys. B **483**, 3 (1997).

[21] J. J. Aubert *et. al*, Nucl. Phys. B **256**, 3 (1985).

[22] G. Curti *et. al*, Nucl. Phys. B **175**, 27 (1982).

[23] M. Cacciari and S. Catani, Nucl. Phys. B **617**, 253 (2001).

[24] J. Blumlein and V. Ravindran, Phys. Lett. B **640**, 40 (2006).

[25] S. Moch and A. Vogt, Phys. Lett. B **680**, 239 (2009).

[26] B. L. Combridge, J. Kripfganz and J. Ranft, Phys. Lett. B **70**, 34 (1977).

[27] D. Buskulic *et. al*, Z. Phys. C **73**, 409 (1997).

[28] E. Barate *et. al*, Phys. Reports **294**, 1 (1998).

[29] B. Adeva *et. al*, Phys. Lett. B **259**, 199 (1991).

[30] Y. K. Li *et. al*, Phys. Rev. D **41**, 2675 (1990).

[31] D. Bender *et. al*, Phys. Rev. D **31**,1 (1984).

[32] G. S. Abrams *et. al*, Phys. Rev. Lett. **64**, 1334 (1990).

[33] A. Peterson *et. al*, Phys. Rev. D **37**, 1 (1988).

[34] R. Akers *et. al*, Z. Phys. C **72**, 191 (1996).

[35] K. Ackerstaff *et. al*, Z. Phys. C **75**, 193 (1997).

[36] K. Ackerstaff *et. al*, Eur. Phys. J. C **7**, 369 (1998).

[37] G. Abbiendi *et. al*, Eur. Phys. J. C **16**, 185 (2000).

[38] G. Abbiendi *et. al*, Eur. Phys. J. C **27**, 467 (2003).

[39] G. Abbiendi *et. al*, Eur. Phys. J. C **37**, 25 (2004).

[40] K. Abe *et. al*, Phys. Rev. D **69**, 072003 (2004).

[41] P. Abreu *et. al*, Phys. Lett. B**398**, 194 (1997).

[42] R. Brandelik *et. al*, Phys. Lett. B **114**, 65 (1982).

[43] W.Braunschweig *et. al*, Z. Phys. C **47**, 187 (1990).

[44] H. Aihara *et. al*, Phys. Rev. Lett. **61**, 1263 (1988).

[45] The RHIC homepage.

[46] B. Alver et al., Phys. Rev. C **83**, 024913 (2011).

[47] K. Aamodt et. al., Phys. Rev. Lett. **105**, 252301 (2010).

[48] I. G. Bearden *et al.*, Phys. Rev. Lett. **93**, 102301 (2004)

[49] R. J. Glauber and G. Matthiae, Nucl. Phys. B **21**, 135 (1970).

[50] M. L. Miller, K. Reygers, S. J. Sanders, and P. Steinberg, Annu. Rev. Nucl. Part. Sci. **57**, 205 (2007).

[51] K. Reygers *et al.*, PHENIX Analysis Note **169** (2003).

[52] D. Sharma, Ph.D. thesis at Weizmann Institute (2010).

[53] P. Kolb, Acta Phys. Hung. A **21**, 243 (2004).

[54] J. D. Bjorken, Phys. Rev. D **27**, 140 (1983).

[55] L. Ahle *et al.*, Phys. Lett. B **332**, 258 (1994).

[56] T. Alber *et al.*, Phys. Rev. Lett. **75**, 3814 (1995).

[57] K. Adkox *et al.*, Phys. Rev. Lett. **87**, 052301 (2001).

[58] S. S. Adler *et al.*, Phys. Rev. C **71**, 034908 (2005).

[59] S. S. Adler *et al.*, Phys. Rev. C **71**, 049901 (2005).

[60] H. Yagi, T. Hatsuda and Y. Miake, "Quark-Gluon Plasma: From Big Bang to Little Bang", Cambridge University Press (2005).

[61] M. A. Shifman, A. I. Vainstein and V. I. Zakharov, Nucl. Phys. B **147**, 385 (1979).

[62] M. A. Shifman, A. I. Vainstein and V. I. Zakharov, Nucl. Phys. B **147**, 448 (1979).

[63] A. Chodos *et al.*, Phys. Rev. D **9**, 3471 (1974).

[64] A. Chodos *et al.*, Phys. Rev. D **10**, 2599 (1974).

[65] Y. Nambu and G. Jona-Lasinio, Phys. Rev. **122**, 345 (1961).

[66] Y. Nambu and G. Jona-Lasinio, Phys. Rev. **124**, 246 (1961).

[67] T. Hatsuda and T. Kunihiro, Phys. Rep. **247**, 221 (1994).

[68] K. Wilson, Phys. Rev. D **10**, 2445 (1974).

[69] F. Karsch, Lect.Notes Phys. **583**, 209 (2002).

[70] F. Karsch, E. Laermann and A. Peikert, Phys. Lett. B478, 447 (2000).

[71] A. Ali Khan *et al.*, Phys. Rev. D **64**, 074510 (2001).

[72] M. Asakawa and K. Yazaki, Nucl. Phys. A **504**, 668 (1989).

[73] A. Barducci *et al.*, Phys. Lett. B **231**, 463 (1989).

[74] A. Barducci *et al.*, Phys. Rev. D **41**, 1610 (1990).

[75] A. Barducci *et al.*, Phys. Rev. D **49**, 426 (1994).

[76] J. Berges and K. Rajagopal, Nucl. Phys. B **538**, 215 (1999).

[77] M. A. Halasz *et al.*, Phys. Rev. D **58**, 096007 (1998).

[78] O. Scavenius *et al.*, Phys. Rev. C **64**, 045202 (2001).

[79] N. G. Antoniou and A. S. Kapoyannis, Phys. Lett. B **563**, 165 (2003).

[80] Y. Hatta and T. Ikeda, Phys. Rev. D **67**, 014028 (2003).

[81] A. Barducci *et al.*, Phys. Rev. D **72**, 056002 (2005)

[82] S. Roessner, C. Ratti and W. Weise, Phys. Rev. D **75**, 034007 (2007)

[83] Z. Fodor and S. D. Katz, JHEP **0203**, 014 (2002).

[84] Z. Fodor and S. D. Katz, JHEP **0404**, 050 (2002).

[85] S. Ejiri *et al.*, Prog. Theor. Phys. Suppl. **153**, 118 (2004).

[86] R. V. Gavai and S. Gupta, Phys. Rev. D **71**, 114014 (2005)

[87] P. de Forcrand and O. Philipsen, Nucl. Phys. B **673**, 170 (2003).

[88] P. de Forcrand and O. Philipsen, Nucl. Phys. Proc. Suppl. **129**, 521 (2004).

[89] P. Braun-Munzinger, I. Heppe, and J. Stachel, Phys. Lett. **B** 465, 15 (1999).

[90] M. M. Aggarwal *et al.*, Phys. Rev. C **83**, 034910 (2011).

[91] B. Abelev *et al.*, Phys. Rev. C **79**, 034909 (2009).

[92] B. Abelev *et al.*, Phys. Rev. C **81**, 024911 (2010).

[93] J. Cleymans *et al.*, Phys. Rev. C **73**, 034905 (2006).

[94] F. Becattini *et al.*, ibid. **64**, 024901 (2001).

[95] A. Adare *et al.*, Phys. Rev. C **81**, 034911 (2010).

[96] S. S. Adler *et al.*, Phys. Rev. Lett. **94**, 232301 (2005).

[97] S. S. Adler *et al.*, Phys. Rev. Lett. **98**, 012002 (2007).

[98] Y. Aoki, Z. Fodor, S. D. Katz and K. K. Szabo, Phys. Lett. B **643**, 46 (2006).

[99] M. Cheng *et al.*, Phys. Rev. D **74**, 054507 (2006).

[100] A. Bazavov *et al.*, Phys. Rev. D **85**, 054503 (2012).

[101] S. Borsanyi, S. Durr. Z. Fodor, C. Hoelbling, S. D. Katz, S. Krieg, D. Nogradi, K. K. Szabo, B. C. Toth and N. Trombitas, JHEP 1208, (**2012**) 126.

[102] T. Umeda *et al.*, PoS LATTICE **2012** (2012) 074.

[103] A. Bazavov *et al.*, Phys. Rev. D **86**, 094503 (2012).

[104] S. Borsanyi, Y. Delgado, S. Durr, Z. Fodor, S. D. Katz, S. Krieg, T. Lippert, D. Nogradi and K. K. Szabo, Phys. Lett. B **713**, 342 (2012).

[105] T. Hatsuda and S. H. Lee, Phys. Rev. C **46**, R34 (1992).

[106] C. E. Brown and Mannque Rho, Phys. Rev. Lett. **66**, 2720 (1991).

[107] M. Naruki *et al.*, Phys. Rev. Lett. **96**, 092301 (2006).

[108] R. Muto *et al.*, Phys. Rev. Lett. **98**, 042501 (2007).

[109] M. H. Wood *et al.*, Phys. Rev. C **78**, 015201 (2008).

[110] M. Nanova *et al.*, Phys. Rev. C **82**, 035209 (2010).

[111] M. Effenberger and U. Mosel, Phys. Rev. C **62**, 014605 (2000).

[112] M. Effenberger *et al.*, Phys. Rev. C **60**, 027601 (1999).

[113] R. D. Pisarski, Phys. Lett. B **110**, 155 (1982).

[114] M. Asakawa and C. M. Ko, Nucl. Phys. A **572**, 732 (1994).

[115] R. Rapp, Phys. Rev. C **63**, 054907 (2001).

[116] M. Harada and C. Sasaki, Phys. Rev. D **74**, 114006 (2006).

[117] Johannes P. Wessels *et al.*), Nucl. Phys. A **715**, 262 (2003).

[118] R. Arnaldi *et al.*), Phys. Rev. Lett. **96**, 162302 (2006).

[119] A. Adare *et al.*, Phys. Rev. D **76**, 051106(R) (2007).

[120] A. Adare *et al.*, Phys. Rev. C **83**, 064903 (2011).

[121] J.Adams *et al.*, Phys. Lett. B **616**, 8 (2005).

[122] A. Adare *et al.*, Phys. Rev. D **83**, 052004 (2011).

[123] B.I. Abelev *et al.*, Phys. Rev. C **75**, 064901 (2007).

[124] A. Adare *et al.*, Phys. Rev. D **83**, 032001 (2011).

[125] S. S. Adler *et al.*, Phys. Rev. C **75**, 024909 (2007).

[126] J.Adams. *et al.*, Phys. Rev. Lett. **92**, 092301 (2004).

[127] A. Adare *et al.*, Phys. Rev. Lett. **97**, 252002 (2006).

[128] A. Adare *et al.*, Phys. Rev. Lett. **101**, 232301 (2008).

[129] B. I. Abelev *et al.*, Phys. Rev. C **80**, 44905 (2009).

[130] S. S. Adler *et al.*, Phys. Rev. C **69**, 034909 (2004).

[131] A. Adare *et al.*, Phys. Rev. C **82**, 011902(R) (2010).

[132] A. Adare *et al.*, Phys. Rev. C **83**, 024909 (2011).

[133] A. Adare *et al.*, Phys. Rev. C **84**, 044902 (2011).

[134] A. Adare *et al.*, Phys. Rev. C **84**, 044905 (2011).

[135] C. Tsallis, J. Stat. Phys. **52**, 479 (1988).

[136] N. M. Kroll and W. Wada, Phys. Rev. **98**, 1355 (1955).

[137] L. G. Landsberg, Phys. Rep. **128**, 301 (1985).

[138] R. I. Dzhelyadin *et al.*, Phys. Lett. B **102**, 296 (1981).

[139] H. J. Behrend *et al.*, Z. Phys. C **49**, 401 (1991).

[140] J. H. Hubbel, H. A. Gimm and I. Overbo, J. Phys. Chem. Ref. Data **9**, 1023 (1980).

[141] H. Bethe and W. Heitler, Proc. R. Soc. Lond. A. **146**, 8 (1934).

[142] "Physics Reference Manual (Version: geant4 9.5.0)"

[143] Y. S. Tsai, Rev. Mod. Phys. **46**, 815 (1974).

[144] Y. S. Tsai, Rev. Mod. Phys. **49**, 421 (1977).

[145] H. A. Bethe and L. C. Maximon, Phys. Rev. **93**, 768 (1954).

[146] R. Vogt, Heavy Ion Phys. **17**, 75 (2003).

[147] C. Peterson *et. al*, Phys. Rev. D **27**, 105 (1983).

[148] V. G. Kartvelishvili *et. al*, Phys. Lett. B **78**, 615 (1978).

[149] P. Collins and T. Spiller, J. Phys. G **11**, 1289 (1985).

[150] G. Colangelo and P. Nason, Phys. Lett. B **285**, 167 (1992).

[151] M. G. Bowler, Z. Phys. C **11**, 169 (1981).

[152] Andre Mischke, Phys. Lett. B **671**, 361 (2009).

[153] K. Aamodt *et al.*, JINST **3**, S08002 (2010).

[154] G. Aad *et al.*, JINST **3**, S08003 (2008).

[155] L. Adamczyk *et al.*, Phys. Rev. C **86**, 024906 (2012).

[156] Y. Akiba *et al.*, Nucl. Instrum. Methods Phys. Res., Sect. A **453**, 279 (2000).

[157] D. Ben-Tzvi and M. B. Sandler, Patt. Reco. Lett., **11**, 167 (1990).

[158] M. Ohlsson, C. Peterson and A. L. Yuille, Comp. Phys. Comm. **71**, 77 (1992).

[159] D. B. Steski *et al.*, Rev. Sci. Instrum. **73**, 797 (2002).

[160] K. Adcox *et al.*, Nucl. Instr. and Meth. A **499**, 469 (2003).

[161] K. Ackermann *et al.*, Nucl. Instr. and Meth. A **499**, 624 (2003).

[162] B. Back *et al.*, Nucl. Instr. and Meth. A **499**, 603 (2003).

[163] M. Adamczyk *et al.*, Nucl. Instr. and Meth. A **499**, 437 (2003).

[164] M. Allen *et al.*, Nucl. Instr. and Meth. A **499**, 549 (2003).

[165] M. Aizawa *et al.*, Nucl. Instr. and Meth. A **499**, 508 (2003).

[166] S.H. Aronson *et al.*, Nucl. Instr. and Meth. A **499**, 480 (2003).

[167] C. Adler *et al.*, Nucl. Instr. and Meth. A **470**, 488 (2001).

[168] S. S. Adler *et al.*, Nucl. Instr. and Meth. A **499**, 433 (2003).

[169] M. Chiu *et al.*, Phys. Rev. Lett. **89**, 012302 (2002).

[170] K. Adcox *et al.*, Nucl. Instr. and Meth. A **499**, 489 (2003).

[171] Y. Akiba *et al.*, Nucl. Instrum. Method Phys. Res., Sect. A **453**, 279 (2000).

[172] H. Fessler *et al.*, Nucl. Instr. and Meth., A **228**, 303 (1985).

[173] L. Aphecetche *et al.*, Nucl. Instr. and Meth. A **499**, 521 (2003).

[174] T. C. Awes *et al.*, arXiv:nucl-ex/0202009 (2002).

[175] T. C. Awes *et al.*, Nucl. Instrum. Method Phys. Res., Sect. A **311**, 122 (1992).

[176] S.S. Adler *et al.*, Nucl. Instr. and Meth. A **499**, 560 (2003).

[177] W. M. Yao *et al.*, Journal of Physics G **33**, 1 (2006).

[178] PHENIX website. (URL: http://www.phenix.gov)

[179] T. Hachiya *et al.*, PHENIX Analysis Note **107** (2002).

[180] J. Nagile *et al.*, PHENIX Analysis Note **113** (2002).

[181] S.S. Adler *et al.*, Phys. Rev. C **75**, 024909 (2007).

[182] J. T. Mitchell *et al.*, Nucl. Instrum. Methods Phys. Res., Sect. A **482**, 491 (2002).

[183] D. Ben-Tzvi and M. B. Sandler, Patt. Reco. Lett., **11**, 167 (1990).

[184] M. Ohlsson, C. Peterson and A. L. Yuille, Comp. Phys. Comm. **71**, 77 (1992).

[185] S.S.Adler *et al.*, Phys. Rev. C **69**, 034910 (2004).

[186] G.I. Kopylov, Phys. Lett. B **50**, 472 (1974).

[187] D. Drijard, H.G. Fischer and T. Nakada, Nucl. Instrum. Methods Phys. Res., Sect. A **225**, 367 (1984).

[188] A. Milov *et al.*, PHENIX Analysis Note **673** (2008).

[189] S. V. Greene *et al.*, PHENIX Analysis Note **422** (2005).

[190] S. S. Adler *et al.*, Phys. Rev. C **72**, 014903 (2005).

[191] K. M. Kijima *et al.*, PHENIX Analysis Note **610** (2008).

[192] T. Dahms *et al.*, PHENIX Analysis Note **614** (2008).

[193] D. Sharma *et al.*, PHENIX Analysis Note **618** (2008)

[194] S. S. Adler *et al.*, Phys. Rev. C **75**, 051902(R) (2007).

[195] D. Ivanishchev *et al.*, PHENIX Analysis Note **535** (2006).

[196] M.Ouchida *et al.*, PHENIX Analysis Note **612** (2007).

[197] A.Milov *et al.*, PHENIX Analysis Note **537** (2006).

[198] A. Kozlov *et al.*, PHENIX Analysis Note **702** (2008).

[199] K. Ozawa *et al.*, PHENIX Analysis Note **411** (2005).

[200] K. Aamodt *et al.*, Phys. Lett. B **696**, 30 (2011).

[201] K. Aamodt *et al.*, Eur. Phys. J. C **68**, 89 (2010).

[202] G. J. Gounaris and J. J. Sakurai, Phys. Rev. Lett. **21**, 244 (1968).

[203] M. Cacciari, P. Nason and R. Vogt, Phys. Rev. Lett. **95**, 122001 (2005).

[204] A. Adare *et al.*, Phys. Rev. Lett. **103**, 082002 (2009).

[205] M. M. Aggarwal *et al.*, Phys. Rev. Lett. **105**, 202301 (2010).

[206] B. Abelev *et al.*, Phys. Lett. B **721**, 13 (2013).

[207] B. Abelev *et al.*, Phys. Lett. B **717**, 162 (2012).

[208] B. Abelev *et al.*, Eur. Phys. J. C **72**, 2183 (2012).

[209] B. Abelev *et al.*, Phys. Rev. D **86**, 112007 (2012).

公表論文

(1) Measurability of ϕ, ω, and ρ mesons via di-electron decays in high-temperature states produced in heavy-ion collisions
Yoshihide Nakamiya and Kensuke Homma
・・・・・・Progress of Theoretical and Experimental Physics, 113H01 (2013)
DOI: 10.1093/ptep/ptt088

参考論文

(1) Nuclear modification factors of ϕ mesons in d+Au, Cu+Cu, and Au+Au collisions at $\sqrt{s_{NN}}$ = 200 GeV
A. Adare *et al.* (PHENIX Collaboration)
・・・・・・・Physical Review C83, 024909 (2011)
DOI: 10.1103/PhysRevC.83.024909

(2) Production of ω mesons in p+p, d+Au, Cu+Cu, and Au+Au collisions at $\sqrt{s_{NN}}$ = 200 GeV
A. Adare *et al.* (PHENIX Collaboration)
・・・・・・・Physical Review C84, 044902 (2011)
DOI: 10.1103/PhysRevC.84.044902